

Piezoelectric Ultrasonic Micromotors

Anita M. Flynn

MIT Artificial Intelligence Laboratory

December, 1997

Abstract

This thesis describes development of a new actuator technology for integrated machines of the future: piezoelectric ultrasonic micromotors. Ultrasonic motors offer the advantages of low speed, high torque operation without the need for gears. They can be made compact and lightweight and provide a holding torque in the absence of applied power due to the traveling wave frictional coupling mechanism between the rotor and the stator.

Whereas ultrasonic motors would typically be made from a bulk ferroelectric ceramic such as lead zirconate titanate, or PZT, this thesis describes the implementation of a new idea – that of using PZT in a sol-gel form deposited directly onto silicon to create high-torque motors compatible with silicon integration technologies. Due to large dielectric constants and increased breakdown strengths of thin-film PZT, ultrasonic micromotors offer a factor of 1000 improvement in energy density over electrostatic micromotors. In a joint project with the Penn State Materials Research Laboratory and MIT Lincoln Laboratory, 2 mm and 5 mm diameter stator structures were fabricated on 1 μm thick silicon nitride membranes. Small glass lenses placed down on top spun at 100-300 rpm with 4 V excitation at 90 kHz.

While generation of appropriate traveling bending waves in the stator is fairly well understood, less is known about how the frictional coupling and surface properties at the rotor-stator interface affect mechanical power output performance. This thesis proposes models for production of torque in rotary ultrasonic motors. Models of line contact, Hertzian contact and linear spring contact for Coulomb and viscous friction have been derived and simulations are presented which predict speed-torque curves, efficiencies and overall output power for various conditions of operating voltage and normal force.

To validate these models, a set of 8 mm diameter \times 3 mm tall motors, in a designed experiment, has been fabricated. These devices have demonstrated maximum stall torques of 10^{-3} Nm, maximum no-load speeds of 1710 rpm and peak power outputs of 27 mW. The resulting peak power density is $108 \frac{\text{W}}{\text{kg}}$, more than double that of human muscle.

This thesis further describes a laser-etching process which has been developed to fabricate more practical piezoelectric ultrasonic micromotors. This laser-based process produces thin-film PZT-on-silicon stators without the need for mask alignment, wet-etching or fragile membranes. The large power densities and stall torques of these piezoelectric ultrasonic motors offer tremendous promise for integrated machines: complete intelligent, electro-mechanical autonomous systems mass-produced in a single fabrication process.

Acknowledgments

I would like to thank a number of people who have been instrumental in guiding this research and providing useful advice throughout its course. My advisor, Prof. Rodney Brooks of the MIT Artificial Intelligence Laboratory and members of my committee, Prof. David Staelin of the MIT Research Laboratory of Electronics, Prof. L. Eric Cross of the Pennsylvania University Materials Research Laboratory, Prof. Nesbitt Hagood of the MIT Aeronautics and Astronautics Department and Dr. Daniel Ehrlich of the MIT Lincoln Laboratory Solid State Division, were able to lend a breadth of expertise to this project which was invaluable.

Many people have been helpful in both discussions of modeling issues of ultrasonic motors and in giving useful comments on earlier drafts of this thesis. I would especially like to thank Andrew Christian of the MIT Artificial Intelligence Laboratory, Andrew McFarland and Timothy Glenn of the MIT Space Engineering Research Center, Prof. Jan Smits of Boston University, Prof. Kim Vandiver of the MIT Ocean Engineering Department, Mary Tolikas of the MIT Laboratory for Electromagnetic and Electronic Systems, Prof. Joerg Wallaschek of Heinz Nixdorf Institut in Paderborn, Germany and Dr. Peter Rehbein of the Robert Bosch Co. in Gerlingen-Schillerhohe, Germany.

The work on the thin-film PZT ultrasonic motors was a collaborative effort amongst a number of people. Dr. K.R. Udayakumar of the Pennsylvania State University Materials Research Laboratory was the driving force behind development of the sol-gel PZT films, along with colleagues Dr. Keith Brooks and Daniel Chen. Silicon micromachining was performed at MIT Lincoln Laboratory and I am indebted to the help of Steve Palmucci, Dr. Carl Bozler and Chet Bukowski. Richard Perilli of the MIT Center for Materials Science and Engineering was helpful in the prepping of wafers and surface characterizations.

Robert Carter and Richard Kensley of Piezo Systems, Inc. were invaluable in the patterning of the bulk ceramics. I also appreciate the assistance of Q. M. Zhang and Hong Wang of the Penn State Materials Research Laboratory in interferometry studies and Dr. Mark Lucente of the MIT Media Laboratory for his assistance in setting up interferometric measurements at MIT.

Finally, I must thank Dean Franck, my undergraduate research assistant, who spent many long hours with me in the lab building and testing little motors.

Contents

1	Introduction	8
1.1	Overview of Ultrasonic Motors	10
2	Ultrasonic Micromotors for Microrobots	13
2.1	Advantages of Piezoelectric Motors	16
2.2	From Materials to Devices	19
2.2.1	Keeping Things Simple	19
2.2.2	Stators and Rotors	21
2.2.3	The Process	24
2.3	Results	26
3	Ultrasonic Motors	29
3.1	Bulk 8 mm Motors	30
3.2	Vibration of Rings	30
3.3	Eigenfrequencies and Wavespeeds	34
3.4	Traveling Waves and Elliptic Motion	35
3.5	Mechanical Modeling of the Stator	38
3.6	Deflection of the Stator	43
4	Electrical Modeling of the Stator	51
5	Energy Conversion	55
6	Contact Mechanics	62
6.1	Line Contact, Coulomb Friction	66
6.2	Line Contact, Viscous Friction	72

6.3	Area Contact, Coulomb Friction	76
6.3.1	Physical Interpretation	76
6.3.2	Hertzian Contact Model	90
6.3.3	Linear Spring Model	103
6.4	Extensions	113
7	Experiments with 8 mm Bulk Motors	114
7.1	Initial Tests With Early Prototypes	114
7.2	Second Generation 8 mm Bulk Motors	118
7.2.1	Bonds and Electrodes	119
7.2.2	Design of Experiments	120
7.2.3	Fabricating Bulk PZT 8 mm Motors	123
7.3	Results From Second Generation 8 mm Motors	125
7.3.1	Design of Experiments Results	125
7.3.2	Speed-Torque Curves	130
7.3.3	Yellow1	130
7.3.4	Fucia1	133
7.3.5	Grey1	135
7.3.6	Magnitude and Phase of Impedance and Damping Measurements . .	139
7.3.7	Interferometric Displacement Measurements	141
7.3.8	Efficiency Measurements and Drive Electronics	147
7.3.9	Coefficients of Friction	148
7.3.10	Matching to a Model	148
7.3.11	Surface Profilometry Measurements	152
7.4	Comparing Motor Figures of Merit	158
7.4.1	Stall Torque and Output Power Densities	158
7.4.2	Comparisons to Other Actuator Technologies	158
8	Laser Etching of Thin-Film PZT Motors	162
9	Conclusion	164
	References	166

A Stator Motion	175
B Variational Methods in Modeling Active Structures	178
B.1 Hamilton's Principle	179
B.2 Laminated Plate Dynamics	187
B.2.1 Simulation Results	196

Chapter 1

Introduction

Ferroelectric thin films incorporated into new ultrasonic micromotors can create actuators with orders of magnitude more energy density than electrostatic micromotors. Because the coupling of vibrational energy from the stator into rotational motion of the rotor involves frictional contact however, these motors are not as well understood as conventional electromagnetic or electrostatic motors. The aim of the research described herein has been two-fold: to develop a new high-torque, low-speed actuator technology useful in micro-robotic applications and to increase our understanding of the frictional coupling mechanism at the rotor-stator interface of an ultrasonic motor.

The research effort undertaken ranges from theoretical modeling of torque production in ultrasonic motors to development of a completely new type of microactuator using sol-gel lead zirconate titanate, PZT. These devices were fabricated in a joint project between the MIT Mobile Robot Group at the Artificial Intelligence Laboratory (the author's home laboratory), the Pennsylvania State University's Material Research Laboratory and MIT Lincoln Laboratory's Solid State Division.

The ultimate goal has been to integrate all the subsystems of a mobile robot, the intelligence system, the sensors, the actuators and the power supply, onto a single silicon substrate and mass-produce robots much the way we mass-produce integrated circuits. This idea of such a *gnat robot* was conceived after initial proposals were made for fabricating electrostatic micromotors on silicon. However, the low-torque, high-speed nature of variable-capacitance electrostatic micromotors made them ill-suited for robot propulsion, hence the search for a better motor.

While ultrasonic motors inherently deliver high torque at low-speed, piezoelectric ultrasonic motors were typically built by bonding a bulk ceramic ferroelectric material with very large piezoelectric coefficients, such as PZT, onto a non-piezoelectric material to create a ring-shaped bimorph structure capable of sustaining traveling flexure waves. Due to the bulk ceramic formulation of the PZT material, ultrasonic motors were not amenable to fabrication in a silicon process. Our idea was to create a sol-gel formulation of PZT, spin it onto a silicon wafer in much the same manner as photoresist and use silicon micromachining techniques to etch motor structures. This report details our initial fabrication attempts and relates subsequent efforts aimed at modeling and improving the devices, in both thin-film and bulk ceramic form, for increased output performance.

Specifically, the contributions of this dissertation include:

- Fabrication of the world's first ferroelectric thin-film motor
- Analysis of models of interface contact mechanics
- Characterization of 8 mm bulk motors based on design-of-experiments techniques
- Development of a laser-machining process for fabricating new thin-film stators which requires no masks and no wet-etching

Subsequent to a brief overview of ultrasonic motors later in this chapter, Chapter 2 details the development of microfabricated ultrasonic motors. Much of this work was originally published in [Flynn et al. 92]. After initial experiments were performed with thin-film PZT ultrasonic micromotors to determine feasibility, the project was split in order to separate further development of the new thin-film PZT materials from development of new devices. Research was undertaken at the Penn State Materials Research Laboratory to fabricate thicker films with larger-area electrode coverage, while a parallel effort was begun at the MIT Artificial Intelligence Laboratory to model, fabricate and test bulk-ceramic 8 mm piezoelectric ultrasonic motors to enhance our understanding of the frictional coupling mechanism.

Chapters 3 through 6 describe these models of ultrasonic motors, from stator vibration analysis through contact mechanics. Models of line contact, Hertzian contact and linear spring contact for Coulomb and viscous friction have been derived and simulations are presented which predict speed-torque curves, efficiencies and overall output power for various

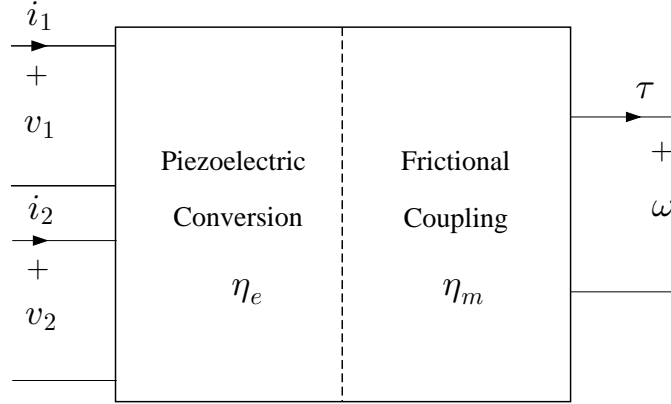


Figure 1-1: There are two levels of energy conversion in a piezoelectric ultrasonic motor. Electrical energy is first converted to strain energy through piezoelectric elements, where time changing electrical fields induce vibratory motion. The high-frequency, small-amplitude vibration is then rectified to lower-frequency unidirectional movement through vibro-impact frictional coupling.

conditions of operating voltage and normal force. Chapter 7 discusses fabrication and testing of the prototype 8 mm diameter bulk motors. It was found that these devices could produce maximum stall torques of 10^{-3} Nm (10 gf-cm), maximum no-load speeds of 1710 rpm and peak power outputs of 28 mW. The resulting peak power density is $108 \frac{W}{kg}$, for these motors weighing on the order of one third of a gram. Chapter 8 discusses a new process developed for creating thin-film PZT-on-silicon motors on the same scale as the 8 mm bulk motors, but free from the wafer and from other constraints of a typical silicon microfabrication process. Chapter 9 gives a summary and conclusions and Appendices A and B relate additional background on mechanics and materials parameters.

1.1 Overview of Ultrasonic Motors

While most electric machines convert electrical energy to mechanical energy through the interaction of currents and magnetic fields, a new class of actuators has arisen which utilizes the effect of electrically induced vibratory motion converted to unidirectional motion through frictional coupling. These actuators, or vibration converters, come in a variety of physical embodiments and can be realized via different modes of vibration. They can be excited through piezoelectric, electrostrictive or magnetostrictive transduction mechanisms, but typically, the exciting transducers are piezoelectric elements and driving frequencies are in the range of 20 kHz to 150 kHz. This subset of vibromotors, piezoelectric ultrasonic motors, was first invented by the Soviets [Vishnevsky et al. 77], [Ragulskis et al. 88], first

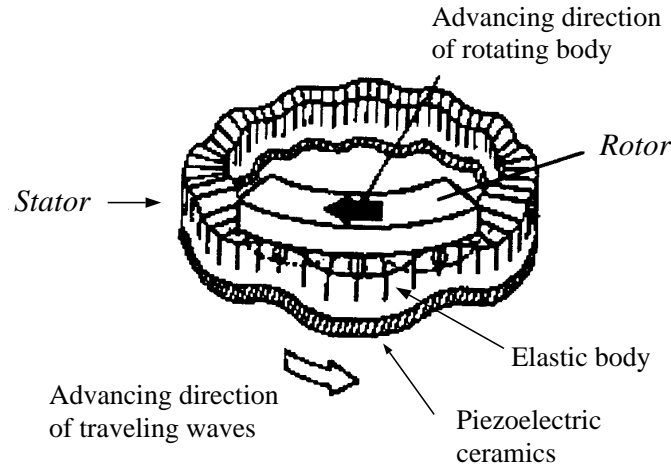


Figure 1-2: Traveling waves can be induced in a waveguide structure such as the annular disk shown here. Points on the surface of the ring move in retrograde elliptical motions. A rotor pressed against the stator is propelled along in the reverse direction from the propagating wave. Figure from [Inaba et al. 87].

commercialized by the Japanese [Inaba et al. 87], [Sashida 82], [Sashida 85], [Shinsei 89], [Okumura and Mukohjima 87], [Hosoe 89], [Kasuga et al. 92], [Sashida and Kenjo 93], [Tomikawa and Ueha 93] and first microfabricated by the Americans [Moroney et al. 89], [Flynn et al. 92].

As shown in Figure 1-1, piezoelectric ultrasonic motors have a two-stage energy conversion process. In the first stage, piezoelectric elements convert electrical energy into oscillatory bending motion. Depending on the geometry of the device and the form of the excitation, longitudinal, torsional or flexural modes of bending can be induced in the structure to produce either standing or traveling waves of deformation. A traveling wave ring-type ultrasonic motor is depicted in Figure 1-2.

Whatever the cause of the motion, all ultrasonic motors have a common form of second-stage energy conversion, wherein high frequency oscillatory vibration of a stator is rectified into macroscopic, unidirectional rotary or linear motion of a rotor or carriage. The mechanism for energy conversion is a frictional impact between the rotor and stator surfaces. While free vibration of the stator in the first stage of energy conversion is a linear phenomenon and the equations of motion can be formulated as an eigenvalue problem, the second-stage conversion of stator to rotor motion is a vibro-impact system and inherently displays non-linear dynamics because vibration cycles of the stator surface cease to be symmetric due to impact with the rotor.

This thesis work concentrates on the second-stage energy conversion process, the frictional interaction between rotor and stator. Specifically, we focus on traveling wave motors which have time-continuous forms of contact between stator and rotor.

We are interested in studying piezoelectric traveling wave ultrasonic motors for a number of reasons. One is that they have been shown to exhibit high-torque, low-speed characteristics without the requirements for gears. The other is that, because the stator structures are planar, ultrasonic motor technology is symbiotic with microfabrication techniques, and early results [Udayakumar et al. 91] have shown that new thin-film forms of piezoceramics can yield energy densities three orders of magnitude larger than energy densities in microfabricated electrostatic motors. High energy densities and high torques are important in robotics applications, especially for autonomous machines which must carry their own power supplies.

While small piezoelectric motors appear promising, there are many phenomena which are not well understood. The form of the friction law describing rotor-stator interaction, impact processes, effects of surface roughness, material hardness, wear, normal pressure, boundary layer regimes and bearings and mounts need to be studied in order to optimize and design efficient, compact ultrasonic motors.

Chapter 2

Ultrasonic Micromotors for Microrobots

Today's robots are large, expensive and not too clever. Robots of the future may be small and cheap (and perhaps still not too clever). But if we could achieve even insect level intelligence while scaling down sizes and costs, there may be tremendous opportunities for creating useful robots. From autonomous sensors to robots cheap enough to throw away when they have completed their task – microrobots provide a new way of thinking about robotics.

Our goal of building gnat-sized robots has been driven by recent successes in developing intelligence architectures for mobile robots which can be compiled efficiently into parallel networks on silicon. Brooks' subsumption-style architectures [Brooks 86] provide a way of combining distributed real time control with sensor-triggered behaviors to produce a variety of robots exhibiting “insect level” intelligence [Brooks 89], [Angle 89], [Connell 90], [Mataric 90], [Flynn, Brooks, Wells and Barrett 89], [Maes and Brooks 90]. This assemblage of artificial creatures includes soda can collecting robots, sonar-guided explorers, six-legged arthropods that learn to walk, and a “bug” that hides in the dark and moves towards noises.

One of the most interesting aspects of the subsumption architecture has to do with the way it handles *sensor fusion*, the issue of combining information from various, possibly conflicting, sensors. Typically, sensor data is fused into a global data structure and robot actions are planned accordingly. A subsumption architecture however, instead of making explicit judgments about sensor validity, encapsulates a strategy that might be termed

sensor fission, whereby sensors are only dealt with implicitly in that they activate behaviors. Behaviors are just layers of control systems that all run in parallel whenever appropriate sensors fire. The problem of conflicting sensor data then is handed off to the problem of conflicting behaviors. “Fusion” consequently is performed at the output of behaviors (*behavior fusion*) rather than the output of sensors. A prioritized arbitration scheme then selects the dominant behavior for a given scenario.

The ramification of this distributed approach to handling vast quantities of sensor data is that it takes far less computational hardware. Since there is no need to handle the complexities of maintaining and updating a map of the environment, the resulting control system becomes very lean and elegant.

The original idea for gnat robots [Flynn 87] came about when this realization that subsumption architectures could compile straightforwardly to gates coincided with a proposal [Bart et al. 88] to fabricate an electrostatic motor on a chip (approximately 100 μm in diameter). Early calculations for this silicon micromotor forecast small but useful amounts of power. Already, many types of sensors (i.e. imaging sensors, infrared sensors, force sensors) microfabricated on silicon are commercially available. If a suitable power supply could be obtained (solar cells are silicon and thin film batteries are beginning to appear in research laboratories), the pieces might begin to fit.

The driving vision is to develop a technology where complete machines can be fabricated in a single process, alleviating the need for connectors and wiring harnesses and the necessity for acquiring components from a variety of vendors as would be found in a traditional large-scale robot. The microrobots would be designed in software through a “robot compiler” and a foundry would convert the files to masks and then print the robots en masse. One critical technology presently missing is a batch-fabricatable micromotor which can couple useful power out to a load.

Various types of intriguing microactuators have recently appeared. One example is the variable capacitance silicon electrostatic motor (which is based on the force created due to charge attraction as two plates move past each other) [Tai, Fan and Muller 89], [Fujita, Omodaka, Sakata and Hatazawa 89], [Mehregany, Bart, Tavrow, Lang and Senturia 90]. Figure 2-1 illustrates one such electrostatic micromotor. Another type of micromotor is a “wobble” motor, where one cylinder precesses inside another, again due to electrostatic forces [Jacobsen et al. 89], [Trimmer and Jebens 89]. Figure 2-2 illustrates a wobble motor.

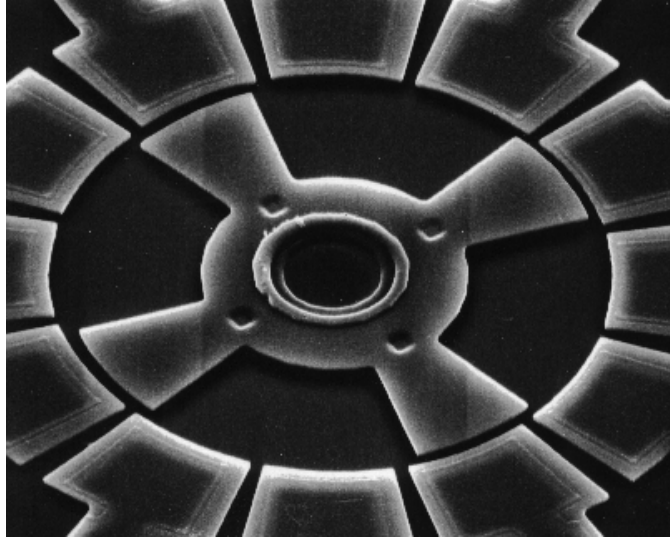


Figure 2-1: A variable capacitance motor has a $100\ \mu\text{m}$ diameter rotor which revolves around a bearing as oppositely placed stators are sequentially stepped with the applied drive voltages. Figure from [Tavrow 91].

In general, electrostatic motors are preferred over magnetostatic motors in the microworld because electrostatic forces scale favorably as dimensions shrink and because dielectric materials are more easily patterned and processed than magnetic materials, especially in the realm of silicon processing. The three-dimensional windings required for magnetostatic motors would be very hard to fabricate in silicon, but the small gap sizes that allow electrostatic motors to take advantage of the ability to withstand increased electric fields before breakdown are easily fabricated using photolithographic techniques. Electrostatic micromotors have demonstrated successes but also uncovered limitations. Problems with these types of motors arise in the areas of friction, fabrication aspect ratio constraints, and low torque-to-speed characteristics.

[Flynn, Brooks and Tavrow 89] provides a detailed summary of these problems and proposes a piezoelectric ultrasonic micromotor as an alternative approach. This structure, fabricated from thin-film lead zirconate titanate, PZT, circumvents many of the drawbacks of electrostatic micromotors.

Our idea is based on the underlying principles of commercially available ultrasonic motors presently popular in Japan [Inaba et al. 87], [Akiyama 87], [Shinsei 89], [Kumada 90], [Sashida and Kenjo 93] and [Ueha and Tomikawa 93], which essentially convert electrical power to mechanical power through a piezoelectric interaction. Mechanical power is then coupled to a load through a frictional phenomenon induced by a traveling wave de-

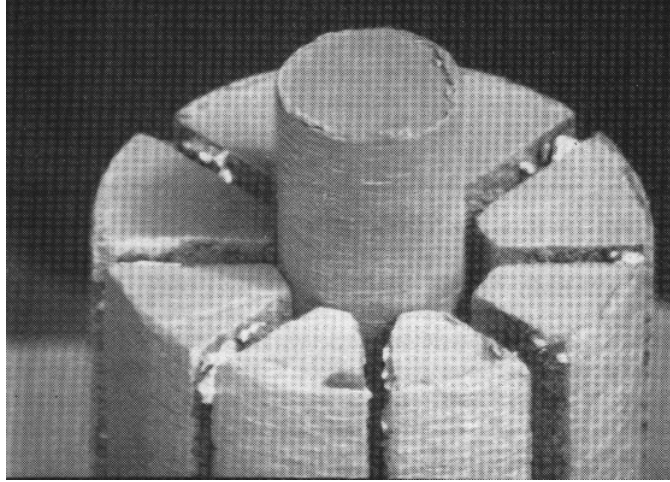


Figure 2-2: The wobble motor contains a rotor which is attracted to active electrodes as the drive voltages are sequenced around the perimeter, similar to a variable capacitance motor. Since the rotor is the bearing, it tends to “wobble”. Figure from [Jacobsen et al. 89].

formation of the material. Piezoelectric motors display distinct advantages over traditional electromagnetic motors such as small size, low noise, and high torque-to-speed ratios. These commercially available motors however, use PZT in its bulk ceramic form, which must be cut and milled.

Our contribution has been to realize that if PZT can be deposited in a thin-film form compatible with silicon processing, then motors can be manufactured in a batch printing process instead of being individually machined.

Additionally, these motors should show significant improvements in performance over bulk PZT motors. That is, because the films are very thin, it is possible to apply much higher electric fields than in thicker bulk devices. This leads to higher energy densities.

2.1 Advantages of Piezoelectric Motors

Energy Density – The argument for pursuing piezoelectric ultrasonic micromotors is based on energy density considerations. The maximum energy density storeable in the air gap of an electrostatic micromotor is

$$\frac{1}{2}\epsilon_{air}E_{bd}^2$$

where E_{bd} is the maximum electric field before breakdown (approximately $10^8 \frac{V}{m}$ for $1 \mu m$ gaps) and where ϵ_{air} is the permittivity of air (equal to that of free space).

For a piezoelectric motor made from a ferroelectric material such as PZT, the energy

density becomes

$$\frac{1}{2}\epsilon_{pzt}E_{bd}^2$$

Thin film PZT can similarly withstand high electric fields ($E_{bd} \cong 10^8 \frac{V}{m}$), but the dielectric constant is three orders of magnitude larger ($\epsilon_{pzt} \cong 1300\epsilon_0$) than air. Other types of thin film piezoelectric (but not ferroelectric) ultrasonic actuators have been produced [Moroney et al. 89] from zinc oxide, but the dielectric constant is only one order of magnitude larger ($\epsilon_{zo} \cong 10\epsilon_0$) than air. The greater the energy density stored in the gap, the greater the potential for converting to larger torques, or useful work out.

Low Voltages – Piezoelectric motors are not required to support an air gap. Mechanical forces instead, are generated by applying a voltage directly across the piezoelectric film. Because these ferroelectric films are very thin (ours are typically $0.3 \mu\text{m}$), intense electric fields can be established with fairly low voltages. Consequently, we drive our thin film PZT motors with two to three volts as opposed to the hundred or so volts needed in air-gap electrostatic actuators.

Geardown – Energy density comparisons may be the primary motivators in pursuing PZT micromotors, but there are other advantages as well. Because this strong dielectric material also *bends* with applied voltage, mechanical power can be coupled out in unique ways. Figure 1-2 illustrated an ultrasonic traveling wave motor marketed by Matsushita (Panasonic). Two bulk ceramic layers of PZT are placed atop one another. Each layer is segmented such that neighboring segments are alternately poled. That is, for a given polarity of applied voltage, one segment contracts while its neighbor expands. These two layers are placed atop one another but offset so that they are spatially out of phase. When also driven temporally out of phase, the two piezoelectric layers induce a traveling wave of bending in the elastic body. Any point on the surface of the stator then moves in an ellipse and by contacting a rotor onto the stator, the rotor is pulled along through frictional coupling. Fast vibratory vertical motions are transformed into a slower macroscopic motion tangential to the surface where peak performance is attained at resonance. This geardown means that we can fabricate motors without the need for gearboxes. This is especially important when we compare to electrostatic variable capacitance micromotors which spin at tens of thousands of revolutions per minute [Bart, Mehregany, Tavrow, Lang and Senturia 90]. Gearing down to a useful speed for a robot from such a motor would require a gear

several feet in diameter. While electrostatic wobble micromotors are also able to produce an inherent gear reduction, they do not incorporate the advantage of high dielectric materials which the piezoelectric motors possess.

No Levitation – Friction is another major player in problems besetting micromotors. In a variable capacitance electrostatic micromotor, frictionless bearings are something to strive for, as the rotor needs to slide around the bearing. Piezoelectric traveling wave motors on the other hand, are based on friction – it is sliding that we need to prevent. Consequently, there is no need to levitate the rotor, a fact which makes a piezoelectric motor much more amenable to designs for transmitting power to a load. Furthermore because the rotor in an electrostatic variable capacitance micromotor flies above the stator, it needs to be very flat. Electrostatic micromotors are small, on the order of $100\ \mu\text{m}$ in diameter, because of the difficulties in fabricating large rotors without warpage. In a piezoelectric ultrasonic motor, the rotor is in physical contact with the stator, so the actuator can scale to much larger sizes for resulting higher torques.

Axial Coupling – The consequences of the effects of friction and stability in various types of micromotors force specific geometries on these actuators. Variable capacitance motors require a radial gap design due to stability considerations. That is, the capacitor plates sliding past each other are radially distributed about the bearing. Since silicon processing techniques cannot create large structures in the vertical dimension, that leaves very little area for energy transduction. Similarly, the physics of wobble motors constrains them to have cylindrical coaxial geometries. Ultrasonic motors however, due to this frictional coupling, can be formed into either linear or rotary motors and in addition, have the advantage that the rotor can sit atop the stator, creating more area over which to couple power out. The large planar area of ultrasonic motors is also symbiotic with planar lithographic techniques.

Rotor Material – Friction coupling (as opposed to charge attraction) leads to another trait characteristic of piezoelectric ultrasonic motors - the rotor can be any material. That is, the rotor need not be a good conductor as in variable capacitance or wobble motors. Rotor conductivity is unimportant, in contrast to an electrostatic induction micromotor. Most importantly, a piezoelectric ultrasonic motor could actuate a pump, and the fluid can then be *any* solution, without regard to conductivity.

Holding Torque – Finally, in terms of complete systems such as autonomous robots

or battery-operated machines, total energy consumption over the lifespan of the system is of critical concern. Piezoelectric ultrasonic motors, again due to friction coupling, can maintain holding torque even in the absence of applied power. This is a unique trait for an actuator that does not contain a gearbox, much less a transmission system or a brake.

2.2 From Materials to Devices

Bulk ceramic PZT has been widely used for decades but thin film ferroelectrics are new arrivals, having only recently been developed for non-volatile memory applications [Ramtron 88], [Udayakumar, Chen, Krupanidhi and Cross 90]. One problem with these new ferroelectric memories is fatigue, as the chips actually *flex* when memory cells switch. But that is exactly the effect we seek to exploit!

We would like films that maximize the piezoelectric effect in order to design useful high torque, low speed micromotors but the leap from materials to devices is a large one. Standing on the shoulders of previous technology is, in general, a good idea (and one which has been the approach in electrostatic micromotor research to this point – some even going so far as to label them “IC-processed micromotors” [Tai, Fan and Muller 89]). Stepping away from known silicon processing techniques and incorporating a new material can be a large undertaking, especially when the aim is to develop a new device. Consequently, the design for the device has to be as simple as possible in terms of materials processing to ensure a reasonable chance of success.¹

2.2.1 Keeping Things Simple

Figure 2-3 and Figure 2-4 illustrate our initial designs for the stators of linear and rotary motors (carriages and rotors have not been microfabricated – at the moment we simply place small glass lenses or other materials down on the stators). A silicon-rich nitride layer is deposited on a silicon wafer and is then patterned on the backside to create a membrane. 120 stator structures are patterned per two-inch wafer. After the membranes are etched, piezoelectric capacitor structures are built. These structures consist first, of a bottom electrode formed from titanium and platinum. The PZT dielectric is then added and finally

¹Experienced designers usually note however, that the first way you design something is always the most complex way [Angle 90].

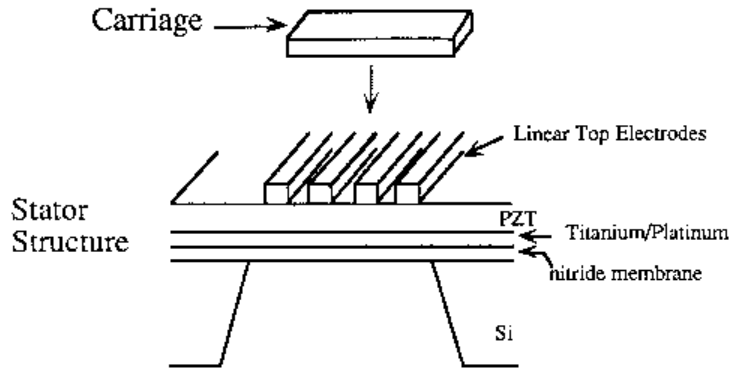


Figure 2-3: Linear motors utilizing thin-film PZT are illustrated here. By etching a membrane into a silicon wafer and patterning the stator on the membrane, the stator will be able to deflect more than if it were trying to bend the entire thickness of the wafer. Silicon-rich nitride is used for the membrane. The stator consists of a bottom electrode of titanium and platinum (ground), the PZT film and the patterned gold top electrodes. A carriage would have to be placed down by hand.

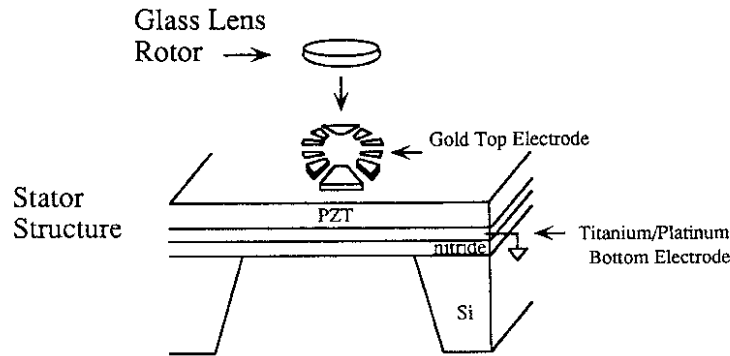


Figure 2-4: A rotary motor is made in the same way except that the top electrodes are patterned in a circle. We typically place down a small glass lens for a rotor.

the patterned gold top electrodes are deposited. The bottom electrode and thin film PZT are laid uniformly over the entire wafer, while gold top electrodes are positioned only above membranes.

A close-up of the membrane cross section is shown in Figure 2-5. Note that the silicon wafer and the silicon nitride membrane provide only structural support for the stator. No electrical properties or charge attraction effects of silicon are presently used in this motor. Future iterations might find other manufacturing technologies more attractive, but for the present we use silicon for its accompanying tools and lithographic techniques.

These stators were designed in this fashion because the materials requirements here are much simpler than in, for instance, a Matsushita motor (Figure 1-2), which would require two layers of ceramics with alternately poled segments throughout each piece. Our

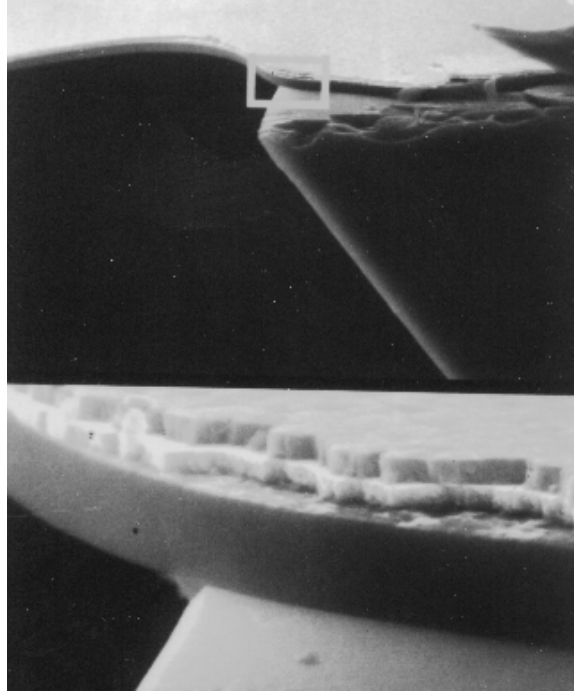


Figure 2-5: This scanning electron micrograph shows a cross section of the nitride membrane structure with PZT and the gold top electrode. The titanium-platinum bottom electrode is too thin to see here.

microfabricated stators require only one layer of PZT and that layer is poled uniformly everywhere. The tradeoff is that our motors now require a four-phase drive to induce a traveling wave, whereas the Matsushita motor requires only two phases. Patterning and wiring is straightforward with photolithography. However, while multilayer materials with various geometries of poling are easily realized in macro-scale assembled motors, these steps would be cumbersome from a microfabrication point of view.

A more recent design is even simpler. We start with thinned wafers which are $75\ \mu\text{m}$ thick (as opposed to the usual $250\ \mu\text{m}$) and omit membranes entirely. Since stress-free nitride is no longer required as an etch stop to create the membranes, the entire layer sequence simply becomes silicon, oxide, Ti-Pt, PZT and then gold (titanium is required for adhesion reasons and oxide is necessary to separate silicon from reacting with the PZT).

2.2.2 Stators and Rotors

In either case, whether utilizing membraned wafers or thinned wafers, there are a variety of possible geometries for patterning the top electrodes for inducing traveling waves. Figure 2-6 shows the simplest layout for a rotary motor. Eight electrodes are patterned radially

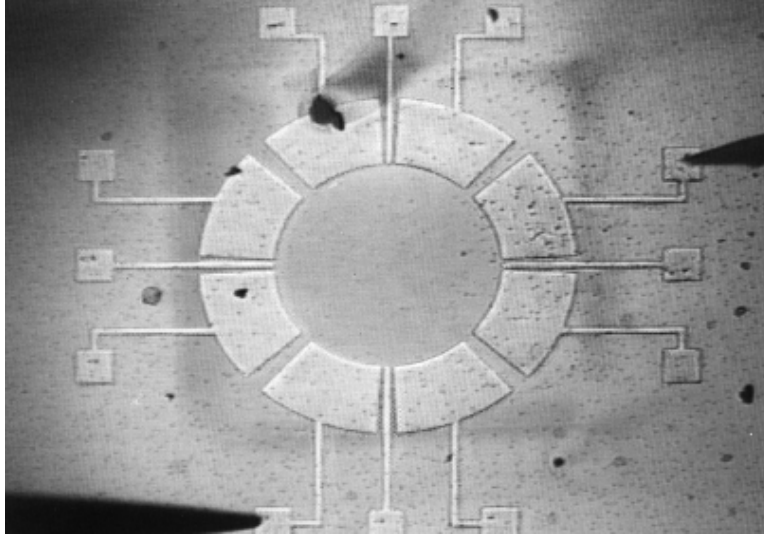


Figure 2-6: This 8-pole stator has an inner diameter of 1.2mm and an outer diameter of 2mm placed over a 2.2mm by 2.2mm square membrane. The eight pads are driven in a four phase sequence (sin, cos, -sin and -cos), repeated twice. The extra four pads at the north, east, south and west positions are undriven pads which can be used as passive piezoelectric sensors. That is, a signal will be generated as the wave passes through the pad.

around a center point and driven four-phase over two wavelengths. Eight probes would be needed to drive the motor in this particular example. However, other patterns on our test wafer use an interconnect scheme between pads to reduce the requirement to four probes. Note in Figure 2-6 that there are four extra pads. These can be used as sensors, since the piezoelectric film is reciprocal, where a bending moment can induce a voltage.

The simplest way to observe electrical to mechanical energy conversion is to place a small object down on the stator as portrayed in Figure 2-7. We have found that glass lenses spin the best, although dust particles dance wildly, signaling the onset of resonance as drive frequencies are swept from 50 kHz through several hundred kilohertz. Typical rotational velocities of the glass lens are on the order of 100–300 rpm. One interesting point to note is that four phases are not necessary to induce spinning. In fact, the lenses rotate with only single pad excitation. This is likely due to wave reflections off the edges of the membranes setting up parasitic traveling waves.

In addition to rotary stators, we have fabricated linear stators as shown in Figure 2-8. These structures can also be used as surface acoustic wave devices for measuring various properties of the ferroelectric film, such as acoustic velocity, etc.

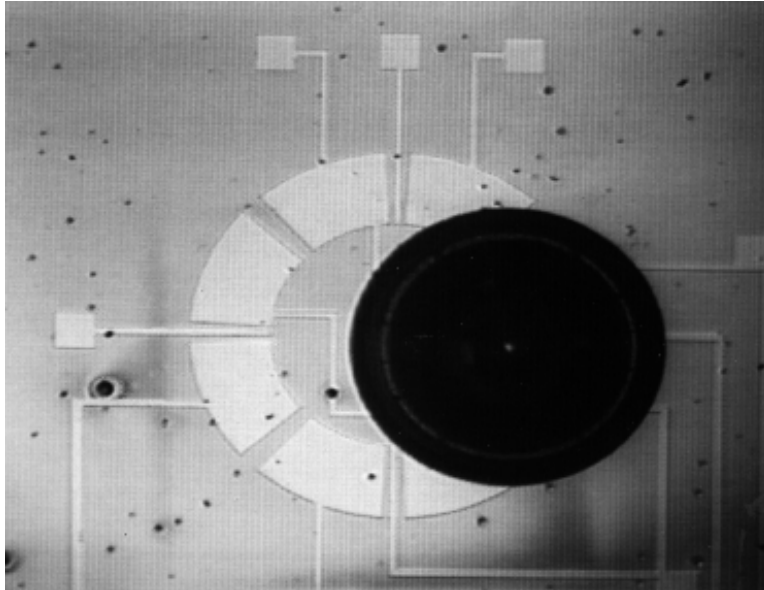


Figure 2-7: Here a plano-convex 1.5 mm diameter glass lens is placed convex surface down upon a rotary stator which has the same dimensions as Figure 2-6. Although there is no bearing, the lens spins at 100–300rpm when the stator is driven at 90 kHz.

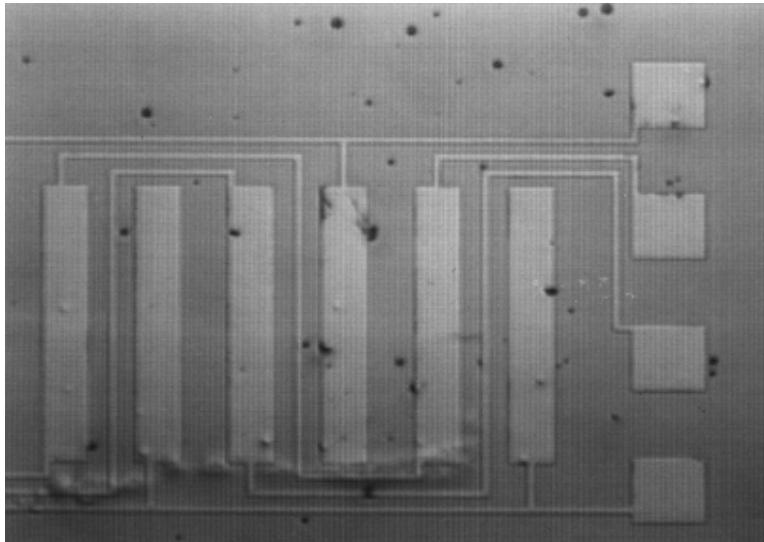


Figure 2-8: Linear stators have also been fabricated. Here, the probe pads to the right are 200 μm square and connect to every fourth electrode for setting up four-phase traveling waves. These structures are patterned over similarly shaped linear membranes.

2.2.3 The Process

Nitride membranes are first fabricated using standard bulk micromachining techniques into two-inch silicon $\langle 100 \rangle$ wafers. A $1\ \mu\text{m}$ thick low-stress chemical vapor deposition silicon-rich (nonstoichiometric) nitride film acts both as the membrane and the mask for the tetra methyl ammonium hydroxide (TMAH) anisotropic silicon etch. The electroded PZT film (for the stators) is then formed on the membranes. The reduced stiffness of the membranes permits larger stator deflections than would be possible on a full thickness wafer.

Electrode material selection is critical to fully utilize the PZT properties. We have used a $0.46\ \mu\text{m}$ thick platinum layer for our bottom electrode which is deposited on top of a 20 nm titanium adhesion layer. The nitride layer together with the titanium-platinum layers act as a separation barrier preventing the silicon from reacting with the PZT.

Sol-gel PZT film is deposited by a spin-on technique in a series of steps. These films have been characterized as reported in [Udayakumar et al. 91] and show significant improvements over bulk PZT, including greater breakdown strength and dielectric constant. Although thin-film PZT was first developed for memory devices, much of that work has focused on sputtering and chemical vapor deposition methods, even though it is very difficult to get the correct PZT makeup with these techniques. Sputtering from three separate elementary targets (or even from a single ceramic PZT target) to get lead, zirconium and titanium atoms all in their proper atomic positions in the crystal lattice is significantly harder than preparing a solution of the proper composition and spinning it onto a wafer as in a sol-gel process. These sol-gel fabricated films do in fact, exhibit the proper perovskite structure and show strong ferroelectric characteristics. For memory applications, piezoelectric flexing is not of interest, but the conformal coating properties of vapor deposited films are. Sol-gel films on the other hand, are planarizing, which can be a problem where uniform thicknesses even over undulating surfaces are required. One critical requirement for preparing quality sol-gel films is cleanliness, as wet spin-on techniques are more susceptible to the particle contamination than vacuum-based methods.

The sol mixture is prepared from the lead precursor, lead acetate trihydrate, together with alkoxides of Ti and Zr in 2-methoxyethanol as the solvent. Films are spun-on in approximately 50 nm layers. The film is pyrolyzed under quartz lamps after each step to remove organics. After 6-8 layers, the film is annealed to crystallize into the perovskite phase, which is the type of crystalline form which brings out the strong ferroelectric and

piezoelectric traits. Annealing is carried out above 500 °C. These PZT films are of the 52-48 mole ratio of zirconium-titanium which places them on the morphotropic phase boundary. The morphotropic phase boundary composition is that composition for which the crystallites have the maximum number of possible domain states because the composition lies at the boundary of the tetragonal phase (6 possible domain states) and the rhombohedral phase (8 possible domain states). This position among the possible spectrum of compositions in the lead zirconate - lead titanate solid solution system is the most amenable for attaining the distinctive ferroelectric properties. One interesting point about these thin films of PZT, in contrast to its bulk form, is that poling, the process of aligning domains in order to bring out these strong ferroelectric characteristics, need no longer be performed at elevated temperatures.

Characteristic measurements, described in more detail in [Udayakumar et al. 91] are summarized in Table I. Similar measurements reported in the literature for bulk PZT [Jaffe, Cook and Jaffe 71] yield some interesting comparisons. The breakdown field strength of $1 \frac{MV}{cm}$ is significantly improved over bulk PZT which is often on the order of $40 \frac{kV}{cm}$. Our sol-gel PZT films also exhibit almost twice the relative dielectric constant, 1300, of (similarly undoped) bulk PZT which is 730.

Table I. Sol-gel PZT Film Characteristics

E_{bd}	$1 \frac{MV}{cm}$	Breakdown field
ϵ_{pzt}	$1300\epsilon_o$	Dielectric constant
$\tan \delta$	0.03	Loss tangent
d_{33}	$220 \frac{pC}{N}$	Longitudinal piezoelectric coefficient
d_{31}	$-88.7 \frac{pC}{N}$	Transverse piezoelectric coefficient
P_r	$36 \frac{\mu C}{cm^2}$	Remanent polarization
k_{33}	0.49	Longitudinal coupling factor
k_{31}	0.22	Transverse coupling factor
k_p	0.32	Planar coupling factor

Once the PZT film has been annealed, 0.5 μ m thick gold electrodes are deposited and patterned by lift-off. A variety of eight- and twelve-pole rotary stators on three sizes of square membranes (0.8 mm, 2.2 mm and 5 mm per side) and various configurations of linear

stators are patterned.

The structures built on thinned wafers are fabricated in an analogous manner except that the membrane etch is skipped and $0.5\ \mu\text{m}$ oxide is used in place of nitride. The oxide layer together with the titanium-platinum layer act as a separation barrier preventing the silicon from reacting with the PZT.

2.3 Results

Initial experiments with these thin film PZT actuators have raised some intriguing questions. On the one hand, we have observed phenomena we expected such as high energy densities, gear down and low voltage operation. A 4 V peak-to-peak drive signal at 90 kHz competently spins a fairly large rotor, a glass lens 1.5 mm in diameter, at 100–300 rpm. On the other hand, the lens spins competently with only one phase excitation, and does not spin any better with four, something we did not expect! Furthermore, changing directions when applying four-phase drive does not cause the rotor to reverse, although in one instance, it did cause the lens to stop. Essentially, we are not inducing traveling waves in the manner we would like, but evidently there is enough energy density that the lenses spin anyway.

We have observed other indications of high energy density. Not only do dust and particles vibrate across the stators upon resonance, but in certain instances in which a pad's impedance is very low, applying a voltage on the order of 10 V causes a static deflection dependent on voltage that can be seen through the microscope as a darkened area where the surface is deformed and reflecting light away from the eyepiece. An example with a unique stress pattern is shown in Figure 2-9. Note that even at 10 V, the electric fields that we can apply across our $0.3\ \mu\text{m}$ thick films contribute to energy densities well beyond those achievable with bulk ceramic PZT motors.

The single-phase drive is intriguing and brings into question the effects of the boundary conditions on the waves imposed by the edges of the membranes. At high enough frequencies (several hundred kHz) standing waves become visible on both square and rectangular membranes as shown in Figure 2-10. Rotors continue to spin however, even though the motors are not working in the manner in which they were designed. The plano-convex glass lenses seem to spin because the contact is a point. We have observed glass lenses, convex side down, jiggling across the stator until brushing up against the inner radius of the gold

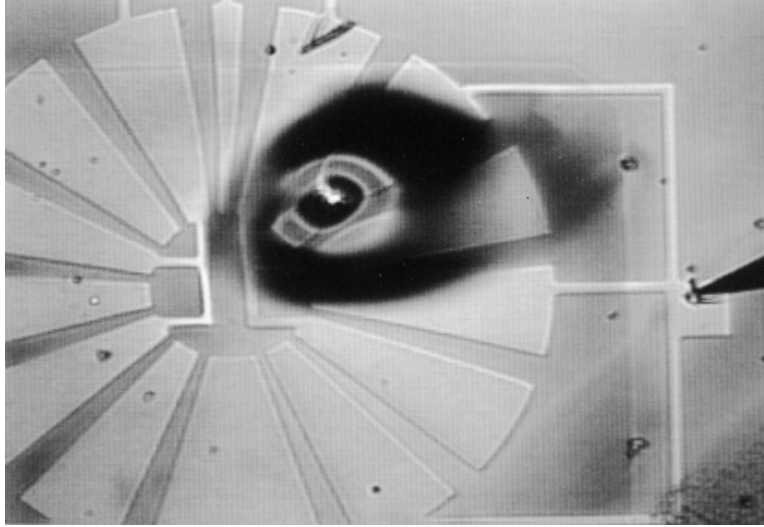
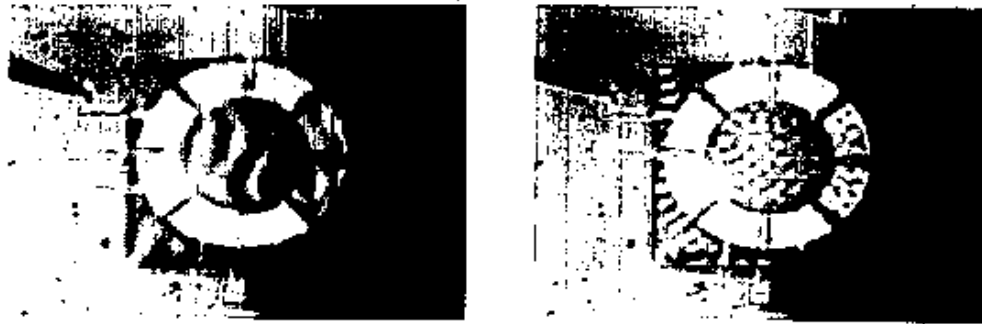


Figure 2-9: Static deflection of this partially shorted stator pad can be seen through the microscope. The darkened portion is deformed, deflecting light away from the eyepiece. 10 V is applied from the electrode at the right across the PZT, to the ground plane beneath it.

electrodes which are approximately $0.5 \mu\text{m}$ tall, whereupon they sit and spin. We have also observed that plano-convex lenses flat side down do not spin, nor do annularly shaped objects such as jeweled bearings.

In this first fabrication sequence, we made no attempt to microfabricate a bearing or etch a rotor in place. Consequently, the amount of frictional coupling is only determined by the weight of the rotor. In fact, it is possible there is no frictional coupling and the lens is merely sliding on air as the surface vibrates. Nevertheless, a mass is spinning and it is possible to calculate a torque by measuring the inertia of the lens and its acceleration when starting. Approximating our lens as a disk 1 mm thick and estimating from visual observation that it reaches a final velocity of 3 Hz in one quarter of a second, the resulting torque is 41 pNm. We can compare to variable-capacitance electrostatic micromotors by normalizing over voltage squared, which gives a figure of merit over a class of experiments. This normalized net torque for such electrostatic micromotors (typically run at 100 V) is $1.4 \times 10^{-15} \frac{\text{Nm}}{\text{V}^2}$. The figure of merit for our piezoelectric motors then becomes, for 5 V excitation, $1.6 \times 10^{-12} \frac{\text{Nm}}{\text{V}^2}$, about three orders of magnitude larger. What this number actually signifies for a piezoelectric motor with no bearing and no traveling wave drive is debatable. Mostly, it serves to underscore that the films are indeed very active, encapsulate high energy densities and can move fairly large objects with low voltages.

True motor action will depend on future attempts to fabricate a bearing and to measure



What went wrong...pinholes and standing waves.



Figure 2-10: Standing waves on a membrane are visible through an optical microscope when a single-phase drive is applied.

torques across a spectrum of normal forces. Further experiments are needed to determine better structures for guiding traveling waves. Instruments need to be developed for visualizing the waves throughout a spectrum of frequencies and for ascertaining the amplitudes of these dynamic deflections. Determining proper rotor-stator interface coatings for high friction contact would also be helpful.

Electrostatic motors are essentially the duals of magnetostatic motors which have been around for years and are well understood. Piezoelectric ultrasonic motors on the other hand are fairly new and ferroelectric thin films are newer still. Many factors conspire to produce complexities and difficulties in analyzing these structures: non-linear materials, coupled electrical and mechanical fields, resonance drives, clamped and unclamped boundary conditions and friction-based interactions between rotors and stators, to name a few.

Chapter 3

Ultrasonic Motors

Due to the constraints of the silicon micromachining process, our first attempts at thin-film PZT microactuators were built on $1\mu\text{m}$ thick membranes. We chose membranes in order to achieve a thin substrate against which the thin film could bend. Due to constraints in fabricating sol-gel PZT, the PZT could not be much thicker than $0.3\mu\text{m}$ or cracking would occur during pyrolyzation.

Consequently, because the membranes acted as drumheads rather than mechanical waveguides, and because the films sometimes shorted due to pinholes, it was difficult to achieve true traveling wave motion. At this junction, we split the project into two separate studies: one to develop thicker, pinhole-free films at the Penn State Materials Research Laboratory, and one, at the MIT Artificial Intelligence Laboratory to develop models for predicting performance of traveling wave motors on ring-type waveguides.

Here, we discuss a succession of models and relate early experiments on prototype motors made at a larger, but still small (and useful for our mini-robot applications) scale, made from commercially available bulk ceramic PZT. These motors are 8 mm in outer diameter with a 5 mm inner diameter. Two generations of these motors were actually prototyped during the course of the project, with significant improvements incorporated into the second batch.

Later, we will describe a new laser-based process for bringing the two projects back together and achieving thin-film PZT-on-silicon micromotors where membranes are circumvented and the motors are cut free from the wafer.

3.1 Bulk 8 mm Motors

Traveling wave piezoelectric ultrasonic motors can be made with a very simple structure. Figure 3-1 illustrates an 8 mm ring-type motor. The stator is composed of a steel ring with piezoelectric elements bonded onto the underside for exciting vibration modes in the ring. When traveling waves are developed, points on the stator surface move in retrograde elliptical motions, creating a tangential component of velocity which propels the rotor. The rotor can be any material, but a normal force must be provided to press the rotor against the stator in order to frictionally couple the vibratory motion of the stator into the rotational motion of the rotor.

The most commonly used material for piezoelectric actuators, and that used in this motor, is lead zirconate titanate, PZT. PZT is a ceramic material that is ferroelectric, meaning that it displays a hysteretic effect between polarization and electric field where the polarization direction can be reversed with opposite polarity drive field – but it also happens to have very large piezoelectric coefficients. Bulk forms of PZT, on the order of several hundreds of microns in thickness, are commercially available and found in bimorph and multi-layer stack actuators. Thin-film PZT, under one micron in thickness, has recently been developed for non-volatile memories, taking advantage of the ferroelectric switching characteristics [Udayakumar 93]. Fundamentals of piezoelectric notation and material properties can be found in Appendix B. Here we will model ultrasonic motors utilizing the piezoelectric properties of both bulk and thin-film PZT.

3.2 Vibration of Rings

An ultrasonic motor is essentially a vibrating annular ring. Vibration of strings, membranes, plates and disks was studied by Lord Rayleigh and Kirchoff in the nineteenth century [Rayleigh 1894] and the equation of motion for free transverse vibration of a circular plate was formulated as:

$$\frac{Eh^2}{3(1-\nu^2)} \nabla^2 \nabla^2 w + \rho \frac{\partial^2 w}{\partial t^2} = 0$$

where

$$\nabla^2 = \frac{\partial^2}{\partial r^2} + \frac{1}{r} \frac{\partial}{\partial r} + \frac{1}{r^2} \frac{\partial^2}{\partial \theta^2}$$

for the coordinate system as shown in Figure 3-2.

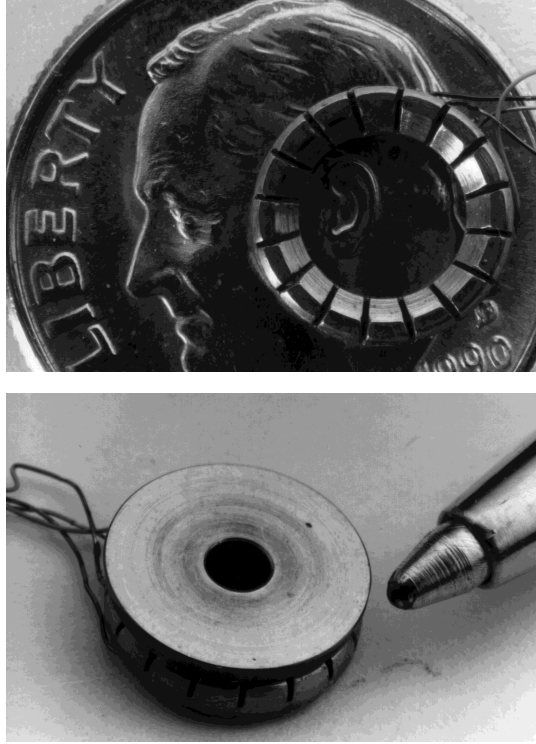


Figure 3-1: This 8 mm diameter piezoelectric ultrasonic motor is composed of two pieces, the stator and the rotor. The stator is shown in the figure at top and is a steel ring with piezoceramics bonded onto the bottom side. A brass rotor is shown atop the stator in the bottom photograph.

Here, w is the transverse deflection of the plate in the z -direction, E is Young's modulus, h is the half-thickness of the plate, ν is Poisson's ratio and ρ is the mass density of the material. Vogel and Skinner [1965] give a detailed analysis with numerical evaluation of various boundary conditions. Solutions to this free vibration problem are of the form:

$$w(r, \theta, t) = A(r) \cos n\theta e^{j\omega t}$$

where the mode shapes are transcendental functions in the θ -direction with scaling factor $A(r)$. Plugging this solution into the equation of motion leads to Bessel function forms for $A(r)$:

$$A(r) = C_1 J_n(\beta r) + C_2 Y_n(\beta r) + C_3 I_n(\beta r) + C_4 K_n(\beta r)$$

where

$$\beta^4 = \frac{3\rho(1-\nu^2)}{Eh^2}$$

and J_n and Y_n are Bessel functions, and I_n and K_n are modified Bessel functions.

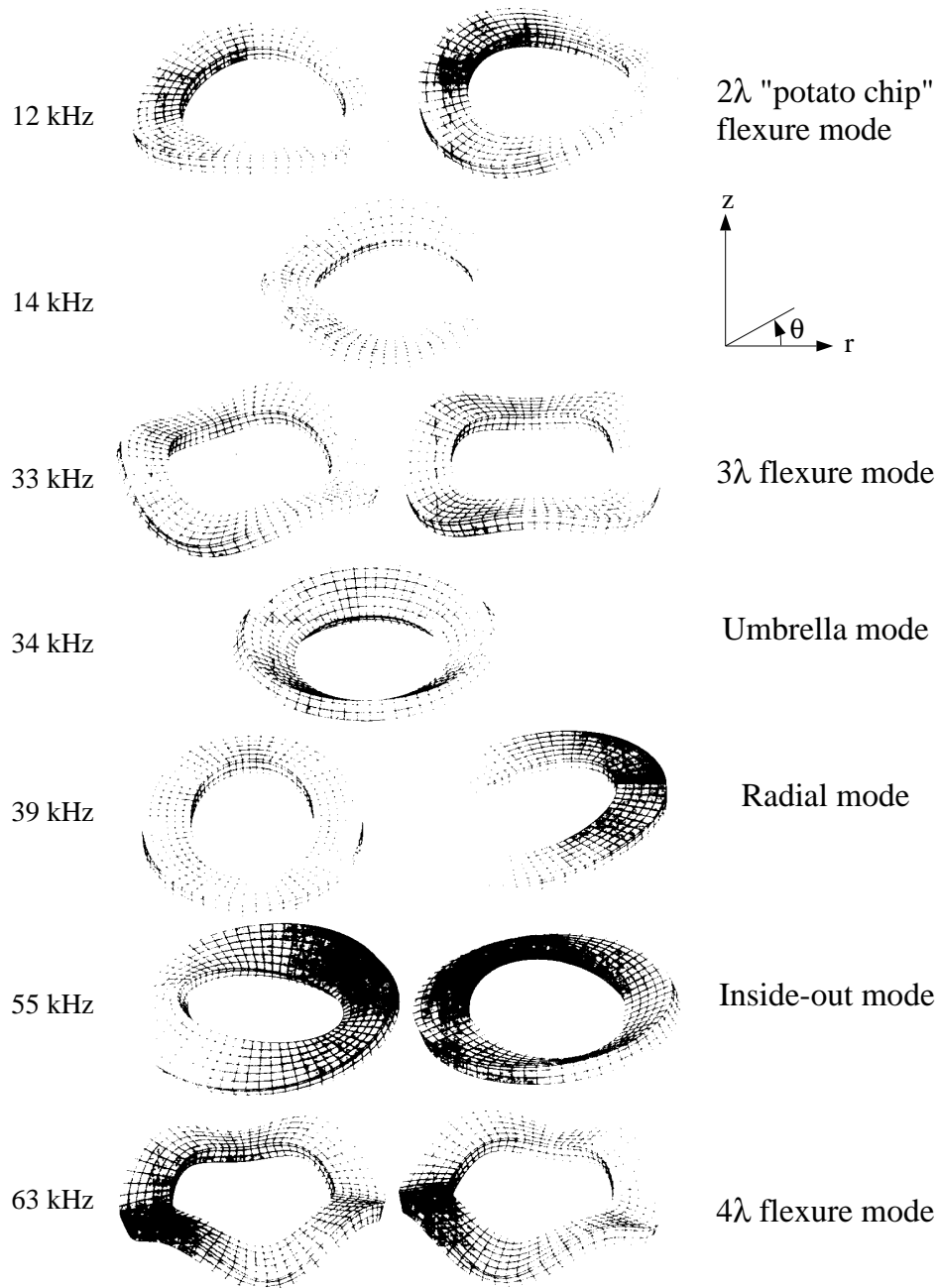


Figure 3-2: Finite element simulations of the modes of vibration for an 8 mm outer diameter, 5 mm inner diameter, composite ring of steel on PZT, show the mode shapes and natural frequencies. The steel layer here is $820 \mu\text{m}$ thick and the PZT layer is $195 \mu\text{m}$ thick.

Figure 3-2 shows finite element simulations (ANSYS finite element package, [Ostergaard 89]) which help to visualize the free vibration of an 8 mm outer diameter, 5 mm inner diameter composite ring, similar to the stator in Figure 3-1. The boundary conditions for these structures are free-free along the inner and outer circumferences.

We can see that simulations show that not all modes of vibration are composed of transverse displacements. Such transverse deformations are known as flexure or bending modes, and the 2-, 3-, and 4-wavelength flexure modes can be seen to have natural frequencies of 12 kHz, 33 kHz, and 63 kHz, respectively. Due to axial symmetry, these modes are degenerate, having eigenvalues of multiplicity two. By exciting both solutions as standing waves, but phased 90 degrees apart in time, traveling waves result due to superposition. For an ultrasonic motor that is top-drive, where the rotor sits atop the stator, we want to induce traveling waves from these flexure modes. Other modes, such as the umbrella mode, will not sustain traveling waves of bending. Note, however, that the 39 kHz radial mode could be used for an ultrasonic motor if the rotor was placed circumferentially around the stator. Kumada has used this technique to produce very thin clock motors [Kumada 91]. Here, we will study top-drive flexural traveling wave motors because we are interested in investigating piezoelectric thin films for excitation, a technology more compatible with top-driven devices.

Because the stator of our motor has free-free boundary conditions at the inner and outer diameters, and the radial dimension of contact with the rotor is very short, we can model the radial variation of vibration amplitude as constant, and unfold the annular ring into a infinite Bernoulli-Euler beam capable of sustaining traveling waves. For a Bernoulli-Euler model and small deflections, rotary inertia and shear forces are neglected and normal cross-sections are assumed to remain normal after bending. While a finite beam can only support standing waves due to reflections at each end, we can model one standing wave component of the traveling wave as a finite beam of the same length as an open, unfolded ring as shown in Figure 3-3.

Figure 3-3(a) represents the four-wavelength flexure mode at which the motors of Figure 3-1 are designed to run and Figure 3-3(b) illustrates the Bernoulli-Euler beam model of one of the standing wave components. Using this model and superposition, eigenfrequencies, traveling-wave speeds and surface-point trajectories can be determined. To predict deflection in the out-of-plane direction, we may take one half-wavelength section of

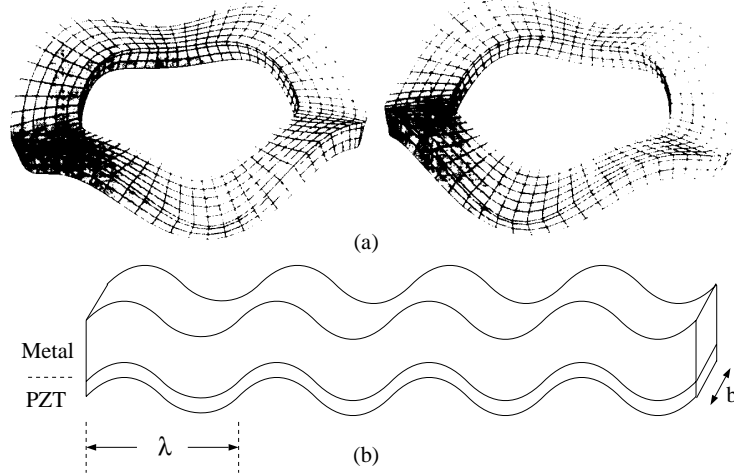


Figure 3-3: (a) The fourth flexure mode vibration pattern of an annular ring. (b) Bernoulli-Euler beam model of the ring in its fourth flexure mode.

this standing-wave beam and model it as a simply-supported piezoceramic-metal-composite beam of length L , where $L = \frac{\lambda}{2}$, the supports being located at the nodes of the standing wave, as illustrated in Figure 3-7 and discussed later.

3.3 Eigenfrequencies and Wavespeeds

With the simple beam model of Figure 3-3(b), we can calculate the natural frequencies of an ultrasonic motor and the corresponding wavespeeds and rotor speeds.

For a beam of transverse displacement w , mass density per unit length ρ , Young's modulus E , cross-sectional moment of inertia I , and cross-sectional area A , the equation of motion of flexural free vibration of a beam is:

$$\frac{\partial^4 w(x, t)}{\partial x^4} + \frac{\rho A}{EI} \frac{\partial^2 w(x, t)}{\partial t^2} = 0$$

Solutions are of the form:

$$w(x, t) = W(x) e^{j\omega t}$$

with pinned boundary conditions at the nodes of a standing wave where $L = \frac{\lambda}{2}$,

$$W(x = 0) = W(x = L) = \frac{d^2 W}{dx^2}(x = 0) = \frac{d^2 W}{dx^2}(x = L) = 0$$

yielding mode shapes with a sinusoidal form:

$$W(x) = C_1 \sin kx$$

Here k is the wavenumber:

$$k = \frac{2\pi}{\lambda} = \frac{\omega}{c_T}$$

λ is the wavelength and c_T is the speed of the transverse bending waves. For a pinned-pinned beam,

$$k = \frac{n\pi}{L}$$

Plugging this solution back into the equation of motion, we find the dispersion relation:

$$k^4 = \omega^2 \frac{\rho A}{EI}$$

and the natural frequencies:

$$\omega_n = \left(\frac{n\pi}{L} \right)^2 \sqrt{\frac{EI}{\rho A}}$$

We can also note that:

$$\sqrt{\frac{E}{\rho}} = c_l$$

where c_l is the longitudinal speed of sound in the material. Furthermore, we can take:

$$\sqrt{\frac{I}{A}} = \kappa$$

where κ is the radius of gyration. This shows that the speed of flexure waves is dependent on excitation frequency:

$$c_T = \frac{\omega}{k} = \sqrt{\omega c_l \kappa}$$

3.4 Traveling Waves and Elliptic Motion

The wavespeed we have just described is the phase velocity of traveling flexure waves along the neutral axis of a beam. However, for a beam of half-thickness h , the points on the surface move in elliptical trajectories. Coupling of this motion to the rotor produces a rotor speed different than the wavespeed.

Flexing Beam
$$\frac{\partial^4 w(x, t)}{\partial x^4} + \frac{\rho A}{EI} \frac{\partial^2 w(x, t)}{\partial t^2} = 0$$

Traveling Wave Solution $w(x, t) = w_o \cos(kx - \omega t)$

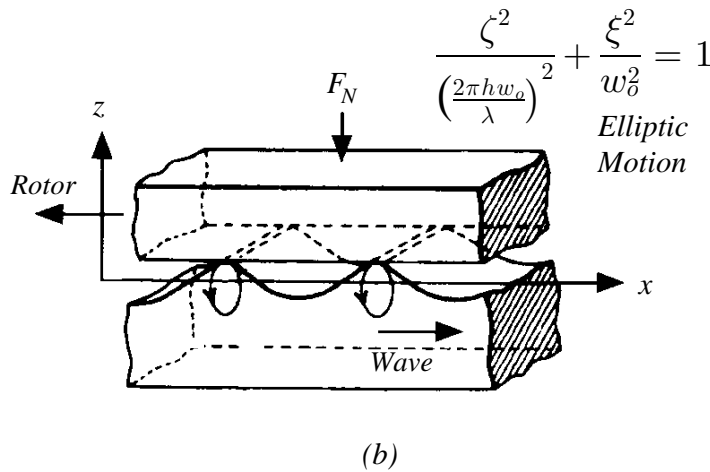
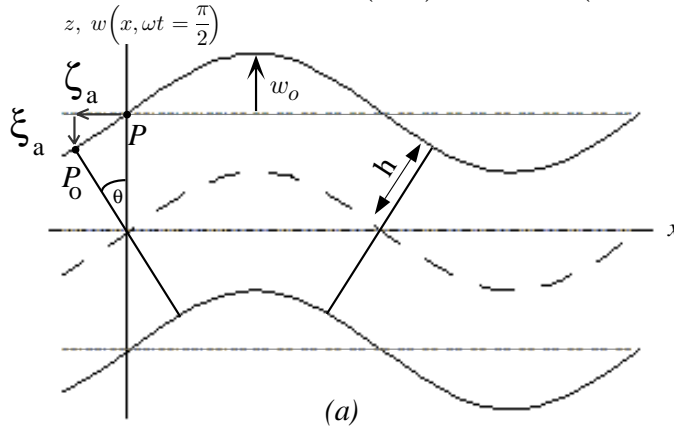
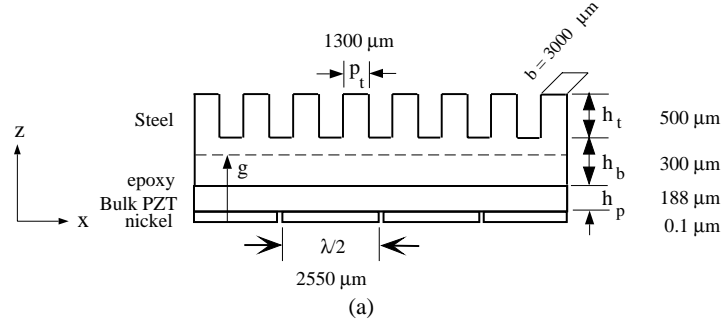


Figure 3-4: (a) For a beam in flexure, a traveling wave is one solution to the beam equation. A vibration of amplitude w_o will cause a point on the surface to displace from P to P_o . (b) Traveling wave excitation causes point P to undergo retrograde elliptical motion. A carriage pressed against this infinite beam is propelled along through friction in the direction opposite to the direction of the traveling wave.



Piezoelectric Constitutive Relations

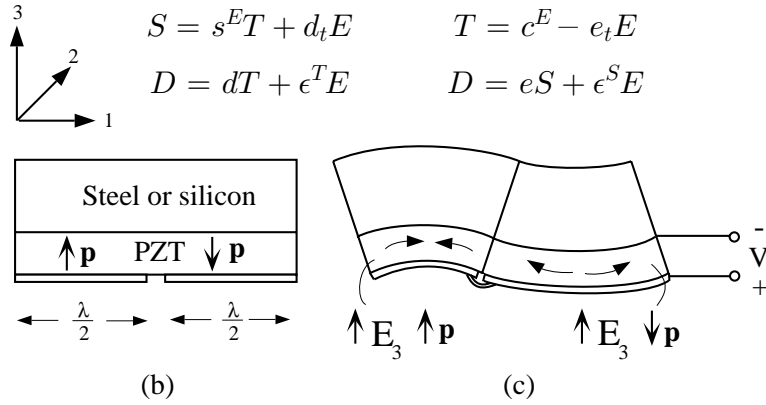


Figure 3-5: (a) A thin glue layer is used to attach an electroded ferroelectric to the underside of a steel ring. (b) The segments are then cut and poled alternately. The poling process aligns domains in the piezoceramic to create a remanent polarization. (c) After poling, two groups of electrodes are connected as shown at the bottom with silver paint, and wires are soldered in place.

Generation of traveling waves and equations of motion for surface points on beams and rings have been reported in the literature [Sashida 86], [Inaba et al. 87], [Zemella 90], [Hagedorn and Wallaschek 92], [Hagedorn et al. 92].

It can be shown (see Appendix A) that for a traveling wave solution of:

$$w(x, t) = w_o \cos(kx - \omega t)$$

a point, P , on the surface of a beam as shown in Figure 3-4(a), moves with horizontal displacement, ζ , and vertical displacement after bending, ξ , where:

$$\xi = w_o \cos(kx - \omega t)$$

$$\zeta = hk w_o \sin(kx - \omega t) = \frac{2\pi h w_o}{\lambda} \sin(kx - \omega t)$$

The velocity of the horizontal displacement of a point on the surface of a beam is:

$$v_h = \frac{\partial \zeta}{\partial t} = -\frac{2\pi\omega h w_o}{\lambda} \cos(kx - \omega t)$$

where it reaches its maximum value at the peak of the deflection contacting the rotor. Assuming no slip between the stator and the rotor, the rotor is propelled in the opposite direction of the traveling wave at a speed of:

$$v_{h, max} = -\frac{2\pi\omega h w_o}{\lambda}$$

This maximum horizontal velocity is simply the no-load speed of the motor. Note that this is very different than the phase velocity, c_T , of the traveling wave:

$$c_T = \sqrt{\omega^4 \frac{EI}{\rho A}}$$

Figure 3-4(b) shows the retrograde elliptical motion on the surface of the stator as the traveling wave moves to the right. The angular velocity of the rotor is

$$\omega_{rotor, max} = \frac{v_{t, max}}{r}$$

where r is the radius of the rotor at the circumference of contact with the stator. Comparing this rotor speed to the frequency of vibration, we find:

$$\frac{\omega_{rotor, max}}{\omega} = -\frac{2\pi h w_o}{\lambda r}$$

3.5 Mechanical Modeling of the Stator

We can model our stator of Figure 3-1 as a composite beam in the manner illustrated in Figure 3-5(a). Teeth are cut in the steel ring to reduce stiffness while maintaining maximum height for mechanical amplification. That is, for calculation of the natural frequencies:

$$\omega_n = \left(\frac{n\pi}{L}\right)^2 \sqrt{\frac{EI}{\rho A}}$$

we model the teeth as not entering into the stiffness term, EI , but as contributing to added

mass per unit length:

$$(\rho A)_{tot} = (\rho A)_{beam} + (\rho A)_{teeth}$$

where $n = 1$ in our model of each half-wavelength piezo-segment acting as a pinned-pinned beam inducing a bending moment in the structure.

The beam is considered as the composite structure of PZT and metal, a momomorph, where the height of the beam is the sum of the PZT thickness and the base portion of the metal thickness, $h_p + h_b$, the pitch of each tooth is p_t , the length of the beam is $L = \frac{\lambda}{2}$, and the depth of the beam is b . The cross-sectional moment of inertia, I , is measured with respect to the neutral axis. The location of the neutral axis is the distance from the bottom of the piezoceramic layer, g , calculated as a fraction of PZT thickness, and weighted by the elasticities (stiffnesses) of each material:

$$\frac{g}{h_p} = \frac{1 + \frac{c_m}{c_p} \left(\frac{h_b}{h_p}\right)^2 + 2 \frac{c_m}{c_p} \frac{h_b}{h_p}}{2 \left(1 + \frac{c_m}{c_p} \frac{h_b}{h_p}\right)}$$

Here, c_m is the elastic modulus of the metal layer and c_p is the elastic modulus of the PZT layer (equal to c_{11}^E in the piezoelectric notation outlined in Appendix B).

The piezoelectric elements are attached to the steel ring in the manner shown in Figure 3-5(b) and Figure 3-5(c). The piezoceramic is purchased with a thin electrode layer of nickel coating on each side. After bonding, the bottommost electrode is cut into sectors. Once the backside electrode is segmented, neighboring segments are poled alternately.

The poling process utilizes a high electric field to initialize a polarization direction in a ferroelectric material to induce its piezoelectric properties. Poling is accomplished by application of 350 V at room temperature for two to three seconds. The convention for coordinate systems describing piezoelectric phenomena is to call the axes 1, 2, and 3, where the poling direction is taken as the 3-direction and the 1 and 2 directions are mutually orthogonal. After poling, the electrodes are silver-painted together and wires are attached to top and bottom electrodes.

Later, when a drive voltage is applied, neighboring segments which are poled up and down, expand and contract respectively in the 1-direction (using d_{31} motor action), causing the structure to buckle. Oscillatory drive voltages near the resonant frequency force the structure to vibrate with maximum amplitude in standing waves.

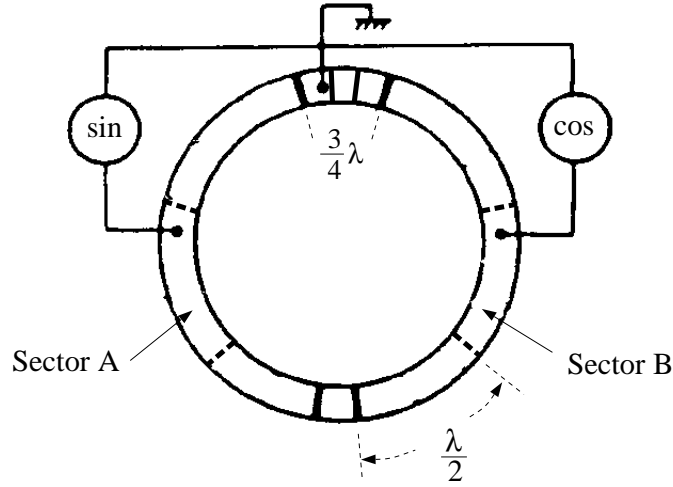


Figure 3-6: A four wavelength traveling wave motor is electroded with six half-wavelength alternately-poled segments and four quarter-wavelength spacer segments.

The piezoelectric elements are designed in a manner so as to induce the fourth flexure mode as was shown in Figure 3-3. To create a four-wavelength traveling wave ultrasonic motor, the electrodes are patterned as illustrated in Figure 3-6. As two neighboring electrodes create one wavelength of bending, eight electrodes are required for a four-wavelength motor. One pair is left passive and cut in quarter-wavelength and three-quarter-wavelength segments respectively, in order to space the two electrode groups by ninety degrees. The two opposing electrode groups are driven out of phase in time, also by ninety degrees, in order to induce traveling waves.

We can investigate the viability of this model by evaluating our four-wavelength motor of Figure 3-1, whose dimensions are noted in Figure 3-5(a). For an average radius of $r = 3.25$ mm, we find that $\lambda = 5.1$ mm and $L = \frac{\lambda}{2} = 2550 \mu\text{m}$. The elastic modulus of steel, c_m , is 200 GPa and the elastic modulus of PZT (PTS-1195) is very close to that of aluminum, $c_p = 70$ GPa [Piezo Systems 85]. The beam is modeled as not including the teeth for purposes of calculating the stiffness and location of the neutral axis. The base portion of the metal layer is then $h_b = 300 \mu\text{m}$, the PZT layer is $h_p = 188 \mu\text{m}$, and the depth of the beam is $b = 3000 \mu\text{m}$. This gives a neutral axis location at $g = 294 \mu\text{m}$ from the bottom of the PZT layer.

The equivalent stiffness of the composite beam is:

$$\overline{EI} = c_p I_p + c_m I_b$$

$$\overline{EI} = c_p b \int_{pzt} z^2 dz + c_m b \int_{base} z^2 dz$$

where z here is measured from the neutral axis. The equivalent stiffness is calculated to be $\overline{EI} = 3.39 \times 10^{-3} \text{ Nm}^2$.

The total mass per length, with the mass density of steel taken as $\rho_{met} = 7860 \frac{\text{kg}}{\text{m}^3}$ and the mass density of PZT as $\rho_{pzt} = 7600 \frac{\text{kg}}{\text{m}^3}$ is:

$$(\rho A)_{tot} = (\rho A)_{pzt} + \rho_{met} (A_{base} + A_{tooth}) = 2.32 \times 10^{-2} \frac{\text{kg}}{\text{m}}$$

The resonant frequency of the motor vibrating in the fourth flexure mode is the first natural frequency in our model of this pinned-pinned beam of length L :

$$\omega_1 = \frac{\pi^2}{L^2} \sqrt{\frac{\overline{EI}}{(\rho A)_{tot}}} = 5.80 \times 10^5 \frac{\text{rads}}{\text{sec}} = 92.3 \text{ kHz}$$

In actuality, the motor runs at several resonant frequencies, one of them being 98.5 kHz. Interferometric measurements verified that this was indeed the fourth flexure mode. The calculated natural frequency then is within:

$$\frac{6.2 \text{ kHz}}{98.5 \text{ kHz}} = 6\%$$

Our model was based on the assumption of a half-wavelength monomorph acting as a Bernoulli-Euler beam where the length of the beam is much greater than the height (usually 10 or 100 times larger). For our 8 mm motor:

$$\frac{L}{h_p + h_b} = 5.2$$

and we find that our beam is far from ideal, so 6% error is not unreasonable.

We can also check the wavespeed and the rotor speed. The phase velocity of the traveling wave along a beam was given as

$$c_T = \sqrt{\omega_1} \sqrt[4]{\frac{\overline{EI}}{(\rho A)_{tot}}} = 471 \frac{\text{m}}{\text{s}}$$

and for our motor of radius $r = 3.25$ mm,

$$\omega_{wave} = \frac{cT}{r} = 1.45 \times 10^5 \frac{\text{rads}}{\text{sec}} = 1.39 \times 10^6 \text{ rpm}$$

The rotor no-load speed, however is:

$$\omega_{rotor,max} = -\frac{2\pi\omega_1 h w_o}{\lambda r}$$

where the minus sign signifies that the rotor moves in the reverse direction from the traveling wave.

Interferometric measurements determined that with no rotor, w_o was $0.1 \mu\text{m}$ when excitation was 10 V peak at 98.5 kHz. With h equal to half the total thickness of the beam, $\frac{1}{2}(h_p + h_b)$, the no-load rotor speed is calculated to be:

$$\omega_{rotor,max} = -5.4 \frac{\text{rads}}{\text{sec}} = -51 \text{ rpm}$$

Experiments with a small glass rotor, similar in dimension to the brass rotor in the lower photograph of Figure 3-1, resulted in rotational velocities of 36 rpm, which is fitting, as the rotor has finite inertia.

It is interesting to compare the final rotor rotational speed to the original excitation frequency:

$$\frac{\omega_{rotor}}{\omega_1} = \frac{5.4 \frac{\text{rads}}{\text{s}}}{5.8 \times 10^5 \frac{\text{rads}}{\text{s}}} \approx \frac{1}{107,000}$$

or to the speed of the traveling wave around the ring:

$$\frac{\omega_{rotor}}{\omega_{wave}} = \frac{5.4 \frac{\text{rads}}{\text{s}}}{1.45 \times 10^5 \frac{\text{rads}}{\text{s}}} \approx \frac{1}{26,900}$$

These large numbers signify the magnitude of the rectification of the high-frequency excitation, enabling resonant vibration and maximum amplitude deflection of the stator to be converted into low-speed rotational velocity of the rotor. Because of this property, ultrasonic motors can run many applications (depending on the torque requirements) without the need for gears.

Before we address the issue of torque production and the mechanisms behind the frictional coupling of vibrational energy of the stator into rotational kinetic energy of the rotor,

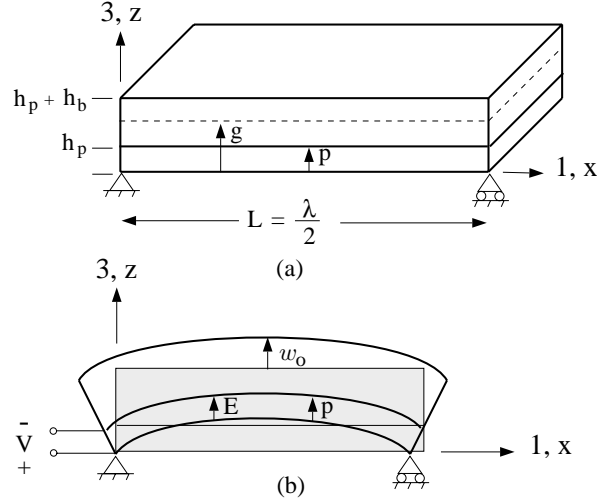


Figure 3-7: (a) One half-wavelength section of the stator is modeled as a simply-supported beam. (b) With polarization and electric fields both in the 3-direction, the monomorph will bow upwards as shown.

let us first look at the conversion process of electrical energy to strain energy of the flexing stator. This will enable us to predict the amount of deformation, w_o , for a given drive voltage.

3.6 Deflection of the Stator

In order to investigate the dynamic deflection of the beam, we begin with an analysis of the static deflection of the stator due to piezoelectric excitation. We examine a half-wavelength portion of the stator modeled as a simply-supported beam as illustrated in Figure 3-7(a). For now, we ignore the teeth on the stator and focus on the monomorph which consists of a bottom layer of piezoceramic of thickness h_p , bonded onto the base metal layer of thickness h_b . Because we model the teeth as contributing only added mass to the structure (and hence mechanical amplification) and not stiffness, only the piezoceramic and base metal layers affect the final bending configuration.

After determining the static deflection of the beam, the deflection magnitude at resonance can be calculated by multiplying the static value by a dynamic amplification factor. The dynamic amplification factor of the composite monomorph structure is the quality factor of the piezoceramic material weighted by the strain energies of the two material layers [Nashif et al. 85] as will be discussed later. First however, we find the static deflection.

For a piezoceramic poled in the positive z -direction and driven with an electric field

also in the z -direction, the piezoceramic will expand in the z -direction and contract in the x -direction causing the structure to bow upwards as shown in Figure 3-7(b). Since the common convention defining a positive bending moment is for the beam to bow downwards, the effect of this polarity drive is to induce a stress field which creates a negative bending moment throughout the structure.

In static equilibrium, force and moment balance equations lead to determination of the curvature in terms of stresses and strains, which can then be related to deflection of a beam, given appropriate boundary conditions. [Lucas 75] describes curvature and deflection of a monomorph cantilever beam and we follow the notation here, but apply our analysis to a simply-supported beam where we are interested in the magnitude of the deflection at the midpoint.

Figure 3-8 illustrates the x -directed stress distribution, $T_1(z)$, acting on the x -faces of the beam ($T_1(z)$ is the reduced matrix notation for $T_{xx}(z)$) where the beam has been subjected to bending with a radius of curvature, ρ_κ . Along the unstrained neutral axis of length ds ,

$$\rho_\kappa d\phi = ds$$

For small deflections,

$$\frac{d\phi}{ds} \approx \frac{d\phi}{dx} = \frac{1}{\rho_k} = \frac{d^2 w}{dx^2}$$

Here, dx is the length of the neutral axis in the initial undeformed state and the curvature, $\frac{1}{\rho_\kappa}$, is equal to the second derivative of the deflection profile, $w(x)$, of the beam.

A longitudinal differential line element at a distance $z - g$ from the neutral axis location, g , exhibits extensional strain of the form:

$$S_1(z) = \frac{z - g}{\rho_\kappa}$$

where $S_1(z)$ is the x -directed strain component acting on the face normal to the x -axis ($S_1(z) = S_{xx}(z)$).

Moment balance requires that the stress distribution, $T_1(z)$, multiplied by the moment arm and integrated over the cross-sectional area of the beam be zero, as there are no

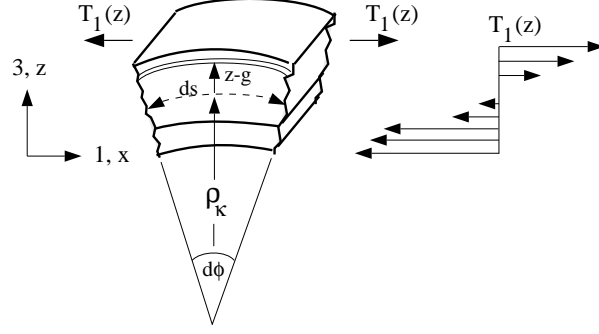


Figure 3-8: The radius of curvature, ρ_κ , due to bending moments caused by contraction of the piezoceramic can be determined from the resulting stresses and strains in the composite beam.

externally applied moments or forces acting on this structure:

$$M = 0 = b \int_z (z - g) T_1(z) dz$$

Next, we use the stress-strain constitutive law to restate this moment balance expression in terms of the curvature. Stress, strain and applied field in the monomorph are related by the piezoelectric strain relations (described in Appendix B):

$$\begin{aligned} \mathbf{S} &= \mathbf{s}^E \mathbf{T} + \mathbf{d}_t \mathbf{E} \\ \mathbf{D} &= \mathbf{d} \mathbf{T} + \epsilon^T \mathbf{E} \end{aligned}$$

where

- \mathbf{S} = Strain tensor
- \mathbf{T} = Stress tensor
- \mathbf{D} = Electric flux density vector
- \mathbf{E} = Electric field intensity vector
- \mathbf{s}^E = Elastic compliance tensor at zero \mathbf{E}
- \mathbf{d} = Piezoelectric strain tensor
- \mathbf{d}_t = Piezoelectric strain tensor transposed
- ϵ^T = Dielectric permittivity tensor at zero \mathbf{T}

Alternatively, the constitutive relationships between stress, strain and applied field can also be expressed in terms of the piezoelectric stress relations:

$$\begin{aligned} \mathbf{T} &= \mathbf{c}^E \mathbf{S} - \mathbf{e}_t \mathbf{E} \\ \mathbf{D} &= \mathbf{e} \mathbf{S} + \epsilon^S \mathbf{E} \end{aligned}$$

where

$$\begin{aligned}
\mathbf{c}^E &= \text{Elastic stiffness tensor at zero } \mathbf{E} \\
\mathbf{e} &= \text{Piezoelectric stress tensor} \\
\mathbf{e}_t &= \text{Piezoelectric stress tensor transposed} \\
\epsilon^S &= \text{Dielectric permittivity tensor at zero } \mathbf{S}
\end{aligned}$$

In the case of the monomorph presented here, the faces normal to the 2- and 3-directions are stress-free surfaces, and so:

$$T_2 = T_3 = 0$$

The stress distributions on the 1-faces due to an applied electric field in the 3-direction are:

$$T_1(z) = c(z) S_1(z) - e_{31}(z) E_3$$

The piezoelectric stress tensor, \mathbf{e} , is related to the piezoelectric strain tensor and the stiffness tensor by:

$$\mathbf{e} = \mathbf{d}\mathbf{c}$$

giving:

$$e_{31}(z) = d_{31}(z) c(z)$$

This results in a stress distribution of the form:

$$T_1(z) = c(z) S_1(z) - d_{31}(z) c(z) E_3$$

where $c(z)$ and $d_{31}(z)$ are step functions at the materials interface:

$$c(z) = \begin{cases} c_m & h_p < z < h_p + h_b \\ c_p & 0 < z < h_p \end{cases}$$

$$d_{31}(z) = \begin{cases} 0 & h_p < z < h_p + h_b \\ d_{31} & 0 < z < h_p \end{cases}$$

Substituting the expression for $S_1(z)$ into $T_1(z)$ gives:

$$T_1(z) = c(z) \left(\frac{z - g}{\rho \kappa} \right) - d_{31}(z) c(z) E_3$$

Plugging this stress expression into the moment balance equation yields:

$$M = 0 = b \int_z \left[c(z) \frac{(z-g)^2}{\rho_\kappa} - (z-g) d_{31}(z) c(z) E_3 \right] dz$$

Solving for the curvature and noting that the second term in the integral exists only in the piezoceramic layer, we find:

$$\frac{1}{\rho_\kappa} = d_{31} c_p E_3 \left\{ \frac{\int_0^{h_p} (z-g) dz}{\int_0^{h_p} c_p (z-g)^2 dz + \int_{h_p}^{h_p+h_b} c_m (z-g)^2 dz} \right\}$$

Integration produces an expression for the curvature in terms of thickness and compliance ratios:

$$\frac{1}{\rho_K} = \frac{3}{2} \frac{d_{31} E_3}{h_p} \frac{1}{r_\kappa}$$

where $\frac{1}{r_\kappa}$ is a dimensionless curvature parameter,

$$\frac{1}{r_\kappa} = \frac{(1-2f_o)}{1-3f_o+3f_o^2+m(3p+3p^2+p^3-6pf_o-3p^2f_o+3pf_o^2)}$$

and

$$m = \frac{c_m}{c_p}$$

$$p = \frac{h_b}{h_p}$$

$$f_o = \frac{g}{h_p} = \frac{1+mp^2+2mp}{2(1+mp)}$$

We can solve for the deflection profile, $w(x)$, from the curvature-displacement relationship,

$$\frac{1}{\rho_\kappa} = \frac{d^2 w(x)}{dx^2} = \frac{3}{2} \frac{d_{31} E_3}{h_p} \frac{1}{r_\kappa}$$

by taking into account the boundary conditions of a simply-supported beam:

$$w(x=0) = 0 \quad w(x=L) = \frac{d^2 w}{dx^2}(x=0) = \frac{d^2 w}{dx^2}(x=L) = 0$$

to determine the constants of integration. The displacement profile becomes:

$$w(x) = \frac{3}{4} \frac{d_{31} E_3}{h_p r_\kappa} \frac{1}{r_\kappa} (x^2 - Lx)$$

and the resulting deflection at the midpoint is:

$$w_{max} \left(x = \frac{L}{2} \right) = -\frac{3}{16} \frac{d_{31} E_3 L^2}{h_p r_\kappa}$$

As the electric field is equal to the applied voltage, V_3 , divided by the thickness of the piezoceramic, we now have an expression for the static deflection of the beam in terms of the applied voltage:

$$w_{max} \left(x = \frac{L}{2} \right) = -\frac{3}{16} \frac{d_{31} V_3 L^2}{h_p^2 r_\kappa}$$

Note that d_{31} is a negative quantity and so the resulting deflection is positive, as expected. What we are really interested in however, is the magnitude of the dynamic deflection of the stator at resonance. At resonance, the system is damping controlled and dependent on the losses in the materials. The resulting dynamic deflection is equal to the static deflection of the beam times the dynamic amplification factor, or quality factor, Q . Damping characteristics of a system are often also expressed in terms of the loss factor, η , where:

$$Q = \frac{1}{\eta}$$

For a composite structure such as the monomorph presented here, the loss factor of the entire structure can be expressed in terms of the loss factor of the piezoceramic material times the ratio of the strain energy of the piezoceramic layer to the strain energy of the entire monomorph [Nashif et al. 85]:

$$\eta_{mono} = \eta_{piezo} \frac{U_{piezo, strain}}{U_{mono, strain}}$$

where the strain energy stored in the flexural mode, U_{strain} , is defined as the integral over the volume of the strain energy density:

$$U_{strain} = \frac{Lb}{2} \int_z S_1(z) T_1(z) dz$$

Substituting in the expressions for stress and strain for flexural energy alone, gives:

$$U_{strain} = \frac{Lb}{2} \int_z c(z) \left(\frac{z-g}{r_\kappa} \right)^2 dz$$

Integration over the appropriate layers results in a stored elastic energy (in Joules) in the piezoceramic layer of:

$$U_{piezo, strain} = \frac{3}{8} Lbh_p d_{31}^2 E_3^2 c_p \frac{(1 - 3f_o + 3f_o^2)}{r_\kappa^2}$$

and in the entire monomorph of:

$$U_{mono, strain} = \frac{3}{8} Lbh_p d_{31}^2 E_3^2 c_p \frac{(1 - 2f_o)}{r_\kappa}$$

The loss factor for the device is then calculated to be:

$$\eta_{mono} = \eta_{piezo} \frac{1 - 3f_o + 3f_o^2}{r_\kappa (1 - 2f_o)}$$

and the dynamic amplification factor:

$$Q_{mono} = Q_p \frac{r_\kappa (1 - 2f_o)}{1 - 3f_o + 3f_o^2}$$

For example, we can calculate the expected deflection for our motors of Figure 3-5, ignoring the teeth and using the dimensions and elasticities given in Section 3.1. We find $m = 2.86$, $p = 1.60$ and $f_o = 1.56$, resulting in a value for the dimensionless curvature parameter of:

$$\frac{1}{r_\kappa} = -0.291$$

One experiment was performed earlier using an interferometer [Zhang, Pan and Cross 88] to measure the deflection of the stator at the fourth flexure mode resonance under an applied voltage of 10 V. (This is a rather low field, $E_3 = 5.32 \times 10^4 \frac{V}{m}$, whereas the maximum depoling field for the ceramic is $E_c = 2.36 \times 10^6 \frac{V}{m}$ [Piezo Systems 85]). For such a drive, we would expect a deflection magnitude of:

$$w_{max} \left(x = \frac{L}{2} \right) = 1.87 \times 10^{-8} m$$

The actual measured value at resonance was $0.1 \mu\text{m}$, which means there was a dynamic amplification factor of the monomorph of 5.4.

For a 10 V drive, the total stored elastic energy in the piezo layer is:

$$U_{piezo, strain} = 1.24 \times 10^{-9} J$$

For the entire monomorph, the total strain energy turns out to be:

$$U_{mono, strain} = 6.47 \times 10^{-9} J$$

The quality factor for the monomorph device then is:

$$Q_{mono} = \frac{6.47}{1.24} Q_p = 5.20 Q_p$$

The loss factor for the PTS-1195 piezoceramic is given as $\eta_{piezo} = 0.015$ [Piezo Systems 85], yielding a Q_p of 67, and a consequent amplification factor of:

$$Q_{mono} = 350$$

Chapter 4

Electrical Modeling of the Stator

We can model the stator both mechanically, as a beam vibrating, and electrically, as an equivalent circuit looking into the electrical terminals. Electrode groups A and B of Figure 3-6 each act to produce standing waves when excited near their resonant frequencies. At these frequencies, the stator can be modeled by the electrical equivalent circuits shown in Figure 4-1. The series- RLC branches are the mechanical arms. The resistive, inductive and capacitive lumped parameters are the mechanical damping, mass and compliance, respectively, transformed into electrical equivalents due to the piezoelectric effect. C_o is the electrical capacitance in the absence of the mechanical motion which is induced at resonance. At resonance, the inductive and capacitive components of the mechanical arm, $j\omega L$ and $\frac{1}{j\omega C}$, become equal in magnitude and opposite in phase, leaving the system damping controlled. This resonant frequency, f_r , shown in Figure 4-2, corresponds to an impedance zero. Above resonance, the series RLC branch becomes inductive and the equivalent circuit reduces to a parallel resonant circuit, displaying an antiresonance at the frequency f_a , corresponding to an impedance maximum. At even larger frequencies, the system again acts capacitively.

The resonance and anti-resonance frequencies of a single electroded slab of piezoceramic (as opposed to the monomorph device used in the ultrasonic motor here) can be related to material properties and the electromechanical coupling coefficient (see Appendix B). Laboratory measurements of the impedance characteristics of a piezoelectric material can then be used to characterize and verify the electromechanical coupling factor, the damping coefficient and the quality factor of the device.

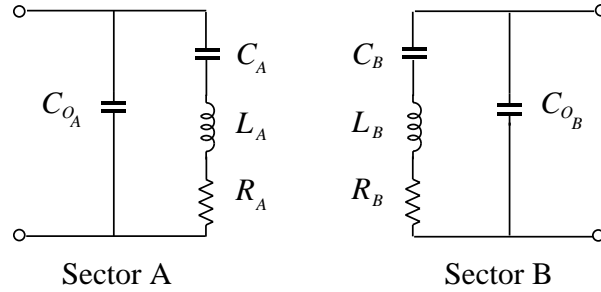


Figure 4-1: The electrical circuit model of an ultrasonic motor consists of two series-resonant circuits, one for each standing wave.

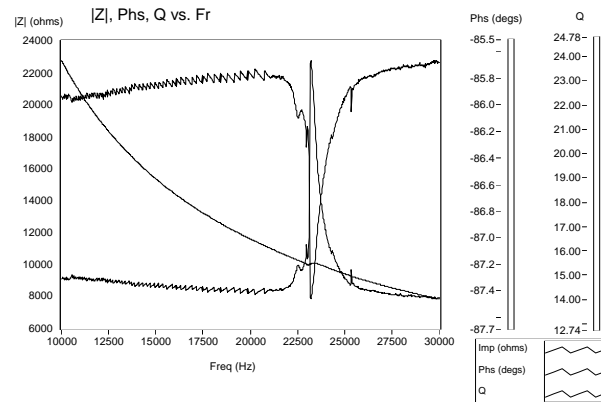


Figure 4-2: Near a resonant frequency, a piezoelectric material has an impedance characteristic displaying both a resonance and antiresonance. This small blip can be seen on the $|Z|$ curve near 26 kHz. The phase, θ and electrical damping factor, Q , also change significantly at this point.

The electromechanical coupling factor for a piezoelectric material where a field is applied in the 3-direction and the output strain is taken in the 1-direction, is k_{31} . [Buchanan 86] gives k_{31} as:

$$k_{31} = \sqrt{\frac{\frac{\pi}{2} \frac{f_a}{f_r} \tan\left(\frac{\pi}{2} \frac{f_a - f_r}{f_r}\right)}{1 + \frac{\pi}{2} \frac{f_a}{f_r} \tan\left(\frac{\pi}{2} \frac{f_a - f_r}{f_r}\right)}} = \frac{d_{31}}{\sqrt{\epsilon_{33}^T s_{11}^E}}$$

However, for a monomorph, the 1-directed strain must work against the stiffness of the non-piezoelectric steel layer, with the result being bending instead of lateral displacement. The *effective* electromechanical coupling factor for a monomorph then would be lower than for a plain slab of piezoceramic. For instance, [Smits and Choi 92] showed that for bimorphs used as cantilever beams (two electroded slabs of piezoceramic bonded together rather than one layer of piezoceramic bonded onto one passive layer), the squares of the effective electromechanical coupling factors, λ_{eff} , when the tip works against a vertical moment, force, or distributed load, are respectively:

$$\lambda_M = 3 \left(\frac{k_{31}^2}{4 - k_{31}^2} \right) \quad \lambda_F = \frac{9}{4} \left(\frac{k_{31}^2}{4 - k_{31}^2} \right) \quad \lambda_P = \frac{5}{3} \left(\frac{k_{31}^2}{4 - k_{31}^2} \right)$$

For our ultrasonic motor, we do not have cantilever beams. Our monomorph structure can, however, be modeled as a simply-supported beam of length $L = \frac{\lambda}{2}$.

The effective electromechanical coupling factor for our simply-supported monomorph, which we denote as Υ_{eff} , will be different than the effective electromechanical coupling factor for a cantilevered bimorph device. For a simply-supported monomorph working against moments applied at the ends (as in the case of a traveling wave motor), we can expect:

$$\Upsilon_M < 3 \left(\frac{k_{31}^2}{4 - k_{31}^2} \right)$$

since a single-layer monomorph structure will be less effective than a bimorph in delivering output moments and forces.

The electromechanical coupling coefficient, k_{31} , for our PZT thin films was measured to be 0.22 [Udayakumar 91], and is given as 0.34 for the PTS-1195 ceramic in the motors of Figure 3-1 [Piezo Systems 85] which leads to the result that the percentage of mechanical energy converted from input electrical energy for our bulk-ceramic motors will be on the order of 11.6%. This does not imply efficiency however, as the remaining 88.4% is not dissipated but stored dielectrically.

Whereas energy *conversion* is described by k_{31} in a slab of piezoelectric material, or by λ_{eff} and Υ_{eff} for devices such as bimorphs and monomorphs, energy *loss* in a piezoelectric material is denoted by the quality factors Q_M (mechanical) and Q_E (electrical, or dielectric).

The equivalent circuit of Figure 4-1 can lead to determination of the mechanical quality factor of a piezoceramic, Q_M , which is the ratio of average energy stored per cycle to average energy dissipated per cycle. [Jaffe 58] gives an expression in terms of electrical equivalent circuit parameters:

$$\frac{1}{Q_M} \cong 4\pi\Delta f |Z_{min}| (C_o + C_A)$$

The electrical quality factor is related to the dielectric dissipation or loss tangent, $\tan\delta$, the form usually specified with the material. $\tan\delta$ is the ratio of the imaginary part of the complex permittivity to the real part:

$$\frac{1}{Q_E} = \tan\delta = \frac{Im\{\epsilon\}}{Re\{\epsilon\}} = \eta$$

This electrical model of each stator section is applicable only in the vicinity of an isolated resonance. Unwanted excitation of nearby modes can result in mode coupling and unwanted forms of deformation.

Chapter 5

Energy Conversion

To this point, we have developed a model of the mechanical and electrical characteristics of the stator portion of an ultrasonic motor, from the input electrical terminals to the output displacements on the stator surface. It would be useful to compare such energy conversion processes across a spectrum of actuator technologies in order to expose relative merits among the possible choices.

[Hollerbach, Hunter and Ballantyne 91], in their comparative analysis of actuator technologies for robotic applications, point to stall torque density as a figure of merit amongst disparate technologies ranging from electromagnetic motors through pneumatics, hydraulics, magnetostrictors, shape memory alloys and piezoelectric inchworm motors. They claim that stall torque density is a better figure of merit than power density, as power density calculations require the proficiency of the drive electronics to be taken into account. [Bart et al. 88] alternatively compare electromagnetic and electrostatic motors based on energy densities storable in the gap between the stator and the rotor. Here, we extend the latter analysis to energy densities storable in piezoelectric ultrasonic motors.

In an electromagnetic motor, the storable energy density, u_{mag} , in the air gap between the stator and the rotor is:

$$u_{mag} = \frac{1}{2} \frac{B^2}{\mu_o}$$

where B is the magnetic flux density and μ_o is the permeability of free space.

In an electrostatic motor, the storable energy density in the air gap is:

$$u_{electrostatic} = \frac{1}{2} \epsilon_o E^2$$

where E is the electric field intensity and ϵ_o is the permittivity of free space.

[Bart et al. 88] note that the maximum flux density available in an electromagnetic motor at saturation is approximately 1.5 T, yielding a maximum energy density of:

$$u_{mag,max} = 9 \times 10^5 \frac{J}{m^3}$$

Similarly, for an electrostatic motor, the maximum electric field before breakdown is on the order of $10^6 \frac{V}{m}$, which gives the maximum energy density attainable as:

$$u_{electrostatic,max} = 4.4 \frac{J}{m^3}$$

For small gaps on the order of $1 \mu m$, achievable with silicon lithographic processes, [Bart et al. 88] also point out that electric fields on the order of $10^8 \frac{V}{m}$ are sustainable, leading to energy densities commensurate with those of electromagnetic motors:

$$u_{thin electrostatic,max} = 4.4 \times 10^4 \frac{J}{m^3}$$

Torques however, are computed from the spatial derivatives (the changes in rotor positions as the rotors slide past the stators) of the total coenergies, U'_{mag} and $U'_{electrostatic}$. For a linear material (i.e. an air gap), the energy, U , is equal to the coenergy, U' . Total coenergy in the air gap of an electromagnetic motor then is the integral over the volume of the energy density:

$$U'_{mag} = \int_{vol} \frac{1}{2} \frac{B^2}{\mu_o} dv = \frac{1}{2} Li^2$$

where dv is a differential volume element, L is the inductance and i is the current.

Total coenergy in an electrostatic motor becomes:

$$U'_{electrostatic} = \int_{vol} \frac{1}{2} \epsilon_o E^2 dv = \frac{1}{2} CV^2$$

where C is the capacitance and V is the voltage.

The torque for an electromagnetic motor can then be calculated by taking the derivative

of the coenergy with respect to the rotor position, θ , keeping i constant:

$$\tau_{mag} = \left. \frac{\partial U'_{mag}}{\partial \theta} \right|_i = \frac{1}{2} \frac{dL}{d\theta} i^2$$

Similarly, for an electrostatic motor, the torque produced is calculated with V held constant:

$$\tau_{electrostatic} = \left. \frac{\partial U'_{electrostatic}}{\partial \theta} \right|_V = \frac{1}{2} \frac{dC}{d\theta} V^2$$

If we look now at piezoelectric motors, we find that the storable energy density is related to the electric field applied across the piezoceramic, “the gap”. In these capacitive-type motors, the gap is no longer air, but the high dielectric material, PZT. The storable electrical energy density input to a piezoelectric motor becomes:

$$u_{piezo,input} = \frac{1}{2} \epsilon_{pzt} \epsilon_o E^2$$

where ϵ_{pzt} is the relative dielectric constant of PZT (1950 for the PTS-1195 ceramic in the motors of Figure 3-1 [Piezo Systems 85] and 1300 for our PZT thin films [Udayakumar 91]). For bulk-ceramic PZT, the electric field breakdown strength is on the order of $10^6 \frac{V}{m}$, similar to the breakdown field of macroscopic electrostatic motors. Thus we see that the storable electrical energy densities of bulk-ceramic piezoelectric motors are three orders of magnitude larger than those of electrostatic motors, due to the large dielectric constant.

The total electrical energy input to a piezoelectric motor is also the integral over the volume of the energy density:

$$U_{piezo,input} = \int_{vol} \frac{1}{2} \epsilon_{pzt} \epsilon_o E^2 dv$$

In a piezoelectric motor however, torque is not generated as the spatial rate of change of total energy, but rather is first converted to strain energy in bending and then converted to output forces through frictional coupling. The amount of input electrical energy converted to strain energy in a slab of piezoceramic is characterized as k_{31}^2 [Lucas 75] as is described in Appendix B. For a monomorph, the ratio is Υ_{eff}^2 .

For example, we can calculate that the maximum allowable energy density input to our

bulk-PZT motors will occur at the breakdown field, $10^6 \frac{V}{m}$:

$$u_{bulk\ piezo, max\ input} = 8.6 \times 10^3 \frac{J}{m^3}$$

The output strain energy density is the total strain energy, $U_{piezo, strain}$, divided by the volume, Lbh_p :

$$u_{piezo, strain} = \frac{3}{8} d_{13}^2 E_3^2 c_p \frac{(1 - 3f_o + 3f_o^2)}{r_\kappa^2}$$

which, using the maximum breakdown field strength, calculates to:

$$u_{bulk\ piezo, max\ strain} = 6.65 \frac{J}{m^3}$$

The ratio of the latter, strain energy density, to the former, input electrical energy density, is Υ_{eff}^2 :

$$\Upsilon_{eff}^2 = \frac{6.65 \frac{J}{m^3}}{8.6 \times 10^3 \frac{J}{m^3}} = 7.7 \times 10^{-4}$$

or

$$\Upsilon_{eff} = 0.028$$

This calculated value is roughly a factor of 12 lower than that calculated from the given (measured) value of $k_{31} = 0.34$:

$$\Upsilon_M < 3 \left(\frac{k_{31}^2}{4 - k_{31}^2} \right) = 0.090$$

When macroscopic electrostatic motors are shrunk to microscopic sizes with gap widths on the order of $1 \mu m$, electric field breakdown strength increases by two orders of magnitude. This is due to the fact that as the gap gets smaller or the pressure in the gap decreases, there is a decreased chance of air molecules colliding, leading to breakdown.

For thin film dielectrics, it is also the case that electric field breakdown strengths see a two-order of magnitude improvement from the roughly $10^6 \frac{V}{m}$ available for PTS-1195 ceramic [Piezo Systems 85] which is $188 \mu m$ thick, to the $10^8 \frac{V}{m}$ possible in PZT thin films [Udayakumar 91] which are $0.3 \mu m$ thick. In thin films, the reason for improved breakdown strength is not a decrease in the pressure-gap product, but rather a decrease in the likelihood of point defects due to thin layers.

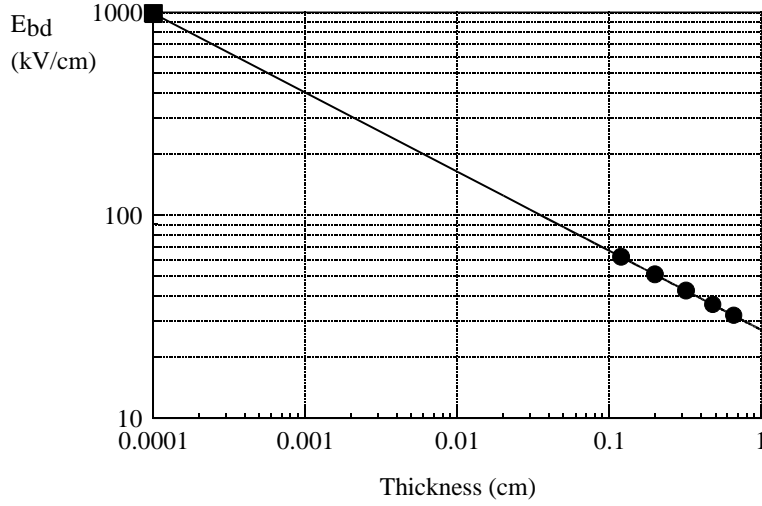


Figure 5-1: The breakdown strength of PZT increases dramatically as the material moves from bulk to thin-film form. The round dots indicate data from [Gerson and Marshall 59] while the square block signifies new data on thin films [Udayakumar 91].

Studies of breakdown strength vs. thickness in bulk PZT samples were first conducted by Gerson and Marshall [Gerson and Marshall 59]. They found that the relationship empirically fit the curve which is illustrated in Figure 5-1 where:

$$E_{bd} = 27.2h_p^{-0.39}$$

Here, E_{bd} is the electric field intensity at breakdown, given in $\frac{kV}{cm}$, and h_p is the thickness of the piezoceramic layer, in centimeters.

Although, at the time, Gerson and Marshall had no thin-film PZT, our recent fabrications runs have shown that thin film breakdown measurements do fit precisely with their earlier work.

We can see then, that while electrostatic micromotors display improved energy densities over electrostatic macromotors, microfabricated piezoelectric motors exhibit the same improvement in breakdown strength, but again contribute three orders of magnitude improvement in energy density due to the large dielectric constant. The maximum energy density then, for piezoelectric micromotors is:

$$u_{thin\ piezo, max\ input} = \frac{1}{2}\epsilon_{pzt}\epsilon_o E_{bd}^2 = 5.8 \times 10^7 \frac{J}{m^3}$$

Plugging in the above expression for E_{bd} , we derive an expression for energy density

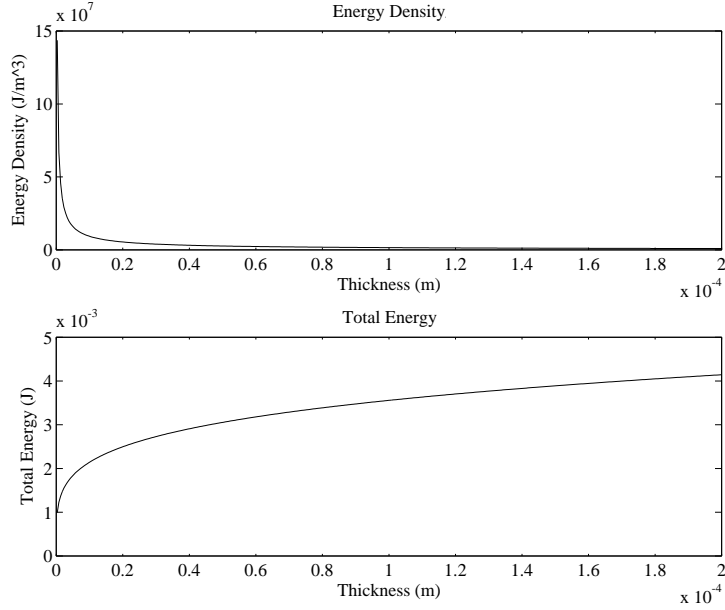


Figure 5-2: Energy density and total energy, for a given active electrode area, depend on piezoceramic thickness.

as a function of piezoelectric thickness which is plotted in the top graph in Figure 5-2.

Converting to mks units for h_p in meters:

$$u_{piezo,input} = \left(4.26 \times 10^4\right) \left((100h_p)^{-0.78}\right) \frac{J}{m^3}$$

Multiplying by the area and thickness, we find the total energy as:

$$U_{piezo,input} = \left(4.26 \times 10^4\right) \left((100h_p)^{-0.78}\right) (A) (h_p) J$$

This expression of total energy as a function of piezo-layer thickness is illustrated in the lower graph in Figure 5-2 for an area equal to the 8 mm outer diameter, 5 inner diameter motor of Figure 3-1. For a film thickness of $0.3 \mu\text{m}$, we find the total input electrical energy for a thin-film PZT version of the motor in Figure 3-1 to be:

$$U_{thin\ piezo,input} = 5.3 \times 10^{-3} J$$

For the same size motor, but using bulk PZT $188 \mu\text{m}$ thick, we find

$$U_{bulk\ piezo,input} = 2.1 \times 10^{-2} J$$

Although the total electrical energy storable in this bulk PZT motor is four times greater than for a thin-film motor of equivalent area, we are interested in the possibilities of lower manufacturing costs which microfabrication holds. If motors can be printed rather than machined, sanded, grinded and soldered, then we can hope to develop small, compact, cheap actuators. In addition, moving away from machine tools and towards microfabrication and lithographic manufacturing processes provides a means for scaling to even smaller dimensions or patterning finer features.

Chapter 6

Contact Mechanics

We have described the energy conversion process which takes place in the *stator* of an ultrasonic motor. That is, we have discussed the first stage of the energy transduction mechanism of a vibromotor which we outlined in Figure 1-1. We have seen how input electrical energy is transformed into output strain energy in the form of mechanical displacements, where the percentage of input electrical energy converted to strain energy is characterized by Υ_{eff}^2 for a monomorph. Losses in this resonant motor were described by the mechanical quality factor, Q_M .

What we are really interested in, however, is how much power can be delivered to a load and what form the speed-torque curve will take. We would also like to know the overall system efficiency and the stall torque density. To answer these questions, we focus on the second stage of the energy conversion process, the vibration rectification achieved through frictional coupling between the rotor and the stator.

Actuators utilizing these mechanisms form a much wider class than the various embodiments of ultrasonic traveling wave motors. Vibratory feeders transporting granular particles on a bed in process-control applications impart a flight phase or sliding phase to the particles to be moved by inducing an oscillatory diagonal motion in the bed [Gaberson 72]. Early piezoelectric actuators used ratchet-style mechanisms, wherein a single-point contact would oscillate and impact against the rotor at an oblique angle, creating a uni-directional drive [Barth 73]. Some modeling of these types of systems is described in [Sashida 82] and [Kobriniskii and Lennox-Napier 69]. In all of these actuators, the stator is in contact with the rotor for one portion of the cycle pushing it in one direction, and is retracted

from contact in the remaining portion of the cycle when the stator point is moving in the opposite direction. A primary disadvantage of this type of actuator is that the stator must be adjusted and held fixed to within a few microns of the rotor when at rest.

One subset of vibromotors, in which the stator and rotor always maintain frictional contact are the hammer-type actuators described in the work of [Higuchi et al. 89], which quasistatically inflict an impulse to a mass which produces a reaction force larger than the frictional sticking force.

Resonant traveling-wave ultrasonic motors which were first invented in the Soviet Union in the sixties [Ragulskis et al. 88] and again in Japan in the eighties [Sashida 83] contributed a means for creating larger amplitude displacements, maintaining continuous rotor-stator contact and allowing for electronic control of bi-directional motion. While much work has been done on modeling the stator energy conversion processes, far less has been reported on modeling the frictional coupling at the rotor-stator interface.

On the friction topic, [Hosoe 89] and [Okumura and Mukohjima 87] have reported on wear problems and efforts at improving efficiency in Canon ultrasonic motors used in auto-focus lenses. [Maeno, Tsukimoto and Miyake 92] have simulated the slip-stick interaction of the Canon motors using finite element analysis and [Maeno and Boggy 92] have investigated the hydrodynamic effects on the coupling. Other studies have been undertaken in Germany to understand the tribological properties of ultrasonic motors [Rehbein and Heinz 92] and experiments with linear ultrasonic motors using a variety of frictional interface materials have been reported by [Endo and Sasaki 87]. While many papers cite output torques and speeds of prototype motors with efficiencies in the range of 35% to 45%, [Kumada 85] claims the highest efficiencies, on the order of 80%.

[Minotti and Lallement 93] have modeled the rotor-stator interaction parameterizing the contact conditions of a non-rigid rotor in terms of angle of contact. [Kurosawa and Ueha 88] have performed closed-form analyses of interface losses, claiming theoretical limits of 70% efficiency for traveling wave motors and [Hirata and Ueha 93] have described lumped parameter equivalent circuits of the frictional coupling.

Our analysis of this process can be divided into several steps. First, we focus on the contact mechanics of a number of simple models of the interface conditions between the rotor and the stator, ignoring the tribological issues associated with surface asperities, hardness, wear and other surface effects. Later, we will make some comments on experiments

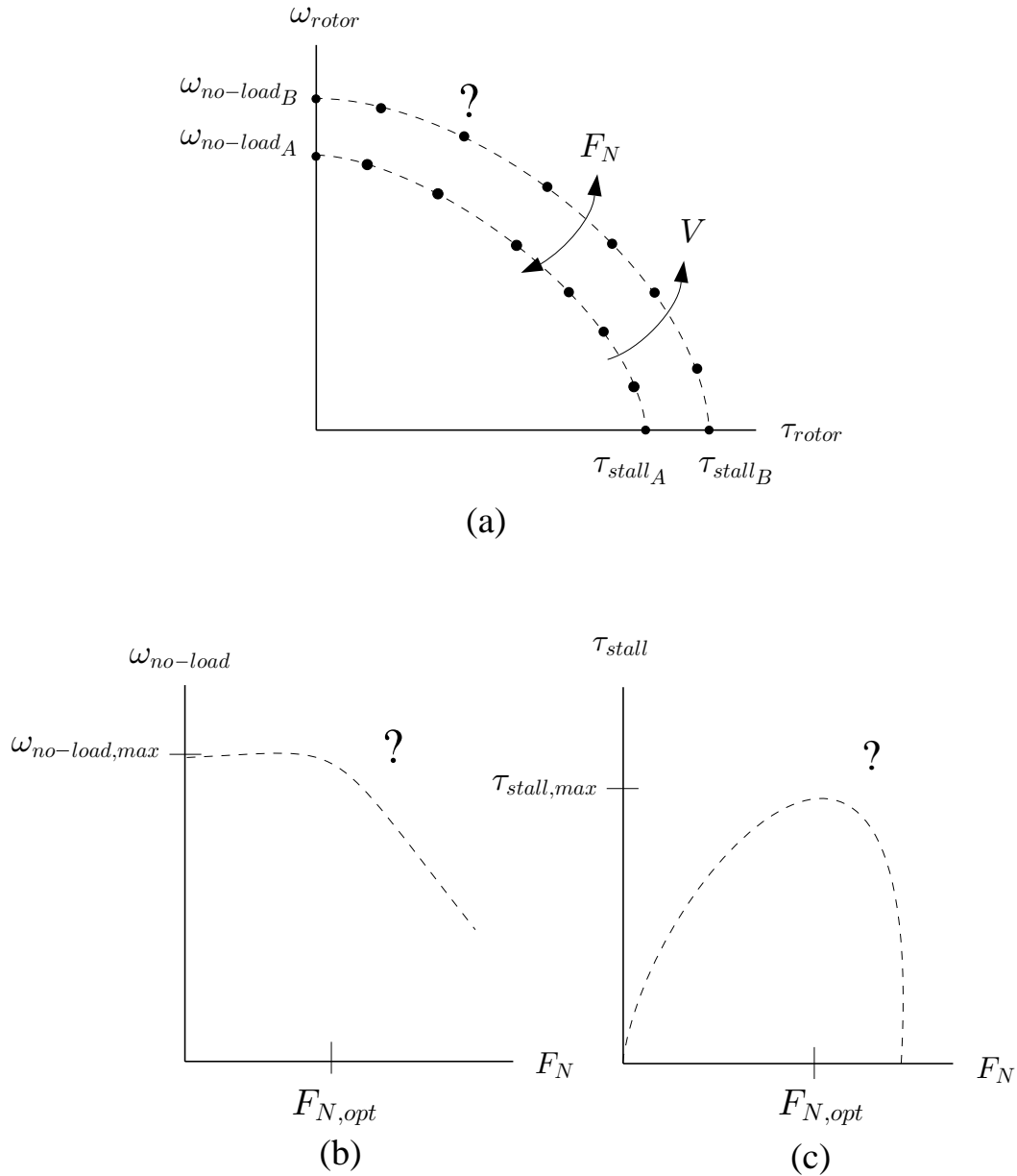


Figure 6-1: (a) We need to determine the form of the speed-torque curve. For each applied normal force, F_N , and applied voltage, V , there will be one curve characterizing the relationship of speed to torque. This curve will shift and possibly change shape as V or F_N is increased. (b) For a given applied voltage, we are interested in determining how the curve shifts with F_N . Parameterizing each curve by $\omega_{no-load}$, we can find a relationship between $\omega_{no-load}$ and F_N . (c) Alternatively, the performance of the motors can be described by parameterizing each curve by τ_{stall} and plotting τ_{stall} vs. F_N . By calculating these curves, we will be able to apply an optimal normal force to these motors such that the power output will be maximized for a given applied voltage.

performed with rotors exhibiting different asperity magnitudes.

The goal is to find a figure of merit for ultrasonic motors in order to compare them to other types of actuators. We have chosen stall-torque density as the metric for judging disparate technologies, and Figure 6-1 illustrates the approach. The torque produced by an ultrasonic motor is determined by the friction force at the rotor-stator interface. For a given excitation voltage and applied normal force, there will be a set of speed-torque operating points at which the motor will run, depending on the load it must drive. With no load, the motor will spin at its no-load speed and when the load is increased to the point that the rotor no longer moves, the motor is delivering its stall torque. The no-load speed and stall torque provide two operating points on the speed-torque curve as illustrated in Figure 6-1(a), but we would also like to know the relationship of speed to torque for the set of points determining the form of drop-off in between.

As the voltage or normal force is varied, the characteristic speed-torque curve will shift in some manner. By setting the drive voltage to the maximum value before depoling occurs and varying the applied normal force, we can determine how the speed-torque curve shifts in relation to a new normal force. Figure 6-1(b) illustrates a succession of characteristic no-load speeds for a set of applied normal forces and a given excitation voltage. We would imagine that if there is no normal force (the rotor does not touch the stator), there will be no rotor speed. When a normal force presses the rotor against the stator, without a side load, the rotor will spin at a certain no-load speed. As the normal force is increased, the no-load speed will change and for some very large normal force, the rotor will not spin at all. For some value of normal force, F_N , there will be a maximum no-load speed. Of course, for every speed-torque curve characterized by a no-load speed, there will be a related stall torque, and the variation of stall torque with normal force can then also be determined as shown in Figure 6-1(c). Once we find the maximum stall torque, we can divide by the mass or volume of the motor to determine our figure of merit, the maximum stall-torque density.

The form the speed-torque curves take will depend on two things: 1) our model of the deformation, and 2) the friction law we choose.

In terms of the friction law, a coefficient of friction describes the relationship between two surfaces and how forces are transmitted across their area of contact. To speak of “the coefficient of friction of a material” is meaningless, as a coefficient of friction describes not a property of a lone material, but the relationship between two. In general, the coefficient

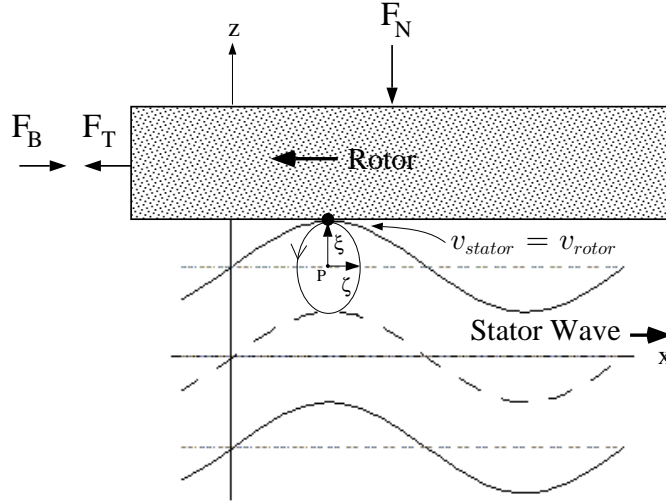


Figure 6-2: If the rotor contacts the stator only at the apex of the traveling wave, the rotor velocity will be equal to the horizontal velocity, $v_{h,max}$, of the stator surface as long as there is no slipping.

of friction of two materials, μ , is not a constant. In Coulomb friction, μ is a constant and is multivalued for dynamic and static scenarios. In rolling friction, such as a plate on a bed of rollers, the coefficient of friction is proportional to the difference in velocities of the plate and the rollers [Bhushan and Gupta 91]. Other, more complicated, friction laws have been proposed to include time histories and hysteresis for phenomena such as earthquakes [Linker and Dieterich 92] and robot joints [Dupont and Bapna 92].

In pursuit of characteristic speed-torque curves, our approach will be to analyze a series of progressively more sophisticated contact mechanisms, along with several different friction laws. We will examine three cases:

- A rigid rotor and a rigid stator contacting along a line, assuming Coulomb friction; $F_T = \mu F_N$.
- A compliant rotor and a rigid stator contacting over an area, also assuming Coulomb friction; $F_T = \mu F_N$.
- A compliant rotor and rigid stator contacting over an area, but assuming viscous friction; $F_T = -\varepsilon [v_{stator}(x) - v_{rotor}] F_N$.

6.1 Line Contact, Coulomb Friction

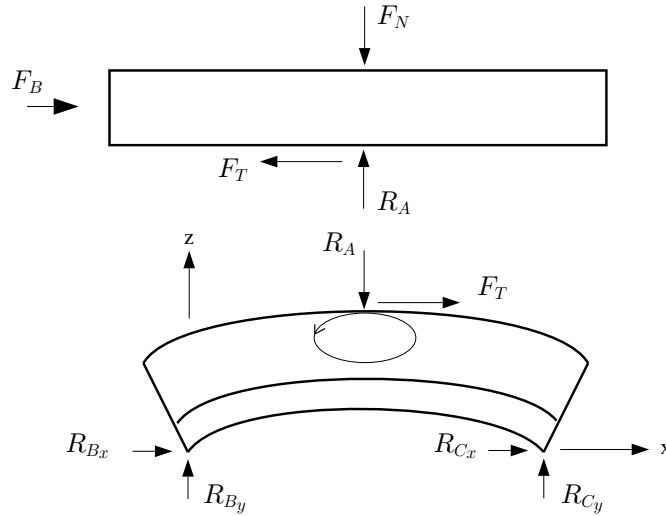


Figure 6-3: Free-body diagram of the rotor and stator with the stator modeled as having only a line contact by the rotor.

The first case is illustrated in Figure 6-2, where we assume the rotor is rigid and contacts the stator only at the peaks of the traveling wave, as the stator bending profile does not distort. The contact between the rotor and the stator then is along a line of length b into the beam. Due to our assumption of the beam having a uniform cross-section, we will use two-dimensional free-body diagrams to depict forces acting on the system. These forces are, however, actually forces per unit length. This ideal case of line contact will lead us to upper bounds for the no-load speed and the stall torque of an ultrasonic motor.

If we assume Coulomb friction and no slipping, then at the line of contact the velocity of the stator will be equal to the velocity of the rotor, as the stator contact point pulls the rotor along.

Figure 6-3 illustrates the forces acting on the rotor and the stator. For line contact between the rotor and stator, the normal force acting on the rotor is transmitted as a force, R_A , acting solely on the apex of the stator ($R_A = F_N$). While in the condition of no slip, when a load or braking force, F_B , is applied to the motor at a level less than that required to stall the motor, then at steady-state, the frictional force, F_T , delivered by the rotor will increase to match it, being equal and opposite to F_B , and the velocity of the rotor will be equal to the velocity of the stator.

There can be slipping, however, when larger loads are applied. The largest load that

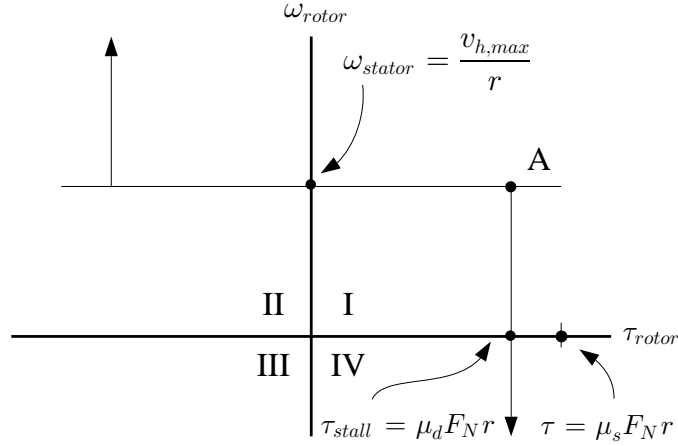


Figure 6-4: For point contact and Coulomb friction, rigid rotor and undistorted stator, the speed-torque curve shows constant rotor speed for any torque in the region of no slipping. For larger loads, slipping occurs and the speed-torque curve is vertical, displaying a constant, maximum torque for any rotor speed.

can be applied without slipping is equal to:

$$F_T = \mu_s F_N$$

where μ_s is the static coefficient of friction.

After sliding is initiated, the friction force becomes:

$$F_T = \mu_d F_N$$

where μ_d is the dynamic coefficient of friction. Figure 6-4 illustrates the speed-torque curve for this ideal case of line contact between a rigid rotor and rigid stator.

The velocity of the stator contact point is determined by examining Figure 6-2. In this figure, the ξ - ζ coordinate system is centered at a point P on the surface of the originally undeformed stator. The thin-dashed horizontal lines in the figure represent the top and bottom surfaces of the undeformed stator. From Appendix A, we saw that when a traveling wave of bending is induced, a stator surface point, P , moves with a transverse displacement of:

$$\xi = w_o \cos(kx - \omega t)$$

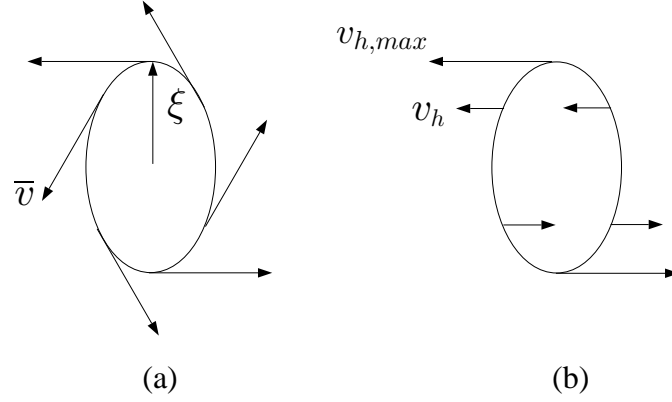


Figure 6-5: (a) The velocity profile for a counter-clockwise elliptical trajectory of a point on the surface of the stator is everywhere at right angles to the displacement. (b) The longitudinal components of velocity point in opposite directions for $\xi > 0$ and $\xi < 0$.

and with a longitudinal displacement of:

$$\zeta = \frac{2\pi h w_o}{\lambda} \sin(kx - \omega t)$$

tracing out an elliptical trajectory which satisfies the equation:

$$\frac{\zeta^2}{\left(\frac{2\pi h w_o}{\lambda}\right)^2} + \frac{\xi^2}{w_o^2} = 1$$

The displacement and velocity profiles of a stator surface point undergoing this elliptical trajectory are shown in Figure 6-5 (a). The longitudinal speed of a surface point is the derivative of the horizontal displacement with respect to time:

$$v_h = \frac{\partial \zeta}{\partial t} = -\frac{2\pi \omega h w_o}{\lambda} \cos(kx - \omega t)$$

The horizontal components, v_h , of each velocity vector in Figure 6-5(a) are shown in Figure 6-5(b).

For the case of a rigid rotor and rigid stator, the rotor contacts the apex of the traveling wave, giving a rotor speed of the maximum horizontal velocity of the surface point:

$$v_{h,max} = -\frac{2\pi \omega h w_o}{\lambda}$$

We see from the speed-torque curve of Figure 6-4 that the rotor speed will be constant

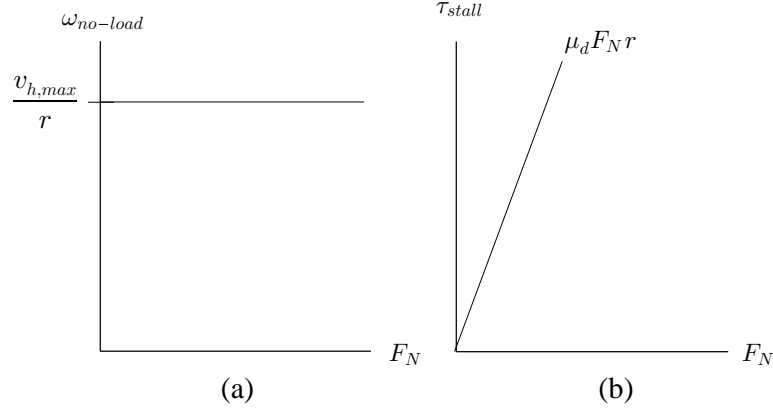


Figure 6-6: (a) For a rigid rotor and rigid stator, the no-load speed is independent of applied normal force. (b) For this case of line contact, the stall torque can be increased arbitrarily by applying larger normal forces.

at the value:

$$\omega_{rotor} = \frac{v_{h,max}}{r}$$

for all load torques within the range of no slipping. Once slipping occurs, the torque delivered by the motor remains constant at:

$$\tau_{rotor} = \mu_d F_N r$$

This describes the motoring action of quadrant I of Figure 6-4. As F_B is increased beyond this point, the motor slows down while still delivering torque equal to $\mu_d F_N r$, until finally the rotor stops moving. Increasing F_B further causes the rotor to spin in the reverse direction as illustrated by quadrant IV behavior. When F_B is directly oppositely to the way it is defined in Figure 6-3, the friction force acts to oppose it and so the rotor and stator velocities remain equal and in the same direction. The rotor torque is thus negative in quadrant II and remains equal and opposite to the pulling force, $-F_B r$, until slipping occurs, at which point the rotor velocity increases and the rotor delivers a constant torque of:

$$\tau_{rotor} = -\mu_d F_N r$$

Once the speed-torque curve has been characterized, we can investigate how it shifts with F_N for a fixed excitation voltage. As the rotor speed is independent of F_N and the torque is directly proportional to F_N , increasing the applied normal force will increase the stall torque of the motor without affecting its speed before stall. Figure 6-6 shows the

no-load speed and stall torque dependencies on F_N . For this case, it seems that the stall torque can be increased by arbitrarily increasing F_N . However it is surely the case that the rotor and stator will deform at some point and the case of point contact will no longer hold. This will lead us to the next case, that of a compliant rotor and rigid stator.

However, continuing with the point contact condition, we note that the mechanical power output by a motor is the product of output speed and drive torque:

$$P_{mech} = \tau_{rotor}\omega_{rotor}$$

Mechanical output power is plotted as a function of rotor torque in Figure 6-7 (a). Since the mechanical output power is $P_{mech} = \tau_{rotor}\omega_{rotor}$, and ω_{rotor} is constant for torques from zero through stall, the output power grows linearly with torque until stall.

In this case, the maximum output power would be delivered at operating point *A* in Figure 6-4:

$$P_{mech,max} = \left(\frac{2\pi\omega h w_o}{\lambda} \right) (\mu_d F_N)$$

where it appears that output power is directly proportional to normal force, F_N .

The efficiency of this second stage of energy conversion is calculated as the ratio of mechanical output power to input power:

$$\eta_m = \frac{P_{mech}}{P_{in}}$$

The power loss in the system is due to frictional forces at the interface causing heating. The power loss is the product of tangential force produced by the rotor times the relative velocity of the two surfaces:

$$P_{loss} = F_T (v_{stator} - v_{rotor})$$

or in angular coordinates:

$$P_{loss} = \tau_{rotor} (\omega_{stator} - \omega_{rotor})$$

The motor efficiency then, is:

$$\eta_m = \frac{P_{mech}}{P_{loss} + P_{mech}} = \frac{\omega_{rotor}}{\omega_{stator}}$$

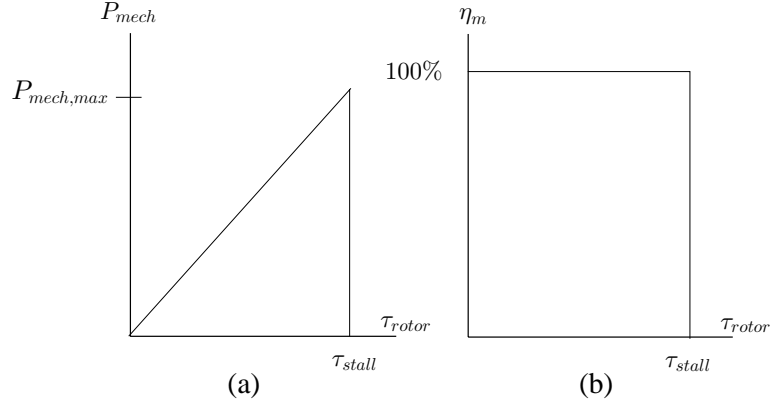


Figure 6-7: (a) The mechanical output power delivered by the motor grows linearly in the region of no slipping, from zero torque up through stall. (b) For the case of line contact, the efficiency of an ultrasonic motor is 100% while there is no slipping.

For line contact, ω_{stator} is a constant and efficiency is linearly related to rotor speed. The relationship of efficiency to rotor torque is illustrated in Figure 6-7(b) where for operating points that incur no slipping, that is, up until stall, the rotor speed is equal to the stator speed and the motor is perfectly efficient.

6.2 Line Contact, Viscous Friction

We can modify the model further by changing the friction law to viscous friction, where the friction force is proportional to the relative velocity between the two surfaces times the normal force:

$$F_T = -\varepsilon [v_{stator}(x) - v_{rotor}] F_N$$

where ε is a coefficient of viscous friction with units of seconds per meter.

For the case of line contact as in Figure 6-2, where the rotor contacts the stator only along a line through the width of the motor at the apex of the wave, then $v_{stator}(x) = v_{stator,max}$ and the rotor no-load speed is:

$$\omega_{no-load} = \omega_{stator,max} = \frac{v_{h,max}}{r}$$

The net friction force that the rotor applies to the load is equal and opposite to the friction force acting on the stator, as in Figure 6-3:

$$F_{T_{net}} = -F_T$$

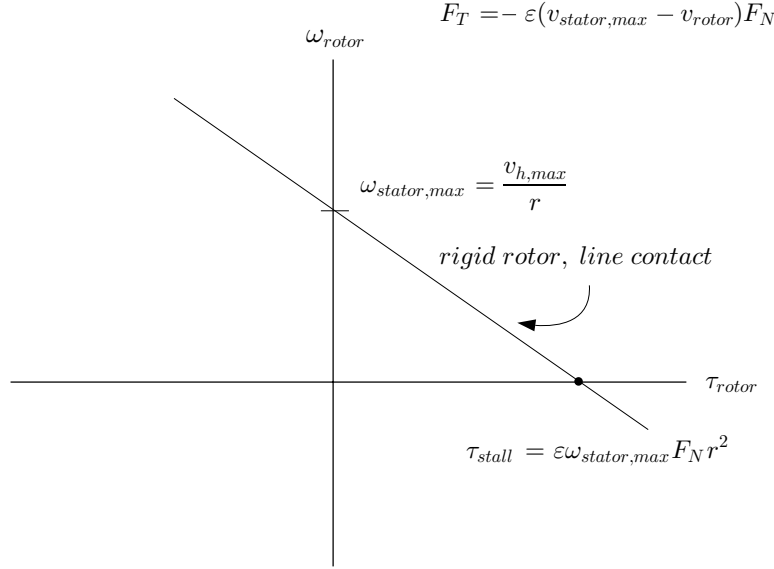


Figure 6-8: For line contact and viscous friction, the speed-torque curve falls off linearly.

and so the rotor torque is, converting to angular coordinates:

$$\tau_{rotor} = \varepsilon (\omega_{stator,max} - \omega_{rotor}) F_N r^2$$

Solving for ω_{rotor} , we see that for viscous friction, the rotor speed falls off linearly with increasing torque:

$$\omega_{rotor} = \omega_{stator,max} - \frac{\tau_{rotor}}{\varepsilon F_N r^2}$$

The resulting speed-torque curve is shown in Figure 6-8 where the stall torque occurs at:

$$\tau_{stall} = \varepsilon \omega_{stator,max} F_N r^2$$

The slope of the curve is determined by F_N . Figure 6-9 illustrates how the slope and stall torque change as F_N is increased. The rotor no-load speed is unaffected, as we have assumed that the stator does not distort and the rotor contacts the stator only along a line at the apex. Consequently, the $\omega_{no-load}$ vs. F_N curve and the τ_{stall} vs. F_N curve look very similar to those of Figure 6-6. In Figure 6-10(a) we see that $\omega_{no-load}$ is constant for all values of F_N . Figure 6-10(b) illustrates how stall torque increases linearly with F_N with a slope of $\varepsilon \omega_{stator,max} r^2$ instead of $\mu_d r$ as in the case of Coulomb friction with line contact.

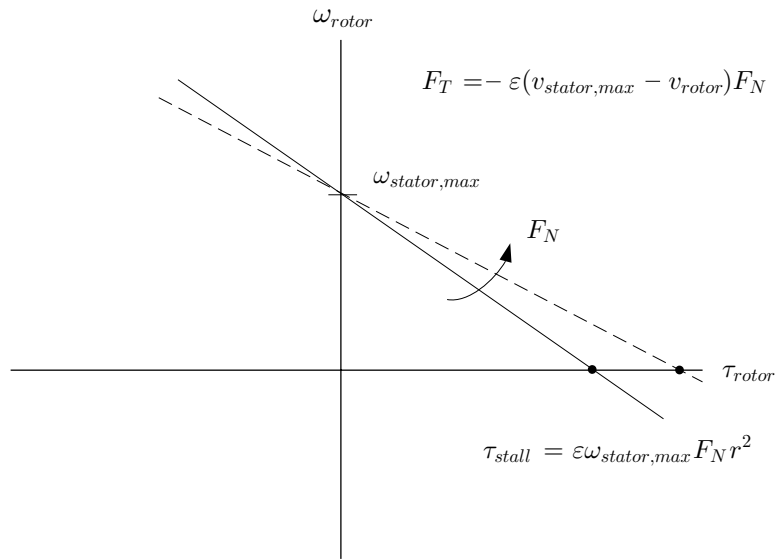


Figure 6-9: For line contact and viscous friction, as the normal force, F_N , is increased, the stall torque shifts out.

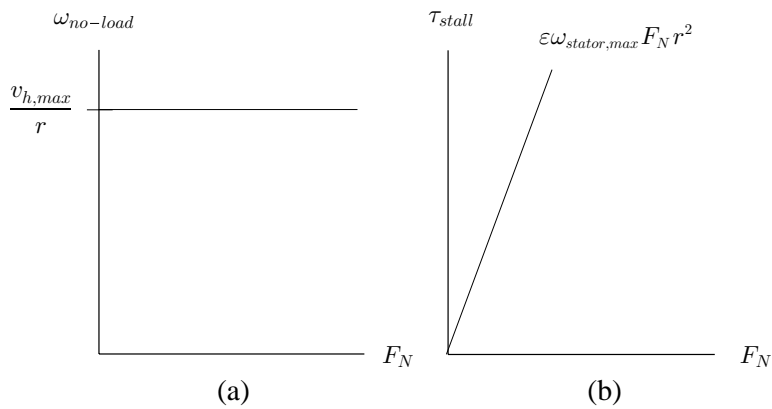


Figure 6-10: (a) For line contact and viscous friction, rotor no-load speed remains constant with F_N . (b) Stall torque increases without bound with F_N .

The output power is again the product of torque and speed:

$$P_{mech} = \omega_{rotor} \tau_{rotor}$$

For this case of viscous friction, the power vs. rotor torque curve is an inverted parabola:

$$P_{mech} = -\frac{\tau_{rotor}^2}{\varepsilon F_N r^2} + \omega_{stator,max} \tau_{rotor}$$

where the maximum power point can be found from:

$$\frac{dP_{mech}}{d\tau_{rotor}} = 0$$

and occurs at:

$$\tau_{rotor,opt} = \frac{1}{2} \varepsilon \omega_{stator,max} F_N r^2$$

or:

$$\tau_{rotor,opt} = \frac{1}{2} \tau_{stall}$$

The rotor speed at $\tau_{rotor,opt}$ is:

$$\omega_{rotor,opt} = \frac{1}{2} \omega_{stator,max}$$

The output power vs. rotor torque curve is plotted in Figure 6-11(a). The resulting maximum power output is:

$$P_{mech,max} = \frac{1}{4} \omega_{no-load} \tau_{stall}$$

The mechanical efficiency of the friction coupling can be found by again calculating the power loss due to frictional heating:

$$\eta_m = \frac{P_{mech}}{P_{mech} + P_{loss}}$$

where P_{loss} is the product of rotor torque and the relative speeds of the sliding surfaces:

$$P_{loss} = \tau_{rotor} (\omega_{stator,max} - \omega_{rotor}) = \frac{\tau_{rotor}^2}{\varepsilon F_N r^2}$$

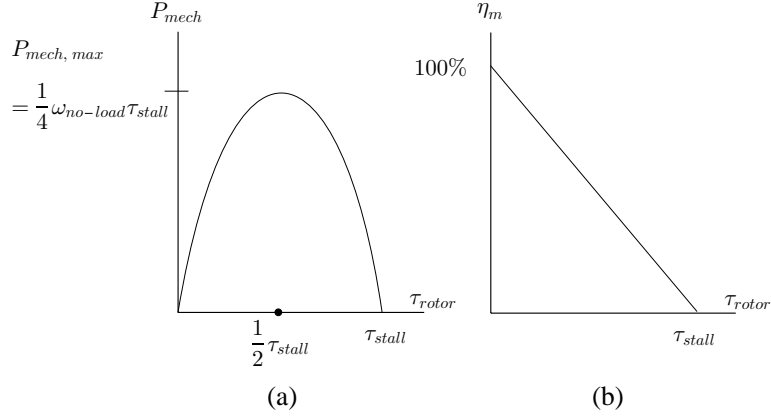


Figure 6-11: (a) Mechanical output power reaches a maximum when the rotor speed is $\omega_{rotor} = \frac{1}{2}\omega_{stator,max}$ and the rotor torque is $\tau_{rotor} = \frac{1}{2}\tau_{stall}$. (b) The efficiency falls off linearly with rotor torque from 100% at zero torque to 0% at stall torque.

yielding a mechanical efficiency of:

$$\eta_m = 1 - \frac{\tau_{rotor}}{\tau_{stall}}$$

Figure 6-11(b) displays the efficiency vs. rotor torque curve which falls off linearly with rotor torque.

6.3 Area Contact, Coulomb Friction

While the line contact assumption was useful in generating theoretical bounds on performance of an ultrasonic motor, line contact is an ideal case. We can make our model more realistic by relaxing the constraints of a rigid rotor and rigid stator. Here, we analyze the contact condition of a rigid stator with a compliant rotor, maintaining the assumption that the friction law acts as Coulomb friction.

6.3.1 Physical Interpretation

By assuming that the stator is rigid (i.e. its displacement profile is undistorted after contact with the rotor), we can say that the rotor conforms to the stator over some finite area and the normal pressure at the interface will be proportional to that displacement. Since we know the displacement of the stator, we then need to determine the area of contact.

This contact condition is illustrated in Figure 6-12. We change the coordinate system here to make the following discussion more straightforward. Whereas earlier diagrams of

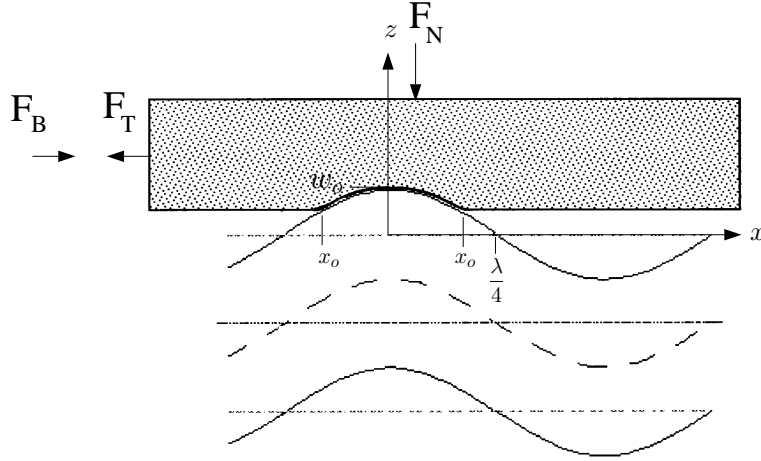


Figure 6-12: For the case of a compliant rotor and rigid stator, the rotor undergoes deformation such that the contact is over a finite area of the stator. The coordinate system here is centered on a peak at the original top surface of the stator.

the deforming stator were drawn for a transverse displacement of $\xi(x, t) = w_0 \cos(kx - \omega t)$ for $\omega t = \frac{\pi}{2}$, here we take $\omega t = 0$ and place the z -axis on a peak of the stator. The x -axis is placed on the top surface of the undeformed stator.

From Figure 6-12 we see that a given normal force will cause the rotor to comply and interpenetrate the stator surface over an area parameterized by x_0 . While the rotor moves with velocity v_{rotor} , the points on the stator surface from $-x_0$ to x_0 all have different horizontal velocities. As was illustrated in Figure 6-5(b), for a traveling wave moving in the positive x -direction, the horizontal components of stator surface point velocities point in the negative x -direction for $\xi > 0$ and in the positive x -direction for $\xi < 0$. Due to symmetry of this problem about the z -axis, we can focus on just the positive x -axis in describing the system. For the moment, we consider the case where the applied normal force is such that the interpenetration of the rotor into the stator is such that $0 < x_0 < \frac{\lambda}{4}$ (i.e. the interpenetration depth is less than w_0). In this case, stator surface points in contact with the rotor all have horizontal velocity components in the negative x -direction, although of different magnitudes.

The operating point of the motor depends on the load applied, F_B . We would like to find the characteristic speed-torque curve as in Figure 6-1(a) for this contact condition and friction law. If the load, F_B , is zero, we can find the no-load speed of the rotor. Figure 6-13(a) illustrates how the stator surface points' horizontal velocities will vary from $v_{h,max}$ at the apex, $x = 0$, to $v_{h,min}$ at the edge of the contact region, $x = x_0$. The rotor, which

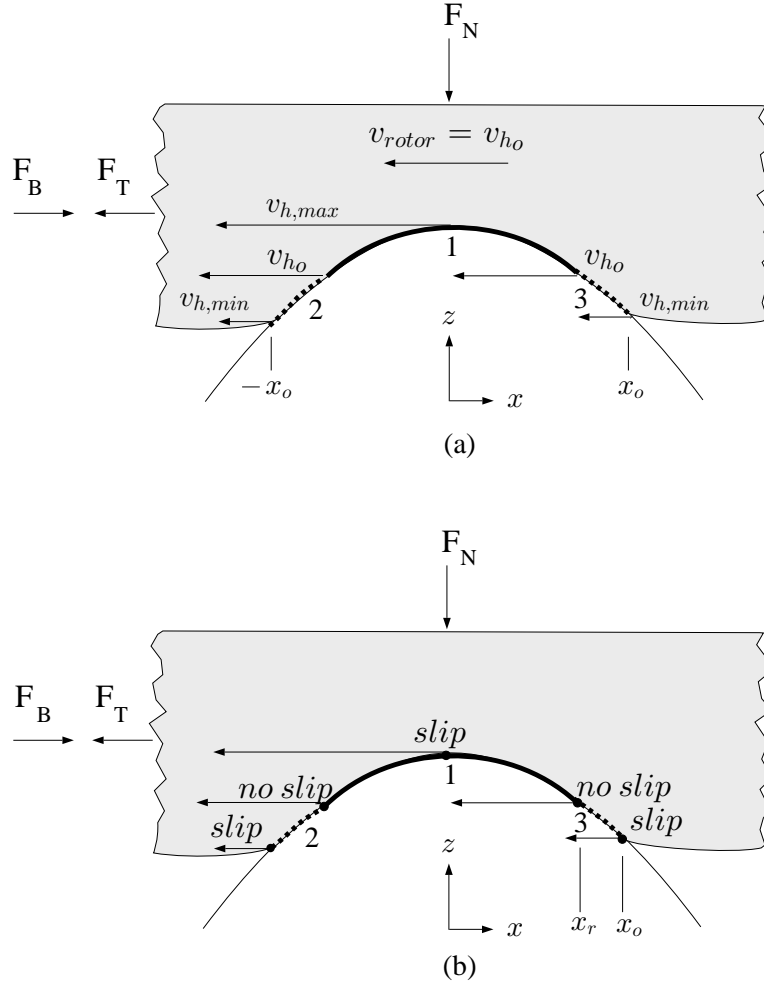


Figure 6-13: (a) The rotor moves at one velocity while individual stator points have different horizontal velocity components. (b) The points of slip and no slip corresponding to the points shown in (a) are marked. In the region $0 < x < x_r$, points on the stator surface have horizontal velocity components larger than the rotor velocity. In the region $x_r < x < \frac{\lambda}{4}$, the stator horizontal velocity components are smaller than the rotor velocity, while at the point x_r , they move at the same speed.

moves at one velocity, will travel at a velocity equal to some stator surface point's horizontal velocity, v_{ho} .

That is, for $F_B = 0$ and a given normal force, F_N , the no-load speed of the rotor is:

$$\omega_{no-load} = \frac{v_{ho}}{r}$$

For all other stator surface points, there will be a relative velocity between the rotor and the stator, which is a slip condition. These slip regions are illustrated in Figure 6-13(b) where for the stator surface point moving at velocity v_{ho} , there is no slip. In region 1, all stator

surface points have horizontal velocities larger than the rotor velocity and in regions 2 and 3, all stator surface points have horizontal velocities smaller than the rotor velocity. When a load F_B is applied, the friction force acts to oppose it, bringing the rotor to a steady-state velocity.

The forces acting on the rotor and stator are shown in Figure 6-14. In the free-body diagram of the rotor, the dotted line represents the deformation the rotor undergoes when contacting the stator under an applied normal force, F_N . This contact condition creates a pressure distribution at the interface. We consider only the normal component of the pressure distribution, $p(x)$, here, as the curvature of the stator turns out to be small and the stator is nearly flat over the region of contact.

The normal force is related to the pressure distribution by the integral of the pressure distribution over the contact area:

$$F_N = \int_{-x_o}^{x_o} p(x) dx$$

For Coulomb friction, the resulting friction force is:

$$F_T = - \int_{-x_o}^{x_o} \frac{\Delta v(x)}{|\Delta v(x)|} \mu_d p(x) dx$$

where the friction force is directed so as to resist motion. The relative velocity, $\Delta v(x)$, is:

$$\Delta v(x) = v_{stator}(x) - v_{rotor}$$

where $v_{stator}(x)$ signifies the horizontal component of the stator velocity.

For instance, in region 1, where the velocity of the stator is greater than the velocity of the rotor, $\Delta v(x)$ is pointed in the negative x -direction. The friction force acting on the stator in that region, F_{T_1} , is positively x -directed to resist the motion. The force acting on the rotor is equal and opposite to F_{T_1} of the stator and contributes a force component propelling the rotor in the negative x -direction. Exactly the opposite effect occurs in regions 2 and 3 where the stator velocity is less than the rotor velocity, contributing force components F_{T_2} and F_{T_3} of the rotor, resisting rotor motion in the negative x -direction.

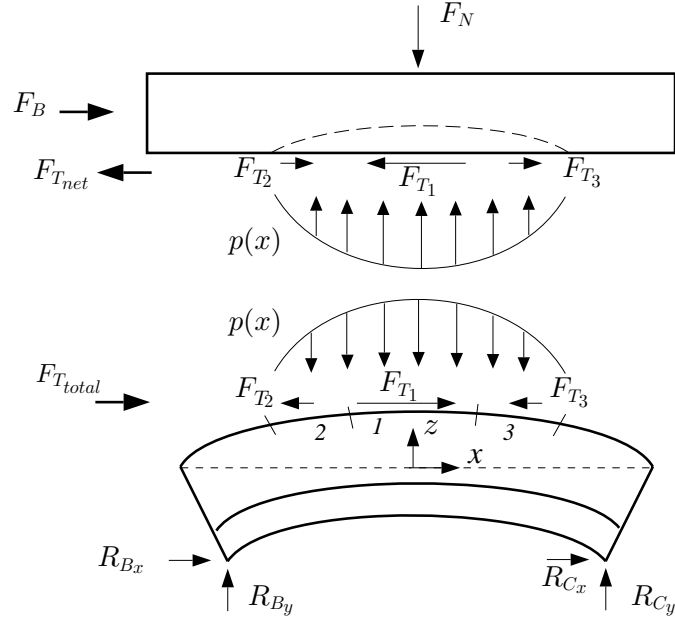


Figure 6-14: These free-body diagrams of the rotor and stator illustrate distributed contact and the ensuing frictional forces which act in the direction opposite to the direction of the relative velocity of the two sliding surfaces. For this region of contact where the rotor and all stator horizontal velocity components are moving to the left, in region 1 the stator horizontal velocity components are larger than the rotor velocity, and in regions 2 and 3 they are smaller. Consequently, the frictional forces in each region are directed as shown.

The resulting force acting on the rotor is:

$$F_B = -F_{T_{net}} = -(F_{T_1} - F_{T_2} - F_{T_3})$$

which is zero, the no-load condition, if:

$$F_{T_1} = -(F_{T_2} + F_{T_3})$$

When F_B is increased from zero, the point of no-slip must move down the stator profile, as region 1 must grow and regions 2 and 3 must shrink for $F_{T_{net}}$ to match F_B in steady-state. The rotor then moves at the new no-slip velocity which is lower than v_{h_o} . The point of no-slip is designated as x_r in Figure 6-13(b) and moves down the velocity profile as F_B is increased. This drop-off in speed with increased torque continues until F_B is increased to where the no-slip point is at the edge of the contact region, propelling the rotor with a velocity of:

$$\omega_{stator,min} = \frac{v_{h,min}}{r}$$

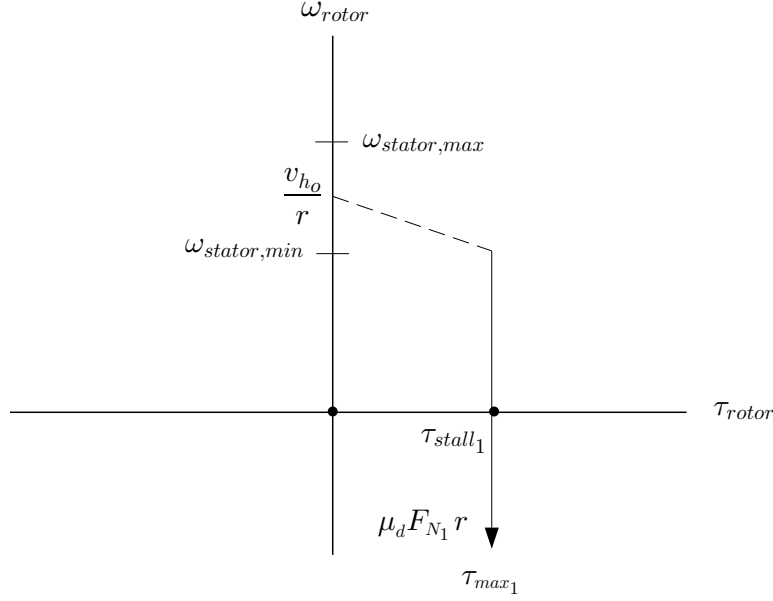


Figure 6-15: For area contact and Coulomb friction, the speed-torque curve falls off with torque from a given no-load speed up until the no-slip point reaches the edge of the contact region, which is moving at $\omega_{stator,min}$. Larger loads, F_B , cause slipping over the entire area of contact and the rotor reaches a limiting maximum torque. The exact shape of the curve in the region marked by the dotted line is yet to be determined and will depend upon the pressure distribution and the model of the contact mechanics at the interface.

For any larger loads, all points of contact will be sliding and the rotor will deliver its maximum torque:

$$\tau_{max_1} = \mu_d F_{N_1} r$$

Maximum torque occurs at the point where $x_r = x_o$. That is, when the braking force, F_B , is increased just to the point where the rotor begins to slip everywhere, the motor is delivering its maximum net frictional force:

$$F_{B_{max}} = -F_{T_{net,max}} = -(F_{T_1} - F_{T_2} - F_{T_3})_{max}$$

$F_{T_{net}}$ is maximized when F_{T_2} and F_{T_3} are zero, which is the case when $x_r = x_o$.

Figure 6-15 depicts the resulting speed-torque curve. The velocity of the stator at its apex, $\omega_{stator,max}$, is fixed by stator geometry and excitation voltage. The stator velocity at the edge of the contact region, $\omega_{stator,min}$, is determined by the interpenetration depth due to F_N . For an interpenetration depth less than w_o , the no-load speed will be some point between $\omega_{stator,max}$ and $\omega_{stator,min}$; $\frac{v_{ho}}{r}$. As F_B is increased above zero, the speed of the motor falls off from $\frac{v_{ho}}{r}$ to $\omega_{stator,min}$. We show a dotted line in the figure as at this stage

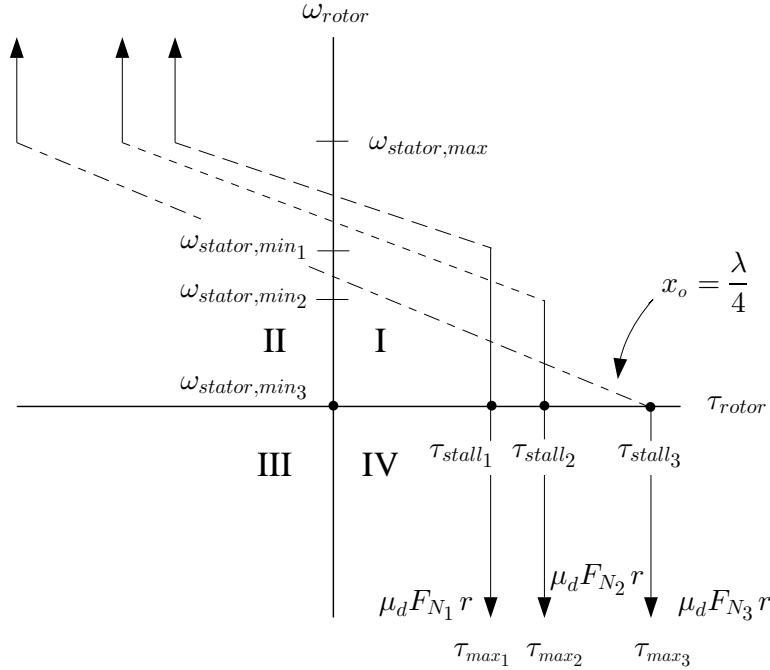


Figure 6-16: Increasing the normal force, F_N , creates a larger area of contact and therefore a lower $\omega_{stator,min}$. The speed-torque curve then shifts down as shown.

the shape of this curve is unknown, and will depend on the deformation at the interface and the pressure distribution.

Once the no-slip point has moved to the edge of the contact region, larger torques cannot be sustained, and the motor reaches its torque limit. Loads larger than this cannot be met with opposing friction forces and so the rotor decelerates. Equilibrium points are shown as the vertical solid line, where increasingly larger loads, F_B , cause the motor to slow down, but the motor cannot push back with any force larger than τ_{max1} . Finally, the speed of the rotor becomes zero and eventually reverses direction.

Note that the point where the speed of the rotor is zero is defined as the stall torque. For contact conditions where $0 < x_o < \frac{\lambda}{2}$, the maximum torque is the same as the stall torque and occurs when $x_r = x_o$, as shown by the vertical line in Figure 6-15.

The speed-torque curve of Figure 6-15 depicts a set of operating points for one given normal force and excitation voltage. Figure 6-16 shows how the speed-torque curve shifts as F_N is increased from the initial value of F_{N1} to F_{N3} , assuming F_{N3} causes an interpenetration depth just equal to w_o . An increase in normal force from F_{N1} to F_{N2} causes the edge of the contact region to move down the stator displacement profile, resulting in a lower $\omega_{stator,min}$. The maximum stator speed, $\omega_{stator,max}$, is not affected by the normal force in this model

which assumes a rigid stator, and so for $F_B = 0$ and $F_N = F_{N_2}$, the no-slip point will start at a lower position on the the stator profile than for $F_N = F_{N_1}$ in order to maintain the no-load equilibrium condition:

$$F_{T_1} = -(F_{T_2} + F_{T_3})$$

As F_B is increased from zero, the no-slip point, x_r , continues to move lower and the rotor velocity falls off with rotor torque until it reaches ω_{stator,min_2} , at the new maximum torque:

$$\tau_{max_2} = \mu_d F_{N_2} r$$

When the normal force is increased to F_{N_3} where the interpenetration depth is w_o , then $x_o = \frac{\lambda}{4}$ and the edges of the contact region are at $x = -\frac{\lambda}{4}$ and $x = \frac{\lambda}{4}$. At these points, the horizontal component of the stator velocity is zero and therefore ω_{stator,min_3} is zero. The no-load speed will be somewhere between $\omega_{stator,max}$ and ω_{stator,min_3} and the velocity of the rotor will drop off with the load torque until the maximum torque is reached at:

$$\tau_{max_3} = \mu_d F_{N_3} r$$

For larger loads, F_B , the rotor begins to decelerate and spin in the other direction as the rotor cannot supply enough torque to match the load.

The scenario just related describes quadrants I and IV behavior. Loads F_B applied in the negative x -direction yield quadrant II behavior where rotor velocity increases from the no-load speed to $\omega_{stator,max}$ up until a limiting negative torque is reached at $-\mu_d F_{N_i} r$ where $i = 1$ to 3. Again, we draw dotted lines in the fall-off region as the exact form of these curves has not yet been determined.

While Figure 6-16 illustrates how a family of speed-torque curves evolves, for quantifying a figure of merit for classifying the performance limits of this class of actuator technology, we are especially interested in how the stall torque for each curve changes as a function of F_N .

Figure 6-17(a) illustrates the condition of τ_{max_1} for a normal force of F_{N_1} . A pressure distribution, $p(x)$, is generated over the area of contact. At the edge of the contact region, $p(x) = 0$. When a braking load of magnitude $F_{B_{max_1}}$ is applied such that the motor is

supplying its maximum net torque, then:

$$-F_{T_{net,max}} = -F_{T_1}$$

and all points on the surface of the stator in the region of contact have horizontal velocity components greater than the rotor velocity, and the no-slip point has reached the edge of the contact region; $x_r = x_o$.

Figure 6-17(b) illustrates the maximum torque condition when the normal force has been increased to F_{N_3} , where $x_o = \frac{\lambda}{4}$. The pressure distribution now extends from $x_o = -\frac{\lambda}{4}$ to $x_o = \frac{\lambda}{4}$ and has a magnitude such that:

$$F_N = \int_{-\frac{\lambda}{4}}^{\frac{\lambda}{4}} p(x) dx$$

For a pressure distribution which is proportional to displacement, most of the total pressure derives from the region near the apex. When a braking load of $F_{B_{max3}}$ is applied, $F_{T_{net,max3}}$ must again be composed solely of contributions from F_{T_1} , and so $x_r = x_o = \frac{\lambda}{4}$. As $F_{T_{net}}$ is related to the normal force by:

$$F_{T_{net}} = \mu_d F_N = \mu_d \int_{-\frac{\lambda}{4}}^{\frac{\lambda}{4}} p(x) dx$$

we realize:

$$F_{T_{net,max3}} > F_{T_{net,max1}}$$

since:

$$F_{N_3} > F_{N_1}$$

Figure 6-18 depicts the geometry of the rotor and stator when the normal force is large enough that the interpenetration of the rotor is greater than w_o . Figure 6-19 illustrates the resulting pressure distribution and maximum torque condition for this case of F_{N_4} where the contact region has moved beyond $x_o = \frac{\lambda}{4}$ and encompasses points on the velocity profile where $\xi < 0$ and stator horizontal velocity components are pointed in the positive x -direction.

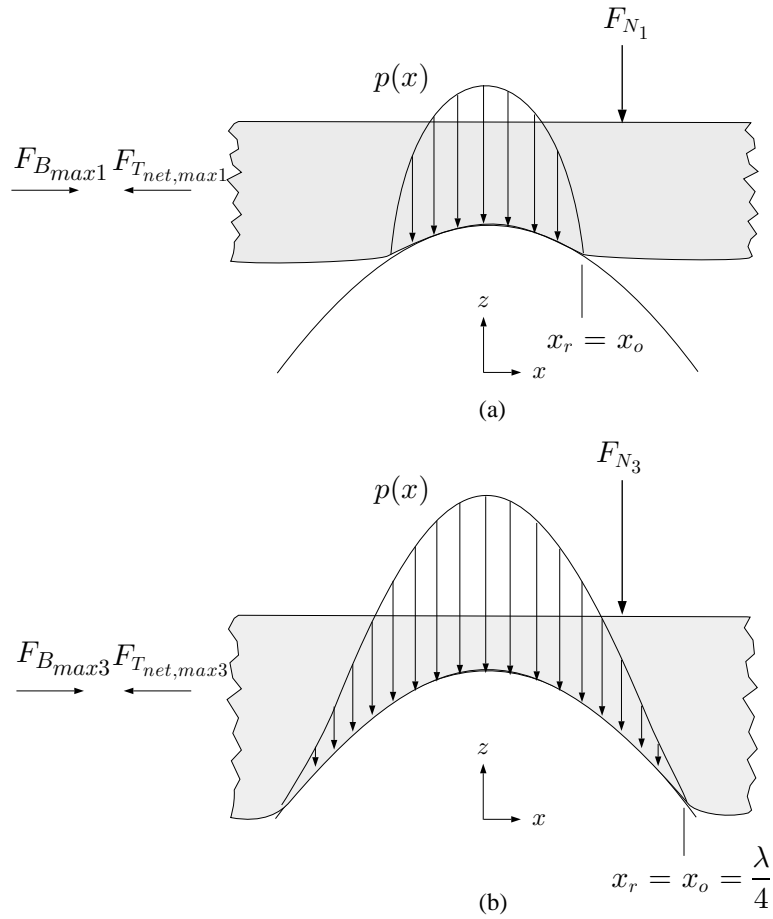


Figure 6-17: (a) Normal force F_{N_1} creates a pressure distribution over the region of contact. As the braking load is made larger and larger, $F_{T_{net}}$ increases to match it as the rotor slows down and the no-slip point, x_r , moves down the velocity profile to $x_r = x_o$. (b) For a larger normal force F_{N_3} , which squishes the rotor and causes it to comply such that $x_o = \frac{\lambda}{4}$, a larger braking load can be applied before $F_{T_{net,max}}$ is reached, since $F_{T_{net}}$ is directly proportional to F_N . In this case, the onset of this max condition occurs when $x_r = x_o = \frac{\lambda}{4}$. At $x_r = \frac{\lambda}{4}$, $\omega_{rotor} = 0$.

In these regions, the stator has horizontal velocity components opposing the direction of the velocity of the rotor. However, due to the larger normal force, F_{N_4} , a larger load, $F_{B_{max4}}$, can be applied than $F_{B_{max3}}$. This condition can occur at a *negative* velocity where $x_r = x_o$ is beyond $\frac{\lambda}{4}$. As shown in Figure 6-20, the onset of τ_{max4} occurs at the negative velocity $\omega_{stator,min4}$, the velocity corresponding to the no-slip point, x_r , being at the edge of the region of contact. While τ_{max4} occurs at a negative velocity, the stall torque corresponding to F_{N_4} is still defined as the torque at which $\omega_{rotor} = 0$. That is, for cases where $\frac{\lambda}{4} < x_o < \frac{\lambda}{2}$, the stall torque occurs at the point where $x_r = \frac{\lambda}{4}$.

Note that in this scenario, τ_{stall4} can be larger than τ_{stall3} , even though the contact area has extended to regions on the displacement profile where stator horizontal velocity components oppose the direction of the rotor velocity. The reason this is possible is that while the normal force, F_{N_4} , is larger (and hence $F_{B_{max4}}$ is larger) than for the case of F_{N_3} , the pressure distribution remains primarily over the apex where stator horizontal velocity components are moving in the same direction as the rotor. Since $p(x)$ has grown in magnitude, relatively small contributions to the friction force due to the relation:

$$F_{T_{net}} = \mu_d \int_{-x_o}^{x_o} p(x) dx$$

come from the additional $p(x)$ at the edges of the contact region covered by this new pressure distribution.

Would it be possible for an even larger normal force, F_{N_5} , to shift the speed-torque curve in such a way that the new stall torque, τ_{stall5} , would be less than τ_{stall4} ? In this model, where we assume the stator profile to be undistorted and the pressure distribution to be proportional to that profile, larger normal forces will only contribute to a larger $F_{T_{net,max}}$ and pick up very little opposition from the edges of the contact region where the pressure is low. For our model here, we would expect the stall torque to asymptotically reach a maximum as F_N is increased to the point where there is complete interpenetration of the rotor into the stator, that is, where $x_o = \frac{\lambda}{2}$. This case is also illustrated in Figure 6-20.

The variations of stall torque and no-load speed with F_N are shown in Figure 6-21. The fall-off trend of no-load speed with normal force for first quadrant operation is plotted in Figure 6-21(a) where we see that $\omega_{no-load}$ decreases as normal force is increased. Comparing this graph to the corresponding curve for line contact, Figure 6-6 (a), we see that the no-

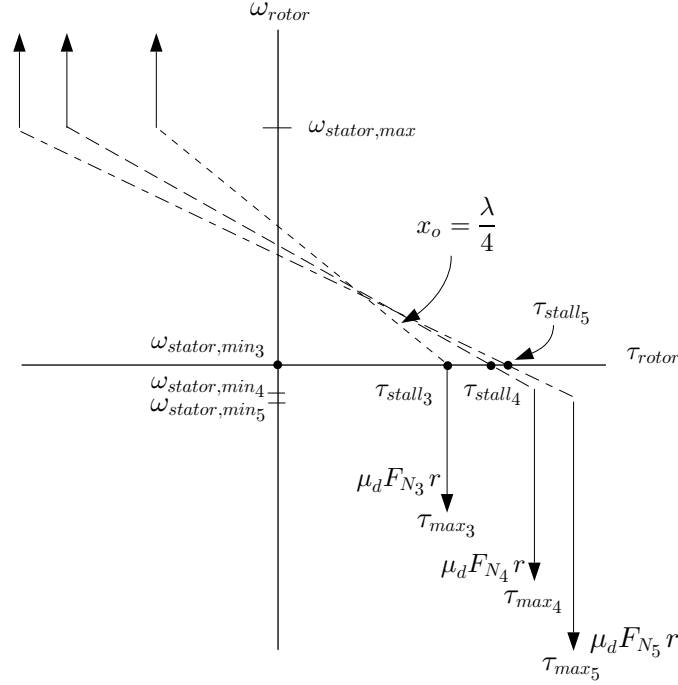
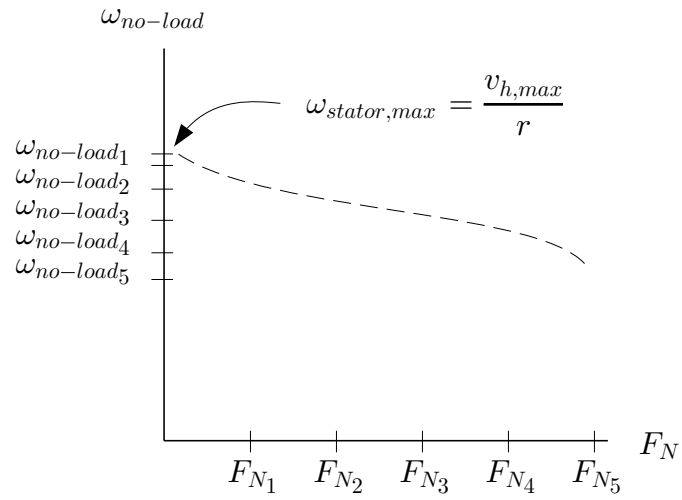


Figure 6-20: When the normal force is increased from F_{N_3} to F_{N_4} , the maximum torque, τ_{max_4} , is increased and the onset of this maximum condition occurs at a negative velocity, ω_{stator,min_4} . Note that τ_{stall_4} can be larger than τ_{stall_3} , even though $x_o > \frac{\lambda}{4}$. For this model of a non-compliant stator, further increases in F_N never coerce the stall torque to decrease.

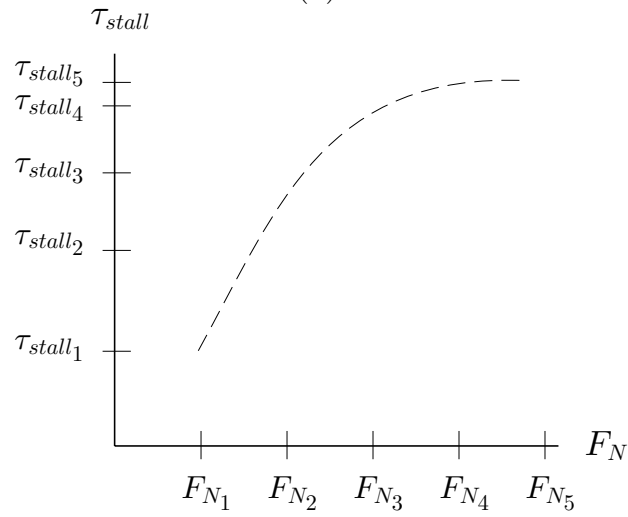
load speed for area contact predicts a drop-in in $\omega_{no-load}$ with F_N as opposed to remaining constant as in the case for line contact.

Similarly, the stall torque variation with F_N is plotted in Figure 6-21(b), where stall torque reaches a maximum at $x_o = \frac{\lambda}{2}$. Comparing to Figure 6-6(b), the τ_{stall} vs. F_N curve for line contact, we see that the area contact condition asymptotically approaches the prediction for the line contact case for small applied normal forces, but falls off for large F_N .

A τ_{stall} vs. F_N relationship like that originally sought in Figure 6-1(a), where τ_{stall} falls to zero for very large values of F_N would not be realized here. Extensions to this model of area contact with Coulomb friction between a rigid stator and compliant rotor to incorporate the condition of a compliant stator would lead towards such expectations, but for now we examine the model here more closely to investigate exactly how the performance curves develop for various assumptions about the contact mechanics at the interface.



(a)



(b)

Figure 6-21: (a) Assuming area contact, Coulomb friction, a rigid stator and compliant rotor, we can predict that the no-load speed will decrease with normal force from a maximum of $\omega_{no-load} = \frac{v_{h,max}}{r}$. (b) Stall torque will increase with F_N , asymptotically reaching a maximum at $x_o = \frac{\lambda}{2}$.

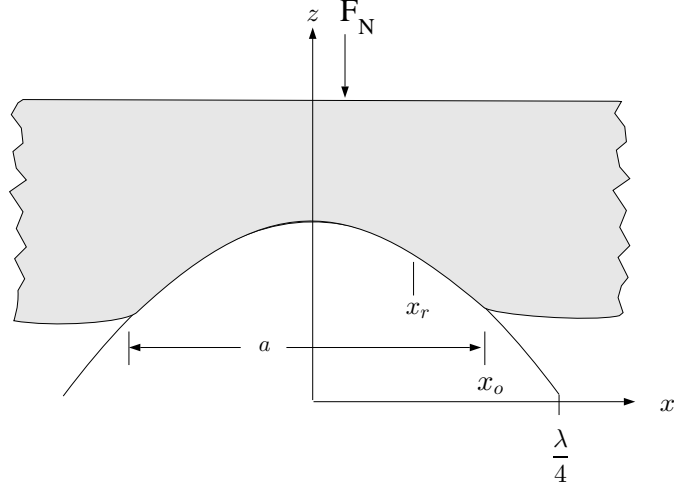


Figure 6-22: The coordinate system for the model of a cylinder contacting an elastic half space is centered on a peak at the original top surface of the undeformed stator and the area of contact is taken as a . The edge of the contact region then, is $x_o = \frac{a}{2}$. In the region $0 < x < x_r$, the horizontal velocity components of the stator surface points are larger than the rotor velocity. In the region $x_r < x < x_o$, the stator horizontal velocity components are moving slower than the rotor. At x_r , the rotor and stator move at the same speed.

6.3.2 Hertzian Contact Model

Arguing physically, we have found bounds for motor torques and identified contact mechanisms for describing how the speed-torque curves shift with normal force. However, the exact form of the speed-torque drop-off, marked by the dotted lines in the previous figures, needs to be determined by examining the pressure distribution and contact area at the interface.

In this section, we investigate the effects of using a Hertzian model of contact [Hertz 1882] to predict the speed-torque characteristics. Figure 6-22 illustrates the coordinate system used here along with the definition of a , the width of the area of the contact region used in Hertzian theory.

We note that the friction force is related to the rotor speed by:

$$F_T = -\mu_d \int_{-x_o}^{x_o} \frac{\Delta v(x)}{|\Delta v(x)|} p(x) dx$$

which is, equivalently:

$$F_T = -2\mu_d \int_0^{x_o} \text{sgn} [\Delta v(x)] p(x) dx$$

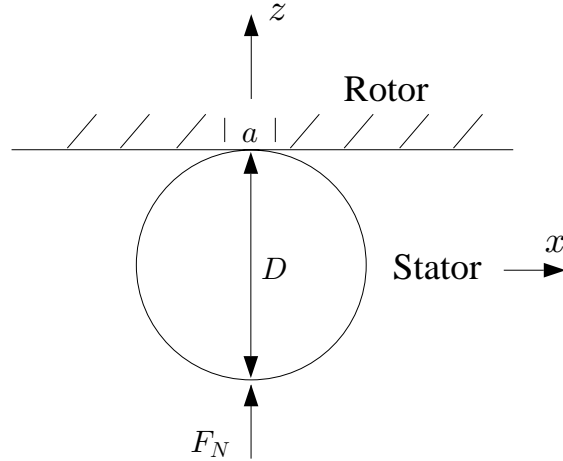


Figure 6-23: One model for a contact pressure distribution is a cylinder contacting an elastic half-space. Here, the stator is modeled as a cylinder with an equivalent radius of curvature and the rotor is modeled as an elastic half-space contacting the cylinder over an area of width a .

where the $sgn [\Delta v(x)]$ function is defined as:

$$sgn [\Delta v(x)] = \begin{cases} 1 & v_{stator}(x) > v_{rotor} \\ 0 & v_{stator}(x) = v_{rotor} \\ -1 & v_{stator}(x) < v_{rotor} \end{cases}$$

and:

$$v_{stator}(x) = v_{h,max} \cos(kx - \omega t)$$

where for this coordinate system, the figures are again drawn for $\omega t = 0$.

Finding the area of contact as parameterized by x_o will lead us to the limits of integration, and our model of the pressure distribution will lead us to $p(x)$. This friction law will then give us a set of operating points along the speed-torque curve for rotor speeds of $v_{h,min} < v_{rotor} < v_{h,max}$. That is, in this section we will be calculating the speed-torque curves valid for the regions drawn by dotted lines in Figure 6-16 and Figure 6-20.

While there are innumerable models of contact mechanics, and [Johnson 85] gives comprehensive coverage in this area, one simple model of contact applicable to the problem here, is that of Hertzian contact of a cylinder contacting an elastic half-space as shown in Figure 6-23, where we model the deformed stator as a cylinder of equivalent radius of curvature. The rotor is modeled as an elastic half-space contacting the cylinder over an area of width, a , when a force per unit length, F_N , is applied. [Young 89] gives the width

of the area of contact, a , for this model as:

$$a = 1.60\sqrt{F_N DC_E}$$

where F_N is the applied normal force per unit length, D is the diameter of the cylinder and C_E takes into account materials parameters:

$$C_E = \frac{1 - \nu_1^2}{E_1} + \frac{1 - \nu_2^2}{E_2}$$

Here, E_1 and E_2 are the moduli of elasticity for the two materials at the interface, and ν_1 and ν_2 are their corresponding Poisson's ratios.

This cylinder model will be adequate so long as the undulating stator can be modeled by the curvature of a cylinder over the region where the stator contacts the rotor. That is, for values of F_N where the rotor interpenetrates only as far as the top half of the stator's sinusoidally-shaped surface, a cylinder on an elastic half-space model should suffice. Certainly for F_N such that the interpenetration depth is larger than w_o , where the stator curvature has an inflection point, we would not expect this model, where a is assumed to grow as the $\sqrt{F_N}$, to apply.

The constants D and C_E are determined by w_o , the stator deflection (which in turn is a function of the applied drive voltage), and the material properties of the frictional interface. For example, for the case of an aluminum rotor contacting a steel stator, if we take the modulus of elasticity for aluminum as $E_{al} = 70$ GPa, the modulus of rigidity of aluminum as $G_{al} = 26$ GPa, the modulus of elasticity for steel as $E_{stl} = 200$ GPa and the modulus of rigidity of steel as $G_{stl} = 77$ GPa, Poisson's ratio can be determined from:

$$G = \frac{E}{2(1 + \nu)}$$

resulting in $\nu_{al} = 0.35$, $\nu_{stl} = 0.38$ and $C_E = 1.68 \times 10^{-11} \frac{m^2}{N}$.

The diameter of the equivalent cylinder, D , is twice the radius of curvature of the deformed stator, $2\rho_\kappa$, which is related to the stator deflection by:

$$\frac{1}{\rho_\kappa} = \frac{\partial^2 \xi(x, t)}{\partial x^2} = k^2 w_o = \left(\frac{2\pi}{\lambda}\right)^2 w_o$$

For our prototype motor of Figure 3-5, $\lambda = 5.1$ mm and $w_o = 0.1$ μm , giving $D = 13.2$ m. The contact area for a unit force per length of $F_N = 1 \frac{N}{m}$ works out to be $a = 24$ μm . That is, the percentage of contact area of a half-wavelength of the motor is approximately 1% for unit normal force per length. In terms of the limits of integration of our friction law, this contact area width, a , is related to x_o by:

$$x_o = \frac{a}{2}$$

After calculating the width of the contact area, the pressure distribution remains to be found. The pressure distribution at the interface can also be modeled to various levels of sophistication [Johnson 85]. Here we assume $p(x)$ is proportional to the transverse displacement of the stator, $\xi(x, t) = w_o \cos(kx - \omega t)$, where, again, the figure of the stator has now been drawn for $\omega t = 0$. Consequently we take:

$$p(x) = A [\cos(kx) + C]$$

where A is a function of F_N (and therefore x_o) with units of $\frac{N}{m^2}$ which satisfies:

$$F_N = \int_{-x_o}^{x_o} p(x) dx$$

Here, C is a constant which accounts for the boundary condition that $p(x)$ must equal zero at $x = -x_o$ and $x = x_o$. We find C to be:

$$C = -\cos(kx_o)$$

As the pressure distribution is symmetric about $x = 0$, the expression for the normal force simplifies to:

$$F_N = 2A \int_0^{x_o} [\cos(kx) - \cos(kx_o)] dx$$

yielding an amplitude of the pressure distribution of:

$$A = \frac{F_N k}{2 [\sin(kx_o) - kx_o \cos(kx_o)]}$$

Now that we have determined $p(x)$, we can substitute it into the equation for the friction force, F_T . The limit of integration, x_o , is calculated from the width of the contact region, a , and is a function of F_N :

$$x_o = \frac{a}{2} = 0.80\sqrt{F_N DC_E}$$

The velocity of the stator is:

$$v_{stator}(x) = v_{h,max}\cos(kx)$$

giving the friction force acting on the stator as:

$$F_{T_{total}} = -2\mu_d A \int_0^{x_o} \text{sgn}[v_{h,max}\cos(kx) - v_{rotor}][\cos(kx) - \cos(kx_o)] dx$$

The net friction force per unit length that the rotor applies to the load is equal and opposite to the friction forces per unit length acting on the stator, as was shown in Figure 6-14:

$$F_{T_{net}} = -F_{T_{total}}$$

$F_{T_{net}}$, then, is:

$$F_{T_{net}} = 2\mu_d A \int_0^{x_o} \text{sgn}[v_{h,max}\cos(kx) - v_{rotor}][\cos(kx) - \cos(kx_o)] dx$$

Breaking the $\text{sgn}[\]$ function into two integrals, where the stator velocity is greater than the rotor velocity for $0 < x < x_r$ and less than the rotor velocity for $x_r < x < x_o$, the net force per unit length that the rotor applies to the load becomes:

$$F_{T_{net}} = 2\mu_d A \int_0^{x_r} [\cos(kx) - \cos(kx_o)] dx - 2\mu_d A \int_{x_r}^{x_o} [\cos(kx) - \cos(kx_o)] dx$$

which, after integration, simplifies to:

$$F_{T_{net}} = \frac{\mu_d F_N}{[\sin(kx_o) - kx_o \cos(kx_o)]} [2\sin(kx_r) - 2kx_r \cos(kx_o) - \sin(kx_o) + kx_o \cos(kx_o)]$$

This can be simplified by taking $\phi(x)$ such that:

$$\phi(x) = \sin(kx) - kx \cos(kx_o)$$

leaving the expression for $F_{T_{net}}$ as:

$$F_{T_{net}} = \frac{\mu_d F_N}{\phi(x_o)} [2\phi(x_r) - \phi(x_o)]$$

The no-slip point, x_r , is the location along the x -axis at the point where $v_{h,max} \cos(kx_r) = v_{rotor}$, yielding for linear or angular coordinates:

$$x_r = \frac{1}{k} \cos^{-1} \left(\frac{v_{rotor}}{v_{h,max}} \right) = \frac{1}{k} \cos^{-1} \left(\frac{\omega_{rotor}}{\omega_{stator,max}} \right)$$

The rotor torque per unit length is the product of the net friction force per unit length and the radius of the motor. After multiplying $F_{T_{net}}$ by r , we find τ_{rotor} as a function of x_r and x_o :

$$\tau_{rotor} = \frac{\mu_d F_N r}{\phi(x_o)} [2\phi(x_r) - \phi(x_o)]$$

This is effectively the speed-torque equation for the motor, as x_r is a function of ω_{rotor} . For a given x_o , as determined by the applied F_N , x_r can be solved for iteratively. The correct root is the value of x_r which satisfies the condition that $0 < x_r < x_o$.

After solving, x_r can be converted to ω_{rotor} via:

$$\omega_{rotor} = \omega_{stator,max} \cos(kx_r)$$

Plotting τ_{rotor} vs. ω_{rotor} gives us the desired speed-torque relationship that we were looking for, as outlined earlier in Figure 6-16. We can use the values taken before, $\mu_d = 0.3$ for the coefficient of dynamic friction, $k = 1.23 \times 10^3 \text{ m}^{-1}$ for the wavenumber, $D = 13.2 \text{ m}$ for the radius of the cylinder modeling the stator, $r = 3.25 \text{ mm}$ for the radius of the motor, $\lambda = 5.1 \text{ mm}$ for the spatial wavelength of the motor, $C_E = 1.68 \times 10^{-11} \frac{\text{m}^2}{\text{N}}$ for the materials interface parameter, and plot the speed-torque curves for various values of F_N . As F_N is increased, the contact area becomes wider and x_o therefore becomes larger. Figure 6-24 illustrates speed-torque curves for F_N values yielding deformation where x_o moves down the sinusoidal stator profile by $\frac{n\lambda}{16}$ where n ranges from 1 to 4. At $x_o = \frac{9\lambda}{16}$, the rotor and

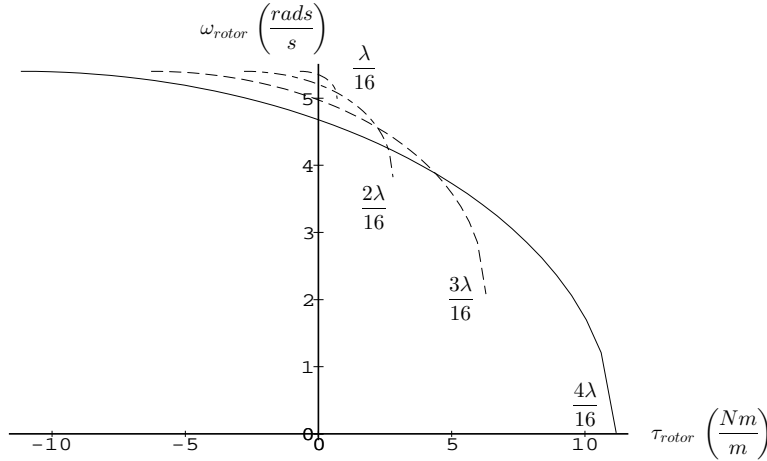


Figure 6-24: These are the speed-torque curves for Hertzian contact and Coulomb friction for different values of F_N such that the edge of the contact region, x_o , moves down the stator profile from $x_o = \frac{\lambda}{16}$ to $x_o = \frac{4\lambda}{16}$.

stator are contacting only along a line at the peak of the wave. At $x_o = \frac{4\lambda}{16}$, the rotor has deformed over the stator from $x = -\frac{\lambda}{4}$ to $x = \frac{\lambda}{4}$. That is, the rotor has deformed over the top half of the cylinder which is depicted in Figure 6-23.

These curves represent the dotted-line regions predicted in Figure 6-16 for quadrants I and II behavior. The curves here are graphed out to the point of maximum positive torque in quadrant I, where they then fall off vertically at positive stall, and out to maximum negative torque in quadrant II, where they increase vertically. Note, that as predicted in Figure 6-16, for large negative torques, the rotor speeds approach $\omega_{stator,max}$. Also, we see that for $x_o = \frac{\lambda}{4}$, the onset of maximum torque, τ_{max3} , occurs at $\omega_{rotor} = 0$ as predicted in Figure 6-16.

We can try to continue utilizing this model of a cylinder contacting an elastic half-space beyond the condition that $x_o = \frac{\lambda}{4}$. That is, if we continue with the model of a growing as $\sqrt{F_N}$ and:

$$x_r = \frac{1}{k} \cos^{-1} \left(\frac{\omega_{rotor}}{\omega_{stator,max}} \right)$$

then we will find speed-torque curves such as those illustrated in Figure 6-25. There we see that as x_o is increased to $x_o = \frac{5\lambda}{16}$ and so on up to $x_o = \frac{\lambda}{2}$ the stall torque continues to increase.

After characterizing the speed-torque curves, we would like to find $\omega_{no-load}$ vs. F_N and τ_{stall} vs. F_N . The no-load speed, $\omega_{no-load}$, can be found by setting $\tau_{rotor} = 0$ in the

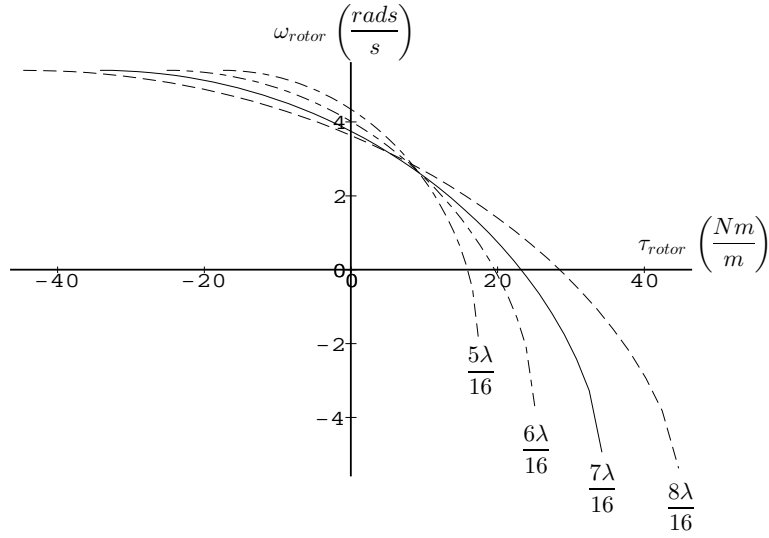


Figure 6-25: For Hertzian contact of a cylinder and an elastic half-space, as x_o is increased beyond $x_o = \frac{\lambda}{4}$, the speed-torque curves shift such that the no-load speeds decrease while the corresponding stall torques increase. Here, x_o moves down the stator profile from $x_0 = \frac{5\lambda}{16}$ to $x_0 = \frac{\lambda}{2}$.

speed-torque equation:

$$0 = \frac{\mu_d F_N r}{\phi(x_o)} [2\phi(x_r) - \phi(x_o)]$$

which reduces to:

$$\phi(x_r) = \frac{1}{2}\phi(x_o)$$

We solve for x_r and convert to $\omega_{no-load}$ with:

$$\omega_{no-load} = \omega_{stator,max} \cos(kx_r)$$

Since each value of x_0 is related to the applied normal force per unit length from:

$$F_N = \frac{1}{DC_E} \left(\frac{x_o}{0.80} \right)^2$$

the $\omega_{no-load}$ vs. F_N performance curve for the motor as outlined in Figure 6-21(a) can be found. $\omega_{no-load}$ is plotted vs. F_N in Figure 6-26(a) for the same constants used earlier and for values of x_o ranging from $\frac{\lambda}{16}$ to $\frac{\lambda}{2}$. We see that $\omega_{no-load}$ falls off with F_N as expected.

Turning to stall torque, we find that the maximum torque per unit length is developed

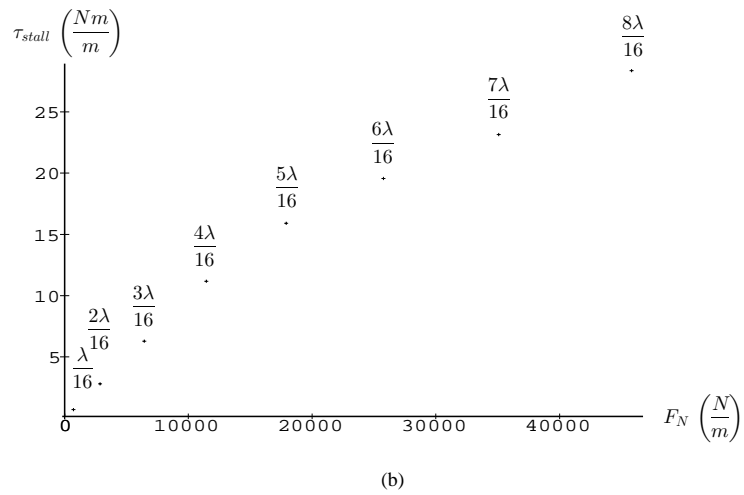
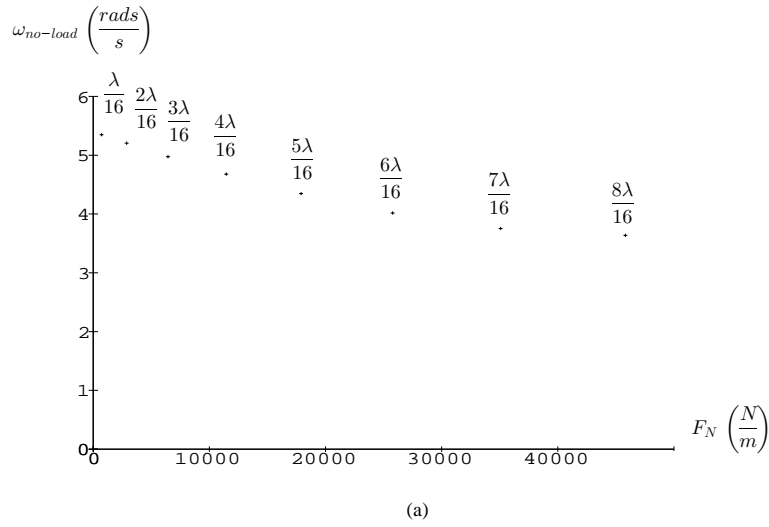


Figure 6-26: (a) $\omega_{no-load}$ is plotted versus F_N for values of F_N creating regions of contact parameterized by x_o ranging from $\frac{\lambda}{16}$ to $\frac{8\lambda}{16}$. (b) The τ_{stall} vs. F_N curve is plotted for the same values of F_N . τ_{stall} is seen to be linear with F_N in this model.

when $x_r = x_o$ in the speed-torque equation, leaving:

$$\tau_{max} = \mu_d F_N r = \tau_{stall} \quad \text{for } 0 < x_o < \frac{\lambda}{4}$$

Again, this is consistent with our physical interpretation in Figure 6-16, where τ_{stall} is directly proportional to F_N up to $x_o = \frac{\lambda}{4}$. For contact beyond $x_o = \frac{\lambda}{4}$, stall torque occurs when $x_r = \frac{\lambda}{4}$.

$$\tau_{stall} = \frac{\mu_d F_N r}{\phi(x_o)} \left[2\phi\left(\frac{\lambda}{4}\right) - \phi(x_o) \right] \quad \text{for } \frac{\lambda}{4} < x_o < \frac{\lambda}{2}$$

Simplifying, τ_{stall} reduces to:

$$\tau_{stall} = \frac{\mu_d F_N r}{\phi(x_o)} [2 - \phi(x_o)] \quad \text{for } \frac{\lambda}{4} < x_o < \frac{\lambda}{2}$$

where for Hertzian contact, F_N and x_o are related by:

$$x_o = 0.80 \sqrt{F_N D C_E}$$

This τ_{stall} vs. F_N curve is plotted in Figure 6-26(b) for normal forces all the way up to deformations of $x_o = \frac{\lambda}{2}$. We see that for $\frac{\lambda}{4} < x_o < \frac{\lambda}{2}$, τ_{stall} increases at a lower rate than for $0 < x_o < \frac{\lambda}{4}$.

Note that τ_{stall} , τ_{rotor} and F_N have been given throughout as torques and forces per unit length. For total torque or force magnitudes, these values should be multiplied by b , the stator width. For the motors of Figure 3-1, b is 3 mm.

The mechanical output power can be calculated as the product of rotor torque and rotor speed in quadrant I operation (i.e. where rotor torque and rotor speed are both positive:

$$P_{mech} = \omega_{rotor} \tau_{rotor}$$

Graphs of output power in this region of operation are shown in Figure 6-27. Peak output power is shown to occur in the graph for $x_o = \frac{\lambda}{2}$ with a value of approximately $31 \frac{W}{m}$ and a torque per unit width of $15 \frac{Nm}{m}$. For the motors of Figure 3-1 where the width, b , of the stator is 3 mm, and the number of wavelengths in the motor is 4, we find maximum total output power to be 370 mW at a total output torque of 0.18 Nm. In reality, our model undoubtedly breaks down in regimes of such large normal forces as it does not take into

account damping and compliance in the stator.

Perhaps more useful figures to keep in mind would be power and torque at a normal force corresponding to $x_o = \frac{\lambda}{8}$. There we find that maximum output power per width for one wavelength is approximately $11 \frac{W}{m}$ at a torque per unit width of $2.5 \frac{Nm}{m}$ and rotor speed of $4.4 \frac{rads}{sec}$ (i.e. 42 rpm). For a 3 mm width and 4 wavelengths, total output power is 130 mW and total output torque is 0.030 Nm (i.e. 3.0 kgf-cm or 4.2 oz.-in.). The normal force here is approximately 8.6 N (i.e. 0.87 kgf or 1.9 lbs.).

The efficiency for this Hertzian model of area contact can also be calculated. The efficiency is the ratio of mechanical power output to power input:

$$\eta_m = \frac{P_{mech}}{P_{in}} = \frac{P_{mech}}{P_{loss} + P_{mech}}$$

where P_{loss} is the frictional heating loss which arises from the product of the rotor torque and the relative velocity of the two surfaces. We formulate P_{loss} using the same integral as was taken earlier to find the rotor torque, but now multiplying the pressure distribution by the relative velocity between the rotor and stator in the integrand:

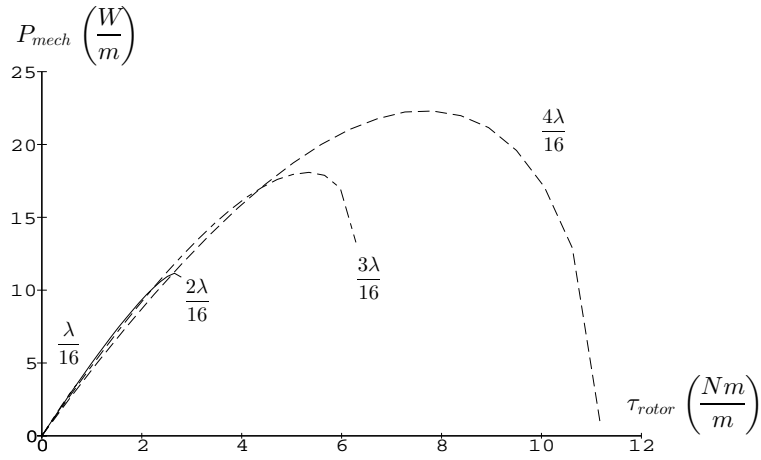
$$P_{loss} = 2\mu_d r \int_0^{x_o} sgn[\Delta\omega(x)] p(x) \Delta\omega(x) dx$$

Here, $\Delta\omega(x)$ is the relative velocity between the rotor and stator, $\omega_{stator} - \omega_{rotor}$, and $sgn[\Delta\omega(x)]$ is the direction of the relative velocity of the rotor and stator as before:

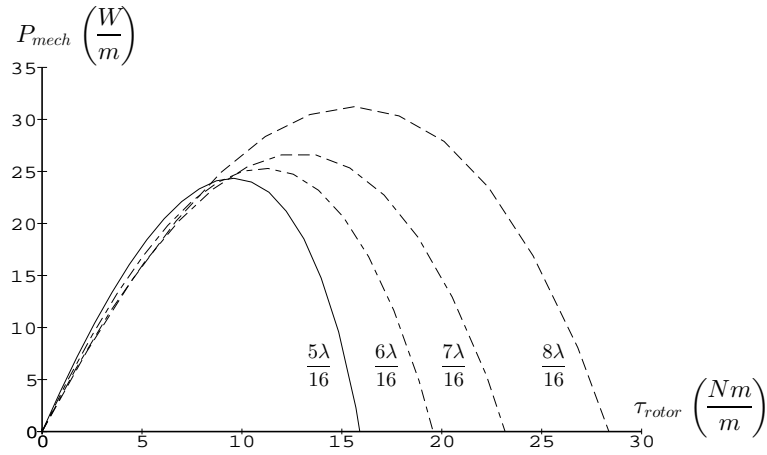
$$sgn[\Delta\omega(x)] = \begin{cases} 1 & \omega_{stator}(x) > \omega_{rotor} \\ 0 & \omega_{stator}(x) = \omega_{rotor} \\ -1 & \omega_{stator}(x) < \omega_{rotor} \end{cases}$$

Splitting the integral into two parts over the separate regions where the relative velocity changes sign, P_{loss} expands to:

$$P_{loss} = 2A\mu_d r \int_0^{x_r} [\cos(kx) - \cos(kx_o)] [\omega_{sm} \cos(kx) - \omega_r] dx \\ - 2A\mu_d r \int_{x_r}^{x_o} [\cos(kx) - \cos(kx_o)] [\omega_{sm} \cos(kx) - \omega_r] dx$$



(a)



(b)

Figure 6-27: (a) Mechanical power output per width, b , of the motor over one wavelength is shown vs. τ_{rotor} for values of x_o from $\frac{\lambda}{16}$ to $\frac{\lambda}{4}$ for quadrant I operation where τ_{rotor} and ω_{rotor} are both positive and the motor is doing work on the external system. (b) The corresponding curves for x_o from $\frac{\lambda}{4}$ to $\frac{\lambda}{2}$ show that mechanical output power reaches a maximum for a normal force which causes $x_o = \frac{\lambda}{2}$.

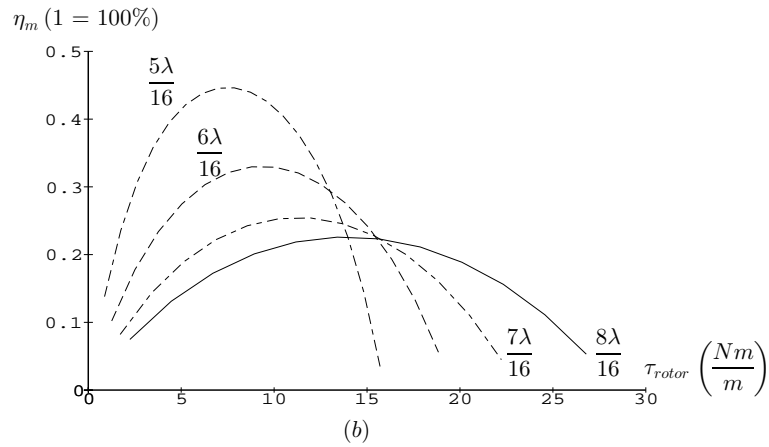
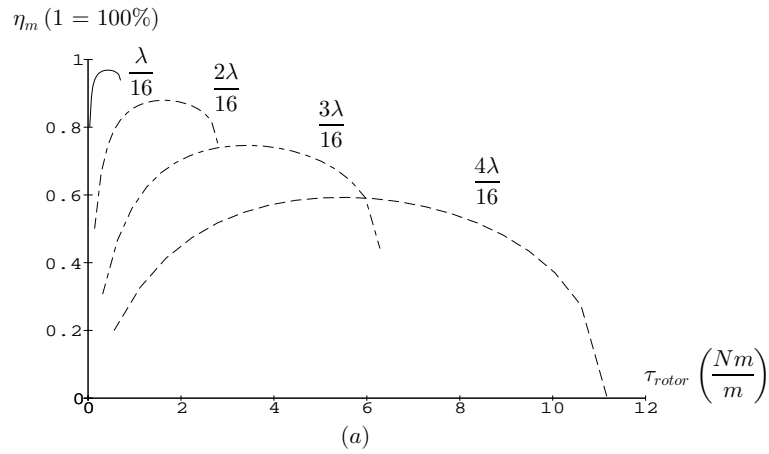


Figure 6-28: (a) Mechanical efficiencies for quadrant I behavior are shown for speed-torque curves where the normal force is such that x_o varies from $\frac{\lambda}{16}$ to $\frac{\lambda}{4}$. (b) Mechanical efficiency decreases with increasing F_N . Graphs here correspond to interpenetration of the rotor into the stator where x_o varies from $\frac{5\lambda}{16}$ to $\frac{\lambda}{2}$.

where we have used ω_{sm} for $\omega_{stator,max}$ and ω_r for ω_{rotor} . After integration and algebraic manipulation, P_{loss} can be expressed in the form:

$$P_{loss} = \frac{\mu_d F_N r}{\phi(x_o)} [2\Phi(x_r) - \Phi(x_o)]$$

where we have substituted $\Phi(x)$ for:

$$\Phi(x) = \frac{1}{2} kx\omega_{sm} + \frac{1}{4} \omega_{sm} \sin(2kx) - [\omega_{sm} \cos(kx_o) + \omega_r] \sin(kx) - kx\omega_r \cos(kx_o)$$

and $\phi(x)$ is, as before:

$$\phi(x) = \sin(kx) - kx \cos(kx_o)$$

Plugging P_{loss} and P_{mech} into our expression for mechanical efficiency:

$$\eta_m = \frac{P_{mech}}{P_{in}} = \frac{P_{mech}}{P_{loss} + P_{mech}}$$

η_m becomes:

$$\eta_m = \frac{\tau_{rotor} \omega_{rotor}}{\frac{\mu_d F_N r}{\phi(x_o)} [2\Phi(x_r) - \Phi(x_o)] + \tau_{rotor} \omega_{rotor}}$$

The mechanical efficiencies for quadrant I operation of the speed-torque curves of Figure 6-24 and Figure 6-25 are plotted in Figure 6-28. We see from Figure 6-28(a) that while maximum efficiencies decrease with increasing F_N , for very light normal forces (i.e. F_N such that $x_o = \frac{\lambda}{16}$), the maximum efficiency approaches that for the ideal case of line contact, as was illustrated in Figure 6-7(b).

6.3.3 Linear Spring Model

In the Hertzian contact model, we used an expression for the contact area that Hertz derived based on the stress distribution in two contacting cylinders, and we assumed a pressure distribution that was proportional to the displacement of the rigid stator. Taking one cylinder to have an infinite radius produced a contact between a cylinder and an elastic half-space. The relationship between F_N and x_o in the Hertzian formula effectively provided a stiffness of the system.

We can see this via a simpler model which considers the rotor to be merely a distributed linear spring. While perhaps less accurate, this viewpoint can be helpful in building in-

tuition. Figure 6-29(a) depicts this model where the rotor has a thickness of h_r and a distributed stiffness of K_r . The rotor is modeled as a series of springs placed in parallel along the rotor. That is, the displacement of the rotor at any position, x , is unaffected by the piece next to it at $x + \Delta x$. If the area of contact for a given normal force per unit length, F_N , extends from $x = -x_o$ to $x = x_o$, we take the normal force per unit length to be related to the pressure distribution by:

$$F_N = \int_{-x_o}^{x_o} p(x) dx$$

and:

$$p(x) = K_r [w_o \cos(kx) - w_o \cos(kx_o)] \quad \text{for } 0 < x_o < \frac{\lambda}{2}$$

as $w_o \cos(kx) - w_o \cos(kx_o)$ is the displacement of each spring at any location x in the region of contact. K_r here has units of $\frac{N}{m^3}$ since F_N is taken as force per length. For a rotor of thickness h_r , K_r is simply the modulus of elasticity of the rotor divided by its thickness:

$$K_r = \frac{E_r}{h_r}$$

Carrying out the integral for the normal force, we find that F_N is related to x_o by:

$$F_N = \frac{2K_r w_o}{k} [\sin(kx_o) - kx_o \cos(kx_o)]$$

Figure 6-29(a) illustrates a contact case where a normal force, F_{N_1} , creates a region of contact where $0 < x_o < \frac{\lambda}{2}$. For some normal force, F_{N_2} , there will be a contact condition where x_o just equals $\frac{\lambda}{2}$ as in Figure 6-29(b). For the scenerio where $x_o = \frac{\lambda}{2}$ and F_N is increased further, the pressure distribution becomes dependent upon the degree of compression of the rotor. For this case, we take a coordinate system as shown in Figure 6-29(b) where the z -axis is pointing down and the origin is centered at the top surface of the rotor just as the bottom of the rotor is touching the valley of the undulating stator. As the normal force is increased from F_{N_2} to F_{N_3} as shown in Figure 6-29(c), the displacement of the spring at $x_o = \frac{\lambda}{2}$ then becomes $h_r - d$ and the resulting pressure distribution is:

$$p(x) = K_r [w_o \cos(kx) - (h_r - d)] \quad \text{for } x_o = \frac{\lambda}{2}$$

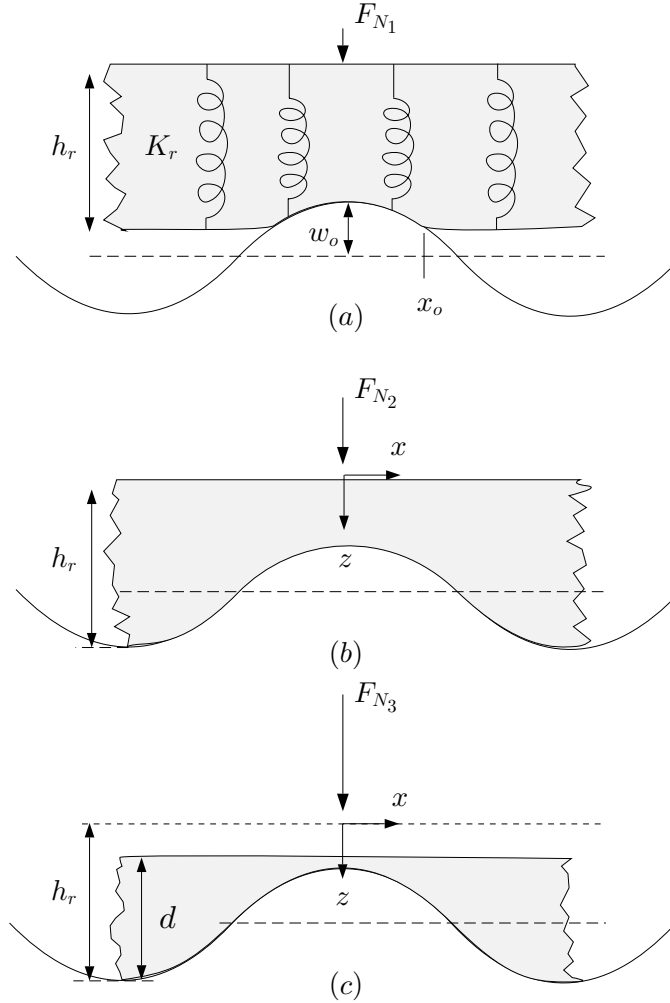


Figure 6-29: (a) This is a model of the rotor as a linear elastic spring with a distributed stiffness of K_r . (b) At complete interpenetration, for a given normal force, F_{N2} , x_o equals $\frac{\lambda}{2}$. (c) If F_N is increased beyond F_{N2} , the rotor becomes compressed at all locations x .

Going back to the case where $0 < x_o < \frac{\lambda}{2}$, we see that the pressure distribution for a linear spring:

$$p(x)_{LinSpr} = K_r [w_o \cos(kx) - w_o \cos(kx_o)] \text{ for } K_r = \frac{E_r}{h_r}$$

is similar in form to the pressure distribution for Hertzian contact:

$$p(x)_{Hertz} = A [\cos(kx) - \cos(kx_o)] \text{ for } A = \frac{F_N k}{2\phi(x_o)}$$

We can find a rotor thickness, h_r , that signifies the equivalence between these two models

by setting:

$$p(x)_{LinSpr} = p(x)_{Hertz}$$

The cosine terms drop out, leaving:

$$A = K_r w_o$$

Substituting in the expressions for A and K_r , h_r is found to be:

$$h_r = \frac{2E_r w_o \phi(x_o)}{k F_N}$$

This can be simplified further by noting that the Hertzian formulation gave a relationship between F_N and x_o of:

$$F_N = \frac{1}{DC_E} \left(\frac{x_o}{0.80} \right)^2$$

where D was related to w_o by the radius of curvature, ρ_κ :

$$D = 2\rho_\kappa \quad \text{and} \quad \frac{1}{\rho_\kappa} = k^2 w_o$$

We find the ratio of w_o to F_N to be independent of D :

$$\frac{w_o}{F_N} = \frac{2C_E (0.80)^2}{k^2 x_o^2}$$

Plugging $\frac{w_o}{F_N}$ into the expression for h_r , h_r can be seen to be a function of x_o :

$$h_r = 2.56 \frac{E_r C_E \phi(x_o)}{k^3 x_o^2}$$

Thus at a given x_o , the Hertzian formulation is equivalent to a linear spring model with a distributed stiffness of:

$$K_r = \frac{E_r}{h_r} = 0.39 \frac{k^2 x_o^2}{C_E \phi(x_o)}$$

The speed-torque equation for this linear spring model is found by solving the friction integral:

$$F_{T_{net}} = 2\mu_d K_r w_o \int_0^{x_r} [\cos(kx) - \cos(kx_o)] dx - 2\mu_d K_r w_o \int_{x_r}^{x_o} [\cos(kx) - \cos(kx_o)] dx$$

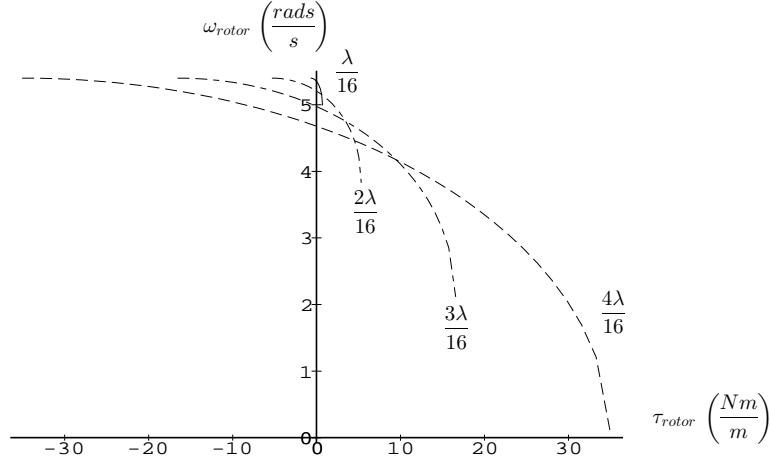


Figure 6-30: These are the speed-torque curves for a linear elastic spring model of the rotor with Coulomb friction for various values of x_o . Here, x_o moves down the stator profile from $x_o = \frac{\lambda}{16}$ to $x_o = \frac{\lambda}{4}$.

After carrying out the integral, $F_{T_{net}}$ is:

$$F_{T_{net}} = \frac{2\mu_d K_r w_o}{k} \times [2\sin(kx_r) - 2kx_r \cos(kx_o) - \sin(kx_o) + kx_o \cos(kx_o)]$$

If we again take $\phi(x)$ such that:

$$\phi(x) = \sin(kx) - kx \cos(kx_o)$$

the expression for $F_{T_{net}}$ reduces to :

$$F_{T_{net}} = \frac{2\mu_d K_r w_o}{k} [2\phi(x_r) - \phi(x_o)]$$

As the speed-torque equation is simply $\tau_{rotor} = F_{T_{net}} r$, we find:

$$\tau_{rotor} = \frac{2\mu_d K_r w_o r}{k} [2\phi(x_r) - \phi(x_o)]$$

We are still assuming that the stator is rigid, and so the velocity profile remains a cosine function and x_r is, as before:

$$x_r = \frac{1}{k} \cos^{-1} \left(\frac{\omega_{rotor}}{\omega_{stator,max}} \right)$$

The resulting speed-torque curves are plotted in Figure 6-30 and Figure 6-31. We have

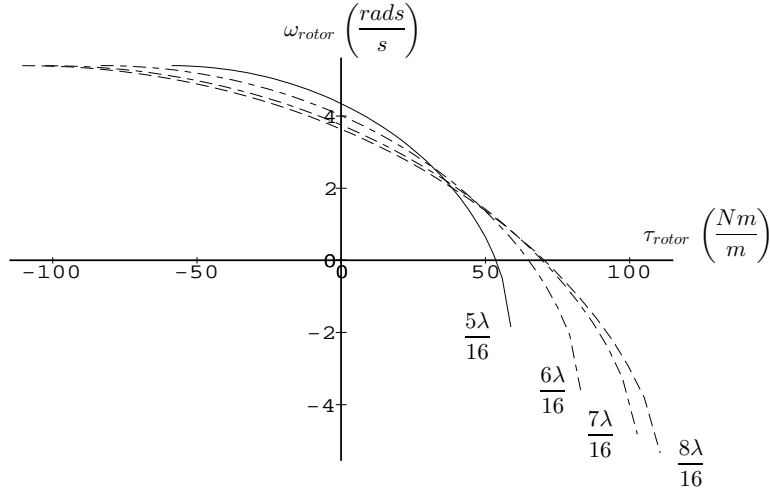


Figure 6-31: These are the speed-torque curves for larger values of F_N such that x_o moves down the stator profile from $x_o = \frac{5\lambda}{16}$ to $x_o = \frac{\lambda}{2}$.

used the same values for the constants, μ_d , w_o and r , as in the speed-torque plots for the Hertzian model of Figure 6-24 and Figure 6-25. For $K_r = \frac{E_r}{h_r}$, we have taken the rotor as aluminum, where $E_r = E_{al} = 70$ GPa as before and we have chosen h_r so as to make K_r be the equivalent stiffness of the Hertzian case for $x_o = \frac{\lambda}{16}$. That is, for the k and C_E values used earlier, h_r works out to be 0.31 mm and K_r to be $2.3 \times 10^{14} \frac{N}{m^3}$.

In comparing the speed-torque curves of the linear spring model to the speed-torque curves of the Hertzian model, we see that while we have set the curves to be the same for $x_o = \frac{\lambda}{16}$, the linear spring model predicts the same no-load speeds for the family of curves, but predicts larger stall torques for a given interpenetration, x_o .

The equivalence of the no-load speed as a function of x_o between the two models can be seen analytically. The no-load speed is calculated by setting $\tau_{rotor} = 0$, giving the same relationship for the Hertzian case:

$$\phi(x_r) = \frac{1}{2}\phi(x_o)$$

However, the relationship of x_o to F_N is different here than in the Hertzian case and we see from comparing Figure 6-32(a) and Figure 6-26(a) where $\omega_{no-load}$ is plotted vs. F_N for each model, that larger normal forces are required here for each subsequent value of x_o after $x_o = \frac{\lambda}{16}$.

The stall torque is also similar to the Hertzian case. For a normal force where $0 < x_o <$

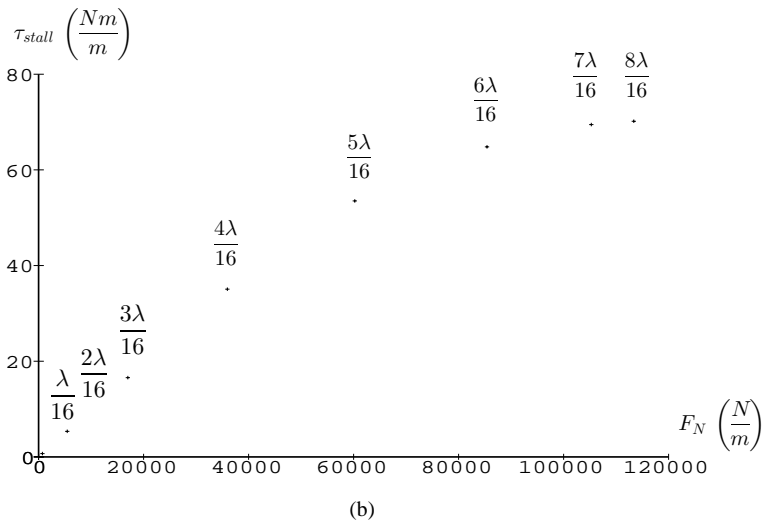
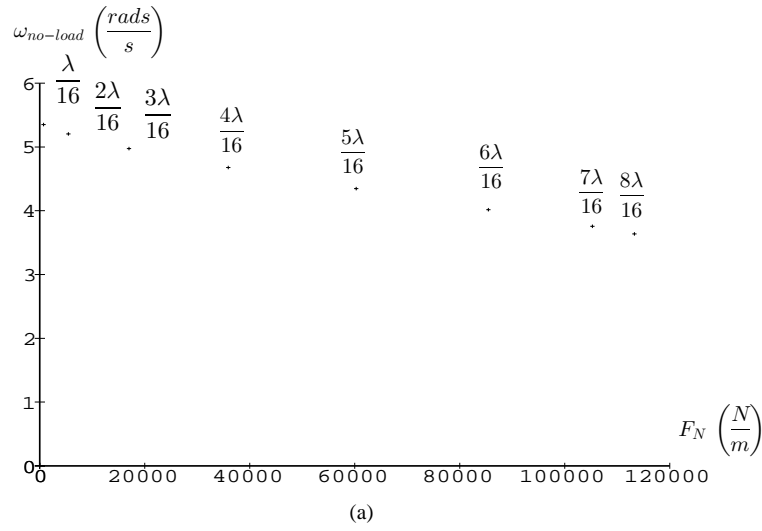
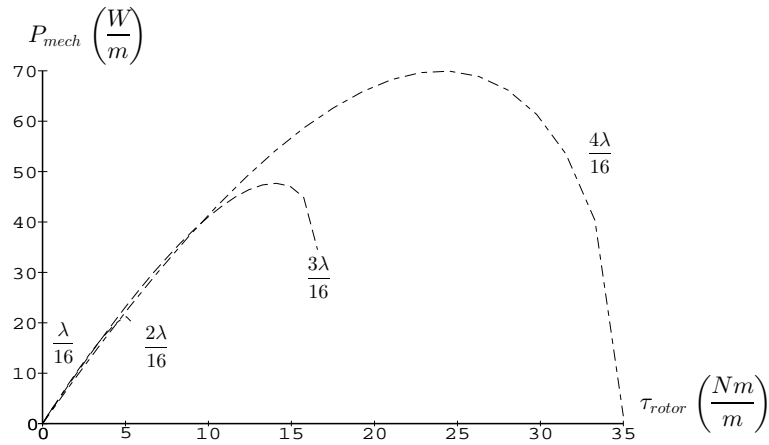
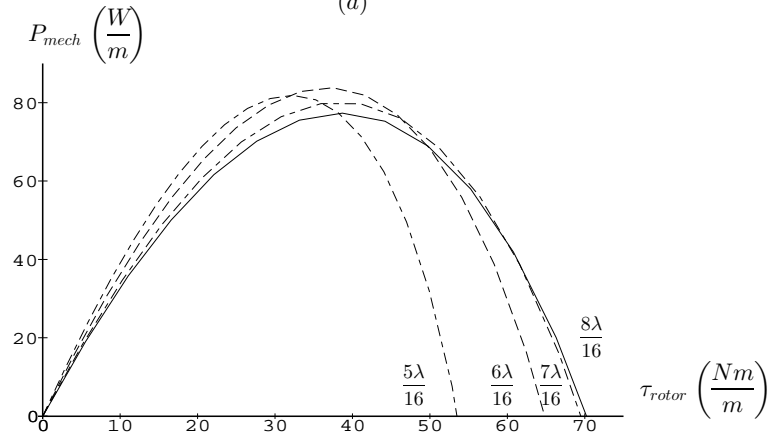


Figure 6-32: (a) $\omega_{no-load}$ is plotted versus F_N for values of F_N creating regions of contact parameterized by x_o ranging from $\frac{\lambda}{16}$ to $\frac{8\lambda}{16}$. (b) The τ_{stall} vs. F_N curve is plotted for the same values of x_o .



(a)



(b)

Figure 6-33: (a) These curves represent the mechanical output power of the motor as a function of torque for normal forces such that x_o varies from $x_o = \frac{\lambda}{16}$ to $x_o = \frac{\lambda}{4}$. (b) Here, output power is graphed for interpenetration of x_o from $x_o = \frac{5\lambda}{16}$ to $x_o = \frac{\lambda}{2}$.

$\frac{\lambda}{4}$, we again have that τ_{stall} occurs when $x_r = x_o$.

$$\tau_{stall} = \frac{2\mu_d K_r w_o r}{k} \phi(x_o) \quad 0 < x_o < \frac{\lambda}{4}$$

In this linear spring model where x_o and F_N are related by:

$$F_N = \frac{2K_r w_o}{k} \phi(x_o)$$

the stall torque reduces to:

$$\tau_{stall} = \mu_d F_N r \quad 0 < x_o < \frac{\lambda}{4}$$

where τ_{stall} is again linearly related to F_N .

We have a similar relationship for τ_{stall} in the regime of $\frac{\lambda}{4} < x_o < \frac{\lambda}{2}$ where τ_{stall} occurs when $x_r = x_o$:

$$\tau_{stall} = \frac{2\mu_d K_r w_o r}{k} [2 - \phi(x_o)] \quad \frac{\lambda}{4} < x_o < \frac{\lambda}{2}$$

Substituting the relationship between x_o and F_N gives the same expression for stall torque as in the Hertzian case:

$$\tau_{stall} = \frac{\mu_d F_N r}{\phi(x_o)} [2 - \phi(x_o)]$$

Comparing Figure 6-32(b) with Figure 6-26(b), we see that the main difference between the two models is the stiffness of each system, where for the linear spring model, which is stiffer, it takes more normal force to achieve the same x_o .

Mechanical output power for this linear spring model is again taken as:

$$P_{mech} = \tau_{rotor} \omega_{rotor}$$

Figure 6-33 graphs this function vs. τ_{rotor} for every operating point along each speed-torque curve. Comparing to Figure 6-27, we see that for a given x_o , power output is uniformly larger than for Hertzian contact as the ability to apply larger normal forces for a given x_o leads to larger torque outputs and hence larger power outputs.

The expressions for P_{loss} and η_m are also the same as for the Hertzian case and graphs of efficiency for the linear spring model are shown in Figure 6-34.

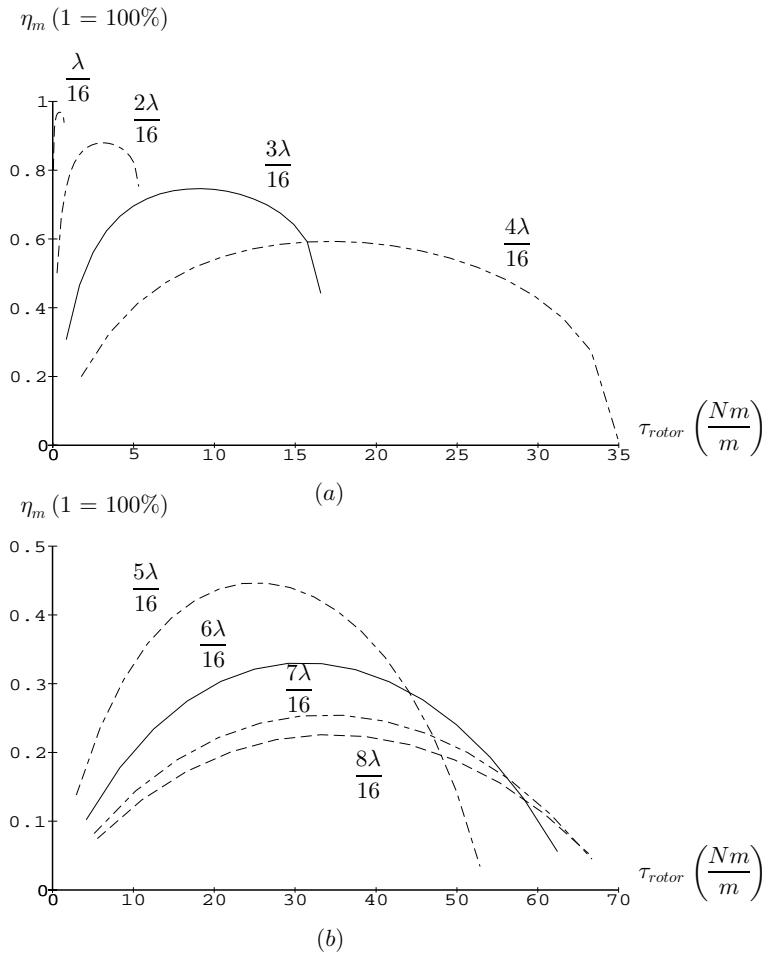


Figure 6-34: (a) Efficiency vs. torque curves for x_o ranging from $\frac{\lambda}{16}$ to $\frac{\lambda}{4}$ are similar in shape to those of Hertzian contact, except that the corresponding stall torques are larger. (b) Efficiency vs. torque curves here range from $x_o = \frac{5\lambda}{16}$ to $\frac{\lambda}{2}$.

6.4 Extensions

The models described to this point are useful in building intuition about which assumptions and constraints impose which kinds of performance behavior. The closed-form solutions developed to this point do not take into account squashing of the stator deformation. The normal force pushing the rotor against the stator will act against the piezoelectric actuation of the stator and create a reduced amplitude of deformation. Approximate solution techniques, such as Rayleigh-Ritz methods, can be used to formulate a model which combines the various models of contact described in this section with stator squashing. [Hagood and McFarland 95] have recently implemented such a model using a linear spring contact mechanism. Appendix B gives background on these variational techniques and shows simulation results for the 8 mm bulk motors discussed here.

Chapter 7

Experiments with 8 mm Bulk Motors

7.1 Initial Tests With Early Prototypes

Measuring speeds and torques of microfabricated ultrasonic micromotors such as the one shown in Figure 2-7, is rather difficult as the torques are quite small, bearings are not incorporated into the fragile membrane structures and the fabrication iterations require significant turn-around time.

Consequently, we have fabricated a number of ultrasonic motors from bulk PZT and steel parts cut in a machine shop at a scale which is easier to handle than the micromotors of Figure 2-7 yet still smaller than any commercially available electromagnetic motors. One



Figure 7-1: This is the stator of an 8 mm bulk PZT ultrasonic motor. A rotor would be pressed against the stator. The stator structure shown here has an inner diameter of 5 mm with a ring of piezoceramics bonded to the bottom in a four-wavelength electrode pattern.

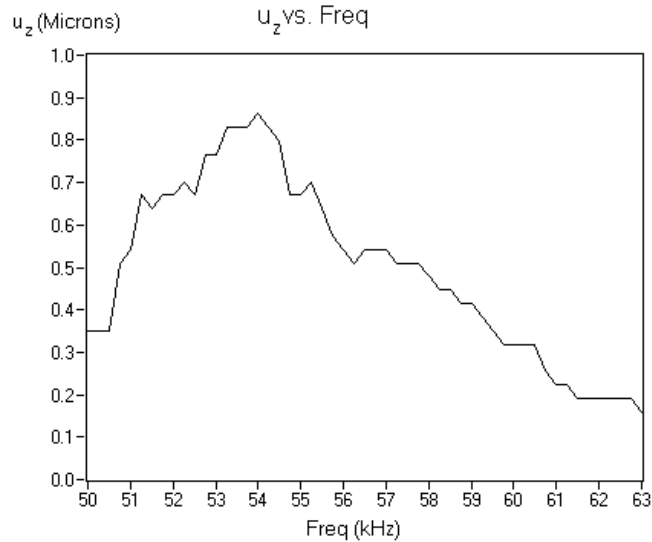


Figure 7-2: Interferometer readings of one place on the stator as the frequency is swept. The amplitude of out of plane deflections as the traveling wave moves through the stator is under $1 \mu\text{m}$ for this 8 mm motor.

of these 8 mm diameter ring-type motors is shown in Figure 7-1. The idea is to study these devices, understand the phenomena at the rotor-stator interface, discern design tradeoffs, and then fabricate a new set of motors using improved thin-film PZT developed, in parallel with these efforts, at the Pennsylvania State University's Materials Research Laboratory. Achieving large-area electrode coverage of thin-film PZT which is free of pinholes is difficult, hence the decision to keep these motors rather small. An 8 mm diameter motor was chosen as a valid tradeoff between ease of handling and testing, and the difficulty of fabricating large-area thin-film PZT devices.

With these bulk 8 mm motors, we have been able to study and measure a number of important characteristics of ultrasonic motors, such as impedance profiles, out-of-plane deflections and speed-torque curves for varying normal forces.

In order to determine which mode shapes correspond to which frequencies, we have run finite element simulations and also used an interferometer at the Penn State Materials Research Laboratory [Zhang, Pan and Cross 88] for measuring deflections. Figure 7-2 illustrates the results of interferometer measurements at one position on the stator as the frequency was swept from 50 kHz through 63 kHz. A resonance occurs near 53 kHz and the maximum deflection is under $1 \mu\text{m}$. This graph shows clearly that on either side of resonance, the displacement falls off. Furthermore, this data emphasizes the need for smooth

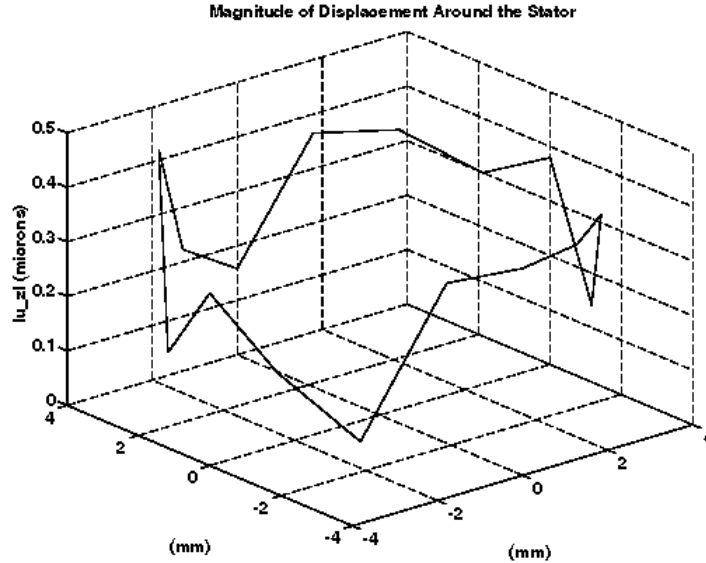


Figure 7-3: Interferometer readings around the stator at one frequency show non-uniform amplitudes of displacements. For traveling wave excitation, all points should see the same amplitude of deflection.

interface surfaces. We have found that glass lenses spin much better than brass rotors turned on a lathe, even after polishing. Subsequent Dektak measurements of surface roughness gave 300 \AA average surface roughness for the glass rotor, as opposed to 7000 \AA average surface roughness for the brass rotor. For out-of-plane displacements of just under $1 \mu\text{m}$, the 7000 \AA asperities of the brass rotor nearly touch the valleys of the traveling wave.

Interferometric measurements were also performed at one frequency but at equally spaced points around the perimeter of the stator. Figure 7-3 graphs the resulting measurements of the amplitude of out-of-plane deflections. For an ultrasonic motor working on a traveling wave principle, all points along the stator should see equal amplitudes of displacement. Here, we see non-uniform displacements, a clear area for improvement. This anomaly could be due to the electrode pattern, which is non-uniform, or to an imperfect bond.

For measuring speeds and torques under varying normal forces, we contracted to Cetehor, the French watch industry's center for research and development in horology, to build a dynamometer to fit these 8 mm motors. Shown in Figure 7-4, the dynamometer is capable of measuring torque from 0 to $60 \times 10^{-4} \text{ Nm}$, and normal forces from 0 to 20 N . An optical encoder delivers 6 pulses per motor turn.

When running the motor in the dynamometer with a glass rotor, as the side loads are



Figure 7-4: This dynamometer, built by Cetehor, measures speeds and torques along a range of operating points and for varying normal forces. The steel stator, with wires attached, sits just below a glass rotor. Above the rotor, is an optical encoder with a wrapped string acting as a friction brake. The string wraps around a leaf spring at the left and attaches behind to an LVDT displacement transducer. The load on the motor is changed by the knob on the left, which pushes on the leaf spring. The normal force is adjusted by the knob at the top of the picture which acts on a spring pushing the rotor against the stator.

increased and the motor delivers more torque, the glass rotor tends to wear and get eaten by the steel stator. It is important then, not only to have very smooth surfaces, but also hard, wear-resistant surfaces. After switching to sapphire rotors, we have been able to measure speed-torque curves for five operating points as shown in Figure 7-5. The no-load speed has been found to be approximately 230 rpm and the stall torque was measured to be 3.0 gf-cm (3.0×10^{-4} Nm).

All of these experiments yielded insight to the workings of these ultrasonic motors, but this was only a preliminary pass and an exercise in putting together the appropriate instrumentation for characterizing such small motors. Unfortunately, just as the experimental setup came together, the motors all broke. They delaminated. Having been only assembled with superglue, the extensive testing on the interferometer while driven at 70 V peak caused the motors to heat up such that the initial stall torques first measured became so small as to be unmeasurable.

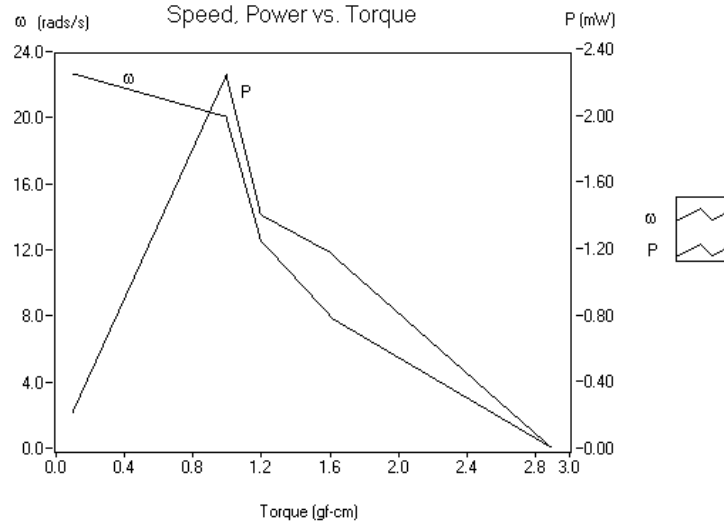


Figure 7-5: Speed and power as functions of torque are shown here for measured operating points of an 8 mm steel stator with sapphire rotor using the Cetehor dynamometer.

7.2 Second Generation 8 mm Bulk Motors

After the initial batch of motors passed away, we undertook fabrication of a second generation of motors incorporating improvements from lessons learned in the first experiments. The goal was to produce as complete a data-set as possible, both to verify proposed models and to provide useful open-literature real data to other researchers in the field.

The second generation of motors was a set whose parameters were chosen using design-of-experiments techniques. Design-of-experiments methods are another approach to creating and fitting a model: a statistical-experimental investigation. The large number of parameters involved in the design of an ultrasonic motor creates a huge design space. Size, geometry, number of teeth, tooth height, base height, type of ceramic, epoxy composition, poling field, drive voltage, drive frequency, electrode pattern, stator material, surface finish, rotor material and normal force are just a few of the parameters to be varied.

Consequently, an experiment consisting of 32 trials, or combinations of stators and rotors, was set up with stall torque and no-load speed taken as the quality parameters to be measured. All of the stators maintained the 5 mm inner diameter and 8 mm outer diameter dimensions, but the stator designs varied 4 parameters in 8 combinations. Three different rotor parameters were combined with these basic stator types. The way in which these 7 parameters were varied in the 32 trials was based on design-of-experiments methods which enable problems of 2^n configurations to be studied with approximately $2n$ experiments,

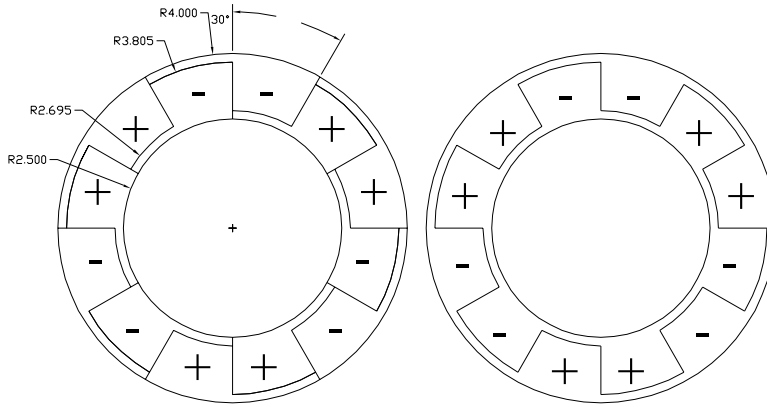


Figure 7-6: This is the second generation electrode pattern used on the set of 8 mm bulk PZT stators. The pattern at left is laser cut, then poled and reconnected to produce the pattern at right. In this manner, the entire electroded surface is utilized and the final number of wires remains three.

where n is the number of parameters.

7.2.1 Bonds and Electrodes

From the preliminary tests run on the first batch of 8 mm motors, we learned of a few problems which we addressed in all motors in the second generation motors. The most obvious realization was that a higher temperature epoxy was needed. After a number of trials, we found Masterbond EPTS-10 conductive epoxy to produce a strong laminate. The second problem addressed was the non-uniformity of out-of-plane displacements. The electrode pattern used for the first set of 8 mm motors was a simple pattern that could be etched by hand with a surgeon's scalpel, poled and reconnected with silver paint, as shown earlier in Figure 3-6. However in that design, the two phases of standing waves were set up on opposing halves of the stator and spacer segments of one wavelength were required. For a four-wavelength motor, fully 25% of the available electrode area was undriven.

In the second generation motors, we switched to a more sophisticated electrode design which leaves no undriven ceramic and which interlaces the two phases of standing waves. The new electrode pattern used is shown in Figure 7-6 and was contracted for from Piezo Systems, Cambridge, MA, and uses PTS-5A ceramic. The pattern on the left is first patterned by laser machining with line widths of 1.95 mm (7.5 mils). The same width spaces are left at the inner and outer edges. Pairs of neighboring segments are then poled and are reconnected after poling to produce the final pattern as shown on the right in Figure 7-6. The inner set of segments is then driven 90 degrees out of phase from the outer set of

segments to produce a traveling wave. Each segment is one quarter wavelength long and so this pattern of 12 segments produces a three-wavelength ultrasonic motor. First tests with this electrode pattern bonded onto a steel stator using Masterbond conductive epoxy gave promising results. Stall torque was measured to be 4.6 gf-cm, 50% higher than any previous measurement.

7.2.2 Design of Experiments

Due to the large number of parameters involved in ultrasonic motors, we used statistical design of experiments methods in our second batch of motors. Design-of-experiments methods are the planning of experiments so that appropriate data is collected which can be analyzed by statistical methods for formulating objective conclusions [Montgomery 91].

The term “experiment” relates to the entire set of 32 trials, or runs. There are 7 parameters, or factors, chosen to be varied: 4 pertaining to the stator and 3 pertaining to the rotor. The 4 stator parameters are the tooth height, the base height, the number of teeth and the stator material. For the rotor, we vary the rotor material, the rotor liner and the lubrication. Voltage and phase are kept constant throughout all the runs. Each motor is run at its third mode resonant frequency and the normal force is adjusted to extract the maximum stall torque or no-load speed.

We use what is known as factorial design, specifically a factor of two design. That is, each parameter is assigned one of two binary possibilities, denoted as ‘+’ and ‘-’. The stator and rotor parameters are assigned the values shown in Figure 7-7.

The stator tooth height is either 30 mils (0.76 mm) or 50 mils (1.3 mm). The base height of the metal below the teeth is either 10 mils (0.25 mm) or 15 mils (0.38 mm). The number of teeth in the stator is either 24 teeth or 36 teeth, and the stator material can be either aluminum or stainless steel.

The rotor parameters are the material composing the rotor (sapphire or 01 tool steel hardened to a Rockwell C scale hardness of 64), the rotor liner (no liner or kapton tape) and the lubrication (no oil or WD-40 oil)

For seven parameters, 2^7 possible combinations result. A fractional factorial design selects a subset of these possibilities and aliases some of the effects. The idea is to alias the main effects with higher-order interaction effects which can be considered negligible. Interactions that can be assumed, a priori, to have significant effects may be left in the

Parameters			
		-	+
1	Tooth Height	30 mils (0.76 mm)	50 mils (1.3 mm)
2	Base Height	10 mils (0.25 mm)	15 mils (0.38 mm)
3	#Teeth	24	36
4	Stator Material	6061 Aluminum	304 Stainless Steel
5	Rotor Liner	None	Kapton
6	Rotor Material	Hardened 01 Tool Steel	Sapphire
7	Lubricant	None	WD-40 Oil

Figure 7-7: The stator and rotor parameters in the designed experiment are one of two possibilities each.

design set unaliased and accounted for in the analysis.

If we seek to perform a smaller number of runs than the 2^7 possible, say 32, we can formulate a one-quarter fraction factorial design, denoted as a 2^{k-2} design, where in this case $k = 7$. Figure 7-8 illustrates the appropriate mapping of the 2^5 combinations. The first three factors, tooth height, base height and the number of teeth (denoted v_1 , v_2 and v_3 respectively) are assigned all possible (2^3) combinations of levels. The fourth factor, the stator material, is assigned to the combination that is equivalent to the interaction between v_2 and v_3 , which is assumed insignificant. Note that column v_{23} is the product of columns v_2 and v_3 . In this way, four parameters can be studied with 8 runs. Figure 7-8 illustrates the designed experiment.

If it is judged that some interactions will be significant, they are explicitly left in additional columns of the matrix, to be taken into account in the analysis of the measured response. For the response, we measure both stall torque and no-load speed. The average column is also included to account for common mode results in each trial.

Each row of Figure 7-8 represents a specific motor trial. Row 1 signifies a motor trial where the stator has a tooth height of 50 mils, a base height of 15 mils, 36 teeth and is made out of steel. The rotor is sapphire with a kapton liner and has a WD-40 oil lubricant. Row 2 signifies the same stator and same rotor, but no lubrication, and so on.

Note that the stator material parameter, S_{mat} or v_{23} , is aliased with the interaction between v_2 and v_3 . Thus we have assumed the interaction between the base height and the number of teeth is insignificant.

For each trial, a response was measured: maximum stall torque and maximum no-load speed, as the normal force was varied. The set of motors fabricated is shown in Figure 7-

8 mm Bulk PZT Ultrasonic Motor Experiment Design									
		Avg	v1	v2	v3	v23	v4	v5	v6
			Tooth	Base	#Teeth	Smat	Liner	Rmat	Oil
1	Violet	+	+	+	+	+	+	+	+
2		+	+	+	+	+	+	+	-
3		+	+	+	+	+	+	-	+
4		+	+	+	+	+	+	-	-
5	Fucia	+	+	+	-	-	+	+	+
6		+	+	+	-	-	+	+	-
7		+	+	+	-	-	+	-	+
8		+	+	+	-	-	+	-	-
9	Tan	+	+	-	+	-	-	+	+
10		+	+	-	+	-	-	+	-
11		+	+	-	+	-	-	-	+
12		+	+	-	+	-	-	-	-
13	Blue	+	+	-	-	+	-	+	+
14		+	+	-	-	+	-	+	-
15		+	+	-	-	+	-	-	+
16		+	+	-	-	+	-	-	-
17	Green	+	-	+	+	+	-	+	+
18		+	-	+	+	+	-	+	-
19		+	-	+	+	+	-	-	+
20		+	-	+	+	+	-	-	-
21	Yellow	+	-	+	-	-	-	+	+
22		+	-	+	-	-	-	+	-
23		+	-	+	-	-	-	-	+
24		+	-	+	-	-	-	-	-
25	Orange	+	-	-	+	-	+	+	+
26		+	-	-	+	-	+	+	-
27		+	-	-	+	-	+	-	+
28		+	-	-	+	-	+	-	-
29	Grey	+	-	-	-	+	+	+	+
30		+	-	-	-	+	+	+	-
31		+	-	-	-	+	+	-	+
32		+	-	-	-	+	+	-	-

Figure 7-8: This one-quarter fraction factorial design selects 32 trials out of a possible 2^7 . The 4-row blocks, given names as the colors violet, fucia, tan, ffbblue, green, yellow, orange and grey, signify the 8 different stators that we have manufactured.

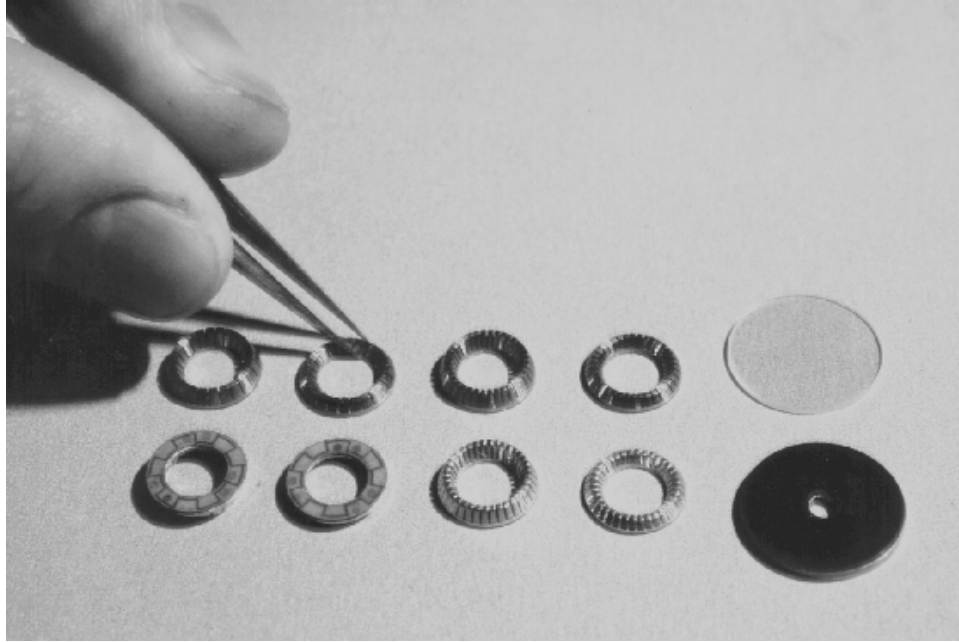


Figure 7-9: This set of eight different 8 mm diameter stators was fabricated for the designed experiment. Two different rotors, with and without liners and/or lubricants combined to make a 32-trial experiment.

9. Design-of-experiments methods provide for a way of analyzing the data and computing both quantitative and qualitative conclusions. [Fieguth, Spina and Staelin 94] describe a software tool for assisting in setting up the design matrix and in processing the results of the trials. A regression analysis is performed on the matrix of plus ones and minus ones, the vector of unknown factor effects and the vector of measured responses. Thus a number is assigned to each of the columns and is the weight in the resulting predictor polynomial for the optimum response. A qualitative result, a sequence of $+ - + - - + +$ values is also determined. This string refers to the optimum combination of variables for obtaining the minimum response, (negative signs are simply input with the measured stall torques and no-load speeds in order to find the maximum response) and this combination may not be one of the trials.

7.2.3 Fabricating Bulk PZT 8 mm Motors

In order to perform these experiments with the new electrode pattern, a more sophisticated process had to be developed for etching the electrode pads. Laser machining offered the potential of a fast, mask-free, process which is ideally suited for building prototypes and changing designs quickly. However, significant amounts of testing had to be done to find

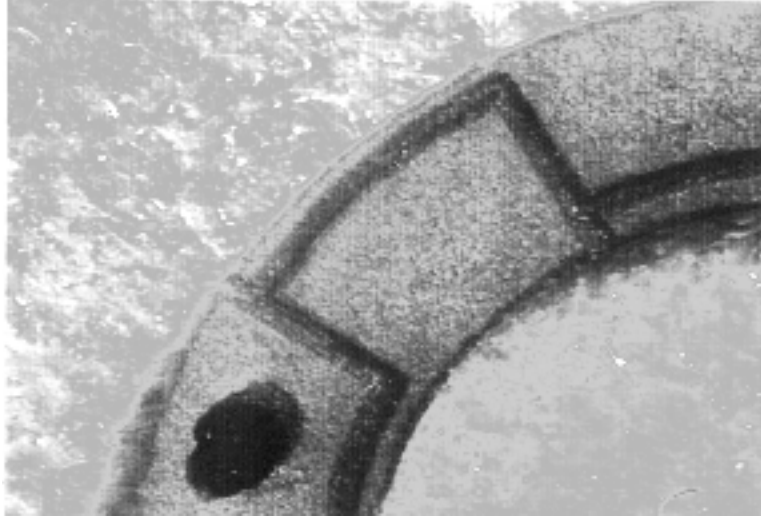


Figure 7-10: PZT-5A material has been cut and etched by Piezo Systems, Cambridge MA, with the electrode pattern required for poling. The dot signifies that pad was poled with positive voltage on that side.

the appropriate laser parameters for both cutting through the thickness of the PZT and for etching the top electrode without burning the material.

We did extensive tests with both YAG and excimer lasers through Laser Services, Westford MA, with limited success. Both laser processes tended to chip and burn the ceramic at the edges of the cuts. Nickel-coated PZT-5A from Piezo Systems, Cambridge MA, was somewhat easier to machine than silver-coated PZT-4 from Transducer Products, Goshen CT, as the silver electrode tended to melt at a lower temperature.

We contracted to Piezo Systems to provide PZT-5A cut in the 8 mm rings and etched with the electrode pattern of Figure 7-6. They used a proprietary laser-machining process and the results are shown in Figure 7-10. These parts are free from burn marks and the ceramic has been successfully poled and used in the second generation of motors.

After this pattern is poled, we reconnect segments by painting conductive epoxy over the appropriate etch. This was done by hand, and details of the procedure and other aspects of the manufacturing process are given in [Franck 95]. We also experimented with a laser direct-write system with the assistance of Dr. Daniel Ehrlich at the MIT Lincoln Laboratory Solid State Division. The laser-direct writing process was also able to perform the reconnect.

Once the electrode interconnect was complete, wires were attached to each of the inner and outer sets of pads. A third wire was soldered to the side of the stator for a ground

contact. Stainless steel stators were not troublesome in this regard, but the aluminum stators were. In order to solder to the aluminum stator, we conductive-epoxied brass shims to one small patch of the stator and then successfully made solder contacts to the shims for ground leads.

The stator teeth are polished on very fine sandpaper to make them all of uniform surface finish. We performed Dektak experiments to characterize the surface finishes of both the stators and the rotors and results are shown later.

Once the stators were completed, the rotors were placed on top of the stators and the combination was then placed into the dynamometer shown in Figure 7-4. The metal head above the optical encoder can be moved up vertically to allow for positioning the motor. Then the head is lowered and normal forces are adjusted by the normal force knob at the top of the dynamometer. The dynamometer provides the bearing for the motor. That is, the rotor and stator are two separate pieces and do not work as a motor outside of the dynamometer. We have postponed developing bearings and building up discrete component motors until the surface interactions and normal force conditions are better characterized. This technique of using the dynamometer as the bearing allows easy switching between rotor and stator combinations for the 32 trials in the experiment.

7.3 Results From Second Generation 8 mm Motors

7.3.1 Design of Experiments Results

The 32 trials in the experiment were run on the Cetehor dynamometer and the normal force and side loads were adjusted to find the maximum stall torque and no-load speeds. Each motor was run at its resonance frequency with a peak voltage of 60 V and the two phases of the drive signal were set 90 degrees apart.

The results of the experiment are tabulated in Figure 7-11. It was found that the motors did not work at all when WD-40 lubricant was applied. Consequently, every other row in the table has a zero result. This means that the matrix can be recast as a 16-trial experiment where the oil parameter column is removed as shown in Figure 7-12, where the frequency and normal forces are also noted.

Figure 7-12 shows that stator Green (0.76 mm tooth height, 0.38 mm base height, 36 teeth, made out of stainless steel), in combination with an unlined sapphire rotor and no

Design of Experiments Results: Stall Torques and No-load Speeds						
	Stator	Liner	Rmat	Oil	Max Stall Torque (gf-cm)	Max No-load Speed (rpm)
1	Violet Exp 1	+	+	+	0	0
2	Violet Exp 2	+	+	-	4.7	1660
3	Violet Exp 3	+	-	+	0	0
4	Violet Exp 4	+	-	-	4.8	1600
5	Fucia Exp 1	+	+	+	0	0
6	Fucia Exp 2	+	+	-	5.5	1750
7	Fucia Exp 3	+	-	+	0	0
8	Fucia Exp 4	+	-	-	4.5	1610
9	Tan Exp 1	-	+	+	0	0
10	Tan Exp 2	-	+	-	2.7	746
11	Tan Exp 3	-	-	+	0	0
12	Tan Exp 4	-	-	-	3.4	893
13	Blue Exp 1	-	+	+	0	0
14	Blue Exp 2	-	+	-	4.7	787
15	Blue Exp 3	-	-	+	0	0
16	Blue Exp 4	-	-	-	4.6	813
17	Green Exp 1	-	+	+	0	0
18	Green Exp 2	-	+	-	10.0	870
19	Green Exp 3	-	-	+	0	0
20	Green Exp 4	-	-	-	8.4	781
21	Yellow Exp 1	-	+	+	0	0
22	Yellow Exp 2	-	+	-	5.3	800
23	Yellow Exp 3	-	-	+	0	0
24	Yellow Exp 4	-	-	-	5.6	840
25	Orange Exp 1	+	+	+	0	0
26	Orange Exp 2	+	+	-	4.8	1060
27	Orange Exp 3	+	-	+	0	0
28	Orange Exp 4	+	-	-	4.6	1100
29	Grey Exp 1	+	+	+	0	0
30	Grey Exp 2	+	+	-	4.3	885
31	Grey Exp 3	+	-	+	0	0
32	Grey Exp 4	+	-	-	5.3	901

Figure 7-11: Resulting stall torques and no-load speeds for the designed experiment.

Design of Experiments Results: Stall Torques and No-load Speeds								
	Stator	Liner	Rmat	Frequency (kHz)	Max Stall Torque (gf-cm)	@FN (gf)	Max No-load Speed (rpm)	@FN (gf)
1	Violet Exp 2	+	+	44.5	4.7	62	1660	6.9
2	Violet Exp 4	+	-	44.5	4.8	66	1600	11
3	Fucia Exp 2	+	+	55.5	5.5	81	1750	11
4	Fucia Exp 4	+	-	55.5	4.5	97	1610	4.8
5	Tan Exp 2	-	+	38.0	2.7	38	746	4.1
6	Tan Exp 4	-	-	38.0	3.4	40	893	21
7	Blue Exp 2	-	+	35.5	4.7	76	787	35
8	Blue Exp 4	-	-	35.5	4.6	83	813	14
9	Green Exp 2	-	+	57.7	10.0	110	870	6.9
10	Green Exp 4	-	-	57.7	8.4	110	781	30
11	Yellow Exp 2	-	+	63.0	5.3	66	800	6.9
12	Yellow Exp 4	-	-	63.0	5.6	59	840	2.8
13	Orange Exp 2	+	+	47.4	4.8	97	1060	17
14	Orange Exp 4	+	-	47.4	4.6	97	1100	14
15	Grey Exp 2	+	+	42.2	4.3	94	885	17
16	Grey Exp 4	+	-	42.2	5.3	110	901	14

Figure 7-12: Resulting stall torques and no-load speeds for the designed experiment with the oil parameter removed. Stator Green, in combination with an unlined sapphire rotor and no lubricant, produced the largest stall torque: 10 gf-cm. Stator Fucia, with a kapton-coated sapphire rotor and no lubricant, produced the highest no-load speed: 1750 rpm.

lubricant, produced the largest stall torque: 10.0 gf-cm. Stator Fucia (1.3 mm tooth height, 0.38 mm base height, 24 teeth, made out of aluminum), with a kapton-coated sapphire rotor and no lubricant, produced the highest no-load speed: 1750 rpm.

The factorial design model represents a quality measure of a system as a linearly weighted sum of the parameters of the system where the parameters are valued as either +1 or -1. For instance, the quality measure for each row of the experiment shown in Figure 7-8 would be represented as:

$$\begin{aligned} \text{Quality Measure} = & W_{avg}v_{avg} + W_1v_1 + W_2v_2 + W_3v_3 \\ & + W_{23}v_{23} + W_4v_4 + W_5v_5 + W_6v_6 \end{aligned}$$

where v_n is +1 or -1, depending on the trial, and the weights, W_n , are found from a regression analysis after performing all trials (measuring stall torques, for instance).

The analysis was performed using a software tool [Fieguth, Spina and Staelin 94] developed in the MIT Leaders for Manufacturing Program which not only determines the weights, W_n , for the predictor polynomial, but also performs a search through the parameter space for the optimal combination of parameters to minimize the quality factor measured.

For the maximum stall torque quality measurement, the analysis results are as follows
(maximum stall torque data were input as negative values for maximizing the result):

Experiment Analysis Program.
Matrix Identification Code: tes114

```
Regression Matrix
Coeff      Column
-5.200000 Average Quality
 0.837500 var1 ( var2-var4 )
-0.900000 var2 ( var1-var4 var3-var23 )
-0.225000 var3 ( var2-var23 )
-0.650000 var23 ( var2-var3 )
 0.387500 var4 ( var1-var2 )
-0.050000 var5
 0.687500 (unassigned) ( var1-var3 var23-var4 )
 0.312500 (unassigned) ( var1-var23 var3-var4 )
 0.012500 (unassigned) ( var1-var5 )
-0.225000 (unassigned) ( var2-var5 )
 0.037500 (unassigned) ( var4-var5 )
-0.075000 (unassigned) ( var3-var5 )
 0.312500 (unassigned)
-0.025000 (unassigned) ( var23-var5 )
 0.062500 (unassigned)
```

```
Optimal Parameter Assignments:
var1 var2 var3 var23 var4 var5
  -   +   +   +   -   +
```

Optimized Quality: -8.250000

```
Free Parameters:      9
RMS Unconfidence:    0.284861
```

The predictor polynomial for maximum stall torque then is:

$$\tau_{stall,max} = -5.200 + 0.8375v_1 - 0.9000v_2 - 0.2250v_3 - 0.6500v_{23} + 0.3875v_4 - 0.0500v_5$$

where the v_n represent +1 or -1 values for tooth height, base height, the number of teeth, the stator material, the rotor liner and the rotor material, respectively, for each trial motor. Plugging in any other combination of parameters will yield a predicted value of stall torque based on the regression analysis of the prototypes fabricated.

The analysis also performs a search through the space of combinations and find the

combination “-+++”, which refers to stator Green, with an unlined sapphire rotor as the optimal configuration for maximizing stall torque. This combination happens to be one of the trials performed, but in general the predictor string may point to an untried combination.

The maximum no-load speeds were also analyzed and the results were found to be:

Experiment Analysis Program.
Matrix Identification Code: tes114

```
Regression Matrix
Coeff      Column
-1068.50000 Average Quality
-163.875000 var1 ( var2-var4 )
-170.375000 var2 ( var1-var4 var3-var23 )
-20.250000 var3 ( var2-var23 )
 31.375000 var23 ( var2-var3 )
-252.250000 var4 ( var1-var2 )
 -1.250000 var5
 27.875000 (unassigned) ( var1-var3 var23-var4 )
-14.000000 (unassigned) ( var1-var23 var3-var4 )
 -2.125000 (unassigned) ( var1-var5 )
-29.875000 (unassigned) ( var2-var5 )
-16.750000 (unassigned) ( var4-var5 )
 6.000000 (unassigned) ( var3-var5 )
 19.125000 (unassigned)
-12.125000 (unassigned) ( var23-var5 )
 7.000000 (unassigned)
```

```
Optimal Parameter Assignments:
var1 var2 var3 var23 var4 var5
  +   +   +   -   +   +
```

Optimized Quality: -1707.875000

```
Free Parameters:      9
RMS Unconfidence:    17.475031
```

Here, the predictor polynomial for maximizing no-load speed turns out to be:

$$N_{no-load,max} = -1069 - 163.9v_1 - 170.4v_2 - 20.25v_3 + 0.31.38v_{23} - 252.3v_4 - 1.25v_5$$

In this case, the predictor variable string is “+++--+”, which is a different combination than any of the trial motors built. This suggests that the next experiment would be to

fabricate such a stator: tall teeth, large base height, large number of teeth, made out of aluminum, with a kapton-coated sapphire rotor, and check. Additionally, replicates should be made of Fucia, as Fucia Experiment 2 actually gave a higher no-load speed, 1750 rpm, than the predictor polynomial for the indicated optimal parameter string.

7.3.2 Speed-Torque Curves

Two complete replicate sets of the eight stators have been fabricated, but the second set has not yet been tested. Of the first replicate set, all motors were measured for maximum no-load speed and maximum stall torque, as discussed in the previous section. Here we refer to stators in the first replicate set as Violet1, Fucia1, Tan1, and so on. Stators in the second replicate set will be referred to as Violet2, Fucia2, Tan2, etc.

In addition to measuring maximum no-load speeds and maximum stall torques, three trial motors of the first replicate set have been tested across a spectrum of operating points: Yellow1 Experiment 2 (unlined sapphire rotor), Grey1 with an unlined sapphire rotor and Fucia1, also with an unlined sapphire rotor. These complete speed-torque curves are shown below in this section for a constant drive voltage of 60 V peak as the normal force is varied.

7.3.3 Yellow1

Figure 7-13(a) illustrates four speed-torque curves for Yellow1 Experiment 2. The Yellow1 stator is an aluminum stator of 24 teeth, with a tooth height of 0.76 mm and a base height of 0.38 mm. The rotor in this run was an unlined sapphire rotor.

It can be seen in Figure 7-13(a), that as the normal force is increased, the no-load speeds fall off and the stall torques increase. For a normal force of 55 gf, the stall torque is 5.2 gf-cm. However, as the normal force is increased to 69 gf, as shown in Figure 7-13(b), the no-load speed continues to drop but the stall torque does not increase. It falls to 4.6 gf-cm. No-load speed versus normal force is plotted in Figure 7-14(a) and stall torque versus normal force is plotted in Figure 7-14(b). The no-load speeds falloff as predicted in Figure 6-21, but the stall torque was predicted in Figure 6-20 to reach an asymptotic value, under the assumption of a rigid stator. Here we see the effect of stator squashing come into play for large normal forces and the stall torque decrease with increasing normal force.

By multiplying speed and torque we can find the power versus torque profiles. Figure 7-15 shows that the peak mechanical output power for Yellow Experiment 2 is 12 mW.

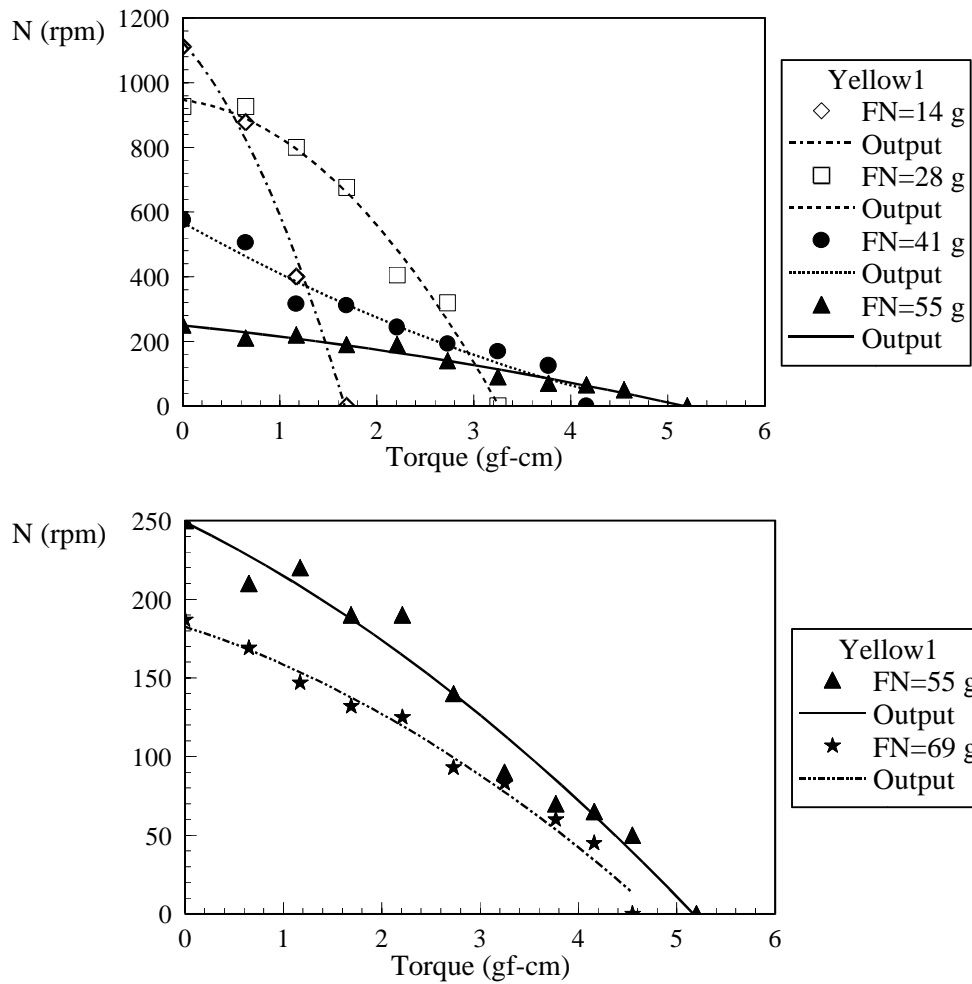


Figure 7-13: (a) The first four speed-torque curves of Yellow Experiment 2 (stator Yellow1 run with an unlined sapphire stator) are shown here with second order regression polynomial curves fit onto the scatter plot. (b) As the normal force is increased from 55 gf to 69 gf in Yellow Experiment 2, the stall torques stops increasing and begins to decrease.

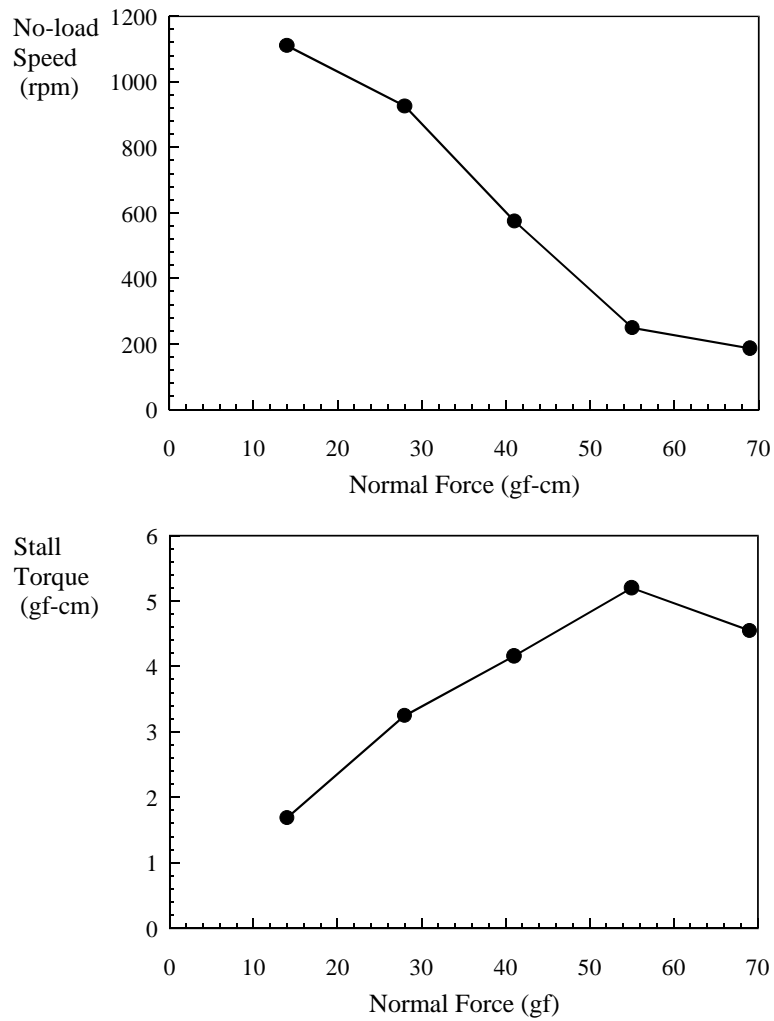


Figure 7-14: (a) The no-load speed versus normal force curve shows a dropoff as predicted. (b) Stall torques versus normal force are plotted here for Yellow Experiment 2. The decrease in stall torque for large normal forces indicates squashing of the stator.

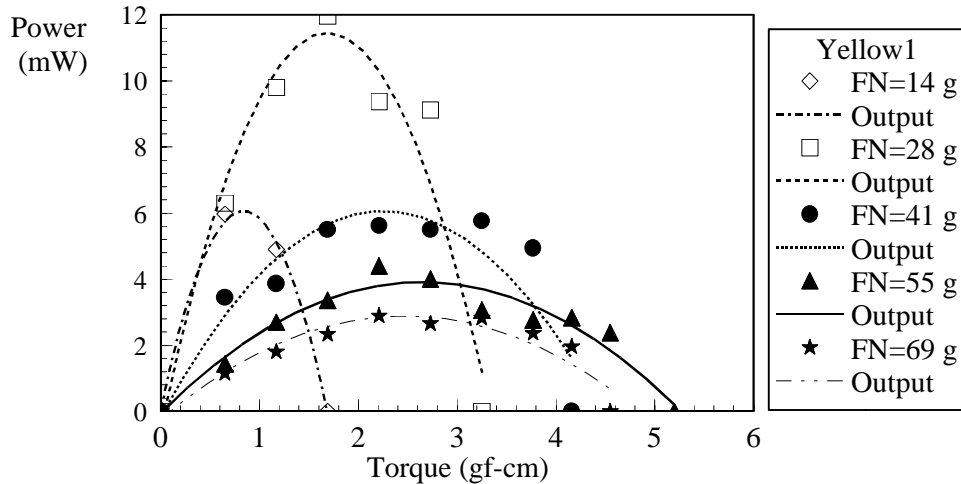


Figure 7-15: Power versus torque is plotted with curve fits. The maximum mechanical output power is 12 mW and occurs at a normal force of 28 gf.

7.3.4 Fucia1

The largest no-load speeds in the trial motors of the designed experiment were exhibited by stator Fucia1 which was made of aluminum, had 24 teeth, a tooth height of 1.3 mm and a base height of 0.38 mm. Although the designed experiment specified a kapton liner for both Fucia1 Experiment 2 and Fucia1 Experiment 4, we also experimented with unlined rotors and found that plain sapphire rotors produced very high speed motion.

Figure 7-16 illustrates speed-torque curves for data taken at various normal forces for operating points closer to no-load speed than stall, in order to measure output power quickly.

Figure 7-17 depicts the resulting power vs. torque curve for Fucia1. Second order polynomial regression curve fits are also shown. The peak power is produced at a normal force of 28 gf and was measured to be 27 mW.

To recognize the significance of this amount of output power, it is interesting to compare this ultrasonic motor to the smallest commercially available component electromagnetic DC motor. In the MIT Mobile Robot Group at the Artificial Intelligence Laboratory, we typically use Namiki DC motors for small mobile robot applications. These motors are 7 mm in diameter and 16 mm tall. They are specified [Namiki 92] to have a stall torque of 1.8 gf-cm and a no-load speed of 12,000 rpm. Taking output power as one-quarter of the product of no-load speed and stall torque gives a peak output power of 57 mW. Thus this ultrasonic motor, Fucia1 with a plain sapphire rotor, produces approximately half the output power of a Namiki motor in 1/6 the volume. Even more importantly, this power

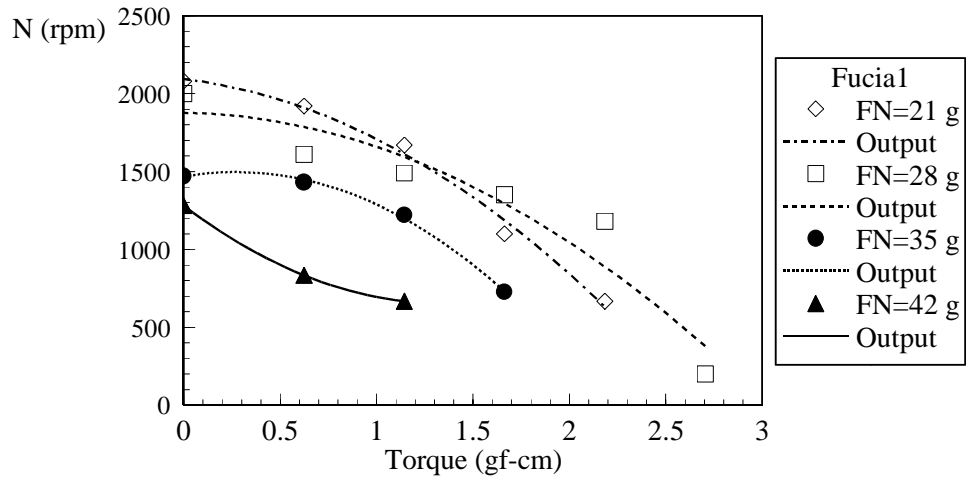


Figure 7-16: Speed vs. torque curves for Fucial1 run with an unlined sapphire rotor (not a trial in the designed experiment) show very large no-load speeds. The peak speed here is 2080 rpm.

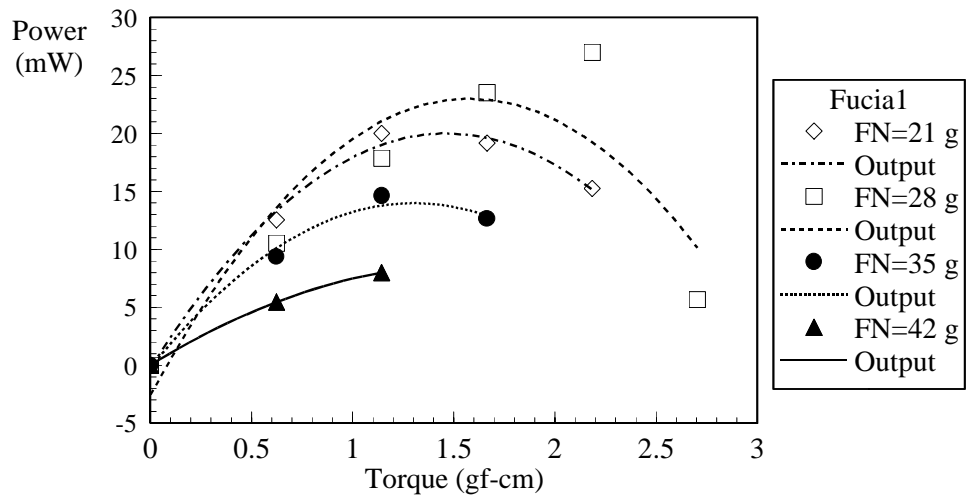


Figure 7-17: The power vs. torque curves for Fucial1 running with an unlined sapphire rotor give the largest mechanical output powers of any motors fabricated here. Peak output power was measured to be 27 mW at a normal force of 28 gf.

is delivered at a much lower speed and higher torque, a better impedance match for most real-world applications.

7.3.5 Grey1

The motor we have collected the most extensive data set on is stator Grey1 with a plain sapphire rotor. Speed-torque curves were measured at seven different normal forces ranging from $F_N=28$ gf to 97 gf. The drive voltage was again 60 V peak and the frequency was 42.2 kHz as noted earlier in Figure 7-12.

If we look back to the speed-torque curves of Figure 7-5, we can compare the number of operating points we were able to resolve on the early prototypes with the number of operating points and speed-torque curves on this second generation batch. The stall torques are approximately a factor of three larger and half a dozen speed-torque curves at different normal forces are resolvable before the stator is completely squashed down. This is likely due to larger displacements of the stator resulting from improved bonds and electrode patterns.

The first four speed torque curves are shown in Figure 7-18(a). The no-load speeds decrease with normal force as the stall torques increase, similarly to Figure 7-13(a). As the normal force is increased from 69 gf to 83 gf, the stall torque grows from 8.4 gf-cm to 8.9 gf-cm. However, as the normal force is increased further to 97 gf-cm, the stall torque falls off to 7.9 gf-cm.

The stall torques and no-load speeds are plotted versus normal force in Figure 7-19. The curves develop in much the same manner as for Yellow1 Experiment 2 shown in Figure 7-14. Again, we see no-load speed drop off with increased normal force. Stall torques also increase with normal force up until a point where stator squashing causes the stall torque to decrease.

The mechanical output power curves can then be calculated and are shown in Figure 7-20. The peak output power is 16 mW at a normal force of 69 gf. The speed-torque operating point is 368 rpm at a load torque of 4.2 gf-cm. Again, this low-speed, high-torque operating point at maximum power compares favorably with electromagnetic motors such as the Namiki DC motor which is commonly used as a vibration alarm in silent pagers. In the pager application, a geardown is not required, simply an eccentric cam to promote shaking. In fact, Namiki motors are not even available with gearboxes. Gearing them down to useful torques and speeds to drive a small robot requires building custom gearboxes.

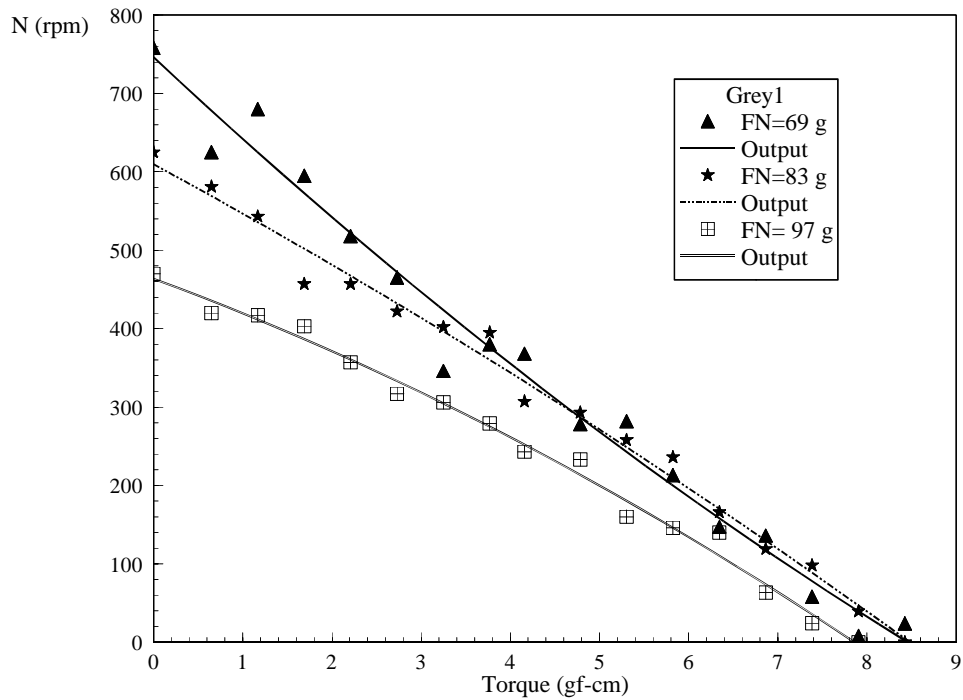
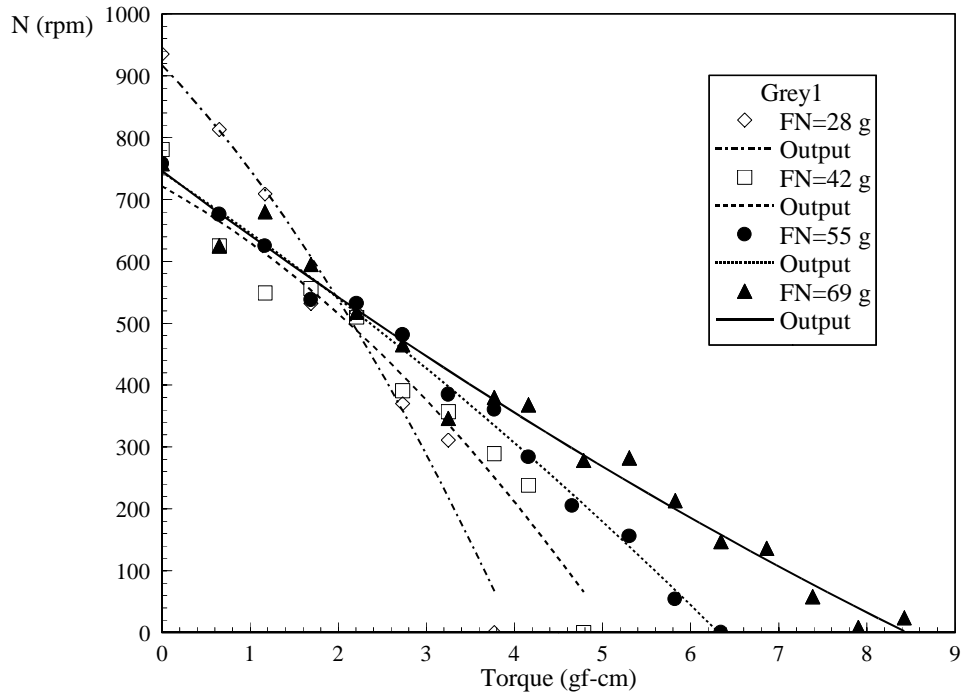


Figure 7-18: (a) The first four speed-torque curves for motor Grey1 with an unlined sapphire rotor, with regression curves. (b) Fifth, sixth and seventh speed-torque curves for motor Grey1 show maximum stall torques of 8.9 gf-cm.

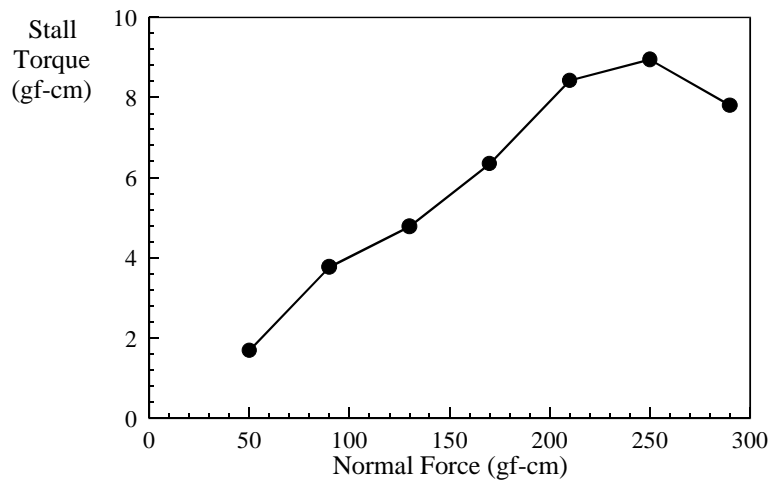
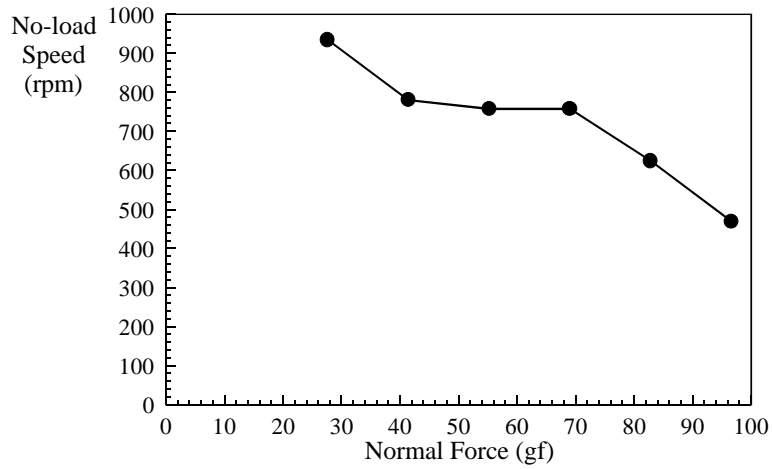


Figure 7-19: (a) No-load speed versus normal force curve for motor Grey1. (b) Stall torque versus normal force for motor Grey1.

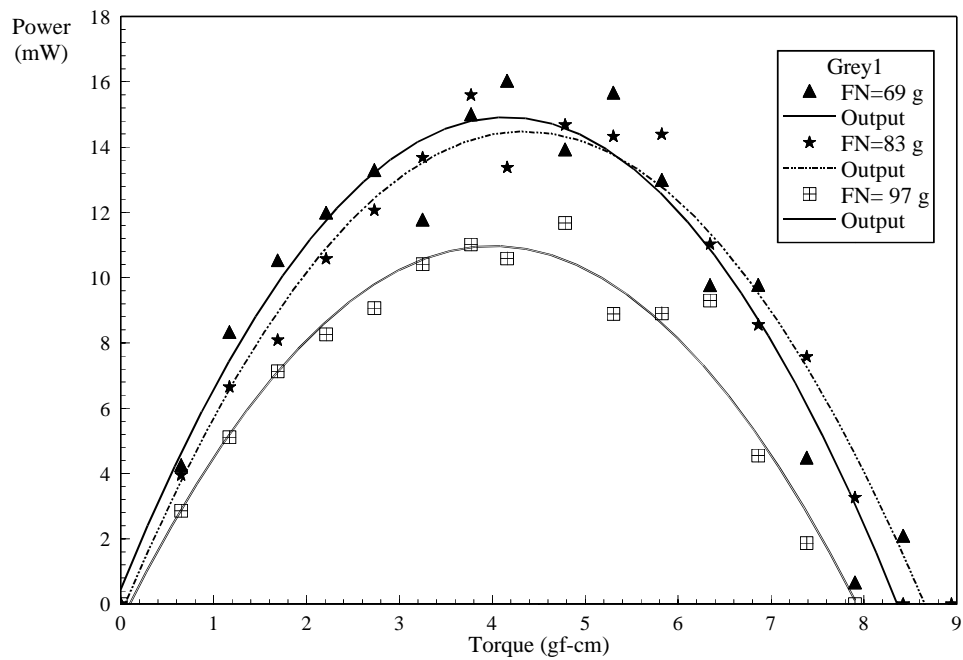
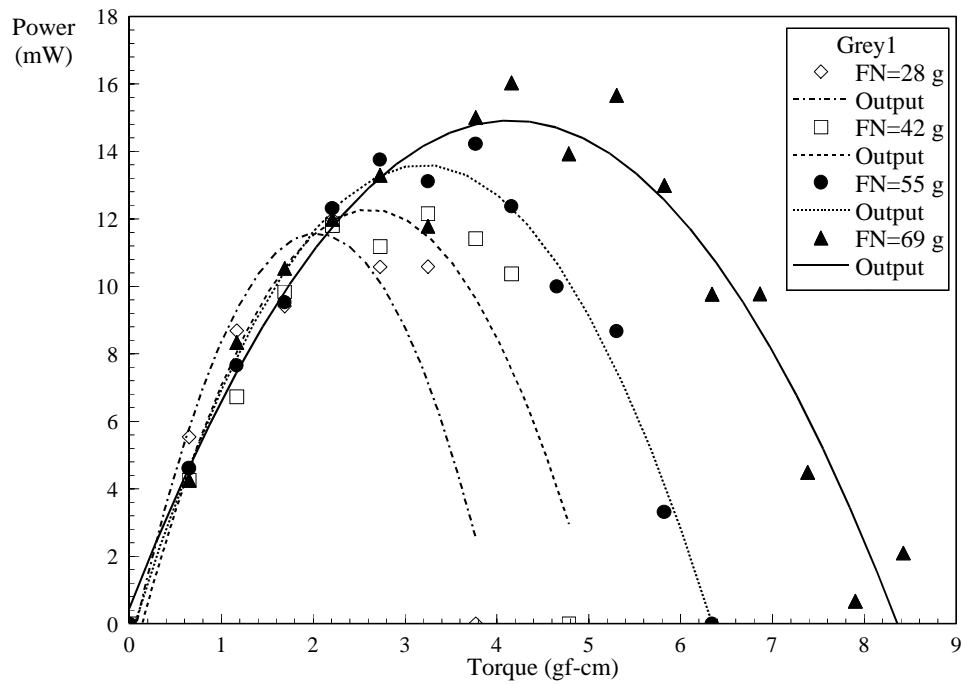


Figure 7-20: (a) The first four power versus torque curves for motor Grey1. (b) Fifth, sixth and seventh power versus torque curves for motor Grey1. Peak output power of 16 mW occurs at a load torque of 4.2 gf-cm under a normal force of 69 gf.

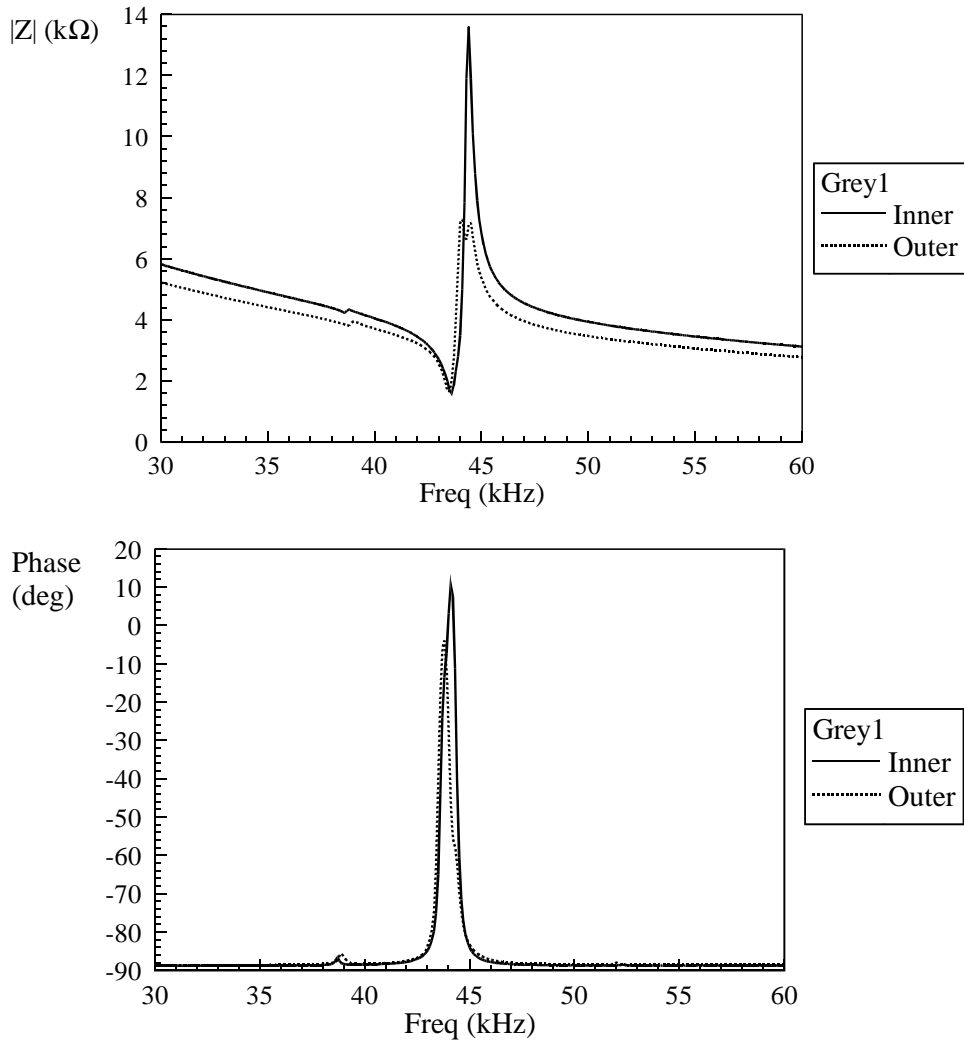


Figure 7-21: (a) The plot of the magnitude of impedance versus frequency shows a resonance at 43.6 kHz and an antiresonance at 44.4 kHz for the inner electrode. (b) The phase of the impedance shows a resonance near 44 kHz and capacitive characteristics away from resonance.

7.3.6 Magnitude and Phase of Impedance and Damping Measurements

All the speed-torque curves just displayed for stator Grey1 were measured at 42.2 kHz, the frequency which produced the largest stall torque. Due to the piezoelectric effect, the mechanical resonance can be viewed electrically, as was discussed in Figure 4-1.

A Hewlett Packard 4192A Low Frequency Impedance Analyzer, which was frequency swept via General Purpose Interface Bus control from an IBM 755C Thinkpad laptop running Labview instrumentation software, was used to measure the magnitude and phase of both the inner and outer electrodes on stator Grey1 as shown in Figure 7-21.

The magnitude of the impedance reaches a minimum at 43.6 kHz and a maximum at

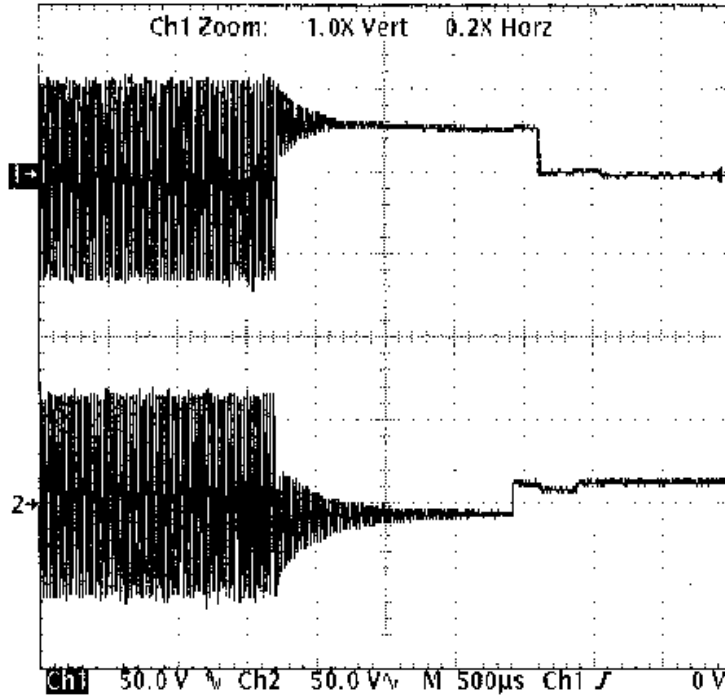


Figure 7-22: The turn-off transient of stator Grey1 from a 60 V peak drive at 42.2kHz displays an initial increase in voltage due to the piezoelectric effect, and then a damped response down to zero.

44.4kHz for the inner electrode. The outer electrode is closely matched. Initial prototypes with the first electrode pattern often did not display such uniformity, most likely due to the fact that the ceramics then were ground by hand and etched with a surgeon’s scalpel. These laser-etched ceramics, even though the two electrode areas are very slightly different, display a better matching of resonance conditions.

The damping of the unloaded stator can be measured either from the frequency response or from the time-domain transient response. Figure 7-22 illustrates the turn-off transient from an initial excitation of 60 V peak at 42.2kHz. The quality factor, Q , can be measured from the turn-off transient. Q is defined as the number of radians in the signal in the time it takes to reach $\frac{1}{e}$ of its initial value [Staelin, Morgenthaler and Kong 94].

Figure 7-22 shows that the two drive signals, sin and cos, are not perfectly matched in their damping characteristics. The channel driving the outer electrode is trace 1 at the top of the oscilloscope display. Using the zoom feature to examine the waveform, it was found that the signal decayed to $\frac{1}{e}$ in $240 \mu s$. At 42.2kHz, or $265,000 \frac{rads}{sec}$, the Q of this signal works out to be on the order of 63. The damping coefficient, ξ , defined by $Q = \frac{1}{2\xi}$ is then $\xi = 0.8\%$ For the second trace, at the bottom of the oscilloscope display, the signal

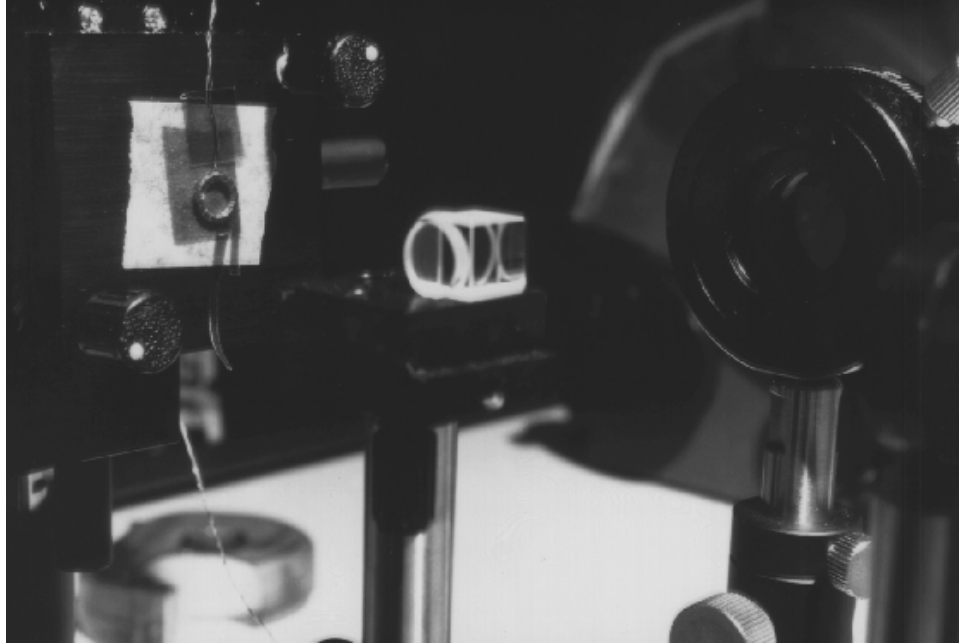


Figure 7-23: The interferometer used to measure displacements on the 8 mm diameter stators. The stator is mounted on the vertical X-Y stage at left such that the laser spot hits the surface of a stator tooth for measuring out-of-plane deflection.

decays to $\frac{1}{e}$ of its value in $460 \mu s$, yielding a Q of 122 and a damping coefficient of $\xi = 0.4\%$. The value of Q is the dynamic amplification factor by which the static deflection will be multiplied at resonance. As the two electrode patterns yield different quality factors, we can expect that each electrode pattern will contribute different amplitudes of deflection to the traveling flexure wave.

7.3.7 Interferometric Displacement Measurements

To get further insight into the mechanisms underlying torque production in ultrasonic motors, we put together a Michelson interferometer to measure out-of-plane displacements of the stators. The interferometer is illustrated in Figure 7-23. The motor can be seen at left mounted on a vertical X-Y stage. The laser is at far right, a polarized beamsplitter with two attached quarter-wave plates is shown at the center and an adjustable polarizer is shown off to center-right. The detector is off the photo beyond the adjustable polarizer. Also out of the picture is the reference-arm mirror of the interferometer which would be across from the adjustable polarizer. A microscope objective is usually placed between the beamsplitter and the stator to focus the beam onto the small surface area of a stator tooth, but is left out of the photo so that the stator can be seen. A spatial filter and collimating

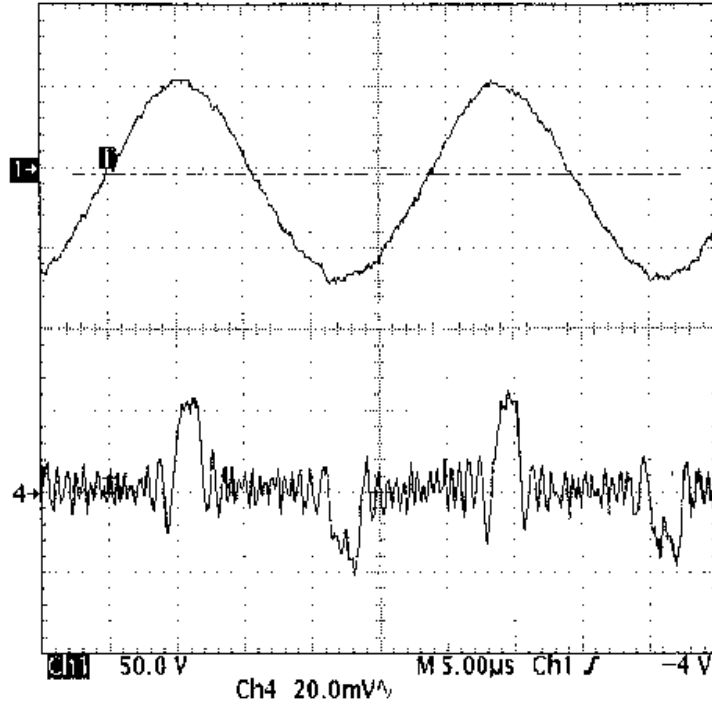


Figure 7-24: Interferometer measurements of displacement on stator Grey1 at 11 o'clock. The stator is driven at 60 V peak and at 42.2kHz. The big blips in the lower trace mark the turn-around points from when the stator deflection changes from moving away from the laser beam to moving towards it. The fringes in between two big blips then yield the peak-to-peak displacement of the motor. Notice that the motor has a peak-to-peak displacement once per drive period.

lens has also been added between the laser and beamsplitter to filter out the structure from the laser light. The entire optical setup is mounted on a vibration-isolated optical table in a basement laboratory. Our original setup on the ninth floor of the Artificial Intelligence Laboratory, with subway trains running underneath, was far too shaky of an environment to achieve interference.

The stator is mounted on the X-Y stage in a free-free manner, much as it is mounted in the dynamometer when speed-torque measurements are taken. In Figure 7-23 the motor can be seen mounted such that the surface of the stator, which would normally be contacting the rotor, is facing the laser spot. The stator is held in place merely by a piece of tape across the lead wires. A piece of kapton tape is placed below the stator on the X-Y stage to prevent electrical shorting by the stage. The only other attachment holding the stator fixed is a thin piece of kapton tape placed over one tooth of the stator at approximately six o'clock. This is also visible in Figure 7-23 as the long piece of tape hanging down off the stator. The stator is mounted in this manner so as to permit as much vibration as possible while preventing rigid body translation or rotation.

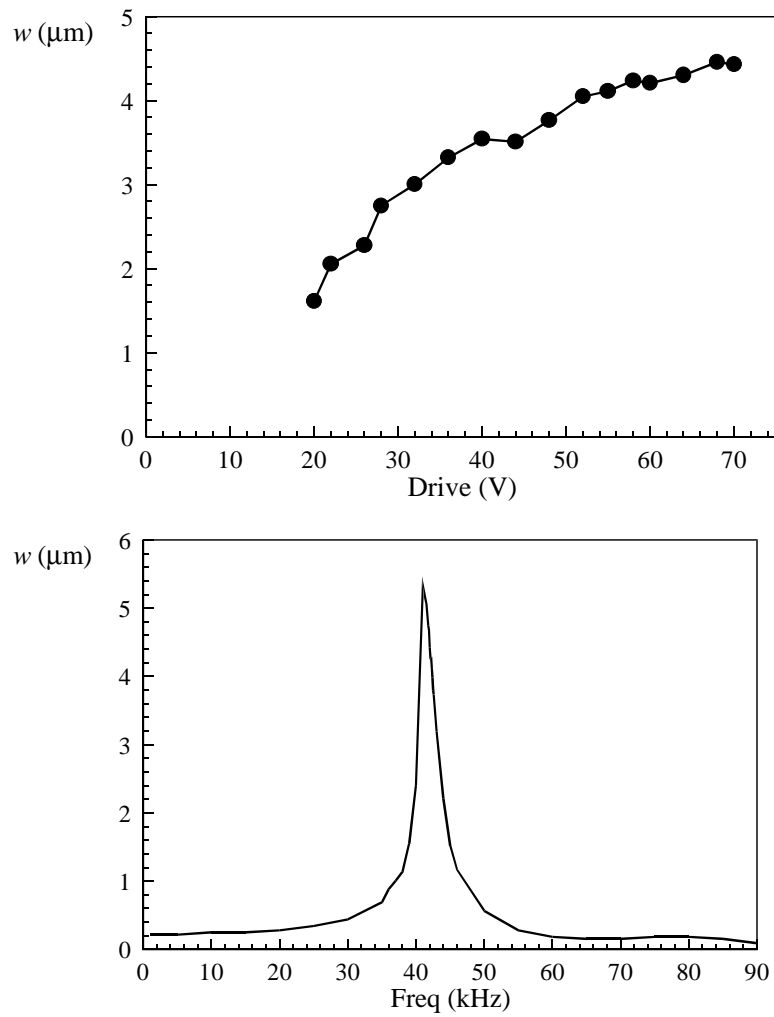


Figure 7-25: (a) Interferometer data showing the magnitude of the displacement at one point on the stator, at 42.2 kHz, as the voltage is swept from 20 V peak to 70 V peak. (b) Interferometer data showing the magnitude of the out-of-plane displacement at one location on the motor as the frequency is swept from 1 kHz through 90 kHz. A resonance is clearly visible.

The fringe pattern resulting from driving the unloaded stator is shown in Figure 7-24. The top trace is one phase of the stator drive signal and the bottom trace is the output of the interferometer's detector. Fringes between turn-around blips on the trace can be counted to find the peak-to-peak out-of-plane displacement of the stator. A helium-neon laser of 632.8 nm wavelength is used in the interferometer. Half the fringe count times the wavelength gives the amplitude of the displacement. Here, the stator is driven at 42.2 kHz, 60 V peak excitation. The laser spot is focused on a tooth positioned at approximately 11 o'clock. While the outer diameter of the stator is 8 mm and the inner diameter is 5 mm, the teeth are canted at such an angle that the actual flat part of the tooth is 0.5 mm wide in the radial direction. That is, the inner edge of the top flat part of the tooth is at a radius of 3.0 mm from the center of the stator and extends to a radius of 3.5 mm. The spot size of the laser is small enough to take about two readings per tooth.

Figure 7-25(a) illustrates how the out-of-plane deflection changes with applied voltage at a frequency of 42.2 kHz. The displacement grows from $1.6\ \mu\text{m}$ at 20 V to $4.5\ \mu\text{m}$ at 70 V.

Figure 7-25(b) shows the displacement on the same tooth of the stator, at a drive voltage of 60 V peak, as the frequency is scanned. A peak displacement of $5.3\ \mu\text{m}$ is achieved at 41.0 kHz.

If we leave the stator drive voltage fixed at 60 V peak and the drive frequency fixed at 42.2 kHz and move the X-Y stage such that the laser beam sequentially measures displacements on each tooth of the stator, we see fringe patterns like those shown in Figure 7-26. Whereas Figure 7-24 was the result of focusing the beam on a tooth at approximately 11 o'clock, Figure 7-26(a) and Figure 7-26(b) illustrate fringe patterns resulting from the beam being focused on teeth at 12 o'clock and 1 o'clock around the stator, respectively. By counting fringes, we find displacements of $4.9\ \mu\text{m}$, $4.9\ \mu\text{m}$ and $3.9\ \mu\text{m}$ at 11-, 12- and 1 o'clock respectively.

Notice that the turn-around blips move to the left, with respect to the reference drive signal in the top trace, in subsequent readings from Figure 7-24, Figure 7-26(a) and Figure 7-26(b). This phase change signifies where the maximum displacement points are with respect to each other as the circumference of the motor is scanned. That is, if we measure the phase with respect to the drive signal, for all points around the stator, we can mark off zero crossings in phase and visualize the mode of the traveling wave that is generated.

Figure 7-27(a) plots the amplitude of displacement for points around the stator and

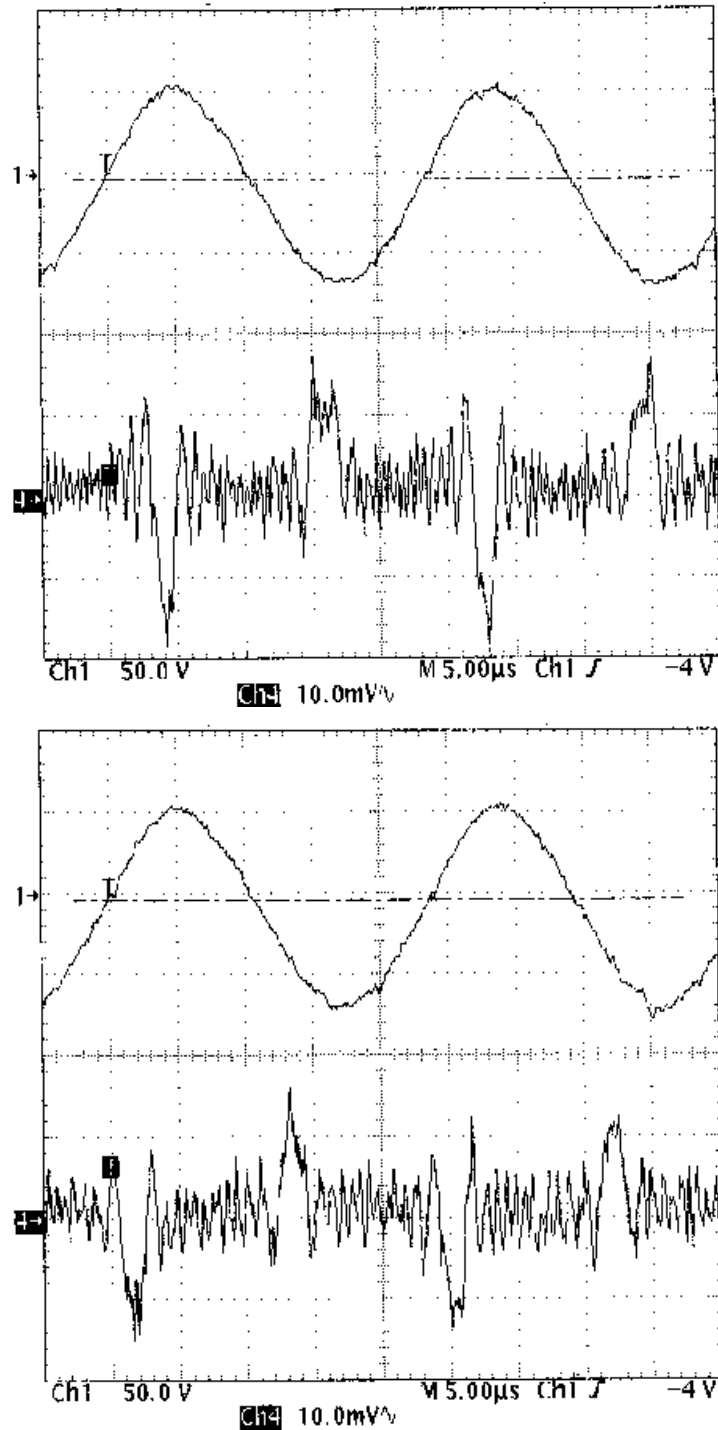


Figure 7-26: (a) Interferometer measurements of displacement on motor Grey1 at 12 o'clock. (b) Interferometer measurements of displacement on motor Grey1 at 1 o'clock.

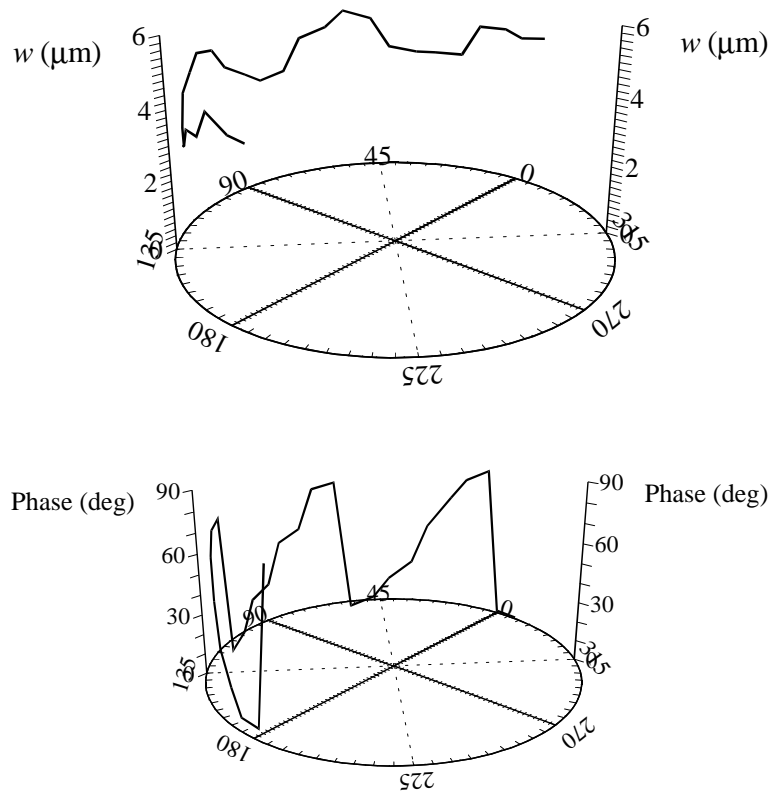


Figure 7-27: (a) Interferometer data showing the magnitude of the displacement, at resonance and 60 V_{peak} drive, around the stator (halfway around and then the interferometer went out of alignment). Shows fairly uniform displacement. (b) Interferometer data showing the phase of the displacement with respect to the drive signal. This shows which mode is acting, namely the third.

Figure 7-27(b) shows the phase relative to the drive signal. Every 180° phase shift is marked as a zero crossing and denotes half a wavelength of the flexure mode. Unfortunately, the interferometer went out of alignment halfway through this experiment, so only half of the readings around the stator were measured in Figure 7-27.

Nevertheless, it can be clearly seen that the magnitudes of the displacements are much more uniform for the traveling wave generated here than for the initial prototype motor's displacement shown earlier in Figure 7-3 where the magnitude of deflection sometimes fell below 0.1 μm.

Here, displacements average roughly 4.5 μm, with some deflections as high as 5.3 μm and some as low as 4.0 μm. For traveling wave deformation, one would expect equal displacements at all points around the stator. However, this is clearly not the case as we can see a standing wave component of deflection superimposed on the traveling wave in Figure 7-27.

This is very likely due to the different resonance characteristics of the two electrode patterns as illustrated in the damping measurements of the last section. A number of reasons are possible for the differences in quality factor between the two electrodes. First, the outer electrode covers a slightly larger area and at a larger distance from the center of the stator than the inner electrode. Second, the ceramic segments may not be poled uniformly, thus granting higher deflections to some areas of the stator than others. Third, the bond may not be perfectly uniform, or weakened in spots. The latter was definitely a possibility in the initial prototypes, but probably is not the case here, where a higher quality epoxy has been used.

However, the sheer magnitude of the improvement in the displacement measured in these stators as compared to the initial prototypes is clearly the reason for the drastic improvement in output performance. We are seeing almost 10 times as much displacement as in the initial prototypes. Again, this is primarily due to improvements incorporated into the second batch of stators of a higher temperature epoxy bond and a full-area coverage electrode pattern.

If we look at Figure 7-27(b), the plot of the phase of the turn-around displacement point with respect to the drive signal, we can see points of zero crossings at 4 locations around the stator. By symmetry, we can see that if we had been able to complete the experiment, that there would be two more zero crossings for a total of 6. Six zero crossings represent three wavelengths, so we can see that a three-wavelength traveling wave has been generated – precisely what the electrode pattern was designed for.

This interferometric method then, gives a nice way of visualizing traveling-wave modes and verifying that the appropriate drive conditions are achieved.

7.3.8 Efficiency Measurements and Drive Electronics

Efficiencies have not yet been measured on the second generation 8 mm bulk PZT ultrasonic motors. While the dynamometer is adequate for measuring mechanical output power, the input power is not easily measured at this point because the currents are rather small and fairly noisy. A little bit of work has to be done on the drive electronics to clean up the signals in order to facilitate ease of measurement of the phase angles offsets between the two current and voltage signals, when calculating average input current.

The drive electronics all reside on two small printed circuit boards. A Motorola 68HC11

processor controls a Qualcomm 2334 2-channel digital frequency synthesizer and also six LCD thumbwheel switches from American Control Technology. The LCD thumbwheel switches have embedded 4-bit microcontrollers and can be used as simple smart input and display devices for changing the frequency, phase and amplitude of the drive signals. The digital frequency synthesizer is controlled by the microprocessor via user input from the LCD thumbwheel switches and outputs two channels of 12-bit data at the appropriate frequency and relative phase. The two 12-bit ports are connected to AD7845 multiplying analog-to-digital converters to produce sin and cos drive signals for the motors. An AD558 analog-to-digital converter, directed from the microprocessor, controls the amplitude of the output of the AD7845 converters. These two resulting channels of drive signals are passed through Apex PA85 high-voltage high-bandwidth (expensive) operational amplifiers to boost the output voltage to 60 V_{peak} typically.

A low-pass filter needs to be added between the AD7845 analog-to-digital converters and the Apex high-voltage stage in order to reduce noise on the output waveforms. The motors run just fine with these inputs, but the current signals are somewhat noisy and make it hard to measure efficiencies. This problem is next on the agenda.

7.3.9 Coefficients of Friction

The coefficients of static friction between the various combinations of rotor and stator materials used in the experiments here and are shown in Figure 7-28. Most combinations gave coefficients on the order of 0.3, but sapphire on aluminum had an extraordinarily high value of 0.5, which makes sense since like materials have very high coefficients of friction and sapphire is aluminum oxide. So aluminum oxide on oxidized aluminum would be expected to have large friction coefficients. Sapphire on stainless steel had the lowest coefficient of friction at 0.22.

7.3.10 Matching to a Model

Once we have measured stator displacements and coefficients of friction between various rotors and stators, we can compare measured output performance to predictions from the sequence of models developed earlier.

First, we look at the case of line contact with Coulomb friction. Examining the data taken on stator Grey1, if we approximate the amplitude of displacement from Figure 7-

Static Coefficients of Friction				
	01 Hardened Steel	Sapphire	Kapton-on-steel	Kapton-on-sapphire
304 Stainless Steel	0.32	0.22	0.38	0.38
Aluminum	0.35	0.49	0.35	0.35

Figure 7-28: The coefficients of static friction for the rotor and stator materials used in the designed experiment are shown here. These coefficients were determined by finding the minimum angle at which a rotor would slide down an inclined piece of stator material.

27(a) as $4.5 \mu\text{m}$, the wavelength as $\lambda = \frac{2\pi r}{3}$, where the radius of contact is 3.25 mm, or $\lambda = 6.8 \text{ mm}$, and the coefficient of static friction between 304 stainless steel and sapphire as 0.22, we can compute the predicted no-load speed and stall torque.

The no-load speed for line contact is:

$$\omega_{rotor} = \omega_{stator,max} = \frac{2\pi\omega h w_o}{\lambda r}$$

where ω_{rotor} is the rotor speed (equal to the no-load speed for all loads up until stall when slipping occurs), ω is the drive frequency in $\frac{rad}{secs}$, h is the half-height of the stator, λ is the wavelength, r is the radius of contact and w_o is the out-of-plane displacement of the stator.

For stator Grey1, which has a tall base and short teeth on top of the PZT ceramic, h is 0.67 mm. The rotor speed then works out to:

$$\omega_{rotor} = 219 \frac{rad}{secs} = 2093 \text{ rpm}$$

Similarly, if we note the normal forces in Figure 7-18 that achieved the largest and smallest stall torques, we see they ranged from $F_N = 28 \text{ gf}$ to $F_N = 97 \text{ gf}$. For a coefficient of friction of 0.22, predicted stall torques are:

$$\tau_{stall} = \mu F_N r$$

which would predict stall torques of 2.0 gf-cm and 6.9 gf-cm, respectively. Figure 7-29 illustrates these two models of line contact superimposed on the data sets from Figure 7-18 for normal forces of $F_N = 28 \text{ gf}$ and $F_N = 97 \text{ gf}$.

It was found that if one goes through all the calculations of the Hertzian contact models for the actual data found from these experiments with the second generation bulk motors, that the contact condition is actually equivalent to that of line contact.

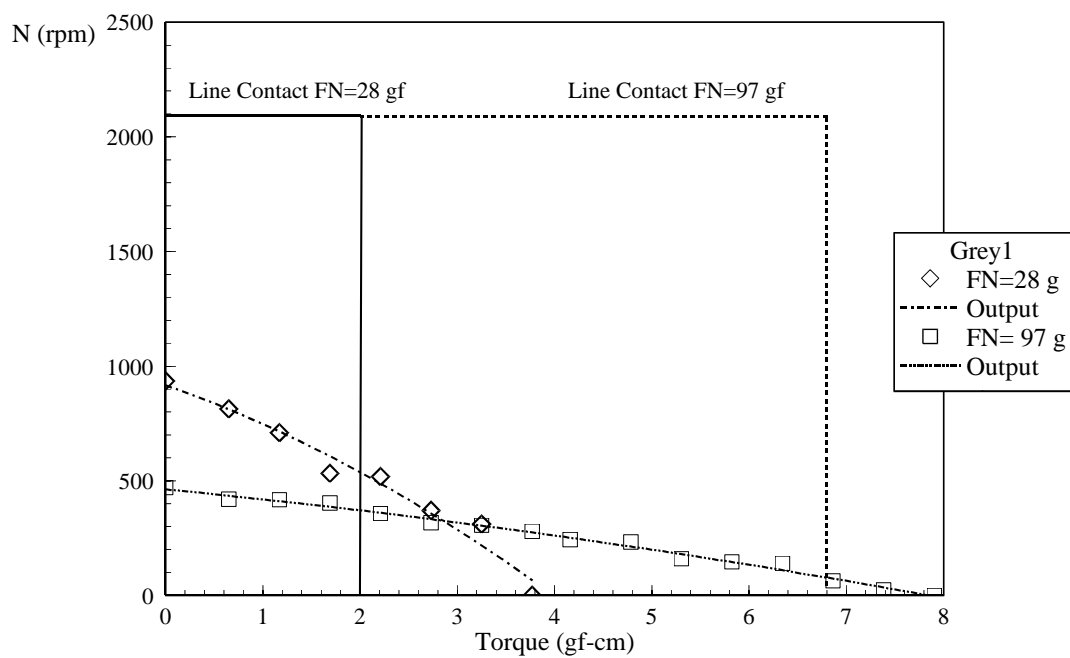


Figure 7-29: Data from the first speed-torque curve for stator Grey1 with a plain sapphire rotor, where the normal force was the lightest, at $F_N=28$ gf is marked by the diamonds. Data from the seventh speed-torque curve where the normal force was the highest, at $F_N=97$ gf is marked by the squares. Predictions based on line contact assuming Coulomb friction are shown for both cases. Hertzian contact assumptions give the same prediction as line contact for the light normal forces only sustained here.

Recall that Hertzian contact theory states that the length of the contact region grows as the square root of the normal force per unit length:

$$x_o = \frac{a}{2} = 0.8\sqrt{F_N DC_E}$$

For 304 Stainless Steel, the Young's modulus is $E = 28 \times 10^6$ psi ($190 \times 10^9 \frac{N}{m^2}$) and Poisson's ratio is $\nu = -0.21$ [Oberg et al. 88] For sapphire, or alumina, the Young's modulus is $E = 54 \times 10^6$ psi ($37 \times 10^9 \frac{N}{m^2}$) and Poisson's ratio is $\nu = -0.20$ [Coors 95]. These materials parameters give a C_E of:

$$C_E = \frac{1 - \nu_1^2}{E_1} + \frac{1 - \nu_2^2}{E_2}$$

where C_E works out to be $C_E = 1.14 \times 10^{-11} \frac{m^2}{N}$.

Taking the displacement of stator Grey1 as $4.5 \mu\text{m}$, the equivalent radius of curvature becomes $\rho_k = 0.26$ m. Modeling the stator as a cylinder of diameter, $D = 2\rho_k$ gives $D = 0.52$ m. Plugging in these materials parameters we find the length of the region of contact is $32 \mu\text{m}$ or $\frac{\lambda}{106}$ for a normal force of $F_N = 28$ gf of $61 \mu\text{m}$ and $\frac{\lambda}{55}$ for a normal force of $F_N = 97$ gf. Looking back at Figure 6-24, the speed-torque curves for Hertzian contact, we see that this condition approaches the case of line contact. Indeed, following through and calculating the speed-torque relations from:

$$\tau_{rotor} = \frac{\mu F_N r}{\phi(x_o)} [2\phi(x_r) - \phi(x_o)]$$

where

$$\phi(x) = \sin(kx) - kx \cos(kx_o)$$

and

$$\omega_{rotor} = \omega_{stator,max} \cos(kx_r)$$

and

$$x_r = \frac{1}{k} \cos^{-1} \left(\frac{\omega_{rotor}}{\omega_{stator,max}} \right)$$

gives essentially the same lines as in Figure 7-29 for line contact. Note that the no-load speeds in reality are lower than the predicted values and the stall torques are higher. The coefficient of friction is the scale factor for the stall torques and is not known with complete accuracy. The no-load speeds are lower than those predicted for line contact, both because

of the assumption of a rigid, unsquashable stator in these closed-form models and because of the decrease in the amplitude of deflection as power is taken out of the system. This shows that it is important to model the squashing of the stator in addition to area contact. Appendix B illustrates variational techniques for producing models that relax the rigidity assumption on the stator.

7.3.11 Surface Profilometry Measurements

The second generation set of 8 mm motors saw significant improvement in performance over the initial prototypes whose speed, torque and power characteristics were plotted in Figure 7-5. With the initial prototypes, we found that glass rotors spun well, while brass rotors turned on a lathe did not work at all. This was understandable when later we found that the mean roughness of the glass rotor was 300 \AA while that of the brass rotor was 7000 \AA . In addition, the amplitude of displacement on those first stators was under $1 \mu\text{m}$ meaning that the out-of-plane displacement of the stator was not much greater than the height of the asperities on the rotor.

In the second generation of motors, we took great pains to achieve large out-of-plane deflections and indeed we have seen a factor of 5 to 10 improvement. We also paid more attention to the surface properties of the rotor and stator materials. We not only chose harder materials, but we polished each surface before testing in the dynamometer. The stators and rotors were lapped flat and then polished with $9 \mu\text{m}$ -, $5 \mu\text{m}$ -, $3 \mu\text{m}$ - and finally $1 \mu\text{m}$ -grit lapping paper.

After polishing, surface properties were examined with a Dektak profilometer. Figure 7-30 illustrates surface profiles for the polished steel and sapphire rotors, respectively. The x -axis shows the length of material over which the stylus was run, measured in microns, while the y -axis denotes the asperity height, measured in angstroms or kilo-angstroms, as noted. The steel rotor, in Figure 7-30(a) had a mean roughness of 115 \AA , polished almost as smoothly as the sapphire surface which displayed a mean roughness of 110 \AA .

The kapton-coated rotors were not so smooth, obviously. Figure 7-31 displays a mean roughness of 768 \AA for the kapton-coated steel rotor and a mean roughness of 411 \AA for the kapton-coated sapphire rotor.

It is important to examine not only the rotors, but also the surface of the stator teeth. Figure 7-32 depicts the surface profile across a tooth of stator Grey1 just after polishing.

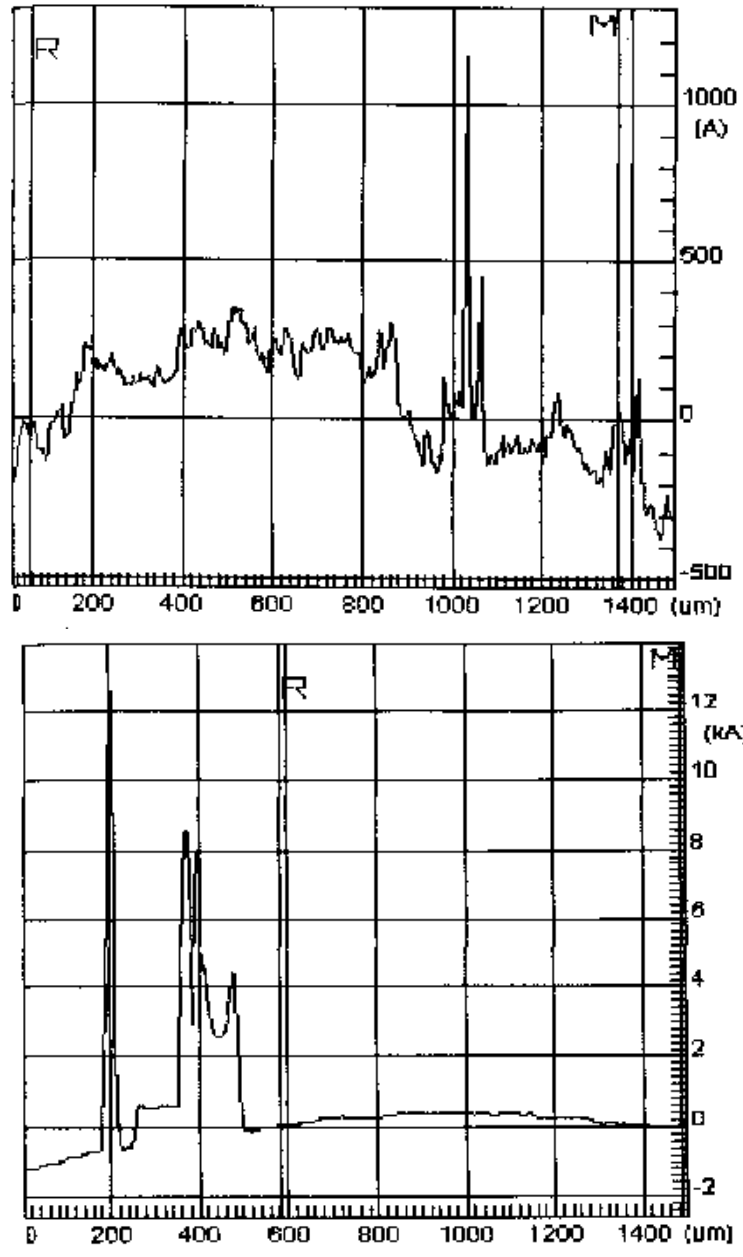


Figure 7-30: (a) A plain steel rotor surface profile after polishing. The arithmetic mean roughness is 115 Å. (b) The sapphire rotor measured displays an arithmetic mean roughness of 110 Å.

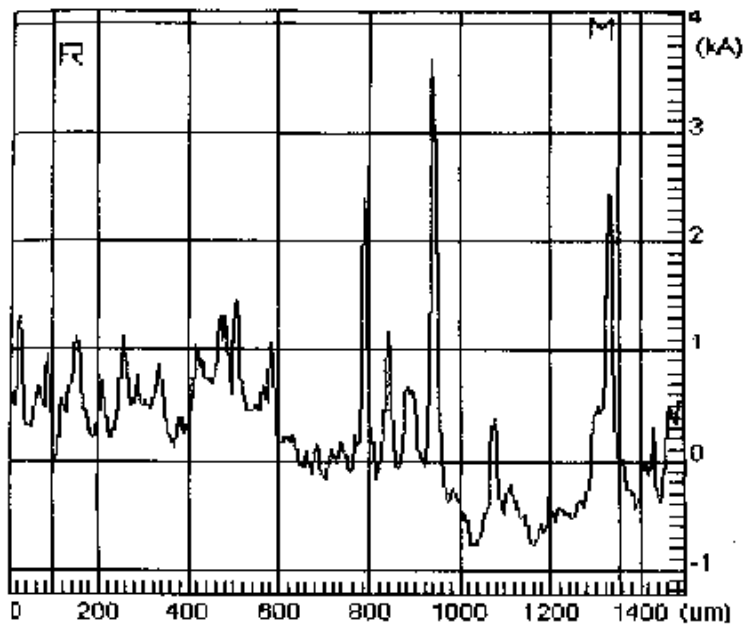
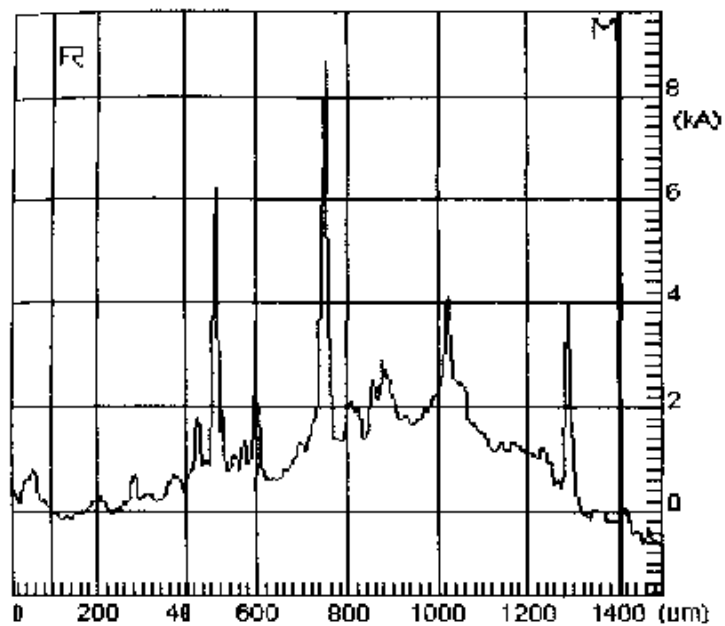


Figure 7-31: (a) The kapton-coated steel rotor measured after polishing displays an arithmetic mean roughness of 768 Å. (b) The kapton-coated sapphire rotor has a mean roughness of 411 Å.

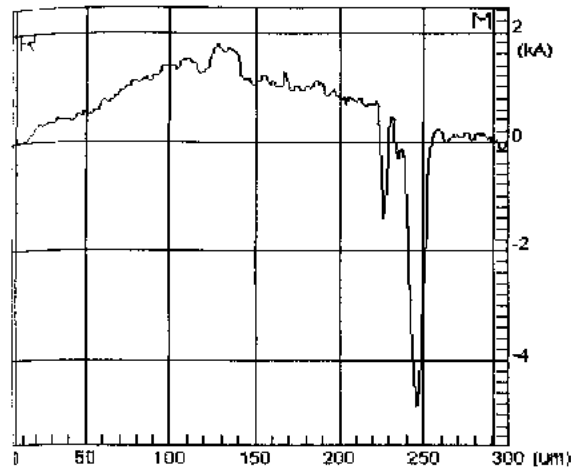


Figure 7-32: This is the stator Grey 1 tooth surface. The arithmetic mean roughness is 631 \AA .

The measured mean roughness here is 631 \AA . These profilometer traces in conjunction with significant improvements in torque output, as compared with initial prototypes, point out the need for out-of-plane displacements to be much larger than surface asperities.

Wear Tests

Surface profile measurements were also performed on the rotors after running in the dynamometer in order to study wear phenomenon. After the rotors are run on the stators for 30 minutes or so, the rotors and stators are removed from the dynamometer and their surfaces inspected. Typically, a discolored ring is seen on the rotor at the radius of contact and the stator teeth have a radial section which is highly polished while the remaining areas are rather dull in color.

Figure 7-33 illustrates wear profiles on plain steel and sapphire rotors after having run on stator Green1, which was stainless steel. The stator makes a circular gouge mark on the rotor and the profilometer is run across the gouge in the radial direction from the center of the rotor out towards the edge. Figure 7-33(a) shows that for the 01 hardened tool steel rotor running on a stainless steel stator, material is deposited on the rotor to a thickness of 1942 \AA . Similarly, Figure 7-33(b) shows that the sapphire rotor, after running on the stainless steel stator, also receives a deposit of 901 \AA . Thus the rotors are harder than the stator and the stator does not gouge the rotor, as was the case in the initial prototypes where the stators ate into the first glass rotors. Here, the rotors actually tend to polish the

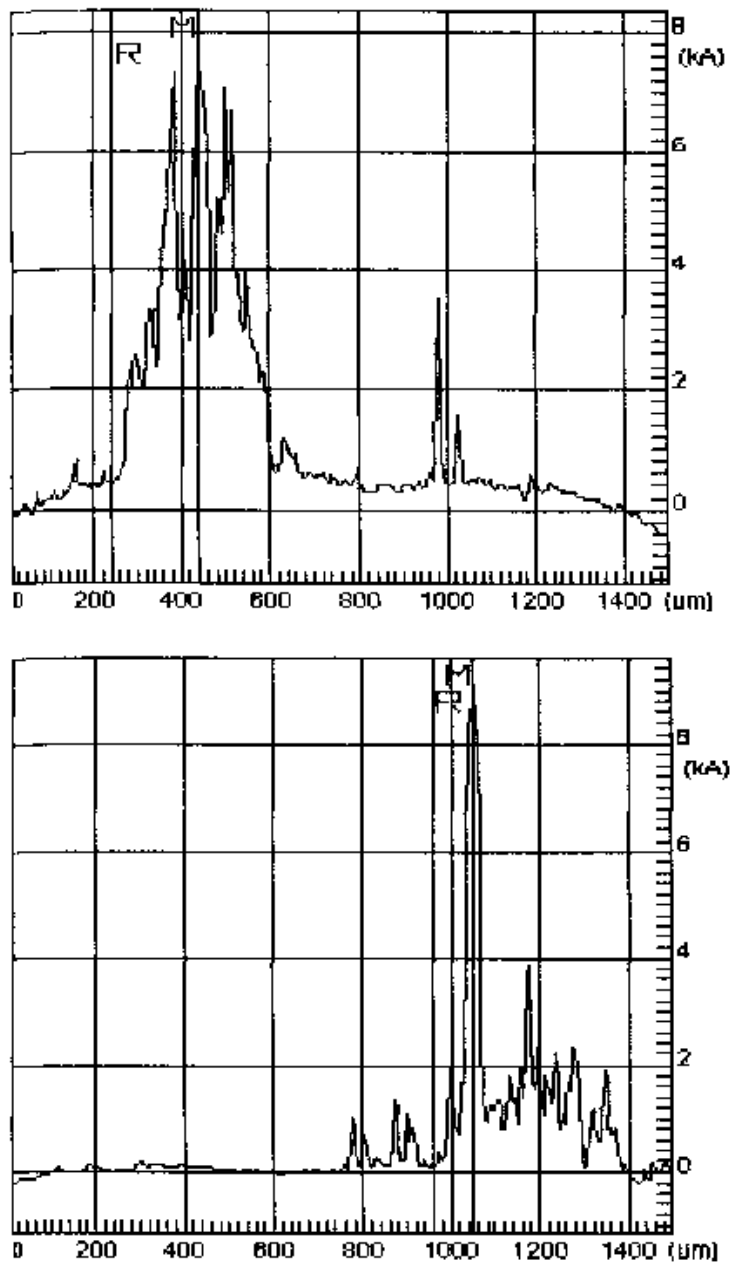


Figure 7-33: (a) The steel rotor, measured across the discolored circular mark, shows a peak of 1942 Å. This rotor was last run on stator Green1 (stainless steel). (b) The sapphire rotor measured across the discoloration, acquires a peak of material 901 Å high. This rotor was also last run on stator Green1.

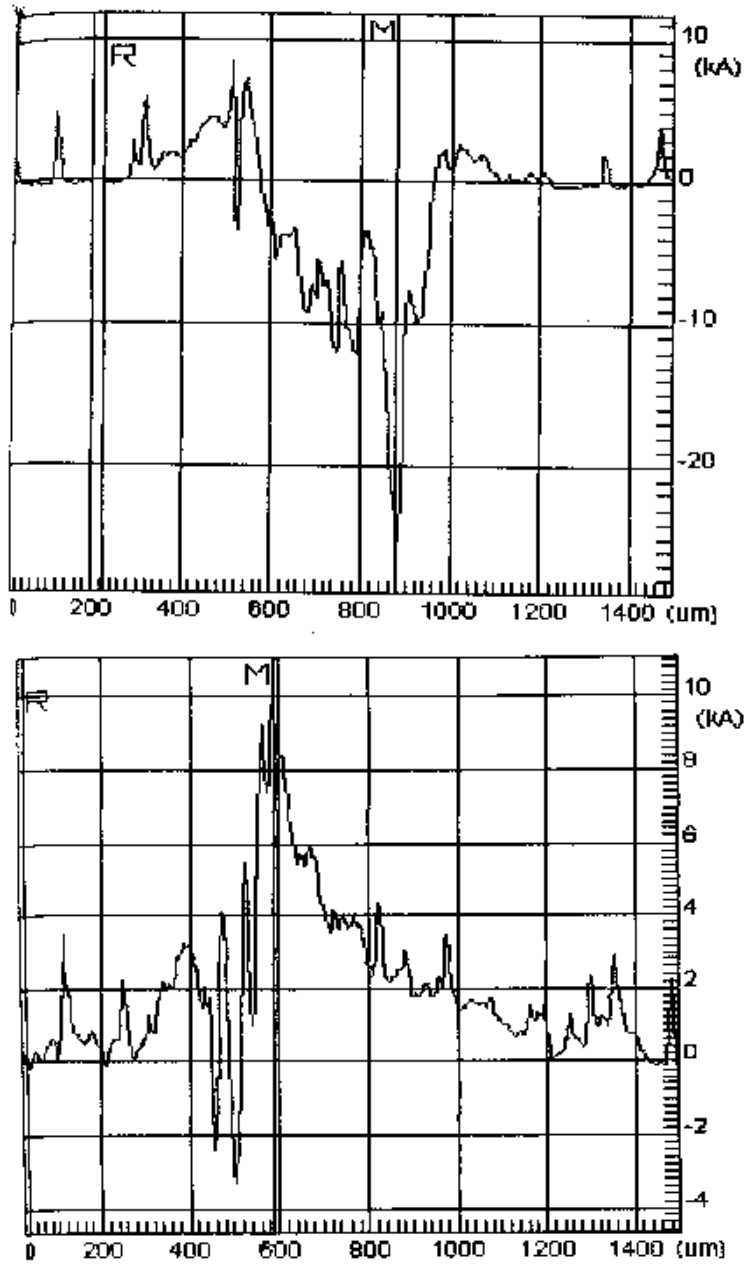


Figure 7-34: (a) The kapton-coated steel rotor measured across the circular mark shows an indentation into the kapton of nearly $2\ \mu\text{m}$. This stator was run on stator Grey1 (stainless steel). (b) The kapton-coated sapphire rotor measured across the circular mark displays a valley of $121\ \text{\AA}$ which is followed by a peak of $1956\ \text{\AA}$.

stators.

Figure 7-34 portrays surface profiles of the kapton-coated rotors after having been run on stator Grey1, which was also stainless steel. Figure 7-34(a) shows what happens to the kapton-coated steel rotor after 30 minutes or so of running. The stainless steel stator eats into the kapton to a depth of nearly $2\ \mu\text{m}$. This is as would be expected since the polymer material is rather soft. Figure 7-34(b) shows a similar result for the kapton-coated sapphire rotor. The difference here, however, is that a valley of $121\ \text{\AA}$ is followed by a peak of $1956\ \text{\AA}$, so the kapton material is smushed to the side as the teeth dig into the polymer.

7.4 Comparing Motor Figures of Merit

7.4.1 Stall Torque and Output Power Densities

By dividing the measured maximum stall torques and output powers by the weight or volume of the stator-rotor assembly, we can examine figures of merit for our motors. [Hollerbach, Hunter and Ballantyne 91] argue that the most useful figure of merit for comparing disparate motor technologies is stall torque density ($\frac{Nm}{kg}$) as power density figures really depend on the associated power electronics.

Figure 7-35 lists the stall torque densities resulting from our 16-trial experiment. The maximum stall torque density of $2.9\ \frac{Nm}{kg}$ is produced by stator Green1 with a sapphire rotor. Note that the motors here do not have bearings, but are held together in the dynamometer. True stall torque density numbers will be smaller after bearings and mounts are added in the future. We have put off working on bearings and mounts until the motors were better understood and useful torques could be shown. This has been achieved and in the near future we will mount a simple bearing to one of these motors.

Figure 7-35 lists the corresponding output power densities for the second generation 8 mm bulk motors. Stator Fucia1 with a sapphire rotor produced the highest power density of $108\ \frac{W}{kg}$.

7.4.2 Comparisons to Other Actuator Technologies

It is interesting to compare piezoelectric ultrasonic motors and see how other actuator technologies measure up. Figure 7-37 [Hollerbach, Hunter and Ballantyne 91] shows how a wide variety of technologies, such as hydraulic systems, pneumatic actuators, shape memory

Design of Experiments Results: Stall Torque Densities						
	Stator	Max Stall Torque (gf-cm)	Mass (g) St+Rot=Tot	Volume (mm ³)	Max Stall Torque Density (Nm/kg)	Max Stall Torque Density (gf-cm/mm ³)
1	Violet Exp 2	4.7	.28+.13=.41	120	1.2	0.039
2	Violet Exp 4	4.8	.28+.37=.65	120	0.74	0.040
3	Fucia Exp 2	5.5	.13+.13=.26	120	2.1	0.046
4	Fucia Exp 4	4.5	.13+.37=.50	120	0.90	0.038
5	Tan Exp 2	2.7	.12+.12=.24	87	1.1	0.031
6	Tan Exp 4	3.4	.12+.36=.48	87	0.71	0.039
7	Blue Exp 2	4.7	.27+.12=.39	87	1.2	0.054
8	Blue Exp 4	4.6	.27+.36=.60	87	0.77	0.053
9	Green Exp 2	10.0	.22+.12=.34	68	2.9	0.15
10	Green Exp 4	8.4	.22+.36=.58	68	1.5	0.12
11	Yellow Exp 2	5.3	.11+.12=.23	68	2.3	0.078
12	Yellow Exp 4	5.6	.11+.36=.47	68	1.2	0.082
13	Orange Exp 2	4.8	.10+.13=.23	61	2.1	0.079
14	Orange Exp 4	4.6	.10+.37=.47	61	1.0	0.075
15	Grey Exp 2	4.3	.20+.13=.33	61	1.3	0.070
16	Grey Exp 4	5.3	.20+.37=.57	61	0.93	0.087

Figure 7-35: Stall torque densities resulting from the 16-trial experiment of 8 mm bulk PZT ultrasonic motors. Stator Green1 (short teeth, thick base, 36 teeth, stainless steel) with a plain sapphire rotor produced $2.9 \frac{Nm}{kg}$ stall torque density.

Power Density							
Stator	Liner	Rmat	Mass (g) St+Rot=Tot	Volume (mm ³)	Peak Power (mW)	Peak Power Density (W/kg)	Peak Power Density (mW/mm ³)
Fucia	-	+	.13+.12=.25	120	27	108	0.23
Yellow Exp 2	-	+	.11+.12=.23	68	12	52	0.18
Grey	-	+	.20+.12=.32	61	16	50	0.26

Figure 7-36: Output power densities for the second generation motors. Power densities as high as $108 \frac{W}{kg}$ have been achieved with stator Fucia1 (tall teeth, thick base, 24 teeth, aluminum) with a plain sapphire rotor.

<i>Actuator</i>	<i>Power Dens. (W/kg)</i>	<i>Stall Torque Dens. (Nm/kg)</i>
McGill/MIT EM Motor	15	200
Sarcos Dextrous Arm electro-hydraulic rotary actuator	120	600
Utah/MIT Dextrous Hand electropneumatic servovalve	20	200
NiTi SMA [Hirose 89]	1	6
PVA-PAA polymeric actuator [Caldwell 90]	17	6
Burleigh Instruments inchworm piezoelectric motor	3	0.1
Magnetoelastic (magnetostrictive) wave motor [Kiesewetter 88]	500	5
Human biceps muscle	20	50
MIT 8 mm Fucia/Green	108	2.9

Figure 7-37: Power density and stall torque density can be used as figures-of-merit to compare actuator technologies.

alloys, piezoelectric inchworms, magnetostrictive materials and human muscle compare in terms of both stall torque density and output power density. We have inserted our recent results into their table where the number for power density refers to the stator Fucia1 running on a plain sapphire rotor and the number for stall torque density refers to the stator Green1 also running with a plain sapphire rotor.

Note that the piezoelectric ultrasonic motors vastly outperform the piezoelectric inchworm drives. This is due the fact that resonance is used to advantage in the ultrasonic motors, whereas the inchworm drives are quasistatic.

While the stall torque densities for the first three actuators in the table are significantly higher than those for our ultrasonic motors, it is useful to note that these are all fairly large actuators. The McGill/MIT electromagnetic motor is also water-cooled. If we compare our 8 mm ultrasonic motors to small DC motors that would typically be the direct competition, our ultrasonic motors compare exceedingly well.

Figure 7-38 gives figures of merit comparing ultrasonic motors reported in the literature with small electromagnetic DC motors typically used in mobile robot applications. The

<i>Actuator</i>	<i>Stall Torque (kgf-cm)</i>	<i>No-load Speed (rpm)</i>	<i>Power Density (W/kg)</i>	<i>Stall Torque Density (Nm/kg)</i>	<i>Peak Eff.</i>
[Micro Mo] 1319E003	0.034	13,500	106	0.29	71%
[Mabuchi] FK-280-2865	0.16	14,500	NA	0.42	53%
[Namiki 92] 7CL-1701	0.0016	9,100	13	0.06	50%
Aeroflex	0.10	4,000	NA	0.04	20%
Maxon	0.13	5,200	NA	1.13	70%
Astro	0.76	11,500	NA	0.21	20%
[Kumada 85]	13.5	120	80	8.8	80%
[Shinsei 89] USR-60	6.0	125	23	3.4	35%
[Panasonic 87] USM-40	0.8	800	NA	1.1	40%
[Hosoe 89] EF35-135	1.2	80	NA	2.3	40%
MIT 8 mm Fucia	0.0055	1750	108	2.1	NA
MIT 8mm Green	0.01	870	NA	2.9	NA

Figure 7-38: This representative sampling of electromagnetic DC motors (without gears), commercially available Japanese ultrasonic motors and our 8 mm ultrasonic motors are presented to give a feel of relative measures of stall torque density and efficiency. Stators Fucia and Green are run with plain sapphire rotors.

first six motors listed in Figure 7-38 are electromagnetic motors, the next four are larger Japanese ultrasonic motors, on the order of 40 mm to 60 mm in diameter.

The smallest commercially available electromagnetic DC motor is the Namiki 7CL-1701. It is 7 mm in diameter and 18 mm long, roughly 5 times the volume of our 8 mm ultrasonic motors, yet stator Fucia running with a sapphire rotor has 35 times the stall torque density and 8 times the power density of the Namiki motor. Stator Green with a sapphire rotor compares even more favorably to the Namiki in stall torque density. Its stall torque density is 48 times larger. Most importantly, however, is that the typical operating speeds of ultrasonic motors are much lower, granting a significantly better impedance match for nearly all loads.

Chapter 8

Laser Etching of Thin-Film PZT Motors

The original impetus for pursuing ultrasonic micromotors was the fact that thin-film PZT could now be deposited directly onto silicon and the resulting increase in breakdown strength provided extremely high energy densities. By depositing PZT in a sol-gel process onto silicon, we do away with the need for an epoxy bond layer and we open the door to possibilities for integration with electronics and microsensors. Because of the high energy densities and because these ultrasonic motors inherently run at high torques and low speeds, we have a promising new technology for creating microfabricated motors which couple useful power to a load.

To this point, we have shown process feasibility in fabricating thin-film actuators and we have modeled and tested larger motors from bulk PZT with very good results. Now we would like to join the two efforts and return to microfabricated ultrasonic motors. However, we are not necessarily interested in making these motors micro-sized, nor are we so constrained, as demonstrated by the larger motors we have built. While silicon electrostatic micromotors are constrained to be under a certain maximum radial dimension due to residual stresses in the rotor vanes causing them to touch down onto the surface below, friction-based ultrasonic motors can be made arbitrarily large in the plane of the stator. The constraint here is the ability to fabricate wide-area coverage films that are pinhole-free.

To get motion out of the plain of the wafer, and to achieve true waveguide structures, it is desirable to cut the stator free from the wafer. Traditional machining is not amenable

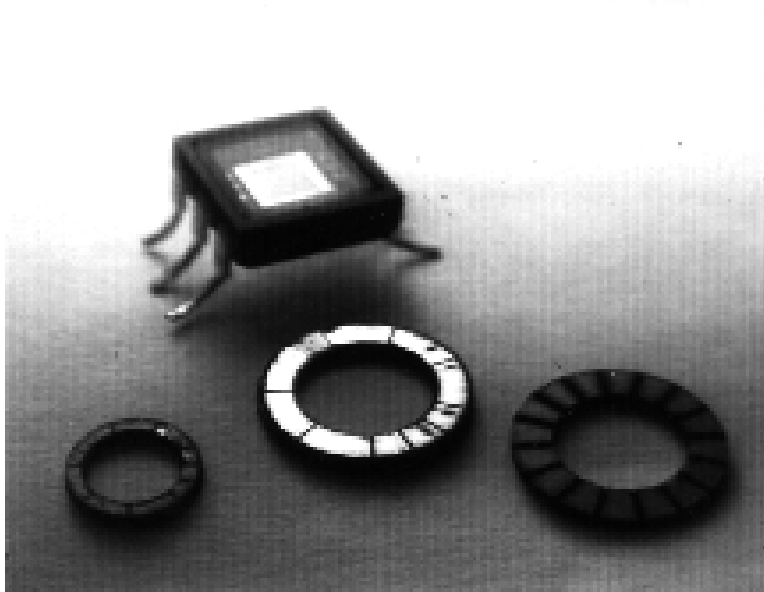


Figure 8-1: The two rings at the bottom right are 8 mm composite rings consisting of layers of silicon, silicon oxide, titanium, platinum, sol-gel PZT and chrome-gold. The stator at left is 5 mm in diameter. The six-pin integrated circuit at top is a serial charge coupled imaging device, to give scale to the picture and to illustrate our desire to build actuators at the same size as our sensors.

as silicon is fairly brittle, and etching processes create sidewalls at the angle of the lattice lines. What would be best is a non-contact cutting tool.

Figure 8-1 shows stators that we have machined using a laser-etching process. The laser etching was performed at a commercial job shop, Laser Services, in Westford, MA. The laser ablation process is used to cut rings out of wafers that have been prepped with all the layers of the necessary films: oxide, titanium, platinum, sol-gel PZT and chrome-gold. The laser process is also used to etch the electrode pattern in the chrome-gold and also the tooth structure on the backside to reduce stiffness. We also start with thinned wafers, and in this manner avoid the need for fragile membranes and silicon-rich nitride films.

To connect to the titanium-platinum ground electrode, a chemical-assist laser-etching and deposition process was used. This step was done with the assistance of Dr. Daniel Ehrlich at MIT Lincoln Laboratory. A platinum gas is used with the laser to deposit a plug in a laser-punched via. This effectively brings up a contact from the bottom electrode to a top chrome-gold pad. In this manner, all the steps of stator microfabrication are accomplished without any masks or wet-etching.

Chapter 9

Conclusion

The technology of micromotors has taken a new turn. Previously, micromotors were fabricated from predominantly silicon integrated-circuit processes. With the incorporation of an electromechanically active material, PZT, into a standard silicon micromachining process, we have been able to produce piezoelectric ultrasonic micromotors displaying significant improvements over previous incarnations of micromotors.

Ultrasonic motors are new and not as well understood as conventional electromagnetic or electrostatic motors. A number of models with closed-form solutions for production of torque have been proposed here, where simplifying assumptions on the contact mechanics have been sequentially relaxed. This analysis has granted insight into the phenomena underlying the frictional coupling mechanism and provided useful upper bounds on performance.

In addition to theoretical results, an experimental component of this research has yielded one of the most complete data sets on bulk piezoelectric ultrasonic motors in the open literature. Providing this data to other researchers in the field will not only contribute to elevating our understanding of these devices, but also hasten growth of this new technology.

We have found that our second generation of bulk motors shows drastically improved performance over our initial prototypes, due to improvements in electrode design, bonding techniques and attention to detail in surface preparation. These new motors work primarily in the region of line contact. The experiments have shown that ultrasonic motors can deliver five times the stall torque of their electromagnetic brethren in $\frac{1}{5}$ the size, with comparable power densities. Power densities of $108 \frac{W}{kg}$ and stall torque densities of $2.9 \frac{Nm}{kg}$ have been

achieved. In addition, the impedance match for these motors to most real-world loads is significantly better than for electromagnetic motors. Peak power operating points occur at speeds on the order of a few hundreds of rpm rather than thousands of rpm. Careful design of the stator geometry can result in operating points tailored to a load such that the need for gear-down can be circumvented.

In the future, we plan to return to thin-film PZT-on-silicon technology and incorporate these high-torque low-speed motors into complete microelectromechanical systems for microrobotic applications. A new laser-based etching process has been developed in this regard which allows for microfabrication of ultrasonic motors without fragile membranes and requires no masks and no wet-etching. This type of process is more amenable to the designer than batch fabrication processes and such a manufacturing capability will further aid the growth of the field by compressing the design, fabrication and testing cycles.

References

- [Akiyama 87] “Present State of Ultrasonic Motors in Japan,” Yuji Akiyama, *JEE*, April.
- [Anderson and Hagood 92] “Simultaneous Piezoelectric Sensing/Actuation: An Analysis and Application to Controlled Structures,” Eric H. Anderson and Nesbitt W. Hagood, *Journal of Sound and Vibration*, Vol. 174, No. 5, pp. 617–639.
- [Angle 89] “Gengis, A Six-Legged Autonomous Walking Robot,” Colin M. Angle, *S.B. Thesis, Massachusetts Institute of Technology*, June.
- [Angle 90] “Personal communication,” Colin M. Angle, *MIT Artificial Intelligence Laboratory*, Cambridge, MA.
- [Bart et al. 88] “Design Considerations for Microfabricated Electric Actuators,” S.F. Bart, T.A. Lober, R.T. Howe, J.H. Lang and M.F. Schlecht, *Sensors and Actuators*, 14(3):269-292.
- [Bart, Mehregany, Tavrow, Lang and Senturia 90] “Measurements of Electric Micromotor Dynamics,” Stephen F. Bart, Mehran Mehregany, Lee S. Tavrow, Jeffrey H. Lang and Stephen D. Senturia, *ASME Winter Annual Meeting on Micromechanical Systems*, Dallas, TX, November 25-30, pp. 19-29.
- [Barth 73] “Ultrasonic Driven Motor,” H.V. Barth, *IBM Technical Disclosure Bulletin*, Vol. 16, No. 7, December.
- [Bhushan and Gupta 91] “Handbook of Tribology,” Bharat Bhushan and B.K. Gupta, *McGraw-Hill*, New York.
- [Brooks 86] “A Robust Layered Control System for a Mobile Robot,” Rodney A. Brooks, *IEEE Journal of Robotics and Automation*, Vol. RA-2, pp.14–23 April.
- [Brooks 89] “A Robot That Walks; Emergent Behavior From a Carefully Evolved Network,” Rodney A. Brooks, *Neural Computation*, Vol. 1.
- [Buchanan 86] “Ceramic Materials for Electronics,” Relva C. Buchanan, *Marcel Dekker, Inc.*, New York.

[Caldwell 90] "Pseudomuscular Actuator for Use in Dextrous Manipulation," D.G. Caldwell, *Med. & Biol. Engrg. & Computing*, Vol. 28, pp. 595-600.

[Connell 90] "Minimalist Mobile Robotics – A Colony-Style Architecture for an Artificial Creature," Jonathan H. Connell, *Academic Press*, San Diego, CA.

[Coors 95] "Technical Data Sheet," Coors Ceramic Co., *Electronic Products Group*, Golden, Colorado.

[Crawley and De Luis 87] "Use of Piezoelectric Actuators as Elements of Intelligent Structures," Edward F. Crawley and Javier de Luis, *AIAA Journal*, Vol. 25, No. 10.

[Crawley and Anderson 90] "Detailed Models of Piezoceramic Actuation of Beams," Edward F. Crawley and Eric H. Anderson, *Journal of Intelligent Material Systems and Structures*, Vol. 1, pp. 4–25.

[Crawley and Lazarus 91] "Induced Strain Actuation of Isotropic and Anisotropic Plates," E.F. Crawley and K.B. Lazarus, *AIAA Journal*, Vol. 29, No. 6, pp. 944-951.

[Dupont and Bapna 92] "Stability of Sliding Frictional Surfaces with Varying Normal Stress," Pierre E. Dupont and Deepak Bapna, *Submitted to Applied Mechanics Reviews*, Boston University, August 25.

[Endo and Sasaki 87] "Investigation of Frictional Material for Ultrasonic Motor," Akira Endo and Nobutoshi Sasaki, *Japanese Journal of Applied Physics*, Vol. 26, Suppl. 26-1, pp. 191-193.

[Fieguth, Spina and Staelin 94] "Conformal Design of Experiments: An Automated Tool Supporting Experiment Design and Analysis for Efficient Improvement of Products and Processes," Paul W. Fiegth, Michelle S. Spina and David H. Staelin, *MIT Leaders for Manufacturing Program Technical Report*, March 10.

[Flynn 87] "Gnat Robots (And How They Will Change Robotics)," Anita M. Flynn, *Proceedings of the IEEE Micro Robots and Teleoperators Workshop*, Hyannis, MA, November.

[Flynn, Brooks, Wells and Barrett 89] "Intelligence for Miniature Robots," Anita M. Flynn, Rodney A. Brooks, William M. Wells III and David S. Barrett, *Journal of Sensors and Actuators*, Vol. 20, pp. 187-196.

[Flynn, Brooks and Tavrow 89] "Twilight Zones and Cornerstones: A Gnat Robot Double Feature," Anita M. Flynn, Rodney A. Brooks and Lee S. Tavrow, *MIT Artificial Intelligence Laboratory Memo 1126*, July.

[Flynn, et. al. 92] "Piezoelectric Micromotors for Microrobots," Anita M. Flynn, Lee S. Tavrow, Stephen F. Bart, Rodney A. Brooks, Daniel J. Ehrlich, K.R. Udayakumar and L. Eric Cross, *IEEE Journal of Microelectromechanical Systems*, Vol. 1, No. 1, pp. 44–51, March.

[Franck 95] “Manufacturing Ultrasonic Minimotors,” Dean L. Franck, *S.B. Thesis, MIT Department of Mechanical Engineering*, June.

[Froelicher, Minotti, Eyraud, Foch and Claeysen 91] “Study and Realization of an Ultrasound Motor,” Electrical Engineering '91, Summary Colloquium of the Research Activities of the Ministere de la Recherche et de la Technologie Proceedings 1991, *M. Froelicher, P. Minotti, L. Eyraud, H. Foch and F. Claeysen*, CETAHOR, LMA, LGEF/INSA, EN-SEEIHT/LEEI and CEDRAT RECHERCHE, in French.

[Fujita, Omodaka, Sakata and Hatazawa 89] “Variable Gap Electrostatic Actuators,” Hiroyuki Fujita, Akito Omodaka, Minoru Sakata and Yasuyoshi Hatazawa, *Technical Digest of the 8th Sensor Symposium*, pp. 145-148.

[Gaberson 72] “Particle Motion on Oscillating Conveyors, Parts I and II,” H.A. Gaberson, *J. Eng. Ind. (Trans. ASME B)*, vol. 94, pp. 50–63.

[Gerson and Marshall 59] “Dielectric Breakdown of Porous Ceramics,” Robert Gerson and Thomas C. Marshall, *Journal of Applied Physics*, Vol. 30, No. 11, November, pp. 1650–1653.

[Hagedorn and Wallaschek 92] “Travelling Wave Ultrasonic Motors, Part I: Working Principle and Mathematical Modelling of the Stator,” P. Hagedorn and J. Wallaschek, *Journal of Sound and Vibration*, Vol. 155, No. 1, pp. 31–46.

[Hagedorn et al. 92] “Travelling Wave Ultrasonic Motors, Part II: A Numerical Method for the Flexural Vibrations of the Stator,” Peter Hagedorn, Wolfgang Konrad and J. Wallaschek, *The Journal of Sound and Vibration*, to appear.

[Hagood, Chung and Von Flutow 90] “Modelling of Piezoelectric Actuator Dynamics for Active Structural Control,” Nesbitt W. Hagood, Walter H. Chung and Andreas von Flutow, *Journal of Intelligent Materials, Systems and Structures*, Vol. 1, July, pp. 327–354.

[Hagood and McFarland 95] “Modeling of a Piezoelectric Rotary Ultrasonic Motor,” Nesbitt W. Hagood and Andrew J. McFarland, *IEEE Transactions on Ultrasonics, Ferroelectrics and Frequency Control*, Vol. 42, No. 2, pp. 210-224, March.

[Hagood and von Flotow 91] “Damping of Structural Vibrations With Piezoelectric Materials and Passive Electrical Networks,” N. W. Hagood and A. von Flotow, *Journal of Sound and Vibration*, Vol. 146, No. 2, pp. 243–268.

[Hamilton and Goodman 66] “The Stress Field Created by a Circular Sliding Contact,” G.M. Hamilton and L.E. Goodman, *Journal of Applied Mechanics*, Vol. 33, pp. 371–376.

[Hertz 1882] “On the Contact of Elastic Solids,” Heinrich Hertz, *J. reine und angewandte Mathematik*, Vol. 92, pp. 156-171.

[Higuchi et al. 89] “Micro Robot Arm Utilizing Deformations of Piezoelectric Elements,”

Toshiro Higuchi, Yutaka Yamagata, Ken-ichi Kudoh and Koji Iwasaki, *Fifth International Symposium of Robotics Research*, Tokyo, Japan, August 28-31.

[Hirata and Ueha 93] “Characteristics Estimation of a Traveling Wave Type Ultrasonic Motor,” H. Hirata and S. Ueha, *IEEE Transactions of Ultrasonics, Ferroelectrics and Frequency Control*, Vol. 40, No. 4, pp. 402–406, July.

[Hirose et al. 89] “Development of Shape Memory Alloy Actuators: Performance Assessment and Introduction of a New Composing approach,” S. Hirose, K. Ikuta and K. Sato, *Advanced Robotics*, Vol. 3, pp. 3–16.

[Hollerbach, Hunter and Ballantyne 91] “A Comparative Analysis of Actuator Technologies for Robotics,” John M. Hollerbach, Ian W. Hunter and John Ballantyne, *In Robotics Review 2*, MIT Press, Edited by Khatib, Craig and Lozano-Perez.

[Hosoe 89] “An Ultrasonic Motor for Use in Autofocus Lens Assemblies,” Kazuya Hosoe, *Techno*, pp. 36-41, May, in Japanese.

[IEEE 87] “Institute of Electrical and Electronics Engineers,” 1987, *IEEE Standard on Piezoelectricity*, ANSI/IEEE Std. 176-1987.

[Inaba et al. 87] “Piezoelectric Ultrasonic Motor,” R. Inaba, A. Tokushima, O. Kawasaki, Y. Ise and H. Yoneno, *Proceedings of the IEEE Ultrasonics Symposium*, pp. 747-756.

[Jaffe 58] “IRE Standards on Piezoelectric Crystals: Measurements of Piezoelectric Ceramics, 1961,” H. Jaffe, *Proceedings of IRE*, July.

[Jaffe, Cook and Jaffe 71] “Piezoelectric Ceramics,” Bernard Jaffe, William R. Cook and Hans Jaffe, *Academic Press*, New York.

[Jacobsen et al. 89] “The Wobble Motor: An Electrostatic, Planetary Armature, Microactuator,” S.C. Jacobsen, R. H. Price, J.E. Wood, T.H. Rytting and M. Rafaelef, *Proceedings IEEE Micro Electro Mechanical Systems*, Salt Lake City, UT, February 20-22, 17-24.

[Johnson 85] “Contact Mechanics,” K.L. Johnson, *Cambridge University Press*, Great Britain.

[Kasuga et al. 92] “Development of Ultrasonic Motor and Application to Silent Alarm Analog Quartz Watch,” Masao Kasuga, Takashi Satoh, Jun Hirotsu and Masayuki Kawata, *4th Congress European de Chronometrie*, Lausanne, Switzerland, 29–30 October, pp. 53–56.

[Kawasaki, Nishikura, Imasaka, Sumihara, Takeda and Yoneno 87] “Ultrasonic Motors,” Osamu Kawasaki, Takahiro Nishikura, Yoshinobu Imasaka, Masanori Sumihara, Katsu Takeda and Hiroshi Yoneno, *Denshi Tokyo*, No. 26.

[Keisewetter 88] “The Application of Terfenol in Linear Motors,” L. Keisewetter, *Proceedings of the Second International Conference on Giant Magnetostrictive and Amorphous Alloys for Sensors and Applications*, pp. 1-18.

[Kobriniskii and Lennox-Napier 69] “Dynamics of Mechanisms with Elastic Connections and Impact Systems,” A.E. Kobriniskii and R. Lennox-Napier, *Illiffe Books, Ltd.*, London.

[Kumada 85] “A Piezoelectric Ultrasonic Motor,” Akio Kumada, *Japanese Journal of Applied Physics*, Vol. 24. Supplement 24-2, pp. 739-741.

[Kumada 90] “Piezoelectric Revolving Motors Applicable For Future Purpose,” Akio Kumada, *Seventh International Symposium on Applications of Ferroelectrics*, Urbana-Champaign, Illinois, June 6-8.

[Kumada 91] “The Motor Stone – An Ideal Ultrasonic Motor,” Akio Kumada, *Proceedings of the 1991 Japanese Materials Research Society Solid State Actuator Symposium*, Kanagawa Science Park, Kanagawa, Japan, December 13–14.

[Kurosawa and Ueha 88] “Efficiency of Ultrasonic Motor Using Traveling Wave,” M. Kurosawa and S. Ueha, *Journal of the Acoustic Society of Japan*, Vol. 44, No. 1, pp. 40–46, in Japanese.

[Lanczos 70] “The Variational Principles of Mechanics,” Cornelius Lanczos, *University of Toronto Press*, Toronto, Canada.

[Linker and Dieterich 92] “Effects of Variable Normal Stress on Rock Friction: Observations and Constitutive Equations,” M.F. Linker and J.H. Dieterich, *Journal of Geophysical Research*, April.

[Lucas 75] “Transformation of Energy in Piezoelectric Drive Systems,” I. Lucas, *Siemens Forsch. u. Entwickl. Ber.*, Bd. 4 Nr. 6.

[Mabuchi 92] “Mabuchi Heavy Duty Series Motor Catalog,” Mabuchi Motor America Corp., 475 Park Ave. (32 St.), New York, NY 10016.

[Maeno, Tsukimoto and Miyake 90] “Finite-Element Analysis of the Rotor/Stator Contact in a Ring-Type Ultrasonic Motor,” Takashi Maeno, Takayuki Tsukimoto and Akira Miyake, *IEEE Transactions on Ultrasonics, Ferroelectrics, and Frequency Control*, Vol. 39, No. 6, November, pp. 668–674.

[Maeno and Bogy 92] “Effect of the Hydrodynamic Bearing on Rotor/Stator Contact in a Ring-Type Ultrasonic Motor,” Takashi Maeno and David B. Bogy, *IEEE Transactions on Ultrasonics, Ferroelectrics, and Frequency Control*, Vol. 39, No. 6, November, pp. 675–682.

[Maes and Brooks 90] “Learning to Coordinate Behaviors,” Pattie Maes and Rodney A. Brooks, *Proceedings of the 1990 American Association of Artificial Intelligence Conference*, August.

[Mataric 90] “Environment Learning Using a Distributed Representation,” Maja J Mataric, *Proceedings of the IEEE Robotics and Automation Conference*, Cincinnati, Ohio, May.

[Mehregany et al. 90] "Principles in Design and Microfabrication of Variable-capacitance Side-drive Motors," M. Mehregany, S.F. Bart, L.S. Tavrow, J.H. Lang and S.D. Senturia, *Journal of Vacuum Science Technology*, Vol. A8, No. 4, pp. 3614-3624, July-August.

[Micro Mo 93] "Micro Mo Miniature Drive Systems Catalog," Micro Mo Corp., *742 2nd Ave. South*, St. Petersburg, FL, 33701.

[Minotti and Lallement 93] "Theoretical Modelization of Rotary Traveling Wave Piezoelectric Motors," P. Minotti and G. Lallement, *Laboratoire de Mecanique Appliquee*, Route de Gray - La Bouloie 25030 Besancon, France, CEDEX, in French.

[Montgomery 91] "Design and Analysis of Experiments," Douglas C. Montgomery, *3rd Edition*, .

[Moroney et al. 89] "Ultrasonic Micromotors," R.M. Moroney, R.M. White and R.T. Howe, *IEEE Ultrasonics Symposium*, Montreal, Canada, October.

[Namiki 92] "Namiki DC Micro Motors Catalog," Namiki Precision Jewel Co., Ltd., *U.S. Office: 15 Warren St., Hackensack, NJ 07601*, (201) 343-3080.

[Nashif et al. 85] "Vibration Damping," Ahid D. Nashif, David I. G. Jones and John P. Henderson, *John Wiley & Sons*, New York.

[Oberg et al. 88] "Machinery's Handbook," Erik Oberg, Franklin D. Jones, Holbrook L. Horton and Henry H. Ryffel, *23rd edition*, Industrial Press, New York.

[Okumura and Mukohjima 87] "A Structure of Ultrasonic Motor for Auto Focus Lenses," I. Okumura and H. Mukohjima, *Proceedings of Motor Control*, September.

[Ostergaard 89] "ANSYS Coupled Field Analysis 4.4 Tutorial," Dale F. Ostergaard, *Swanson Analysis Systems*, Houston, PA.

[Nye 85] "Physical Properties of Crystals," J.F. Nye, *Oxford University Press*, Oxford.

[Pan and Cross 89] "A Sensitive Double Beam Laser Interferometer for Studying High-Frequency Piezoelectric and Electrostrictive Strains," W.Y. Pan and L.E. Cross, *Review of Scientific Instruments*, *60 (8)*, August.

[Panasonic 87] "Ultrasonic Motor," Panasonic Technical Reference, *Panasonic Industrial Co., Division of Matsushita Electric Corp. of America*, 1 Panasonic Way, Secaucus, NJ.

[Piezo Systems 85] "Piezo Design Aid," Piezo Systems, Inc., *Cambridge, MA*, 02139.

[Piezo Systems 95] "Piezo Systems Product Guide," Piezo Systems, Inc., *Cambridge, MA*, 02139.

[Ragulskis et al. 88] "Vibromotors for Precision Microrobots," K. Ragulskis, R. Bansevicius,

- R. Barauskas and G. Kulvietis, *Hemisphere Publishing Co.*, New York.
- [Ramtron 88] “Nonvolatile Ferroelectric Technology and Products,” Ramtron Corp., *Technical Report*, Colorado Springs, CO.
- [Rayleigh 1894] “The Theory of Sound,” John William Strutt, Baron Rayleigh, *MacMillan and Company*, New York.
- [Rehbein and Heinz 92] “Personal communication,” Tribology Group, Dept. ZWM, *Robert Bosch Co.*, Schillerhohe, Germany.
- [Rogers, Liang and Jia 89] “Behavior of Shape Memory Alloy Reinforced Composite Plates: Part I: Model Formulations and Control Concepts,” C. A. Rogers, C. Liang and J. Jia, *1989 AIAA Structures, Structural Dynamics and Materials Conference*, AIAA paper #89, 1389 cp.
- [Rymuza 89] “Tribology of Miniature Systems,” Zygmunt Rymuza, *Elsevier Science Publishers*, Amsterdam, The Netherlands.
- [Sashida 82] “Trial Construction and Operation of an Ultrasonic Vibration Drive Motor: Theoretical and Experimental Investigation of its Performances,” T. Sashida, *Oyo Butsuri*, Vol. 51, No. 6, pp. 713-720, in Japanese.
- [Sashida 83] “Approach to Development of an Ultrasonic Motor with Low-Speed, High-Torque Characteristics,” Toshio Sashida, *Mechanical Automation*, Vol. 15, No. 12, pp. 31-35, in Japanese.
- [Sashida 85] “Ultrasonic Motors,” Toshiiku Sashida, *Japanese Journal of Applied Physics*, Volume 54, No. 6, pp. 589 (65) - 590 (66), in Japanese.
- [Sashida 86] “Traveling Wave Ultrasonic Motors,” Toshiiku Sashida, *Ultrasonic Motors and Actuators*, Edited by Akiyama, Chapter 4, Trikepps, in Japanese.
- [Sashida and Kenjo 93] “Introduction to Ultrasonic Motors,” Toshiiku Sashida and Takashi Kenjo, *Oxford University Press*, Oxford, UK.
- [Schadebrodt and Salomon 90] “The Piezo Traveling Wave Motor, a New Element in Actuation,” G. Schadebrodt and B. Salomon, *PCIM*, July.
- [Shinsei 89] “Operation Manual for the Ultrasonic Motor,” Shinsei Corporation, *1-8, Kasuya 2-chome, Setagaya-ku, Tokyo, 157 Japan, in Japanese*, FAX: +81 3 329-0066.
- [Slobodnik, Conway and Delmonico 73] “Microwave Acoustics Handbook – Vol. 1A, Surface Wave Velocities,” A.J. Slobodnik, Jr., E.D. Conway, R.T. Delmonico, eds., *Air Force Cambridge Research Laboratories, LG. Hanscom Field*, Bedford, Massachusetts.
- [Smits and Choi 92] “The Effectiveness of a Piezoelectric Heterogeneous Bimorph to Perform

Mechanical Work Under Various Load Conditions,” Jan G. Smits and Wai-shing Choi, *Ferroelectrics*, Vol. 135, pp. 447–459.

[Staelin, Morgenthaler and Kong 94] “Electromagnetic Waves,” David H. Staelin, Ann W. Morgenthaler and Jin Au Kong, *Prentice Hall*, Englewood Cliffs, NJ.

[Suh 86] “Tribophysics,” Nam P. Suh, *Prentice-Hall, Inc.*, Englewood Cliffs, NJ.

[Takeda, Sumihara, Nishikura, Kawasaki and Yoneno 88] “The Design Method of a Vibrating Stator of a Disc Ultrasonic Motor,” Katsu Takeda, Masanori Sumihara, Takahiro Nishikura, Osamu Kawasaki and Hiroshi Yoneno, *Proceedings of the Association of Electronic Information Communication*, p. 43, US88-54, in Japanese.

[Tai, Fan and Muller 89] “IC-Processed Micro-Motors: Design, Technology and Testing,” Yu-Chong Tai, Long-Sheng Fan and Richard S. Muller, *Proceedings of the IEEE Micro Electro Mechanical Systems*, Salt Lake City, UT, February 20-22, 1-6.

[Tavrow 91] “A LOCOS-Based Microfabricated Radial-Gap Electric Motor,” Lee S. Tavrow, *MIT Ph.D thesis in Electrical Engineering and Computer Science*, February.

[Tiersten 67] “Hamilton’s Principle for Linear Piezoelectric Media,” H.F. Tiersten, *Proc. IEEE*, Vol. 55, pp. 1523-1524.

[Tiersten 69] “Linear Piezoelectric Plate Vibrations,” H.F. Tiersten, *Plenum Press*, New York.

[Timoshenko and Goodier 87] “Theory of Elasticity, Third Edition Reissue,” S.P. Timoshenko and J.N. Goodier, *McGraw-Hill*, New York.

[Tomikawa, Kondo, Ogasawara, Sugawara and Konno 87] “Fundamental Considerations of Excitation of a Flexural Progressive Wave and its Application,” Yoshiro Tomikawa, Tetsuya Kondo, Toshiharu Ogasawara, Sumio Sugawara and Masashi Konno, *Japanese Journal of Applied Physics*, Vol. 26, Suppl. 26-1, pp. 194-196.

[Tomikawa, Ogasawara and Takano 89] “Ultrasonic Motors - Constructions, Characteristics, Applications,” Y. Tomikawa, T. Ogasawara and T. Takano, *Ferroelectrics*, Vol. 91, pp. 163-178.

[Trimmer and Jebens 89] “An Operational Harmonic Electrostatic Motor,” W. Trimmer and R. Jebens, *Proceedings IEEE Micro Electro Mechanical Systems*, Salt Lake City, UT, February 20-22, 13-16.

[Udayakumar et al. 95] “Ferroelectric Thin Films Piezoelectric Micromotors,” K.R. Udayakumar, S.F. Bart, A.M. Flynn, J. Chen, L.S. Tavrow, L.E. Cross, R.A. Brooks and D.J. Ehrlich, *Ferroelectrics*, Vol. 160, pp. 347-356.

[Udayakumar 93] “Piezoelectric Thin Films for Electronic Applications,” K.R. Udayakumar,

Pennsylvania State University PhD Thesis in Solid State Science, January.

[Ueha 89] “Present State of the Art of Ultrasonic Motors,” Sadayuki Ueha, *Japanese Journal of Applied Physics*, Vol. 28, Suppl. 28-1, pp. 3-6.

[Ueha and Tomikawa 93] “Ultrasonic Motors: Theory and Applications,” S. Ueha and Y. Tomikawa, *Oxford University Press*, Oxford, UK.

[Vishnevsky et al. 77] “Piezoelectric Motor Structures,” Vladimir Vishnevsky, Vladimir Kavertsev, Igor Kartashev, Vyacheslav Lavrinenko, Mikhail Nekrasov and Alexei Prez, *U.S. Patent 4,019,073*, April 19.

[Vogel and Skinner 65] “Natural Frequencies of Transversely Vibrating Uniform Annular Plates,” S.M. Vogel and D.W. Skinner, *Journal of Applied Mechanics*, December, pp. 926-931.

[Young 89] “Roark’s Formulas for Stress and Strain,” Warren C. Young, *McGraw Hill*, New York.

[Zemella 90] “Design and Development of a Linear Travelling Wave Motor,” Ricardo J. Zemella, *MIT Master’s Thesis in Aeronautics and Astronautics*, May.

[Zhang, Pan and Cross 88] “Laser Interferometer for the Study of Piezoelectric and Electrostrictive Strains,” Q.M. Zhang, W.Y. Pan and L.E. Cross, *Journal of Applied Physics*, 2492-96.

Appendix A

Stator Motion

[Inaba et al. 87] described elliptical motion on the surface of a beam due to a traveling wave as illustrated in Figure 3-4, where one solution to the beam equation is the sum of two standing wave oscillations offset by $\frac{\lambda}{4}$ in space and time:

$$w(x, t) = w_o(\sin kx \sin \omega t + \cos kx \cos \omega t)$$

which is simply the equation of a wave traveling along the neutral axis,

$$w(x, t) = w_o \cos(kx - \omega t)$$

For a beam of half-thickness h , however, the displacement of a point on the surface moving from P to P_o has a horizontal displacement ζ_a and a vertical displacement ξ_a :

$$\xi_a = -(h - h \cos \theta) + w_o \sin kx \sin \omega t$$

$$\zeta_a = -h \sin \theta$$

To solve for θ , we note that the slope of the normal to the neutral axis is the negative reciprocal of the slope of the tangent to the neutral axis at that point.

$$\tan\left(\frac{\pi}{2} + \theta\right) = -\frac{1}{\frac{dw}{dx}}$$

$$-\frac{1}{\tan \theta} = -\frac{1}{\frac{dw}{dx}}$$

$$\text{Flexing Beam } \frac{\partial^4 w(x, t)}{\partial x^4} + \frac{\rho A}{EI} \frac{\partial^2 w(x, t)}{\partial t^2} = 0$$

$$\text{Traveling Wave Solution } w(x, t) = w_o \cos(kx - \omega t)$$

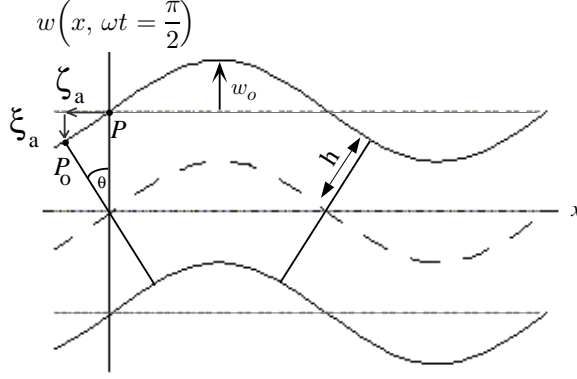


Figure A-1: (a) For a beam in flexure, a traveling wave is one solution to the beam equation. A vibration of amplitude w_o will cause a point on the surface to displace from P to P_o .

For small deformations, θ is small and

$$\sin \theta \cong \theta$$

$$\cos \theta \cong 1$$

Therefore $\frac{1}{\theta} \cong \frac{1}{\frac{dw}{dx}}$ or we can say,

$$\theta = \frac{dw}{dx} = w_o k \cos kx \sin \omega t$$

$$\xi_a = w_o \sin kx \sin \omega t$$

$$\zeta_a = -h\theta = -hw_o k \cos kx \sin \omega t$$

If a second standing wave is induced which is spatially and temporally 90 degrees out of phase from the first, the displacements will be:

$$\xi_b = w_o \sin(kx + \frac{\pi}{2}) \sin(\omega t + \frac{\pi}{2}) = w_o \cos kx \cos \omega t$$

$$\zeta_b = -hk w_o \cos(kx + \frac{\pi}{2}) \sin(\omega t + \frac{\pi}{2}) = -hk w_o \sin kx \cos \omega t$$

Superimposing these two waves gives the displacements due to traveling waves:

$$\xi = \xi_a + \xi_b = w_o(\sin kx \sin \omega t + \cos kx \cos \omega t)$$

$$\zeta = \zeta_a + \zeta_b = hkw_o(\cos kx \sin \omega t - \sin kx \cos \omega t)$$

From the trigonometric identities,

$$\cos(\alpha - \beta) = \cos \alpha \cos \beta + \sin \alpha \sin \beta$$

$$\sin(\alpha - \beta) = \sin \alpha \cos \beta - \cos \alpha \sin \beta$$

we see that traveling waves result, with:

$$\xi = w_o \cos(kx - \omega t)$$

$$\zeta = hkw_o \sin(kx - \omega t) = \frac{2\pi hw_o}{\lambda} \sin(kx - \omega t)$$

The relationship between the transverse and longitudinal displacements of a point on the surface can be seen to be elliptical if we square and add ξ and ζ :

$$1 = \sin^2(kx - \omega t) + \cos^2(kx - \omega t) = \frac{\zeta^2}{\left(\frac{2\pi hw_o}{\lambda}\right)^2} + \frac{\xi^2}{w_o^2}$$

Appendix B

Variational Methods in Modeling Active Structures

Closed-form solutions cannot be formulated for the majority of structural systems which include active, or electromechanically coupled materials. For systems which exhibit complex geometry, boundary conditions and load configurations, approximation techniques based on energy methods and variational principles are employed. This appendix gives background for modeling active structures using variational methods such as Rayleigh-Ritz assumed-mode solution techniques.

The aerospace community has a long history of using sophisticated analysis tools for modeling complex structures, such as composite load-bearing members which must be lightweight yet strong and subject to a wide range of forcing conditions, from mechanical to aerodynamic in origin. Active control of such structures is often employed to increase rigidity, dampen vibration or steer precision optical components. Recently, incorporation of active materials such as piezoelectrics, electrostrictors, magnetostrictors and shape-memory alloys into controlled structures has been a prolific area of research as a route to further reduce system size and weight by alleviating the need for discrete actuation mechanisms and linkages.

Much of this recent work has helped to bridge the gap between the materials science and aerospace communities by developing engineering models of complex electromechanically coupled materials which can be used in the analysis tools employed for the design of active structures [Crawley and De Luis 87], [Crawley and Anderson 90] and [Rogers, Liang and

Jia 89]. While the aerospace devices being modeled are often large-scale structures such as space-station truss elements, heavy-lift launch vehicles, satellite optical systems or twistable helicopter rotor blades, many of the analysis techniques can be extended to the new field of microelectromechanical systems where the active materials may be thin films deposited directly onto silicon, the interest here.

The remainder of this appendix gives background, fills in details, and equates notation from three papers which use these Rayleigh-Ritz methods to model piezoelectric structural elements such as static and dynamic beams and plates, [Hagood, Chung and Von Flutow 90] and [Crawley and Lazarus 91], and more recently, ultrasonic motors [Hagood and McFarland 95]. At the end of this section we show a simulation of the latter model for the 8 mm ultrasonic motors characterized in this thesis work. It is hoped that this exposition will be helpful to the microelectromechanical systems community for modeling active materials incorporated into microstructures.

B.1 Hamilton's Principle

Hamilton's Principle is the starting point from which the dynamic equations of motion are formed in [Hagood, Chung and Von Flutow 90]. The use of Hamilton's Principle in modeling piezoelectric plates is also discussed in [Tiersten 67] and [Tiersten 69]. Hamilton's Principle states that a system will evolve along a trajectory in such a manner as to minimize the action, where the action is defined as an integral over time of a variational indicator of the system. The deflections of the static system in [Crawley and Lazarus 91] are derived in a similar manner, but from the Principle of Minimum Potential Energy, which simply states that the variation of the variational indicator is zero. In a dynamic system, the action is minimized if the variation of the action is equal to zero:

$$\delta \int_{t_1}^{t_2} (V.I.) dt = 0$$

Figure B-1 illustrates the variation of a function. [Lanczos 70] describes the calculus of variations and its relationship to mechanical systems in which infinitesimal displacements and virtual work processes are applied. We assume here linear variations of a function $f(x)$

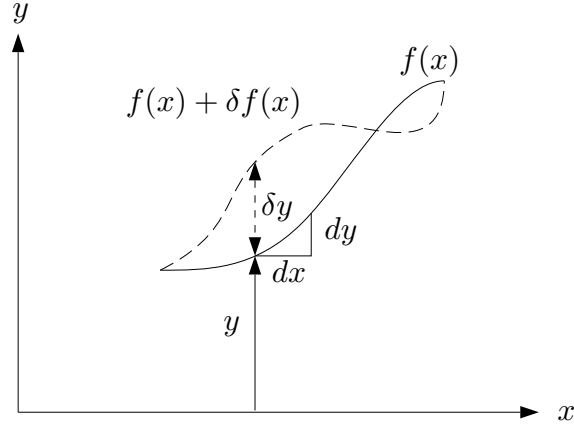


Figure B-1: A variation of a function is related to its dependent variable by $\delta f = \frac{\partial f}{\partial x} \delta x$.

by a function $\phi(x)$ such that the variation of $f(x)$ is:

$$\delta f(x) = \epsilon \phi(x)$$

where ϵ is infinitesimally small and the variation at the endpoints of the path are zero:

$$\delta f(x)_{x=a} = \delta f(x)_{x=b} = 0$$

A variation of a function is related to its dependent variables by the chain rule:

$$\delta f = \frac{\partial f}{\partial x_1} \delta x_1 + \frac{\partial f}{\partial x_2} \delta x_2 + \dots + \frac{\partial f}{\partial x_n} \delta x_n$$

The technique of applying an arbitrary variation in position to determine the virtual change in potential energy (a function of position) is the step which allows the equations of motion to be extracted from an accounting of energy.

The particular form of the variational indicator chosen by [Hagood, Chung and Von Flutow 90] for inclusion into Hamilton's Principle specifies stress and electric field as the independent variables. Stress and electric field are typically the control parameters available in driving active structures in actuator configurations. The interaction of these mechanical and electrical field variables is derived from thermodynamics.

The first law of thermodynamics states that heat added or work done on a system

increases the total internal stored energy density of the system:

$$dU^{tot} = dQ + dW$$

where U^{tot} is the total internal energy density, Q is the heat per volume added and W is the work per volume acting on the system. Assuming a linear electro-elastic-thermal system, the change in total internal energy density due to infinitesimal changes in strain and electric displacement in the presence of uniform stress and electric field, becomes:

$$dU^{tot} = \theta d\sigma + T_{ij}dS_{ij} + E_k dD_k$$

where θ is temperature, σ is entropy, T_{ij} is a component of the stress tensor as defined in Figure B-2, S_{ij} is a component of the strain tensor as illustrated in Figure B-3, E_k is a component of the electric field vector and D_k is a component of the electric displacement vector.

Legendre transformations can be applied to the energy expression to switch the independent variables from (S,D) to (S,E) [Nye 85]. The Electric Gibb's Free Energy expression is one such transformation and is defined as:

$$G = U^{tot} - \theta\sigma - E_k D_k$$

where

$$dG = dU^{tot} - d(\theta\sigma) - d(E_k D_k)$$

and

$$dG(\theta, S, E) = -\sigma d\theta + T_{ij}dS_{ij} - D_k dE_k$$

By noting that:

$$dG(\theta, S, E) = \frac{\partial G}{\partial \theta} d\theta + \frac{\partial G}{\partial S} dS + \frac{\partial G}{\partial E} dE$$

we find the relationships between the dependent variables and G :

$$\sigma = - \left(\frac{\partial G}{\partial \theta} \right)_{T,E} \quad T_{ij} = \left(\frac{\partial G}{\partial S_{ij}} \right)_{\theta,E} \quad D_k = - \left(\frac{\partial G}{\partial E_k} \right)_{\theta,T}$$

where the subscripts signify variables that are held constant. Expanding the change in

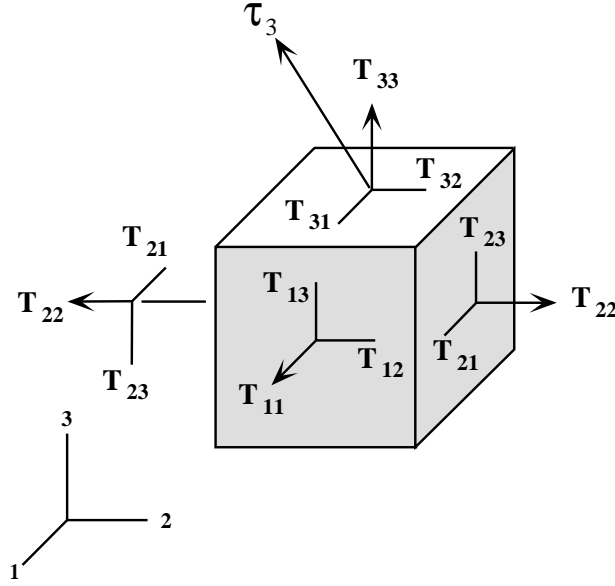


Figure B-2: A force per unit area applied to any given face of a cube (a traction vector) has stress components in three directions. The stress tensor is a 3×3 matrix of components T_{ij} and is symmetric. The six independent components can then be written in reduced matrix notation as a 1×6 vector.

dependent variables as:

$$dT(\theta, S, E) = \frac{\partial T}{\partial \theta} d\theta + \frac{\partial T}{\partial S} dS + \frac{\partial T}{\partial E} dE$$

$$dD(\theta, S, E) = \frac{\partial D}{\partial \theta} d\theta + \frac{\partial D}{\partial S} dS + \frac{\partial D}{\partial E} dE$$

and assuming isothermal conditions, gives the constitutive relation coefficients for the linearly electromechanically coupled piezoelectric system:

$$c_{ijkl}^{E,\theta} = \left(\frac{\partial T_{ij}}{\partial S_{kl}} \right)_{E,\theta} = \left(\frac{\partial^2 G}{\partial S_{ij} \partial S_{kl}} \right)_{E,\theta}$$

$$e_{ijk}^{T,\theta} = \left(\frac{\partial D_k}{\partial S_{ij}} \right)_{T,\theta} = - \left(\frac{\partial^2 G}{\partial S_{ij} \partial E_k} \right)_{T,\theta}$$

$$\epsilon_{kl}^{T,\theta} = \left(\frac{\partial D_k}{\partial E_l} \right)_{T,\theta} = - \left(\frac{\partial^2 G}{\partial E_k \partial E_l} \right)_{T,\theta}$$

where $c_{ijkl}^{E,\theta}$ is the stiffness tensor at constant electric field and temperature, $e_{ijk}^{T,\theta}$ is the piezoelectric stress tensor at constant stress and temperature and $\epsilon_{kl}^{T,\theta}$ is the dielectric permittivity tensor at constant stress and temperature.

Because the stress tensor is symmetric:

$$\begin{bmatrix} T_{11} & T_{12} & T_{13} \\ T_{21} & T_{22} & T_{23} \\ T_{31} & T_{32} & T_{33} \end{bmatrix} = \begin{bmatrix} T_1 & T_6 & T_5 \\ T_6 & T_2 & T_4 \\ T_5 & T_4 & T_3 \end{bmatrix}$$

we can write T in a reduced matrix form:

$$\mathbf{T} = \begin{bmatrix} T_1 \\ T_2 \\ T_3 \\ T_4 \\ T_5 \\ T_6 \end{bmatrix} = \begin{bmatrix} T_{11} \\ T_{22} \\ T_{33} \\ T_{23} \\ T_{31} \\ T_{21} \end{bmatrix} = \begin{bmatrix} \sigma_x \\ \sigma_y \\ \sigma_z \\ \tau_{yz} \\ \tau_{zx} \\ \tau_{xy} \end{bmatrix}$$

where σ, τ is traditional notation in uncoupled systems for normal and shear stresses and is used in [Crawley and Lazarus 91]. The strain tensor is also symmetric and can similarly be written in reduced matrix notation:

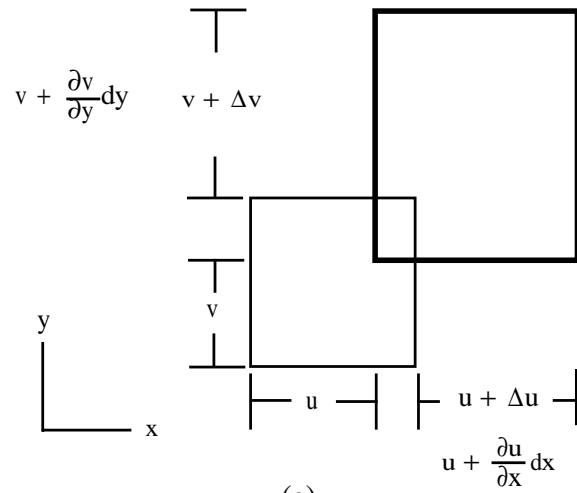
$$\mathbf{S} = \begin{bmatrix} S_{xx} & 2S_{xy} & 2S_{xz} \\ 2S_{xy} & S_{yy} & 2S_{yz} \\ 2S_{xz} & 2S_{yz} & S_{zz} \end{bmatrix} = \begin{bmatrix} S_1 & S_6 & S_5 \\ S_6 & S_2 & S_4 \\ S_5 & S_4 & S_3 \end{bmatrix}$$

The strain-displacement relations are defined in cartesian coordinates in Figure B-3 and given as:

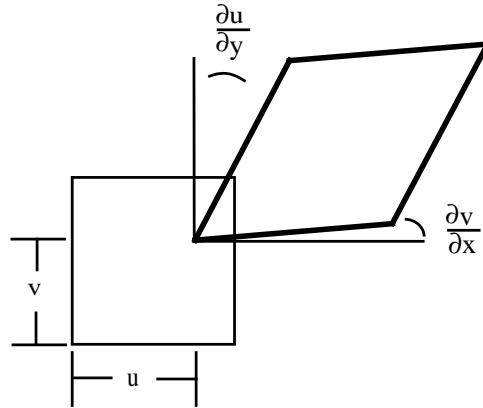
$$\mathbf{S} = \begin{bmatrix} S_1 \\ S_2 \\ S_3 \\ S_4 \\ S_5 \\ S_6 \end{bmatrix} = \begin{bmatrix} S_{11} \\ S_{22} \\ S_{33} \\ 2S_{23} \\ 2S_{31} \\ 2S_{21} \end{bmatrix} = \begin{bmatrix} \epsilon_x \\ \epsilon_y \\ \epsilon_z \\ \gamma_{yz} \\ \gamma_{zx} \\ \gamma_{xy} \end{bmatrix} = \begin{bmatrix} \frac{\partial u}{\partial x} \\ \frac{\partial v}{\partial y} \\ \frac{\partial w}{\partial z} \\ \frac{\partial w}{\partial y} + \frac{\partial v}{\partial z} \\ \frac{\partial w}{\partial x} + \frac{\partial u}{\partial z} \\ \frac{\partial u}{\partial y} + \frac{\partial v}{\partial x} \end{bmatrix}$$

where ϵ, γ is engineering notation for normal and shear strains, also used in [Crawley and Lazarus 91]. Assuming isothermal conditions, the piezoelectric constitutive relations can now be written in compact form [IEEE 87]:

$$\begin{bmatrix} \mathbf{T} \\ \mathbf{D} \end{bmatrix} = \begin{bmatrix} \mathbf{c}^E & -\mathbf{e}_t \\ \mathbf{e} & \epsilon^T \end{bmatrix} \begin{bmatrix} \mathbf{S} \\ \mathbf{E} \end{bmatrix}$$



(a)



(b)

Figure B-3: (a) Strain produced by positive normal stresses. (b) Strain produced by positive shear stresses.

where the stiffness tensor at constant electric field, \mathbf{c}^E , becomes a 6×6 matrix in reduced form, the piezoelectric stress tensor transposed, \mathbf{e}_t , becomes a 3×6 matrix and the permittivity tensor at constant stress, ϵ^T , remains 3×3 :

$$\begin{bmatrix} T_1 \\ T_2 \\ T_3 \\ T_4 \\ T_5 \\ T_6 \end{bmatrix} = \mathbf{c}^E \begin{bmatrix} S_1 \\ S_2 \\ S_3 \\ S_4 \\ S_5 \\ S_6 \end{bmatrix} - \mathbf{e}_t \begin{bmatrix} E_1 \\ E_2 \\ E_3 \end{bmatrix}$$

$$\begin{bmatrix} D_1 \\ D_2 \\ D_3 \end{bmatrix} = \mathbf{e} \begin{bmatrix} S_1 \\ S_2 \\ S_3 \\ S_4 \\ S_5 \\ S_6 \end{bmatrix} + \epsilon^T \begin{bmatrix} E_1 \\ E_2 \\ E_3 \end{bmatrix}$$

For PZT, the material coefficient matrices take the following form:

$$\mathbf{c}_{PZT}^E = \begin{bmatrix} c_{11}^E & c_{12}^E & c_{13}^E & 0 & 0 & 0 \\ c_{12}^E & c_{11}^E & c_{13}^E & 0 & 0 & 0 \\ c_{13}^E & c_{13}^E & c_{33}^E & 0 & 0 & 0 \\ 0 & 0 & 0 & c_{44}^E & 0 & 0 \\ 0 & 0 & 0 & 0 & c_{55}^E & 0 \\ 0 & 0 & 0 & 0 & 0 & 2(c_{11}^E - c_{12}^E) \end{bmatrix}$$

$$\epsilon_{PZT}^T = \begin{bmatrix} \epsilon_{11}^T & 0 & 0 \\ 0 & \epsilon_{11}^T & 0 \\ 0 & 0 & \epsilon_{33}^T \end{bmatrix}$$

$$\mathbf{e}_{PZZT_t} = \begin{bmatrix} 0 & 0 & e_{13} \\ 0 & 0 & e_{13} \\ 0 & 0 & e_{33} \\ 0 & e_{15} & 0 \\ e_{15} & 0 & 0 \\ 0 & 0 & 0 \end{bmatrix}$$

Alternate Legendre transformations of the energy expression can be used to state the constitutive relations in terms of other combinations of independent variables, such as (T,E) [Jaffe, Cook and Jaffe 71]:

$$\begin{bmatrix} \mathbf{S} \\ \mathbf{D} \end{bmatrix} = \begin{bmatrix} \mathbf{s}^E & +\mathbf{d}_t \\ \mathbf{d} & \epsilon^S \end{bmatrix} \begin{bmatrix} \mathbf{T} \\ \mathbf{E} \end{bmatrix}$$

where \mathbf{d} is the piezoelectric strain matrix, \mathbf{s}^E is the compliance matrix at constant electric field and ϵ^S is the dielectric permittivity matrix at constant strain. The compliance matrix is related to the stiffness matrix by:

$$\mathbf{c}^E = (\mathbf{s}^E)^{-1}$$

The piezoelectric strain matrix is related to the piezoelectric stress matrix by:

$$\mathbf{e} = \mathbf{d} (\mathbf{s}^E)^{-1}$$

and the constant strain and constant stress permittivity matrices are related by:

$$\epsilon^S = \epsilon^T - \mathbf{d} (\mathbf{s}^E)^{-1}$$

With the constitutive equations defined, we return to the formulation of the variational indicator used in Hamilton's Principle. In matrix notation and under isothermal conditions, the change in the Electric Gibb's Free Energy, where G' is in units of energy rather than energy density, is:

$$dG'(\mathbf{S}, \mathbf{E}) = \int_V (\mathbf{T} \cdot d\mathbf{S} - \mathbf{D} \cdot d\mathbf{E}) dV$$

We take:

$$dU = \int_V \mathbf{T} \cdot d\mathbf{S}dV \quad dW_{elec} = \int_V \mathbf{D} \cdot d\mathbf{E}dV$$

Integrating, we find expressions for U and W_{elec} :

$$U = \int_V \frac{1}{2} \mathbf{S}^T \mathbf{T} dV \quad W_{elec} = \int_V \frac{1}{2} \mathbf{D}^T \mathbf{E} dV$$

We can then set up an energy expression:

$$U - W_{elec} = W_{mech}$$

where U is the stored mechanical energy of the system, W_{mech} is the work of mechanical origin done on the system and W_{elec} is the work of electrical origin done on the system:

The work of mechanical origin, W_{mech} , includes components involving accelerations. Rearranging so as to separate out this kinetic energy term, T_{kin} , we can define:

$$W_{mech} = T_{kin} + W$$

where W is the work of mechanical origin not involving accelerations. Substituting the resulting variational principle back into Hamilton's Equation, we find:

$$\delta \int_{t_1}^{t_2} (T_{kin} - U + W_{elec} + W) = 0$$

which is the form of Hamilton's Principle used in Equation (1) of [Hagood, Chung and Von Flutow 90]

B.2 Laminated Plate Dynamics

[Hagood, Chung and Von Flutow 90] continues by considering the dynamic excitation of a beam structure. Here, we show the derivation of the dynamic equations of motion of a laminated plate from Hamilton's Principle using Rayleigh-Ritz assumed modes and the consistent plate hypothesis of [Crawley and Lazarus 91], and correlate the notation therein to that of [Hagood, Chung and Von Flutow 90]. We also describe an implementation of the model in both rectangular and cylindrical coordinates [Hagood and McFarland 95] and show deformation predictions of microstructures.

Hamilton's Principle can be used with specific geometries, materials and loads to find the equations of motion of a structure. The constitutive equations and external work terms are substituted into the energy expressions and assumed forms of the deformation shapes can be used to approximate the solutions.

For the thin plate shown in Figure B-4(a), plane-stress assumptions can be made which leave only the T_1 , T_2 and T_6 terms in the constitutive equations. By setting T_3 , T_4 and T_5 to zero in:

$$\begin{bmatrix} \mathbf{S} \\ \mathbf{D} \end{bmatrix} = \begin{bmatrix} \mathbf{s}^E & \mathbf{d}_t \\ \mathbf{d} & \epsilon^S \end{bmatrix} \begin{bmatrix} \mathbf{T} \\ \mathbf{E} \end{bmatrix}$$

and converting the resulting reduced \mathbf{s}^E , \mathbf{d} and ϵ^S matrices back into the form required in:

$$\begin{bmatrix} \mathbf{T} \\ \mathbf{D} \end{bmatrix} = \begin{bmatrix} \mathbf{c}^E & -\mathbf{e}_t \\ \mathbf{e} & \epsilon^T \end{bmatrix} \begin{bmatrix} \mathbf{S} \\ \mathbf{E} \end{bmatrix}$$

the plane-stress materials matrices can be found. The materials matrices for various layers of materials in the plate may have to be further modified if they are orthotropic and skewed with respect to the laminate axes as shown in Figure B-5. Appropriate tensor transformations must be applied to find the equivalent coefficients in the plate coordinate system. Such a transformation can make the stiffness matrix fully populated, creating the effect of an anisotropic material, the characteristic which [Crawley and Lazarus 91] use to achieve twisting of their cantilevered plate.

The strain-displacement relations for a plate can also be simplified by making approximations as illustrated in Figure B-4(b) where the Bernoulli-Euler assumption of plane sections perpendicular to the midline remaining perpendicular after bending, is shown. The displacements in the x, y and z directions become:

$$u(x, y, z) = u_o - z \frac{dw_o}{dx}$$

$$v(x, y, z) = v_o - z \frac{dw_o}{dy}$$

$$w(x, y, z) = w_o$$

where u_o , v_o and w_o are the centerline displacements in the x , y and z directions, respectively. Plugging these deformation expressions into the strain-displacement relations, the

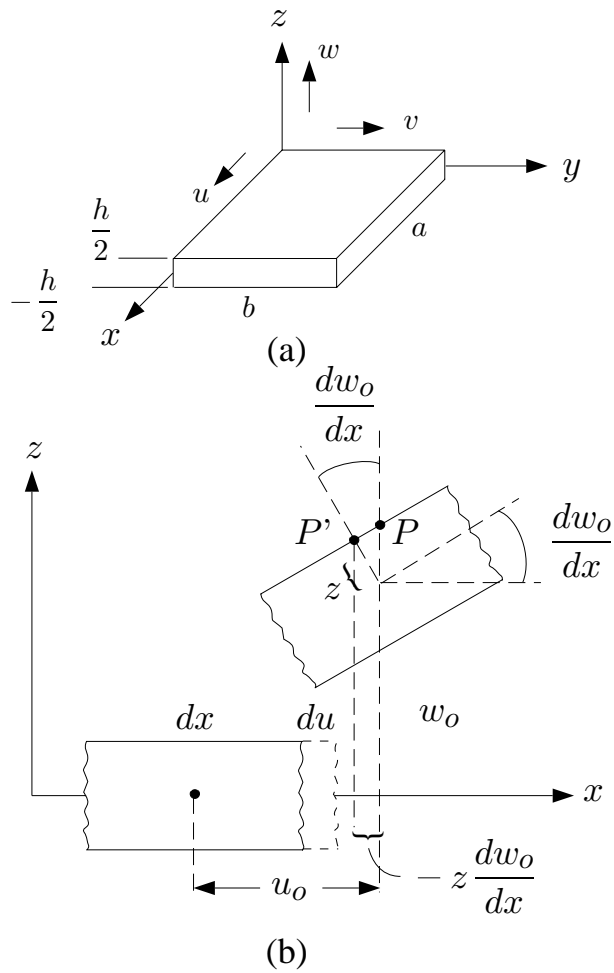


Figure B-4: (a) For a thin plate, plane stress assumptions are used, where all but the in-plane stresses are assumed negligible. (b) The strain-displacement equations are found by observing a section of the plate and assuming that perpendicular sections remain perpendicular to the midline after bending.

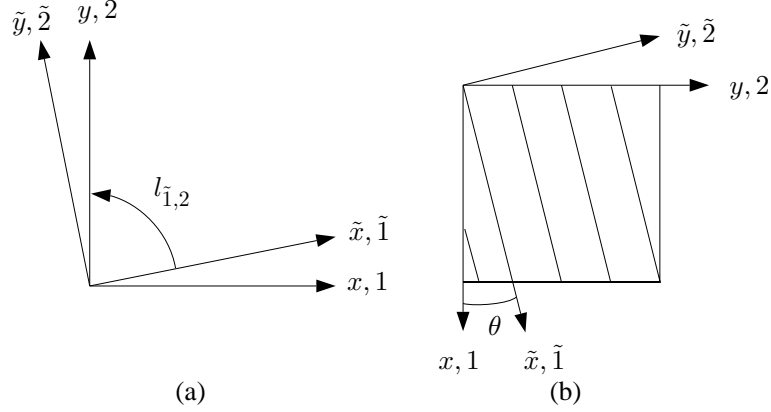


Figure B-5: (a) Definition of direction cosines, $l_{\tilde{m},n}$, for rotating material tensors. (b) An orthotropic material, such as a fiber composite, may be oriented with its principal axes skewed from the plate axes. Rotating into plate coordinates creates a fully-populated stiffness matrix, an anisotropic characteristic.

strain vector results:

$$\begin{bmatrix} S_1 \\ S_2 \\ S_6 \end{bmatrix} = \begin{bmatrix} \frac{\partial u_o}{\partial x} - z \frac{\partial^2 w_o}{\partial x^2} \\ \frac{\partial v_o}{\partial y} - z \frac{\partial^2 w_o}{\partial y^2} \\ \frac{\partial u_o}{\partial y} + \frac{\partial v_o}{\partial x} - 2z \frac{\partial^2 w_o}{\partial x \partial y} \end{bmatrix}$$

where centerline strains and z -dependent terms can be separated:

$$\mathbf{S} = \epsilon_o + z\kappa$$

Here, ϵ_o represents the vector of midplane strains and κ represents the vector of curvatures. The ϵ_o - κ vector can then be written as a differential matrix operator acting on the midplane displacements:

$$\begin{bmatrix} \epsilon_o \\ \kappa \end{bmatrix} = \begin{bmatrix} \frac{\partial}{\partial x} & 0 & 0 \\ 0 & \frac{\partial}{\partial y} & 0 \\ \frac{\partial}{\partial y} & \frac{\partial}{\partial x} & 0 \\ 0 & 0 & -\frac{\partial^2}{\partial x^2} \\ 0 & 0 & -\frac{\partial^2}{\partial y^2} \\ 0 & 0 & -2\frac{\partial^2}{\partial x \partial y} \end{bmatrix} \begin{bmatrix} u_o \\ v_o \\ w_o \end{bmatrix} = \mathbf{L}_o \psi_p(x, y) p(t)$$

where Rayleigh-Ritz assumed solutions are inserted for the centerline displacements and the differential matrix operator is defined here as \mathbf{L}_o . In [Crawley and Lazarus 91] this matrix is called \mathbf{D} but is mistyped, as transposed. [Hagood, Chung and Von Flutow 90] create a similar differential matrix operator, \mathbf{L}_u , the difference being that \mathbf{L}_u incorporates the factor

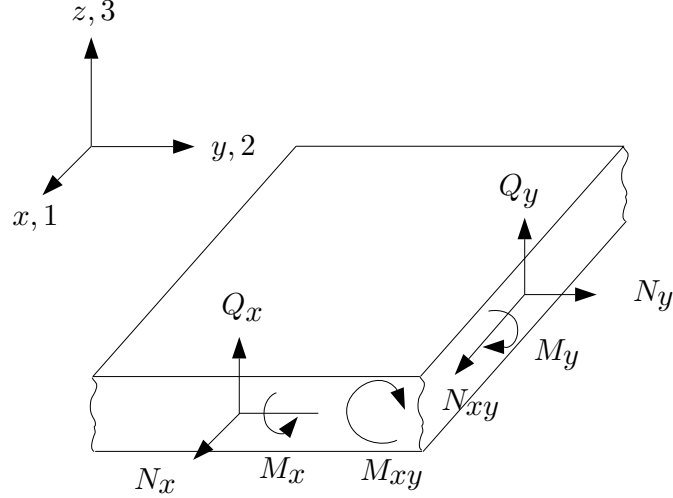


Figure B-6: Cutting the plate and integrating over an area gives the stress resultants, \mathbf{N} , \mathbf{M} and \mathbf{Q} for the deformed plate.

of z multiplying the curvature terms to produce the \mathbf{S} vector rather than the $\epsilon_0\text{-}\kappa$ vector. For a laminated plate of many layers, it is convenient to separate out the z -dependence explicitly in calculating the stress resultants.

Before proceeding to Hamilton's Principle, we note one more construction for the laminated plate problem, the stress resultants, as shown in Figure B-6. By taking a section of a plate and integrating the stresses through the thickness, the stress resultants can be found. N_x , N_y and N_{xy} are the in-plane stress resultants, M_x , M_y and M_{xy} are the moment stress resultants and Q_x and Q_y are the shear stress resultants (assumed small):

$$\begin{bmatrix} \mathbf{N} \\ \mathbf{M} \end{bmatrix} = \begin{bmatrix} N_x \\ N_y \\ N_{xy} \\ M_x \\ M_y \\ M_{xy} \end{bmatrix} = \int_{-\frac{h}{2}}^{\frac{h}{2}} \begin{bmatrix} T_1 \\ T_2 \\ T_6 \\ T_1 z \\ T_2 z \\ T_6 z \end{bmatrix} dz$$

Plugging in the constitutive relations and taking the coordinate system for the laminate as shown in Figure B-6, the stress resultants become:

$$\begin{bmatrix} \mathbf{N} \\ \mathbf{M} \end{bmatrix} = \sum_{k=1}^n \int_{z_{k-1}}^{z_k} \begin{bmatrix} (\mathbf{c}^{(E)}\mathbf{S} - \mathbf{e}_t\mathbf{E})_k \\ (\mathbf{c}^{(E)}\mathbf{S} - \mathbf{e}_t\mathbf{E})_k z \end{bmatrix} dz$$

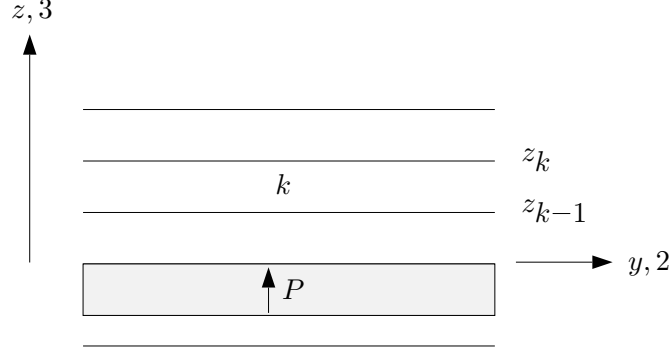


Figure B-7: For a laminated plate of varying materials and thicknesses, the coordinate system is defined such that the k^{th} layer has bottom coordinate z_{k-1} and top coordinate z_k . Layers may be of arbitrary thickness and material.

where $\mathbf{c}^{(E)}$ signifies \mathbf{c} for a passive layer and \mathbf{c}^E for a piezoelectric layer. In non-active layers, $\mathbf{e} = 0$. Substituting in the strain-displacement relations:

$$\begin{bmatrix} \mathbf{N} \\ \mathbf{M} \end{bmatrix} = \sum_{k=1}^n \int_{z_{k-1}}^{z_k} \begin{bmatrix} \left(\mathbf{c}^{(E)} \begin{bmatrix} \epsilon_o \\ z\kappa \end{bmatrix} - \mathbf{e}_t \mathbf{E} \right)_k \\ \left(\mathbf{c}^{(E)} \begin{bmatrix} \epsilon_o \\ z\kappa \end{bmatrix} - \mathbf{e}_t \mathbf{E} \right)_k \end{bmatrix} dz$$

This now reduces to the form given in [Crawley and Lazarus 91] of:

$$\begin{bmatrix} \mathbf{N} \\ \mathbf{M} \end{bmatrix} = \begin{bmatrix} \mathbf{A} & \mathbf{B} \\ \mathbf{B} & \mathbf{D} \end{bmatrix} \begin{bmatrix} \epsilon_o \\ \kappa \end{bmatrix} - \begin{bmatrix} \mathbf{N}^{elec} \\ \mathbf{M}^{elec} \end{bmatrix}$$

where:

$$A_{ij} = \sum_{k=1}^n c_{ij}^{(E)k} (z_k - z_{k-1})$$

$$B_{ij} = \frac{1}{2} \sum_{k=1}^n c_{ij}^{(E)k} (z_k^2 - z_{k-1}^2)$$

and:

$$D_{ij} = \frac{1}{3} \sum_{k=1}^n c_{ij}^{(E)k} (z_k^3 - z_{k-1}^3)$$

The components of the stress resultants due to electromechanical coupling are:

$$\begin{bmatrix} \mathbf{N}^{elec} \\ \mathbf{M}^{elec} \end{bmatrix} = \sum_{k=1}^n \int_{z_{k-1}}^{z_k} \begin{bmatrix} \mathbf{e}_t \mathbf{E} \\ \mathbf{e}_t \mathbf{E} z \end{bmatrix} dz$$

Substituting into Hamilton's Principle, we can find the dynamic equations of a laminated plate and relate the notation for the mass, stiffness and electromechanical coupling matrices

of [Hagood, Chung and Von Flutow 90] to those of [Crawley and Lazarus 91]. Hamilton's Principle can be written:

$$\int_{t_1}^{t_2} \delta (T_{kin} - U + W_{elec} + W) dt = 0$$

For a system driven only by electrical excitation with no external forcing, $W = 0$. The variation in electrical work done on the system is also zero:

$$\delta W_{elec} = \int_V \delta \left(\frac{1}{2} \mathbf{E}^T \mathbf{D} \right) dV = \int_V (\mathbf{D} \cdot \delta \mathbf{E}) dV = 0$$

as there is no variation in electric field if it is prescribed and where we have used the relation:

$$\delta f = \frac{\partial f}{\partial x} \delta x$$

The variation in internal stored energy is given as:

$$\delta U = \int_V \delta \left(\frac{1}{2} \mathbf{S}^T \mathbf{T} \right) dV = \int_V (\mathbf{T} \cdot \delta \mathbf{S}) dV$$

which is equal to:

$$\delta U = \int_x \int_y \left\{ \begin{bmatrix} \mathbf{N}_t & \mathbf{M}_t \end{bmatrix} \begin{bmatrix} \delta \epsilon_o \\ \delta \kappa \end{bmatrix} - \begin{bmatrix} \delta \epsilon_{ot} & \delta \kappa_t \end{bmatrix} \begin{bmatrix} \mathbf{N}^{elec} \\ \mathbf{M}^{elec} \end{bmatrix} \right\} dx dy$$

where the t subscripts signify a transpose of the vector. In terms of the resultant stiffness matrices, \mathbf{A} , \mathbf{B} and \mathbf{D} , the variation in internal stored energy is:

$$\delta U = \int_x \int_y \left\{ \begin{bmatrix} \epsilon_{ot} & \kappa_t \end{bmatrix} \begin{bmatrix} \mathbf{A} & \mathbf{B} \\ \mathbf{B} & \mathbf{D} \end{bmatrix} \begin{bmatrix} \delta \epsilon_o \\ \delta \kappa \end{bmatrix} - \begin{bmatrix} \delta \epsilon_{ot} & \delta \kappa_t \end{bmatrix} \begin{bmatrix} \mathbf{N}^{elec} \\ \mathbf{M}^{elec} \end{bmatrix} \right\} dx dy$$

Replacing the midline strains and curvatures by the differential matrix operator and the Rayleigh-Ritz assumed solutions gives:

$$\delta U = \int_x \int_y \left\{ \begin{bmatrix} \mathbf{L}_o \psi_p \end{bmatrix}^T \mathbf{p}(t) \begin{bmatrix} \mathbf{A} & \mathbf{B} \\ \mathbf{B} & \mathbf{D} \end{bmatrix} \begin{bmatrix} \mathbf{L}_o \psi_p \end{bmatrix} \delta \mathbf{p} - \begin{bmatrix} \mathbf{L}_o \psi_p \end{bmatrix}^T \begin{bmatrix} \mathbf{N}^{elec} \\ \mathbf{M}^{elec} \end{bmatrix} \delta \mathbf{p}(t) \right\} dx dy$$

The first term on the right can be written:

$$\mathbf{Kp}(t) \delta \mathbf{p}(t)$$

where \mathbf{K} is as used in [Crawley and Lazarus 91]:

$$\mathbf{K} = \int_x \int_y [\mathbf{L}_o \psi_p]^T \begin{bmatrix} \mathbf{A} & \mathbf{B} \\ \mathbf{B} & \mathbf{D} \end{bmatrix} [\mathbf{L}_o \psi_p] dx dy$$

The second term on the right has a dependence on the electric field. As voltage is the negative of the gradient of the electric field, \mathbf{E} can also be expressed as a differential operator acting on a matrix of assumed potential shapes and a generalized electrical coordinate $\mathbf{v}(t)$:

$$\mathbf{E} = \mathbf{L}_v \psi_v(x, y, z) \mathbf{v}(t)$$

The components of the stress resultants due to electromechanical coupling become:

$$\begin{bmatrix} \mathbf{N}^{elec} \\ \mathbf{M}^{elec} \end{bmatrix} = \sum_{k=1}^n \begin{bmatrix} \mathbf{e}_t(z_k - z_{k-1}) \\ \mathbf{e}_t \frac{(z_k + z_{k-1})}{2} (z_k - z_{k-1}) \end{bmatrix} \mathbf{L}_v \psi_v \mathbf{v}(t)$$

The second term in the expression for the variation in internal stored energy then is:

$$\int_x \int_y [\mathbf{L}_o \psi_p]^T \sum_{k=1}^n \begin{bmatrix} \mathbf{e}_t(z_k - z_{k-1}) \\ \mathbf{e}_t \frac{(z_k + z_{k-1})}{2} (z_k - z_{k-1}) \end{bmatrix} \mathbf{L}_v \psi_v dx dy \mathbf{v}(t) \delta \mathbf{p}(t)$$

This statement can be rewritten as:

$$\theta \mathbf{v}(t) \delta \mathbf{p}(t)$$

where θ is the electromechanical coupling matrix formulated in [Hagood, Chung and Von Flutow 90]:

$$\theta = \int_x \int_y [\mathbf{L}_o \psi_p]^T \sum_{k=1}^n \begin{bmatrix} \mathbf{e}_t(z_k - z_{k-1}) \\ \mathbf{e}_t \frac{(z_k + z_{k-1})}{2} (z_k - z_{k-1}) \end{bmatrix} \mathbf{L}_v \psi_v dx dy$$

If T_{kin} for a plate is zero and the plate is only deflected statically by an applied \mathbf{v} ,

Hamilton's Principle reduces to:

$$\int_{t_1}^{t_2} (\mathbf{K}\mathbf{p} - \theta\mathbf{v}) \delta\mathbf{p} dt = 0$$

Since the variation, $\delta\mathbf{p}$, is arbitrary, it must be the case that:

$$\mathbf{K}\mathbf{p} - \theta\mathbf{v} = 0$$

which is the equation of motion for the statically driven plate. The modal amplitudes can be found by inverting the stiffness matrix:

$$\mathbf{p} = \mathbf{K}^{-1}\theta\mathbf{v}$$

The final deformations are then calculated by multiplying the mode shapes by the modal amplitudes and summing.

For a dynamic plate:

$$T_{kin} = \int_V \frac{1}{2} \rho \dot{\mathbf{u}}^T \dot{\mathbf{u}} dV$$

Ignoring rotary inertia and assuming \mathbf{u} is the vector of centerline displacements, \mathbf{u}_o , and substituting Rayleigh-Ritz assumed solutions, gives the variation in kinetic energy as:

$$\delta T_{kin} = \int_V \rho \psi_p^T \dot{\mathbf{p}} \psi_p \delta \dot{\mathbf{p}} dV$$

Integrating by parts:

$$\int_{t_1}^{t_2} \delta T_{kin} dt = - \int_{t_1}^{t_2} \int_V \rho \psi_p^T \psi_p \ddot{\mathbf{p}} \delta \mathbf{p} dV dt$$

The mass matrix as defined in [Hagood, Chung and Von Flutow 90] is then seen to be for a plate:

$$\mathbf{M} = \int_x \int_y \psi_p^T \sum_{k=1}^n \rho_k (z_k - z_{k-1}) \psi_p dx dy$$

Hamilton's Principle now becomes:

$$\int_{t_1}^{t_2} (-\mathbf{M}\ddot{\mathbf{p}} - \mathbf{K}\mathbf{p} + \theta\mathbf{v}) \delta\mathbf{p} dt = 0$$

Because the variation in the modal amplitudes, $\delta \mathbf{p}$, is arbitrary, the dynamic equations of an electromechanically coupled plate result:

$$\mathbf{M}\ddot{\mathbf{p}} + \mathbf{K}\mathbf{p} - \theta \mathbf{v} = 0$$

By calculating the \mathbf{M} , \mathbf{K} and θ matrices for a laminated plate as derived, the time evolution of the dynamic system can be computed.

B.2.1 Simulation Results

The model of [Hagood and McFarland 95] was implemented for an asymmetric free-free composite piezoelectric plate in cylindrical coordinates and compared to measured results of a free-standing stator, Grey1.

In cylindrical coordinates, plane-stress assumptions lead to displacements of the form:

$$u(r, \theta, t) = u_o - z \frac{\partial w_o}{\partial r}$$

$$v(r, \theta, t) = v_o - z \frac{1}{r} \frac{\partial w_o}{\partial \theta}$$

$$w(r, \theta, t) = w_o$$

where u , v and w are displacements in the r , θ and z directions, respectively. Strain-displacement relations in cylindrical coordinates, [Timoshenko and Goodier 87], are derived from cutting a cylindrical section of a thin plate as in Figure B-8. Figure B-8(a) illustrates the radial and tangential deformations while Figure B-8(b) depicts in-plane shear deformations. The deformation of section $abcd$ to $a'b'c'd'$ involves a rotation, $\frac{v}{r}$, which must be subtracted from the total angular change, $\frac{1}{r} \frac{\partial u}{\partial \theta} + \frac{\partial v}{\partial r}$. The plane-stress strain-displacement relations become:

$$\begin{bmatrix} S_1 \\ S_2 \\ S_6 \end{bmatrix} = \begin{bmatrix} \frac{\partial u}{\partial r} \\ \frac{1}{r} \frac{\partial v}{\partial \theta} + \frac{u}{r} \\ \frac{1}{r} \frac{\partial u}{\partial \theta} + \frac{\partial v}{\partial r} - \frac{v}{r} \end{bmatrix}$$

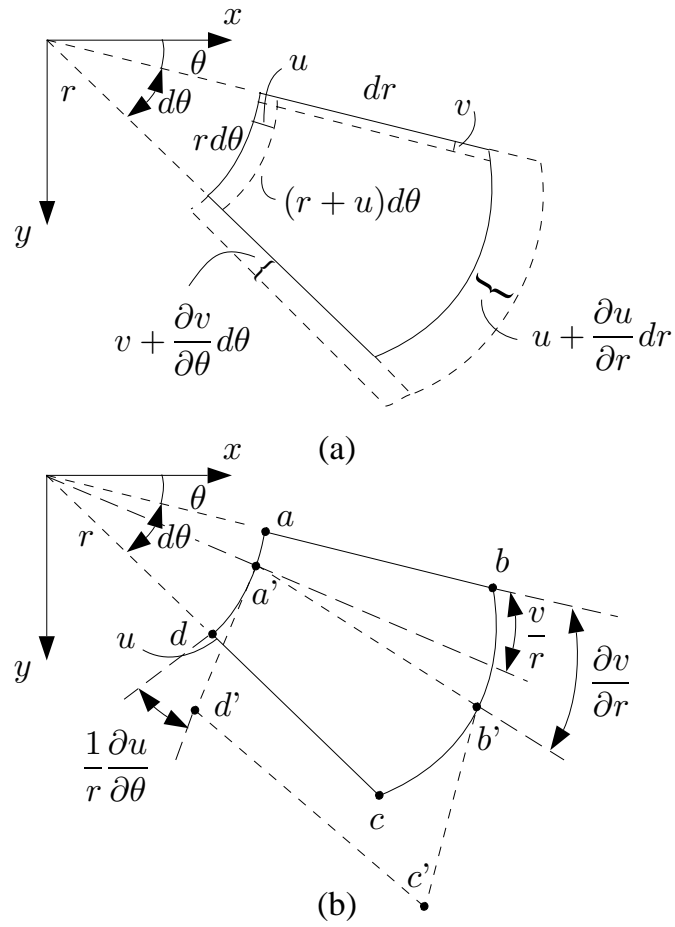


Figure B-8: In cylindrical coordinates, the strain-displacement relations take on a new form. (a) The in-plane extensional strain is a function of radial displacement, u , while the in-plane tangential strain is a function of both the radial displacement, u , and the tangential displacement, v . (b) In-plane shear strains formulations must make sure to subtract off rotations.

which results in an ϵ_o - κ vector of:

$$\begin{bmatrix} \epsilon_o \\ \kappa \end{bmatrix} = \begin{bmatrix} \frac{\partial}{\partial r} & 0 & 0 \\ \frac{1}{r} & \frac{1}{r} \frac{\partial}{\partial \theta} & 0 \\ 0 & 0 & 0 \\ 0 & 0 & -\frac{\partial^2}{\partial r^2} \\ 0 & 0 & \left(-\frac{1}{r} \frac{\partial}{\partial r} - \frac{1}{r^2} \frac{\partial^2}{\partial \theta^2} \right) \\ 0 & 0 & \left(-\frac{2}{r} \frac{\partial^2}{\partial \theta \partial r} + \frac{2}{r^2} \frac{\partial}{\partial \theta} \right) \end{bmatrix} \begin{bmatrix} u_o \\ v_o \\ w_o \end{bmatrix}$$

If we are interested in the out-of-plane deflection of the neutral axis of the plate, ignoring small in-plane extensions, we solve only for w_o . We take the Rayleigh-Ritz assumed solutions for w_o for the annular plate as a sum of products of mode shapes (independent of time) and modal amplitudes (independent of geometry):

$$w_o(r, \theta, t) = \sum_i \psi_{p_i}(r, \theta) p_i(t)$$

To simulate our motor, we choose two mode shapes to meet the geometric free-free boundary conditions at the inner and outer circumferences, one with no radial variation and one linearly proportional to r :

$$\psi_p = [\cos(3\theta) \quad \left(\frac{r-a}{b-a} \right) \cos(3\theta)]$$

For an unsymmetric (in the z -direction) plate, the ϵ_o vector is not the vector of midplane strains, but more precisely, the neutral axis strains. The neutral axis location, g , from the bottom of the plate is taken as a ratio of weighted stiffnesses:

$$g = \frac{\int z c_{11}^{(E)} dz}{\int c_{11}^{(E)} dz}$$

where $z_{(k-1)}$ of the 0^{th} layer is then equal to $-g$. The \mathbf{L}_o matrix can now be found and the \mathbf{M} and \mathbf{K} matrices calculated.

The electromechanical coupling term, $\theta \mathbf{v}$, determines the forcing in this system. The piezoelectric layer is segmented and poled alternately in such a manner as to induce a three-wavelength bending mode, as shown in Figure 7-6. The generalized electrical coordinates, $\mathbf{v}(t)$, are taken as the applied voltages, V , while the mode shapes are either +1 or -1

depending on the poling direction of the segment. As the electric field is the negative of the gradient of the potential, the differential operator, \mathbf{L}_v , can be taken as the reciprocal of the layer thickness. The θ matrix is then computed using:

$$E_3 = \pm \frac{V}{z_k - z_{k-1}}$$

For a static plate deformation, the modal amplitudes are found from:

$$\mathbf{p} = \mathbf{K}^{-1}\theta\mathbf{v}$$

and combined with the mode shapes to find the neutral axis deflection in the z -direction, w_o :

$$w_o(r, \theta, t) = \psi_{p_1}(r, \theta)p_1(t) + \psi_{p_2}(r, \theta)p_2(t)$$

Dynamical properties of the system can also be calculated. System characteristics are found by examining the undriven response of the system. For no forcing, the equation of motion is simply:

$$\mathbf{M}\ddot{\mathbf{p}} + \mathbf{K}\mathbf{p} = 0$$

When we take:

$$p_i(t) = P_i e^{j\omega t}$$

we have an eigenvalue problem and can solve for the eigenfrequencies and mode shapes by taking derivatives:

$$[-\omega^2\mathbf{M} + \mathbf{K}]\mathbf{P} = 0$$

Natural frequencies are computed by calculating the eigenvalues of the $\mathbf{K} - \omega^2\mathbf{M}$ matrix:

$$[\mathbf{K} - \omega^2\mathbf{M}] = 0$$

The solution produces repeated roots which correspond to orthogonal modes of equal amplitude variation, $R(r)$. A new mode shape matrix is created to model the appropriate *sin* and *cos* modes for generating the traveling wave:

$$\psi'_p(r, \theta) = [R(r) \cos(3\theta) \quad R(r) \sin(3\theta)]$$

The radial dependence of each mode, $R(r)$, is composed by using the eigenvector, \mathbf{P} , to weight the two radial dependence terms of the initial assumed-modes matrix, ψ_p :

$$R(r) = P_1 + P_2 \left(\frac{r - a}{b - a} \right)$$

The \mathbf{M} , \mathbf{K} and θ matrices are then recalculated using the new ψ'_p mode-shape matrix. The new \mathbf{M} and \mathbf{K} matrices then become diagonal and we assume a proportional damping matrix \mathbf{C} :

$$C_{ii} = 2\xi\omega M_{ii}$$

where ξ is the damping coefficient related to the quality factor by $Q = \frac{1}{2\xi}$. The complete dynamical system can then be expressed as:

$$\mathbf{M}\ddot{\mathbf{p}} + \mathbf{C}\dot{\mathbf{p}} + \mathbf{K}\mathbf{p} = \theta\mathbf{v}$$

This equation can be re-expressed in terms of the modal amplitudes as:

$$\ddot{\mathbf{p}} = \mathbf{M}^{-1}\mathbf{C}\dot{\mathbf{p}} - \mathbf{M}^{-1}\mathbf{K}\mathbf{p} + \mathbf{M}^{-1}\theta\mathbf{v}$$

where this second order differential equation can be reduced to two first order differential equations by taking:

$$\mathbf{n} = \dot{\mathbf{p}}$$

The equation of motion can then be written in state-space form as:

$$\begin{bmatrix} \dot{\mathbf{n}} \\ \dot{\mathbf{p}} \end{bmatrix} = \begin{bmatrix} -\mathbf{M}^{-1}\mathbf{C} & -\mathbf{M}^{-1}\mathbf{K} \\ \mathbf{I} & \mathbf{0} \end{bmatrix} \begin{bmatrix} \mathbf{n} \\ \mathbf{p} \end{bmatrix} + \begin{bmatrix} \mathbf{M}^{-1}\theta\mathbf{v} \\ \mathbf{0} \end{bmatrix}$$

Once the modal amplitudes, \mathbf{p} , are found, they are combined with the modes of ψ'_p to calculate w_o :

$$w_o(r, \theta, t) = R(r)\cos(3\theta)p_1(t) + R(r)\sin(3\theta)p_2(t)$$

Figure B-9 shows simulation results for the driven response of a neutral axis out-of-plane displacement, w_o , of a composite plate similar to stator Grey1, consisting of PZT-5A material, product number PSI-5A from Piezo Systems, Cambridge, MA, [Piezo Systems 95], bonded onto a steel substrate. The composite plate has an inner diameter of 5 mm and an

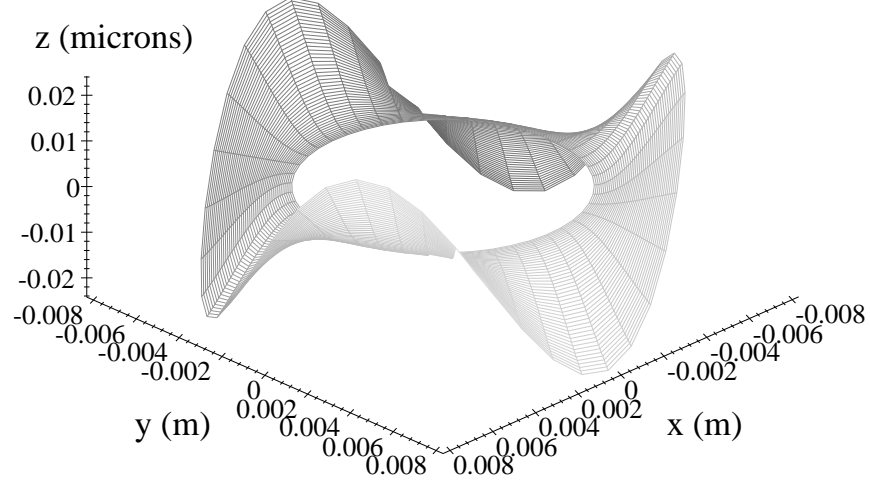


Figure B-9: A cylindrical plate with a piezoelectric layer bonded onto a steel substrate. The piezoelectric segments are driven dynamically at 60 V_{peak}, 90 degrees out of phase at 18 kHz. The damping is 0.2%.

outer diameter of 8 mm. The PZT layer is 0.191 mm thick and the base height of the stator is 0.381 mm thick. The density of PSI-5A used in the simulation is $7750 \frac{kg}{m^3}$ and the density of stainless steel is $7860 \frac{kg}{m^3}$. The measured value of stator Grey1's damping coefficient, $\xi = 2\%$ was used for the calculation of the modal damping matrix, \mathbf{C} . The initial conditions are taken at rest and the plot in Figure B-9 is drawn at 0.01 seconds after turn-on.

The materials matrices characterizing the PZT layer are the plane-stress piezoelectric matrix, \mathbf{e}_{PZT}^* :

$$\mathbf{e}_{PZT}^* = \begin{bmatrix} 0 & 0 & 0 \\ 0 & 0 & 0 \\ e_{31}^* & e_{31}^* & 0 \end{bmatrix} = \begin{bmatrix} 0 & 0 & 0 \\ 0 & 0 & 0 \\ -14.9 & -14.9 & 0 \end{bmatrix} \frac{C}{m^2}$$

and the plane-stress stiffness matrix, $\mathbf{c}_{PZT}^{E^*}$:

$$\mathbf{c}_{PZT}^{E^*} = \begin{bmatrix} c_{11}^{E^*} & c_{12}^{E^*} & 0 \\ c_{12}^{E^*} & c_{11}^{E^*} & 0 \\ 0 & 0 & c_{66}^{E^*} \end{bmatrix} = \begin{bmatrix} 67.0 & 20.1 & 0 \\ 20.1 & 67.0 & 0 \\ 0 & 0 & 23.5 \end{bmatrix} \times 10^9 \frac{N}{m^2}$$

For stainless steel, the Young's modulus is $190 \times 10^9 \frac{N}{m^2}$, giving the isotropic material a stiffness matrix of:

$$\mathbf{c}_{steel} = \begin{bmatrix} c_{11} & 0 & 0 \\ 0 & c_{11} & 0 \\ 0 & 0 & c_{11} \end{bmatrix} = \begin{bmatrix} 190 & 0 & 0 \\ 0 & 190 & 0 \\ 0 & 0 & 190 \end{bmatrix} \times 10^9 \frac{N}{m^2}$$

The simulation predicted a resonant frequency of 18.0 kHz and a deflection of approximately $20 \mu\text{m}$ at resonance. The actual measured natural frequency at the third bending mode was 42.2 kHz and the amplitude of deflection was on the order of $4.5 \mu\text{m}$. The discrepancy in natural frequency can be attributed to the fact that the materials parameters used in the simulation may not be accurate, the teeth of the stator are not modeled, the interconnects on the electrode patterns are not modeled, the electrodes are not perfectly matched in terms of resonance characteristics and/or the epoxy bond layer is ignored. As the deflection amplitudes are dependent on the drive frequency, we expect the predicted amplitudes to be off if the predicted natural frequencies are not correct. We also know that stator Grey1 does not exhibit complete uniformity in traveling wave amplitude at all points around the stator, so it is not acting in quite the manner that it is modeled.

Rotor coupling can be appended to this model by calculating modal forces in the directions tangential and normal to the stator surface. [Hagood and McFarland 95] illustrates this process for a symmetric ring-type motor clamped at the inner circumference where the equations of motion for the stator are written as:

$$\mathbf{M}\ddot{\mathbf{p}} + \mathbf{C}\dot{\mathbf{p}} + \mathbf{K}\mathbf{p} = \theta\mathbf{v} + \mathbf{F}_{modal,N} + \mathbf{F}_{modal,T}$$

and the rotor is modeled by equations of motion in the rotary direction, parameterized by the angle, α :

$$I_{rotor}\ddot{\alpha} + C_{\alpha}\dot{\alpha} = \tau_{int} - F_B r$$

and in the z -direction, parameterized by the flexure height, w_f , the distance between the undeformed stator height and the rotor lower surface:

$$M_{rotor}\ddot{w}_f + C_z\dot{w}_f = F_{int} - F_N$$

where τ_{int} and F_{int} are the interface torques and forces coupling the stator and rotor models. The rotor equations of motion can be written in state-space form as:

$$\begin{bmatrix} \dot{\alpha} \\ \ddot{\alpha} \\ \dot{w}_f \\ \ddot{w}_f \end{bmatrix} = [A_r] \begin{bmatrix} \alpha \\ \dot{\alpha} \\ w_f \\ \dot{w}_f \end{bmatrix} + [B_r] \begin{bmatrix} \tau_{int} - F_B r \\ F_{int} - F_N \end{bmatrix}$$

and combined with the stator model to model the entire assembly.

This method of [Hagood and McFarland 95] can be extended here for an asymmetric free-free ring and the contact models discussed earlier can be superimposed to compare their predictions and yet take into account the decrease in stator deflection due to the applied normal force and the extraction of mechanical work.